Discovery and Investigation of High-Capacity Cathode Materials for Next Generation Li-ion Batteries



Rong Hao

Hertford College

Department of Materials

University of Oxford

A thesis submitted in fulfilment of the requirements for the Degree

of

Doctor of Philosophy (D.Phil.)

Michaelmas 2017

谨以此论文

献给我至爱的父母

感激他们的辛勤养育和无私的爱

我深爱他们

祝福他们在未来的日子里健康幸福，平安喜乐

To my beloved father and mother

For they raising me and their selfless love to me

I love them deeply in my soul

With all my heart, I wish them healthy, peaceful, and happy in life

DECLARATION OF ORIGINALITY

I, the undersigned Rong Hao, hereby declare that all work presented in this thesis for the *Doctor of Philosophy (D.Phil.)* Degree, which is approximately 40,000 words in length, is original and where the work of others has been included it has been clearly referenced and acknowledged. This thesis is an account of work carried out at the School of Chemistry, University of St Andrews between October 2013 and November 2014 and the Department of Materials, University of Oxford between November 2014 and December 2017, under the supervision of Prof. Peter G. Bruce. No part of this thesis has been submitted towards another degree at the University of Oxford or elsewhere.

Signature



Rong Hao

09 January 2018

ACKNOWLEDGEMENT

I would like to gratefully acknowledge Prof. Peter G Bruce FRS for offering me the privilege to study and work in a world-class laboratory and to collaborate with world's top-level researchers. His passion towards science motivates me to pursue the true science and his supervision inspires me to give my best in delivering high-quality scientific outputs. What I have learnt from him and this laboratory have not only broadened my knowledge and views, but also shaped me as a person. This unforgettable journey will surely be life-time treasure for me. I sincerely appreciate the generous financial support throughout my D.Phil. from School of Chemistry, University of St Andrews, Department of Materials and Hertford College, University of Oxford, and Dyson Limited.

A special thanks goes to Dr Matthew Roberts for being a great mentor, generously sharing his knowledge, and patiently providing me great advice and support during my D.Phil. I would also like to thank all of the members of the Peter G Bruce's group for them being such great colleagues and companions.

To highlight, a very special thanks and gratitude goes to my father Denghua Hao and my mother Wenying Zhang, for their selfless love and support in my life. From the moment of my birth, I have been immersed in the love of family. Over the years, they taught me to be a person with dignity, loyalty and glory, just as who they are. From every aspect, they have sacrificed a lot for me. However, I feel deeply sorry that I haven't neither done enough for them as a son nor accompanied with them for a long

period, due to pursuing further education. How I wish to be their side more and enjoy the love and time of family. I would like to credit this remarkable achievement of mine to both of them. I hope I have made them proud and lived up to their expectation. They are indeed the most important people in my life and I pray for them for being healthy peaceful, and happy in life.

As a boy from a small town in China, I am extremely lucky to have the privilege to be educated in the world's top University and I have walked so far to get here. I sincerely thank those families, mentors, and friends, who have helped me on this journey.

Finally, as promised at the very beginning of my D.Phil., a very special "thank you" to the one I loved, Ms Yufeng Peng, for the happiness she brought, the time and experiences we went through together, her company in the past years, and the memory we shared.

CONTENTS

ABSTRACT 1

CHAPTER 1 INTRODUCTION 3

1.1. Li-ion Batteries 3
1.1.1. History 3
1.1.2. Principle 5
1.1.3. Components for Li-ion Batteries 8
1.2. Conventional Cathode Materials for the Li-ion Batteries 18
1.2.1. Layered Cathode Materials 19
1.2.2. Spinel Structured Cathode Materials 23
1.2.3. Olivine Structured Cathode Materials 24
1.3. Layered Li-rich Cathode Materials 26
1.3.1. Origin and Structure complexity 26
1.3.2. Challenges 30
1.3.3. Underlying Chemistry 32

CHAPTER 2 EXPERIMENTAL METHODOLOGIES 35

2.1. Chemicals 35
2.2. Synthesis Methodologies 35
2.2.1. Solid-State Synthesis 35
2.2.2. Co-precipitation Synthesis 36
2.2.3. Sol-Gel Synthesis 37
2.3. Characterization Methodologies 37
2.3.1. Scanning Electron Microscope (SEM) 37
2.3.2. Energy Dispersive X-Ray Spectrometry (EDX)[192] 39
2.3.3. Inductively Coupled Plasma Optical Emission Spectrometry (ICP-OES)[193] 40
2.3.4. Powder X-Ray Diffraction (PXRD) 41
2.3.5. Electrochemical Measurements 46
2.3.6. Differential Electrochemical Mass Spectrometry (DEMS) 49
2.3.7. Raman Spectroscopy 50
2.3.8. X-ray Absorption Near Edge Structure (XANES) 52
2.3.9. Soft X-ray Absorption Spectroscopy (SXAS) 54
2.3.10. Resonant Inelastic X-Ray Scattering (RIXS) 56

CHAPTER 3 PREPARATION AND CHARACTERIZATION OF THE LAYERED LI-RICH CATHODE MATERIAL 58

3.1. BACKGROUND 58
3.2. RESEARCH GOAL 59
3.3. EXPERIMENT DETAILS 59
3.3.1. CARBONATE CO-PRECIPITATION SYNTHESIS 59
3.3.2. OXALATE CO-PRECIPITATION SYNTHESIS 60
3.3.3. RESORCINOL - FORMALDEHYDE GEL (R-F GEL) SYNTHESIS 61
3.3.4. COMPOSITION, MORPHOLOGY AND STRUCTURE CHARACTERIZATION 62
3.3.5. ELECTROCHEMICAL TESTS 63
3.4. RESULTS AND DISCUSSION 64
3.4.1. COMPOSITIONS, MORPHOLOGY AND CRYSTALLOGRAPHIC STRUCTURE 64
3.4.2. ELECTROCHEMISTRY 71
3.5. CONCLUSION 81

CHAPTER 4 BINDER EFFECTS ON THE ELECTROCHEMICAL PERFORMANCE OF LI-RICH CATHODE MATERIAL 83

4.1. BACKGROUND 83
4.2. RESEARCH GOAL 84
4.3. EXPERIMENT DETAILS 85
4.3.1. ELECTRODE PROCESSING 85
4.3.2. ELECTROCHEMICAL TESTS 86
4.3.3. TOPOGRAPHY AND ELEMENTAL DISTRIBUTION CHARACTERIZATION 87
4.4. RESULTS AND DISCUSSION 88
4.4.1. PTFE BINDER EFFECTS 88
4.4.2. CMC-NA BINDER EFFECTS 96
4.5. CONCLUSION 101

CHAPTER 5 OXYGEN REDOX IN THE LAYERED LI-RICH CATHODE MATERIAL 103

5.1. BACKGROUND 103
5.2. RESEARCH GOAL 104
5.3. EXPERIMENTAL DETAIL 105
5.3.1. SYNTHESIS AND BASIC CHARACTERIZATIONS 105
5.3.2. OPERANDO DEMS 105
5.3.3. XANES 105
5.3.4. SXAS AND RIXS 106
5.3.5. RAMAN SPECTROSCOPY 106
5.4. RESULTS AND DISCUSSION 107
5.4.1. OXYGEN LOSS ON CHARGE 108
5.4.2. THE HOLE STATES OXIDATION 112
5.4.3. NATURE OF THE HOLES ON OXYGEN 116
5.4.4. MODEL FOR THE FORMATION OF ELECTRON-HOLE STATES ON OXYGEN 120
5.5. CONCLUSION 122

CHAPTER 6 OXYGEN REDOX IN A NOVEL CATION DISORDERED ROCK-SALT LI-RICH MATERIAL 124

6.1. BACKGROUND 124
6.2. RESEARCH GOAL 126
6.3. EXPERIMENT DETAILS 127
6.3.1. SOLID-STATE SYNTHESIS 127
6.3.2. BASIC CHARACTERIZATIONS 127
6.3.3. OPERANDO PXRD (OPXRD) 128
6.3.4. OPERANDO DEMS, RAMAN SPECTROSCOPY AND XANES 129
6.3.5. SXAS AND RIXS 129
6.4. RESULTS AND DISCUSSION 130
6.4.1. DISORDERED ROCK-SALT LI-RICH MATERIAL 130
6.4.2. GAS EVOLUTION ON CHARGE 133
6.4.3. THE HOLE STATES REDOX 136
6.4.4. NATURE OF THE HOLES ON OXYGEN 143
6.4.5. REVERSIBILITY OF OXYGEN REDOX AND STRUCTURE REVOLUTION 147
6.5. CONCLUSION 152

CHAPTER 7 GENERAL CONCLUSIONS AND FUTURE WORK 156

7.1. GENERAL CONCLUSIONS 156
7.2. FUTURE WORK 158

APPENDIX 160

APPX. 1. UNIT CELL PARAMETERS AND D-SPACING OF CRYSTAL SYSTEMS 160
APPX. 2. SYNTHESIS OF ^{18}O-LABELLED $Li_{1.2}Ni_{0.13}Co_{0.13}Mn_{0.54}O_2$ 161
APPX. 3. POSSIBILITY ON THE FORMATION OF ^{18}O-LABELLED O_2 AND CO_2 162
APPX. 4. OPERANDO DEMS USING ^{18}O-LABELLED $LiNi^{II}_{0.5}Mn^{IV}_{1.5}O_4$ 164
APPX. 5. CALCULATIONS RELEVANT TO TRANSITIONS OF THE O K EDGE SXAS SPECTRA 166
APPX. 6. PXRD OF THE BALL-MILLED $Li_{1.2}Mn_{0.4}Ti_{0.4}O_2$ 168
APPX. 7. MN AND TI K EDGE XANES SPECTROSCOPY OF $Li_{1.2}Mn_{0.4}Ti_{0.4}O_2$ AT DIFFERENT STATE OF CHARGE 169

LIST OF PUBLICATIONS 171

ABBREVIATION 172

LIST OF FIGURES 174

LIST OF TABLES 180

REFERENCES.....181

ABSTRACT

Lithium ion (Li-ion) batteries are the current state of the art for electrochemical energy storage and there is increasing demand for Li-ion batteries with a higher energy density. To achieve such a goal, cathode materials with higher capacity are required. Layered lithium rich (Li-rich) cathode materials are considered as a potential cathode candidate for future high capacity Li-ion batteries, mainly due to their large reversibly capacity of about 250 mAh g^{-1}. However, the underlying chemistry of these materials remains unclear. The goal of this D.Phil. project is to investigate the underlying chemistry of these materials, especially the origin of the extra capacity; then to explore new Li-rich cathode materials with high capacities.

The Resorcinol - Formaldehyde gel (R-F gel) method was selected from three different synthesis methods for preparing the layered Li-rich materials, as the material obtained by this method presented stable and enhanced electrochemical performance. By using a variety of characterization methodologies, a detailed study on the 1st cycle of $Li_{1.2}Ni_{0.13}Co_{0.13}Mn_{0.54}O_2$, an archetypal example of layered Li-rich materials, were carried out and the extra capacity was attributed to a reversible oxygen redox process. A model of this oxygen redox process was also proposed, suggesting the balance between ionicity and covalency of metal-oxygen (M-O) bond is essential for activating this reversible oxygen redox. Additionally, a study of the binder effects on a layered Li-rich cathode was carried out. It was demonstrated that different binders used in electrodes would influence the electrochemical performance of the layered Li-rich

cathode.

A subsequent work was to synthesize and investigate $Li_{1.2}Mn_{0.4}Ti_{0.4}O_2$, a disordered rock-salt Li-rich material, which also exhibits enormous capacity and 1st cycle load curve similar to the layered Li-rich materials. A reversible oxygen redox process was demonstrated to be responsible for its extra capacity by using a variety of characterization methodologies. Moreover, the rock-salt structure was found remaining stable in the 1st cycle. The study of disordered rock-salt $Li_{1.2}Mn_{0.4}Ti_{0.4}O_2$ brings a new perspective to the study of oxygen redox in Li-rich cathode materials.

CHAPTER 1 Introduction

Today, increasing concerns surround global warming and the demand rises on decarbonizing our energy system for a better and sustainable future. The storage of electrical energy is more crucial for human beings than ever before[1]. Rechargeable batteries (also called secondary batteries) have been used as effective devices for energy storage for more than one century starting with the invention of the Lead-acid battery. Among all the rechargeable batteries, the Lithium Ion (Li-ion) batteries are the current state of the art[2-4]. These devices are now providing energy storage solutions for everything from portable electronics to Electric Vehicles (EVs) and today are being considered as a potential grid storage solution. The Li-ion batteries are revolutionizing how human society stores and utilizes electrical energy and will revolutionize it further in the coming years[2-4].

In this chapter, a brief introduction about Li-ion batteries is given, including the history, principle and different components, among which cathode materials for Li-ion batteries are introduced in detail. Particularly, as the focus of my D.Phil. research, the layered Li-rich transition metal oxides and their relevant research are discussed comprehensively to provide sufficient background to the subsequent documents.

1.1. Li-ion Batteries

1.1.1. History

A forerunner of Li-ion batteries was lithium batteries which ultilize lithium metal as the

anode and had been intensively researched since the report of reversible de-/intercalation of Li^+ in Li_xTiS_2 by Exxon[5,6]. Commercial products were introduced to markets, such as Li/MoS_2 (Moli Energy) and Li/MnO_2 systems[7,8]. However, a series of accidents focused attention on the safety issues surrounding these lithium batteries. The use of a metal anode resulted in the growth of lithium dendrites which can result in the formation of short circuits. It consequently causes a rapid discharging of the battery and the generation of enormous amount of heat which can ultimately result in explosions[9]. Besides, the $LiClO_4$ salt, a component of the electrolyte formulation, is unstable and shock-sensitive. Additionally, an excess of lithium anode was needed in these batteries to compensate the poor cycling efficiency of the lithium, yet it was still insufficient for the long-term cycling. Consequently, these lithium batteries never became a significant part of the rechargeable battery market.

It is commonly agreed that the 1st commercialization of a Li-ion battery was achieved with $LiCoO_2$/Carbon (petroleum coke) system by Sony in 1991[10]. Such an achievement should also be credited to the "rocking-chair" concept[11] and the discovery of $LiCoO_2$[12]. Proposed by Armand in the late 1970s, the "rocking-chair" concept is to use two intercalation compounds of different electrochemical potential as two electrodes and Li^+ moves back and forth to de-intercalate at one side and intercalate at the other. In 1980, J. Goodenough *et al.*[12] at University of Oxford discovered that a family of lithium transition metal oxides in α-$NaFeO_2$ structure (space group #166, *R-3m*) is capable of de-/intercalating Li^+, among which $LiCoO_2$ appears to be the most promising one for battery application due to its advantages in capacity, reversibility, and rate

performance[13].

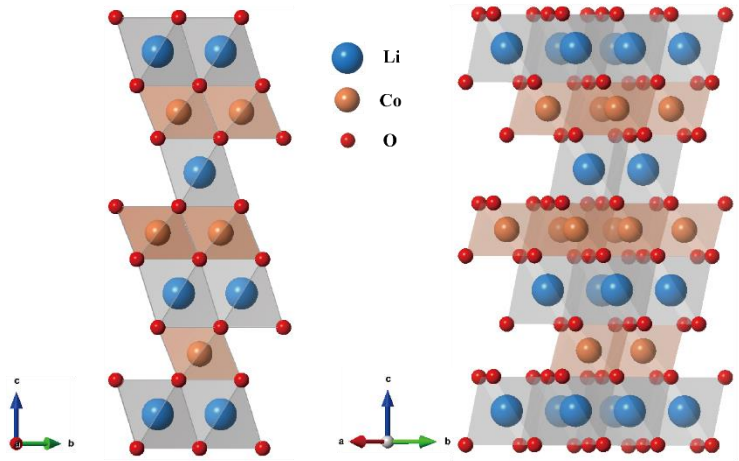

Figure 1-1 Schematic of a layered $LiCoO_2$ in *R-3m* space group (#166). The Li, Co, and O atoms are represented in blue, orange, and red spheres, respectively. The LiO_6 and CoO_6 octahedra are coloured in light grey and light orange, respectively.

Ever since the commercialization, Li-ion batteries have been continuously and intensively studied both in academia and in industry to drive them towards better energy storage devices. Nowadays, the market of Li-ion batteries is growing every year due to the transition from combustion engine vehicles to EVs. Although a few new battery systems, such Li-S, Li-Air and Na-ion, have been proposed and are receiving academic study, Li-ion batteries and their relevant research remain the mainstream and will continuously drive the future of energy storage.

1.1.2. Principle

A Li-ion battery consists of cathode, anode, electrolyte, separator and current collector. To be noticed, the electrodes, both the cathode and anode, consist of active materials, conductive additive(s) and binder(s). The active material is the actual component for charge storage, while the conductive additive, normally carbon in various forms,

disperses between active material particles to enhance the electronic conductivity. The binder works to bind the active material and conductive additive(s) together, and to adhere them onto the metallic current collector(s). Generally, the phrase "cathode material" (or "anode material") refers to the "cathode active material" (or "anode active material"). The cathode material in a Li-ion battery is normally a lithium transition metal oxide or lithium transition metal phosphate that can de-/intercalate Li^+ and they operate at a relatively higher electrochemical potential (versus the reference electrode). The anode material, on the other hand, is a compound that can be de-/lithiated and it operates at a relatively lower electrochemical potential. It does not necessarily need to be a de-/intercalation compounds (e.g. $Li_4Ti_5O_{12}$[14]), but can also be de-/insertion materials (e.g. graphite[15] and hard carbon[16]), de-/alloy materials (e.g. Si[17] and SnO_2[18]) or even de-/conversion materials (e.g. α-Fe_2O_3[19] and Co_3O_4[20]). The electrolyte for current Li-ion batteries is normally lithium salt containing non-aqueous liquid, which transports Li^+ between the cathode and anode back and forth during battery operation. The separator is a porous insulating membrane that prevents short-circuit between cathode and anode but allows the Li^+ ions to migrate freely.

Upon charging a Li-ion battery, Li^+ ions are deintercalated from the cathode material with electron (e^-) extraction and cathode material oxidation. These ions then migrate through the electrolyte and lithiate the anode material while the e^- flows through the external circuit to the anode. On discharging such process reverses, in which the anode material is delithiated and the cathode material is reduced while Li^+ ions are intercalated. Altogether, the charge and discharge of a Li-ion battery rely on the charge transfer

between cathode and anode and its associated electrochemical redox reaction(s).

The theoretical charge and discharge capacity of an electrode can be calculated based on the charge transferred using the Faraday's law.

$$Q = \frac{nF}{M} \bullet \frac{1000}{3600} \qquad \text{(Equation 1-1)}$$

Where n is the charge transferred (e^-), F is the Faraday constant (96485.33289(59) C mol^{-1} or sA mol^{-1}), M is the molar mass of the active material (in g mol^{-1}), and Q is the theoretical capacity of the active material (in mAh g^{-1}).

Consequently, the theoretical charge and discharge capacity of a Li-ion battery is limited by either the cathode or anode material that has lower theoretical capacity. This limiting factor is normally the cathode material for the case of today's Li-ion batteries.

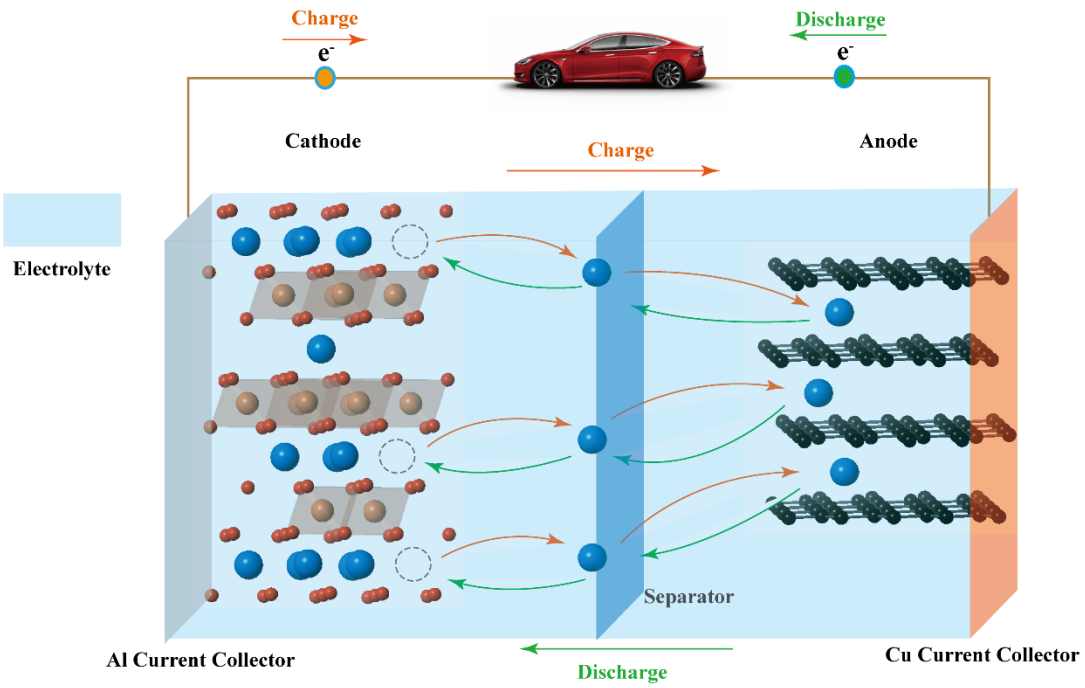

Figure 1-2 Schematic of a Li-ion battery with $LiCoO_2$ as the cathode active material and graphite as the anode active material

In Figure 1-2, a Li-ion battery, containing a $LiCoO_2$ based cathode, graphite based anode and $LiPF_6$ based electrolyte, is used as an example to better illustrate the mentioned principle.

The reactions which take place at the two electrodes are expressed in the following equations, respectively:

$$\text{Cathode: } LiCo^{+3}O_2 \underset{\text{Intercalation}}{\overset{\text{Deintercalation}}{\rightleftharpoons}} Li_{1-x}Co^{+(3+x)}O_2 + xLi^+ + e^- \quad \text{(Equation 1-2)}$$

$$\text{Anode: } xLi^+ + C_6 + xe^- \underset{\text{Delithiation}}{\overset{\text{Lithiation}}{\rightleftharpoons}} Li_xC_6 \quad \text{(Equation 1-3)}^{21}$$

Assuming that theoretically one Li^+ could be de-/intercalated per formula unit while the redox reaction of Co^{3+}/Co^{4+}, the theoretical charge and discharge capacity of $LiCoO_2$ could be calculated as:

$$Q_{LiCoO_2} = \frac{1(e^-) \bullet 96485.33289}{97.873} \bullet \frac{1000}{3600} \text{ mAh g}^{-1} = 273.8394 \text{ mAh g}^{-1}$$

However, in practice, only about 0.5 Li^+ could be de-/intercalated per formula unit for $LiCoO_2$, which makes its capacity limited to 136.9196886 mAh g^{-1}. This is discussed in detail in section 1.2.1.

1.1.3. Components for Li-ion Batteries

As mentioned above, a Li-ion battery consists of several different components. In this section, a brief introduction is given to these components, including the anode materials, electrolyte, separator and current collector. The cathode materials will be introduced in more detail in sections 1.2 since this is the major focus of this thesis.

1.1.3.1. Anode Materials

Ideal anode materials for Li-ion batteries would have a high specific capacity, good reversibility, high coulombic efficiency (delithiation capacity/lithiation capacity) and a low and flat voltage plateau versus Li^+/Li redox couple during de-/lithiation. Additionally, safety is of a major concern. Possible Li plating and dendrites formation during lithiation of the anode at a low-voltage versus Li^+/Li must be avoided when considering an anode material. Therefore, it is also preferable for anode materials to have a chemically stable surface on combination with the electrolyte at low potentials to form a stable Solid-Electrolyte-Interface (SEI)[i], which prevents further side reactions and in some cases prevents dendrites formation and growth. In the following, a few industrially favourable anode materials are introduced.

Carbon Based Materials

Today, carbon based materials are the most commonly used anode materials for Li-ion batteries. They can be generally categorized into to two classes - soft and hard carbon - based on the degree of crystallinity and carbon stacking. The soft carbon, or graphitizable carbon, has its crystallites stacked in ordered orientation, whereas the hard carbon, or non-graphitizable carbon, has its crystallites stacked in disordered orientations[24-26]. The soft carbon materials, such as graphite, are favourable for the commercial application, due to its advantages in reversible specific capacity (350-360

[i] SEI: The SEI model is, proposed by Peled in 1979, valid for all alkali metals or an electrode being applied at a negative potential in a non-aqueous electrolyte[22]. It forms instantaneously upon contact of the electrode and the electrolyte and consists of insoluble and partially soluble reduction products of electrolyte component[23].

mAh g^{-1}), reversibility, cycle life, coulombic efficiency (>90%) and low cost[27-29]. However, the specific capacity of soft carbon materials is still insufficient for the high energy density applications, such as EVs. Thus, the research community is exploring alternatives for enhancing specific capacity. Hard carbon has the advantage of higher specific capacity (> 500 mAh g^{-1} reported[30]). The main drawbacks of hard carbon are (a) poor rate performance (slow Li^+ diffusion); (b) low coulombic efficiency and (c) low tap density, which are all to do with the its disordered orientation[26].

Spinel $Li_4Ti_5O_{12}$

Another commercial anode material in use is the spinel lithium titanium (IV) oxide $Li_4Ti_5O_{12}$ (LTO). The structure conforms to be an ordered rock-salt structure when lithiated to $Li_7Ti_5O_{12}$ and returns to its original spinel structure when delithiated. The extremely low volume change (<0.2%) in this process enables its excellent reversibility and long cycle life[31,32]. As a result of its relatively high operation voltage plateau versus Li^+/Li, this material also avoids the problem of lithium dendrite formation and eliminates the safety concern[32]. However, it also brings up one of the drawbacks of LTO. This relatively high operation voltage plateau lowers the voltage of the Li-ion cell (the difference between the voltage of cathode and anode materials). Together with the low theoretical specific capacity of LTO (175 mAh g^{-1}), it results in a low energy density of a Li-ion cell using LTO anode. Moreover, in order to optimize the electronic conductivity of LTO, nano-sizing the LTO particles is necessary[32], which leads to a low tap density[ii]. In addition, the cost of LTO, both of the raw materials (mainly Li

[ii] Tap density is a critical parameter for the commercial application of electrode materials. It is an

precursors like Li_2CO_3) and production process, remains much higher and thus uncompetitive compared with carbon based anode materials.

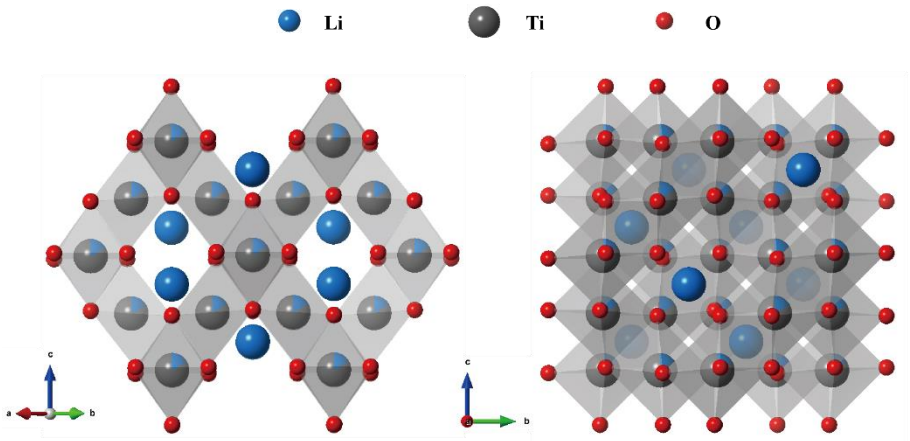

Figure 1-3 Schematic of a spinel $Li_4Ti_5O_{12}$ in Fd-3m space group (#227), in which 1/6 of octahedral sites (16d site) are occupied by Li. The Li, Ti, and O atoms are represented in blue, dark grey, and red spheres, respectively. The TiO_6/LiO_6 octahedra are coloured in light grey

Silicon (Si)

Si anode are currently receiving significant interests due to its high theoretical gravimetric[33,34] (4200 mAh g^{-1}, $Li_{22}Si_5$) and volumetric capacity[26] (9786 mAh cm^{-3}). In addition, the low lithiation voltage plateau versus Li^+/Li, around 0.4 V (close to graphite), enables a high operation voltage of Li-ion cells. The Si anode follows a de-/alloy mechanism rather than a de-/intercalation mechanism. A series of intermetallic Li-Si alloys, such as $Li_{12}Si_7$, Li_7Si_3, $Li_{15}S_4$ and $Li_{22}Si_5$, involve in the de-/alloy process, which is the origin of the enormous capacity. However, it also rises the severe issue of volume expansion/contraction (around 300% for $Li_{15}Si_4$ and >400% for $Li_{22}Si_5$) [29,35-37] during lithiation/delithiation, resulting in pulverization of the Si while cycling. This not

increased bulk density attained after mechanically tapping a container containing the powder sample. A higher tap density ensures higher active material loading on the electrode and consequently a higher energy density of the entire battery.

only causes the problem of losing contacts between particles, but also of consuming extra Li^+ to continuously form SEI layer on the fresh particle surfaces. Consequently, Si anodes suffer from poor reversibility and cycle life[33]. Therefore, in practice, the capacity of a Si anode is normally limited by purpose to control the degree of volume expansion. Various researches[26,29,33,38,39] have been conducted to tackle this problem, such as employing Si in different morphologies, nano-sizing the Si particles and confining its expansion in a matrix (e.g. carbon networks), and using Si-metal alloying instead of pure Si. Nevertheless, Si remains the most attractive anode material for the future of high energy density Li-ion batteries and it is believed that Carbon-Si or Carbon-Si-metal alloy composite materials has been commercialized by companies, such as Panasonic, LG and Samsung SDI, in small-scale for some high energy density Li-ion batteries already[39].

1.1.3.2. Electrolyte

The electrolytes used in Li-ion batteries are mainly non-aqueous liquid solutions, which contains at least one lithium salt as a solute, typically $LiPF_6$, and a mixture of non-aqueous liquids as a solvent, normally organic carbonates[25,40-44]. Particularly, for the electrolytes used in the commercial batteries, several additives are added[25,40,42-45] and ionic liquids may also be used[46]. This is both company and application specific. In addition, compared to conventional liquid electrolytes, polymer and solid-state electrolytes[47] are considered as a future systems, however, it is beyond the scope of this thesis to discuss them further. The following section will provide further details on the lithium salts (solute) and organic carbonate (solvent) liquid electrolytes.

Lithium Salts for Non-Aqueous Liquid Electrolytes

The lithium salts for non-aqueous liquid electrolytes should meet several minimum requirements[41,48], including (a) fully dissolving and dissociating in the non-aqueous liquid; (b) high transference number[iii] of the dissociated Li^+ ions; (c) high stability of the anion against oxidative decomposition; (d) being inert to electrolyte solvent(s) and other battery components; (e) high thermal stability and non-toxic. Crucial requirements as such lead to rather limited choices of lithium salts for non-aqueous liquid electrolytes. For instance, early work[49] by Dahn *et.al.* to measure the conductivity of different electrolytes showed more than 120 combinations of non-aqueous liquid solvents but only 5 available lithium salts.

Historically, $LiClO_4$ was considered as one of the candidates, owing to its promising ion mobility and dissociation constant. It, then, was regarded as impractical due to its extremely poor thermal and current stability (radically reacting with most organic species) and high shock-sensitivity to cause explosion[50]. $LiAsF_6$ also caught the interest for industrial applications due to not only its high ion mobility and dissociation constant, but also its anodic stability up to 4.5 V versus Li^+/Li in certain solvents[51,52]. However, the concern for its commercialization was the risk of toxicity of As. It was found that at about 1.15 V vs. Li^+/Li the reduction of As^{5+} (non-toxic) to As^{3+} (toxic) or even As^o

iii The transference number t_{Li^+} refers to the fraction of electric current carried by the Li+ compared with the total electric current, $t_{Li^+} = I_{Li^+} / I_{total}$. Ideally, the transference number should be equal to 1, whereas in practise, it is preferred to be as close to 1 as possible.

(toxic) would occur[53].

$LiPF_6$ was used in the first commercial Li-ion battery by Sony[41]. Even nowadays, it is the only candidate to be widely used in commercial Li-ion batteries[41,48,54]. Although it is not superior in any specific property compared with the other salts, such as $LiAsF_6$ and $LiBF_6$, it is still the most well-balanced one and meets all the requirements. However, it is not perfect as expected, mainly for that follow:

(a) it is chemically and thermally instable[55,56], due to the following equilibrium:

$$LiPF_6 \rightleftharpoons LiF(s)+PF_5(g) \quad \text{(Equation 1-4)}$$

As the gaseous PF_5 is formed, the chemical equilibrium of this equation tends to shift to the right side forming gaseous PF_6 even at ambient temperature. Particularly, this process is highly favourable at elevated temperature. As a strong Lewis acid, PF_5 tends to trigger a series of reactions with the electrolyte solvents, such as ring opening polymerization[41,48,55-57], which then destroys the stability of the electrolyte system.

(b) $LiPF_6$ is highly sensitive towards moisture even at trace amounts in the electrolyte solvent, which results in hydrolysis[55,56]. The resulting product HF leads to severe decay of battery performance.

(c) The difficulties in the production and purification of $LiPF_6$, due to its moisture sensitivity, chemical and thermal instability causes high cost of this salt[41,48].

Organic Solvents for Non-aqueous Liquid Electrolytes

The organic solvents for non-aqueous liquid electrolytes should meet several minimum requirements[41,54]: (a) high dielectric constant that benefits dissolving lithium salts to a

sufficient concentration; (b) low viscosity that benefits fast ion migration and diffusion; (c) inert to all chemicals and cell components in Li-ion batteries, particularly, the charged surface of cathode and anode; (d) wide thermal stability window, including the stability against thermal decomposition and remaining as low viscosity liquid; (e) high flash point regarding safety concerns, low or better non-toxic and economical for large scale industrial applications.

Among a wide range of polar organic solvents being studied, the most attractive candidates fall into the family of either esters or ethers[41,54]. The preference of ethers in early research was mainly due to its low viscosity. However, the ether-based compounds decompose on the oxidative cathode surface at relatively low potentials[58-60], which is not ideal for most of the commercial cathode materials over 4 V versus Li^+/Li. As a result, the commonly used organic solvents for Li-ion batteries are esters.

Propylene carbonate (PC) received much attention in the early application of lithium metal anode based batteries[61-64], due to its high dielectric constant and wide thermal range. However, batteries using PC based electrolytes were found to have severe capacity fading in long-term cycling and formation of dendrites[62-64] due to complicated mechanism attributed to both the PC solvent and the lithium metal anode[22,63-68]. However, the same failings of PC based electrolytes with lithium metal were not found in Li-ion cells and in fact, the 1st generation Sony Li-ion battery used PC as the solvent.

At present, most of the electrolyte solvents are a combination of Ethylene Carbonate (EC) with other linear organic carbonates[41,54], such as Dimethyl Carbonate (DMC)[52,69],

Diethyl Carbonate (DEC)[70-72]. The high dielectric constant ($\varepsilon = 53$)[43] of EC promotes the dissolution of lithium salts[73]. Additionally, EC shows improvements in the interfacial properties such as low polarization on cathode materials surfacess[41,74]. Particularly, it contributes to form effective SEI layers on the surface of anodes to prevent further electrolyte decomposition. The only issue is its relatively high melting point but the presence of solute[75] and linear organic carbonate as a co-solvent[52,69] manage to maintain the electrolyte in liquid phase over a wide thermal range. The mixture not only have the advantage of lowering the melting point, but also has lower viscosity for higher ion conductivity owing to the low viscosity nature of the linear organic carbonates. Surprisingly, the mixtures even show extended anodic stability of the electrolyte (oxidative stability at the cathode) up to 5 V on the spinel cathode surface[76], whereas linear carbonates on their own would be oxidized at about 4 V[77]. The fundamental reason underlying this remains unknown yet.

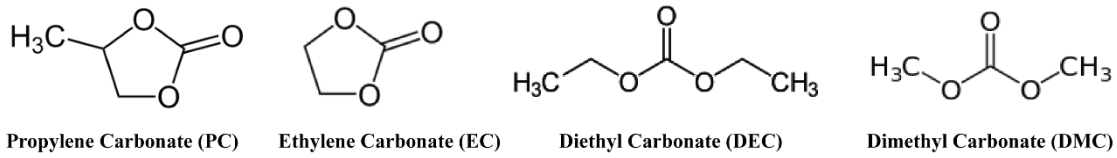

Figure 1-4 structures of different solvents

1.1.3.3. Binder

As mentioned in section 1.1.2 , an electrode for Li-ion batteries normally contains active materials (cathode or anode materials), conductive additive(s) and binder(s). The binder, normally an electric insulating polymer, works to bind the active material and conductive additive together, and to adhere them onto the metallic current collector. In

commercial Li-ion batteries, although the binder generally only counts for 2 wt% to 5 wt% of the electrode, it is essential for obtaining optimized electrode performance, particularly the cyclability[78]. This is mainly due to: (1) the binder holds active material particles and conductive additive together, which avoids them losing contact with each other caused by the volume expansion/contraction of active material particles during Li^+ de-/intercalation[79-83]; (2) the binder holds the electrode film onto the metallic current collector, which prevents the electrode film from detaching from the metallic current collector over long-term cycling[84,85]; (3) the electric resistivity of binder contributes to the total electric resistivity of electrode, thus a binder with low electric resistivity is preferable[78,82,86,87]; (4) the binder need to be chemically and electrochemically inert as to maintain its steady and proper function in a harsh environment over long duration[88]. Today, the most commonly used binder in commercial Li-ion batteries is Polyvinylidene Fluoride (PVDF).

Further introduction and discussion of binder are given in the CHAPTER 4, as it is the main topic of the CHAPTER 4 to discuss the binder effects on layered Li-rich cathode materials.

1.1.3.4. Separator

Presently, the most widely used commercial separators are microporous polymeric membrane separators mainly based on polyolefin, such as polyethylene and polypropylene[89,90]. There is also an increased trend of using ceramic coated polymeric membrane and ceramic based (Al_2O_3/SiO_2) membrane for enhanced performance and improved safety of the Li-ion batteries[89,91,92].

The function and working environment of the separator require it to be[89,91,93]: (a) chemically and electrochemically stable to the battery components, such as electrolyte and electrode materials, in a wide thermal and voltage range; (b) mechanically robust at various temperatures; (c) excellent in wettability of the electrolyte; (e) in appropriate and homogeneous in porosity, pore size and thickness. Additionally, the cost of the separator is rather essential as it actually contributes to a considerable ratio of the total cost of Li-ion batteries[89].

1.1.3.5. Current Collector

The current collectors for both cathode and anode should have common requirements including[94,95]: (a) being inert to chemical and electrochemical reactions with electrode and electrolyte; (b) good cohesion with electrodes; (c) reliable mechanical strength; (d) low electric and contact resistivity; and (e) thin thickness. Additionally, for the current collector at anode, it should not alloy with Li^+ under electrochemically reducing conditions[94]. Presently, in most of commercial applications, Al and Cu foil are employed as the current collector for cathodes and anodes, respectively. However, the concerns lay mainly on their cost and the corrosion of Al in contact with organic carbonate based electrolytes[94-96]. Coating of the current collector and adding additives to form passivation layers are the main strategies employed to prevent the corrosion of current collector[94-96].

1.2. Conventional Cathode Materials for the Li-ion Batteries

The cathode material, normally a lithium transition metal oxide or phosphate, is an

extremely critical component in Li-ion batteries. Li-ion batteries are typically assembled in a discharged state. During charging of the batteries to store energy, Li^+ is deintercalated[8,42,43] from the cathode material while normally the oxidation of transtion metal ions compensates this process to balance the charge. Thus, the amount of energy stored in batteries is highly dependent on cathode materials. The means to elevate the energy of Li-ion batteries is to enhance its capacity and voltage. Presently, the capacity of a commercial cathode materials is generally lower than 190 mAh g^{-1} [76,97,98], whereas the capacity of commercial anode materials is much higher, normally at about 320 mAh g^{-1} [27-29]. Therefore, the capacity of the Li-ion batteries is mainly limited by the cathode materials. On considering the cell voltage, the potential of the anode materials is already close to Li^+/Li redox potential, making increasing the voltage of the cell more of a cathode material challenge. Therefore, high voltage and high capacity cathode materials are the key to high energy density Li-ion batteries. In this section, the introduction is given to conventional cathode materials, mainly those commercialized ones. The layered Li-rich cathode materials which are the major focus of this thesis, are a significantly important family of high-voltage and high-capacity cathode materials which will be introduced separately in the section 1.3.

1.2.1. Layered Cathode Materials

The 1st commercialized cathode material for Li-ion batteries is the layered $LiCoO_2$, which belongs to a family of lithium transition metal oxides in α-$NaFeO_2$ structure (space group #166, *R-3m*)[12]. In this structure, Li and Co are almost completely ordered

into alternative layers and accommodated at the octahedral sites of edge-sharing oxygen octahedra[12]. $LiCoO_2$ shows attractive volumetric capacity, excellent cyclability and promising rate performance[13]. Even today, it is still the dominant cathode materials of Li-ion batteries for portable devices. However, it is not perfect mainly due to the following reasons: (a) its reversible capacity is limited, as only 0.5 Li^+ per formula unit can be reversibly de-/intercalated, corresponding to about 150 mAh g^{-1}. Although surface treatment of $LiCoO_2$ has made further Li^+ extraction possible up to about 0.7 Li^+, corresponding to 4.5 V cut-off versus Li^+/Li, the capacity is unlikely to sustain in long-term cycling[13,99], due to the structural evolution to monoclinic CoO_2 structure (ordered - disordered transition)[100,101]; (b) its poor thermal and chemical stability lead to decomposition and O_2 release[iv], which rises severe safety concerns; (3) the high cost of Co significantly increases its cost.

$LiNiO_2$, an isostructure compound of $LiCoO_2$ was also considered as alternative cathode material candidate[13,99]. However, it was difficult to synthesize it in an ordered layered structure[13,99,103], as the presence of Ni in the Li interlayer and vice versa, known as "cation mixing"[103], were observed due to the close ionic size of Li^+ (0.76 Å) and Ni^{3+} (0.69 Å)[104]. The partially substitution of Ni by other transition metal ions, such as Co and Al, was demonstrated effective in suppressing cation mixing and promoting ordering[105]. The optimized composition, $LiNi^{III}_{0.8}Co^{III}_{0.15}Al_{0.05}O_2$ (NCA), exhibits promising energy density, good cyclability and rate performance[7,106], which has been

iv *3d* band of Co^{4+} is known to be pinned on top of O^{2-} *2p* band. Therefore, further extraction of Li^+ would initiate the O oxidation and then release as O_2 [4,102].

successfully applied in Li-ion batteries for EVs[7]. However, its thermal stability, especially when cycled at elevated temperature, remains a concern[107,108]. Additionally, as the high Ni content in NCA is extremely sensitive to moisture, and critical synthesis conditions such as O_2 atmosphere and moisture control are required in its production[106], which can result in increased cost.

Another series of widely used commercial cathode materials, $LiNi_xCo_yMn_zO_2$ (x+y+z=1) (NCM), is also an isostructure compound of $LiCoO_2$. The idea of using Mn^{4+} to substitute Co^{3+} benefits the thermal stability of materials[108,109] and reduces the total cost due to the nature abundance and economical price of Mn, while introducing Ni^{2+} which provides additional transition metal redox, as the active redox couples upon cycling are $Ni^{2+}/Ni^{3+}/Ni^{4+}$ and Co^{3+}/Co^{4+} whereas Mn^{4+} remains inactive[99,110-112]. The 1st synthesized and commercialized NCM material was $LiNi^{II}_{0.33}Co^{III}_{0.33}Mn^{IV}_{0.33}O_2$, also being referred as "333" or "111" in industry, since the x:y:z ratio in $LiNi_xCo_yMn_zO_2$ equals to "333"("111"). Later on, the trend of commercialization of this series developed towards more redox active and less redox inactive transition ions, such as "442", "523" and "622", in which the x:y:z ratio in $LiNi_xCo_yMn_zO_2$ equals to "4:4:2", "5:2:3" and "6:2:2", respectively. Particularly, Ni is more favourable due to the relatively lower price of Ni than Co. However, Co-free is not an option, as the presence of Co in NCM materials is essential for sustaining the ordering of transition metal ions in the transition metal layers and suppressing cation mixing[113,114]. It also improves the electronic conductivity of the NCM materials[99,115]. Currently, the trend to commercialize the "811" material appears to be clear, although challenges such as

moisture sensitivity, critical synthesis conditions, and structure and thermal stability remains[116], similar to the other Ni-rich layered cathode material NCA. Nevertheless, as the one of the dominant cathode materials in industry, NCM materials exhibits high capacity[116] (up to around 180 mAh g^{-1} depending on the compositions, at a 4.3 V cut-off versus Li^+/Li) and a promising balance of energy and power density, cyclability and thermal stability[7].

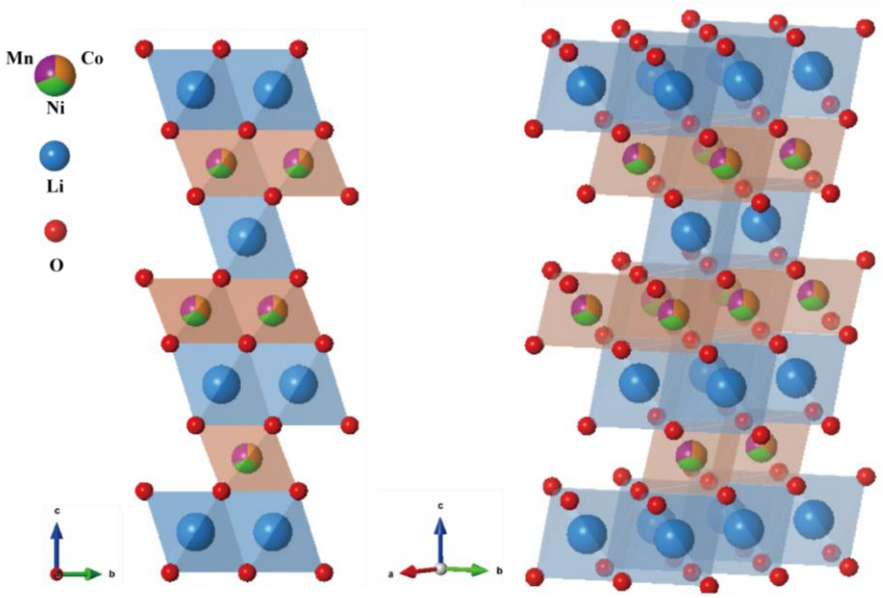

Figure 1-5 Schematic of a layered $LiNi_{0.33}Co_{0.33}Mn_{0.33}O_2$ in *R-3m* space group (#166), in which transition metal (TM) ions are occupying the same crystallographic site (*3b* site). The Li, Ni, Co, Mn and O atoms are coloured in blue, green, orange, purple and red, respectively. The LiO_6 and TMO_6 octahedra are coloured in light blue and light orange, respectively.

1.2.2. Spinel Structured Cathode Materials

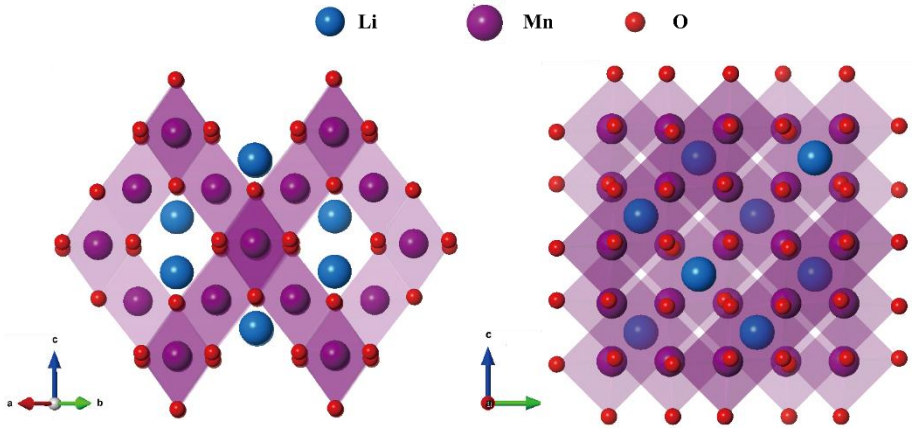

Figure 1-6 Schematic of a spinel $LiMn_2O_4$ in Fd-3m space group (#227). The Li, Mn, and O atoms are represented in blue, purple, and red spheres, respectively. The MnO_6 octahedra are coloured in light purple

Proposed by the J.B. Goodenough group at Univerity of Oxford again[117], $LiMn_2O_4$, in which Mn is in a mixed oxidation state of +3 and +4, is an alternative cathode material for $LiCoO_2$ in early Li-ion batteries, owing to the natural abundance of Mn and correspoding ecomonical price[13]. It was then extensively developped by the Bellcore labs[118,119] and used as the cathode materials for EVs Li-ion batteries on a few genearations of the Nissan LEAF[7]. $LiMn_2O_4$ is in cubic-spinel structure (space group #227, Fd-3m)[117,120], in which Li and Mn ions occupy the tetrahedal sites (8a) and octahedral sites (16d), respectively, and the LiO_3 tetrahedron shares four faces with the adjacent MnO_6 octahedra[121]. O ions (32e) are cubically close-packed[99]. This stoichiometric spinel structure provides unique stability, resulting in good thermal stability of $LiMn_2O_4$[121]. Achieved by the redox reaction between Mn^{3+} and Mn^{4+}, it exhibits a reversible capacity of about 120 mAh g^{-1} at approximately 4 V versus Li^+/Li[121] and a good rate performance (power capability)[7]. However,the main problems

of $LiMn_2O_4$ are capacity fading and unsatified cycablilty[7,13,121]. This is due to (a) the dissolution of Mn via a disproportionation reaction of Mn^{3+} to Mn^{2+}(soluable) and Mn^{4+}(insoluble), especially at elevated temperature or when trace amount of HF is presented in electrolyte[13,121]; (b) the onsite Jahn-Teller distortion of Mn^{3+} and the over-lithiation of the surface rather than the bulk of the particles during discharge[121], leading to an average oxidation states lower than +3.5. Various optimizaiton routes have been considered[13,118,121], including surface modification, partial substitution of cation or anion and synthesis of slightly over-lithiated and Mn-deficient $Li_{1+\delta}Mn_{2-\delta}O_4$

1.2.3. Olivine Structured Cathode Materials

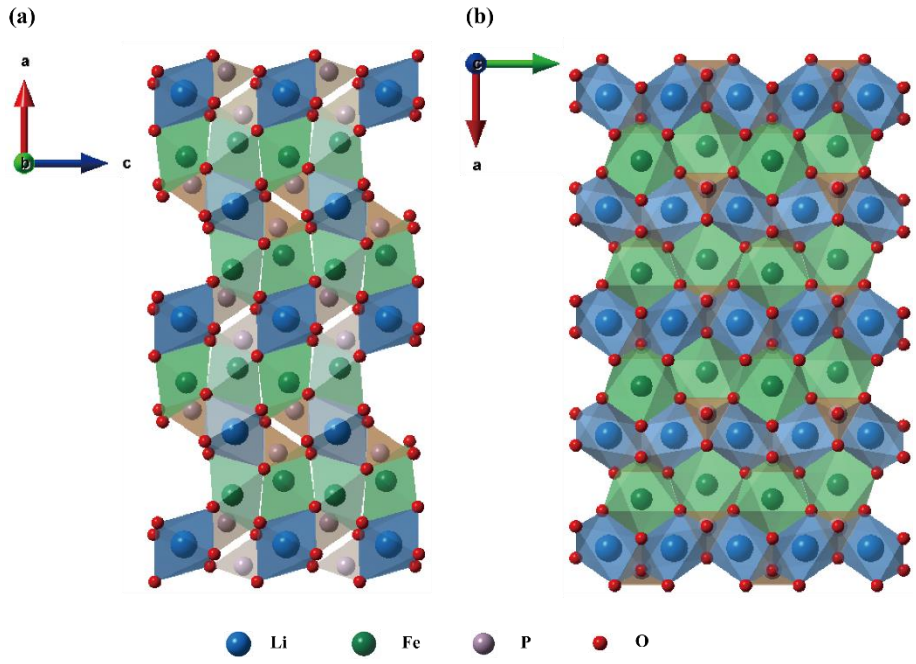

Figure 1-7 Schematic of an olivine $LiFePO_4$ in Pnma space group (#62). The Li, Fe, P, and O atoms are represented in blue, green, dark purple and red spheres, respectively. The LiO_6 and FeO_6 octahedra, and PO_4 tetrahedra are coloured in light blue, light green and light brown.

The triphylite $LiFePO_4$ (LFP), which adopts an olivine structure[122], is another widely used cathode material for commercial Li-ion batteries in a variety of devices from

portable devices[7,13], EVs to stationary storage. Its structure can be described in Pnma space group (# 62), in which Li and Fe distribute peculiarly at octahedral sites along $[001]_{Pnma}$ (Figure 1-7(a)) and P is accommodated at tetrahedral sites[122,123]. The FeO_6 octahedra share corners between each other. Besides, the FeO_6 octahedra also share corner with four PO_4 tetrahedra and one edge with another PO_4 tetrahedra[122,123]. Consequently, the Fe^{II}-O distance is longer than expected for Fe^{2+} octahedral coordination[123], resulting the high operation voltage of LFP at 3.45 V versus Li^+/Li[124]. The unique structure of LFP shows extraordinary stability, which is the origin of both the high thermal stability of LFP and high reversibility of Li^+ extraction (good cycability)[7,99]. However, the Li diffusion within the lattice is confined in the $[010]_{Pnma}$ direction[123] (Figure 1-7(b)), also known as "1D diffusion channel"[99], resulting in its poor ionic conductivity (about 10^{-11} S cm^{-1} at room temperature)[125]. Additionally, its intrinsic electronic conductivity is also poor (about 10^{-9} S cm^{-1} at room temperature)[125]. Thereby, both conductivity issues present a challenge when using LFP. Two main routes, nano-sizing and carbon coating the LFP particles, have helped to make LFP an ideal commercial cathode materials with good capacity, excellent rate performance (power capability) and cycability[7,42,43]. However, it should be noted that nano-sizing of LFP leads to a low tap density of the LFP, which is not favourable for the mass loading on the cathode.

From an industry perspective, the synthesis of Fe^{2+} containing LFP requires critical condition control due to its sensitivity to air and moisture[123,126-128]. Otherwise,

impurities are easily formed[v]. This increases the cost the LFP. Additionally, the nano-sizing process also adds cost. Therefore, the total cost of LFP is not as competitive as one would have expected, although the Fe is natural abundant and economic in price.

1.3. Layered Li-rich Cathode Materials

1.3.1. Origin and Structure complexity

As mentioned in the section 1.2.1, only a fraction of Li^+ is allowed to be reversibly de-/intercalated from Li layer in layered lithium transition metal oxides. Otherwise, pushing the Li^+ de-/intercalation beyond this limit would break the structure stability of layered lithium transition metal oxides and raise a series of issues, such as unit cell volume shrinkage[129], transition metal dissolution[130], oxygen loss[131], and a reduction in capacity[132] and operating voltage due to the change of local structure[133]. To obtain a larger capacity from the layered lithium transition metal oxides, strategies must be applied to stabilize their structures so that Li^+ could be reversibly de-/intercalated. The idea of layered Li-rich cathode materials was a strategy initiated independently by both Thackery's and Dahn's Group in early 2000s[6].

Inspired by the earlier work on $xLi_2O{\cdot}MnO_2$[134], Thackeray *et al.* adopted the same strategy to insert a structurally compatible component, monoclinic Li_2MnO_3 (space

[v] In reducing atmosphere, conductive metal phosphides are formed, such as FeP and Fe_2P; in a slightly oxidizing atmosphere, Fe^{3+} containing phases are formed, such as $LiFePO_4OH$, $Li_3Fe_2(PO_4)_3$, $FePO_4$, and $LiFeP_2O_7$.

group #12, *C2/m*), into rhombohedral $LiMO_2$[vi] (space group #166, *R-3m*), aiming to increase the stability of its structure over a wider composition range[135,136]. Previously, Li_2MnO_3 was regarded electrochemically inactive, until Kalyani *et al.* [137] first found that it could be electrochemically activated by charging up to 4.5 V versus Li^+/Li. This made the idea of inserting Li_2MnO_3 into $LiMO_2$ more interesting, as more Li^+ would potentially be de-/intercalated. It turns out that such materials exhibit a reversible capacity over 250 mAh g^{-1} if cycled up to a 4.6 V cut-off or even higher versus Li^+/Li, which outperforms conventional layered lithium transition metal oxides in terms of both reversible capacity and operating voltage window[135,136].

Dahn *et al.* reported the strategy to substitute Li^+ and Mn^{4+} with Ni^{2+} in $Li[Li_{1/3}Mn_{2/3}]O_2$, forming $Li[Ni_xLi_{1/3-2x/3}Mn_{2/3-2x/3}]O_2$, which also exhibits a reversible capacity of 225 mAh g^{-1} between 2 V and 4.8 V versus Li^+/Li[138].

The enormous capacity and elevated operation voltage window of these layered Li-rich transition metal oxides soon led to great interests from both industry and academia. Companies, such as BASF and 3M, were interested in implementing these materials into next generation high-voltage and high-capacity Li-ion batteries[6]; academic interests mainly laid on the study of their structures and associated electrochemical behaviour(s), improving its electrochemical performance and understanding the underlying fundamental chemistry of these materials.

In general, the layered Li-rich transition metal oxides could be understood as layered

[vi] M for transition metal ions

lithium transition metal oxides with excess Li substituting transition metal ions in the transition metal layer. Thus, it could be written as $Li[Li_xM_{1-x}]O_2$ or $Li_{1+x}M_{1-x}O_2$. Particularly, following the idea of $Li_2M'O_3$ stabilized $LiMO_2$, it could also be expressed in another notation $xLi_2M'O_3\bullet(1-x)LiMO_2$[136,139]. In both notations, the average oxidation state of cations in the transition metal layer should be at +3 oxidation state, while the transition metal ion (M') in the stabilizer $Li_2M'O_3$ remains at +4 oxidation state.

The two notations in fact present two proposed structure models of these compounds: integrated nanocomposites and solid solutions. The former considers these materials contain two components: a monoclinic phase $Li_2M'O_3$ (space group *C2/m*, #12), which also could be written in a layered notation as $Li[Li_{1/3}M'_{2/3}]O_2$; and a rhombohedral phase $LiMO_2$ (space group *R-3m*, #166). The two phases share close compatibility, since both could be considered as in layered structure, in which metal ions are occupying the octahedral sites of close packed oxygen arrays. The latter considers these materials as solid solutions, as the cell parameter changes linearly with the compositions following the Vegard's rule[140,141]. Early researches worked intensively on solving the structure controversy, as it is essential for understanding its electrochemical process(es) and the underlying reaction mechanism(s).

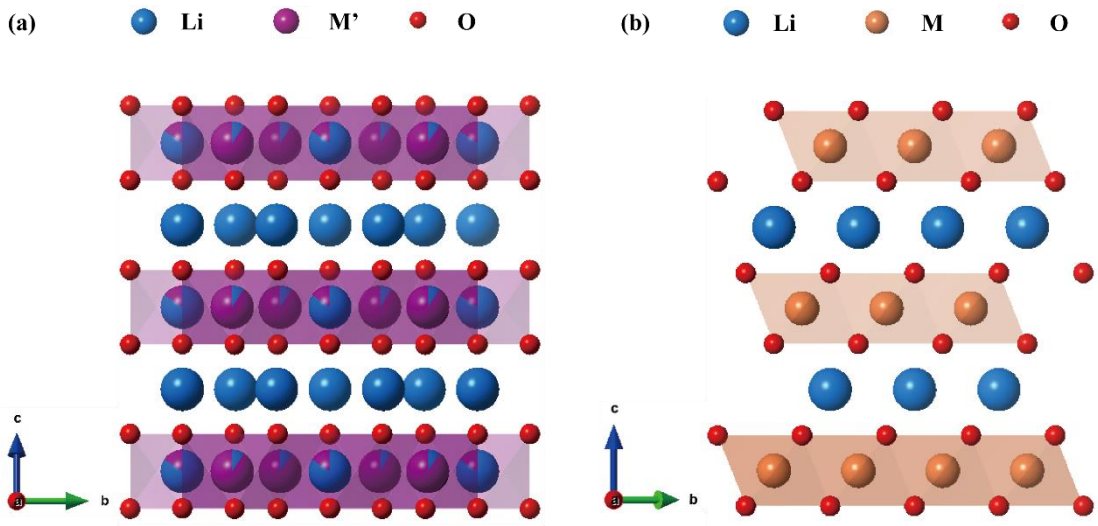

Figure 1-8 Schematic of (a) a monoclinic $Li_2M'O_3$ structure in *C2/m* space group (#12), and (b) a rhombohedaral $LiMO_2$ (M= Ni, Co, Fe, Mn, Fe, Cr *etc.*) in *R-3m* space group (#166). Both are viewed from [100] direction. The Li, M', M, and O atoms are represented in blue, purple, orange, and red spheres, respectively. The $M'O_6$ and MO_6 octahedra are coloured in light purple and light orange.

A variety of characterization methods, mainly X-ray/Neutron diffraction and electron microscopy, were employed to identify the structure of these materials. High resolution X-ray Diffraction (XRD) patterns of these compounds often present weak diffraction peaks at low angle region, corresponding to (020), (110), and (-111) plane of monoclinic $Li_2M'O_3$ phase. The XRD data can be well-refined by Rietveld refinement based on a two-phase model consisting of *R-3m* and *C2/m* space group[142]. Besides, the co-existence of $Li_2M'O_3$-like and $LiMO_2$-like domains were also directly illustrated by using electron microscopy in different compositions. For example, in $Li_{1.2}Co_{0.4}Mn_{0.4}O_2$, the Li_2MnO_3-like and $LiCoO_2$-like domains were observed in a homogenous long-range mixing over the length scales of ≥ 2-3 nm[143,144]; a similar case was also observed in $Li_{1.2}Mn_{0.61}Ni_{0.18}Mg_{0.01}O_2$[145].

Although above mentioned results point to the integrated nanocomposites model, some researchers consider these materials as a solid solution with either *R-3m*[146,147] or *C2/m*

symmetry[148,149]. For instance, Delmas *et al.* studied $Li_{1.20}Mn_{0.54}Co_{0.13}Ni_{0.13}O_2$ synthesized at different temperatures and found the resulting materials were all solid-solutions while the local structure ordering of materials was sensitive to compositions[146]. In fact, factors such as compositions, synthesis methods and conditions, play important roles in determining whether the resulting materials are in integrated nanocomposites or solid solutions. Such examples have been presented in the study of Li−Co−Mn-O and Li-Ni-Mn-O pseudoternary diagrams by Dahn *et al.*[150-153].

To the best of my knowledge, the controversy about the structural models of these layered Li-rich transition metal oxides remains but is not among the main research interests of the field any more. To clarify this controversy is also beyond the scope of this thesis.

1.3.2. Challenges

Although the layered Li-rich transition metal oxides exhibit enormous capacity and high operating voltage, which are desirable for the application of next generation Li-ion battery cathode materials, several severe problems still hinder its development towards commercialization.

In the 1st cycle, these materials present a very low couloumbic efficiency normally less than 80%, which corresponding to an irreversible capacity about 60 to 100 mAh g^{-1} [154,155]. In the subsequent cycles, both the capacity and average voltage of these materials fade gradually, causing continuous energy fading[6,140,156,157]. This is problematic for direct current applications[140], in which stable energy supply, especially stable voltage,

is essential. In addition, the rate performance of these materials is also poor as compared to the other layered lithium transition metal oxides such as $LiCoO_2$ and NCM.

Intensive research has been carried out to reveal the origin(s) of these problems and correspondingly to tackle them. Methods such as surface coating, surface treatment, and doping are commonly seen to be adapted for better electrochemical performance of these materials. For example, surface coating these oxides with fluorides (AlF_3)[158], oxides (Al_2O_3, MgO, V_2O_5)[159-161], and metal phosphates ($AlPO_4$, $LiNiPO_4$ and $LiCoPO_4$)[162] shows improvement on both the 1st cycle coulombic efficiency and rate performance. It also stabilizes the capacity and voltage of these materials over long-term cycling. Surface treatment using ammonia was previously employed to create oxygen vacancies in spinel materials for capacity and stability enhancement[163]. When applied to treat the surface of these layered Li-rich transition metal oxides, it also improves the discharge capacity and rate performance, and stabilizes the average discharge voltage[164-166]. This is ascribed to not only the formation of oxygen vacancies, but also due to the structural changes of both the surface and bulk after the ammonia treatment[164-166]. Doping these materials with foreign cations[139,160,167-170], such as Na, Mg, Al, Cr, Zr, Sn, is illustrated to be effective to stabilize the capacity and voltage of these materials in the prolonged cycles as well, as the dopants are believed to hinder the cation migration and the resulting layered-spinel transition in these materials.

Despite the above-mentioned issues on its electrochemical behaviour, these layered Li-rich transition metal oxides normally have a relatively lower tap-density as compared to $LiCoO_2$ and NMC, which affects the actual mass loading on the electrode in actual

batteries.

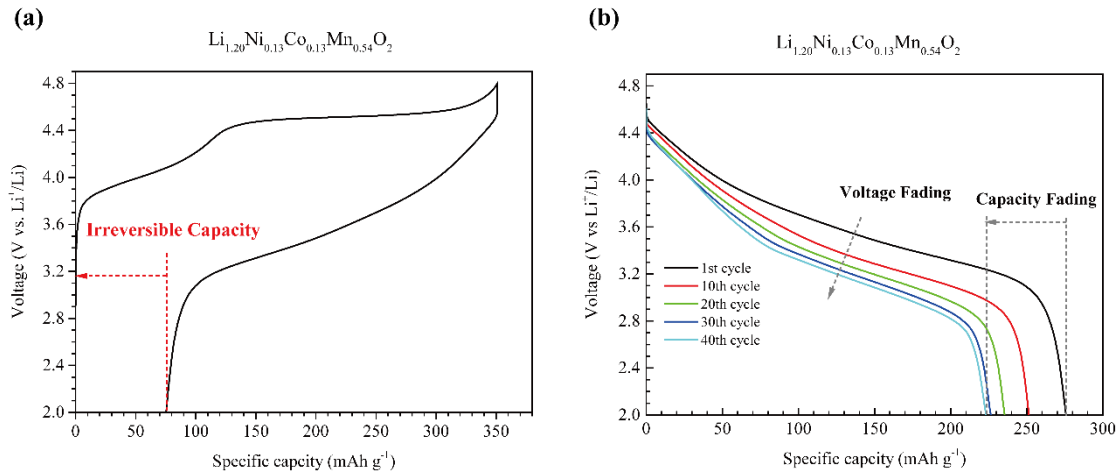

Figure 1-9 Issues of layered Li-rich transition metal oxides, taking $Li_{1.2}Ni_{0.13}Co_{0.13}Mn_{0.54}O_2$ as an archetypal example. (a) 1st cycle load curve showing its large irreversible capacity and low couloumbic efficiency, and (b) multiple cycle discharge curves in the 1st, 10th, 20th, 30th, and 40th cycle, showing the voltage and capacity fading.

1.3.3. Underlying Chemistry

To understand the underlying chemistry, especially the redox mechanism(s) and the structural evolution during cycling, is the key to tackle the above-mentioned problems of these layered Li-rich transition metal oxides.

Earlier research agrees that at low-voltage region of the 1st cycle, normally < 4.4 V versus Li^+/Li, the charge compensation during charging these materials are realized by oxidizing transition metal ions while de-intercalating Li^+ from the lattice. Regarded the high-voltage region of the 1st cycle, the research mainstream agrees with the model proposed by both Dahn *et al.*[138] and Thackeray *et al.*[171], which the Li^+ and O are simultaneously removed from lattice beyond the transition metal oxidation. Other ideas such as complex reaction mechanisms of formation and decomposition of CO_2 and carbonates have also been proposed by different authors[172-175].

A series of experimental evidence supports the former model. Armstrong *et al.* first directly observed the oxygen release by using the Differential Electrochemical Mass Spectrometry (DEMS)[176]. It has also been directly observed by Novak *et al.*[172] but not by the others[177]. Shinichi *et al.* proved the simultaneous Li^+ and O removal at the first charge and corresponding structural rearrangement by synchrotron XRD. Based on the real-time gas analysis and *ex-situ* chemical analysis, Kang *et al.* confirmed the formation of oxygen containing species in the high-voltage region and consequently proposed a detailed reaction schematic to account for the oxygen evolution[175]. By Soft X-ray Absorption Spectroscopy (SXAS) and Raman spectroscopy, Hwang *et al.* found traces of surface transition-metal ions migrating to the bulk while oxygen leaves the lattice[178].

Recently, intensive research has been done to further reveal the Li^+ and O removal process, especially the reversible oxygen redox process[76,139,146,156,179-184]. The progress in this direction broadens our understanding of the redox mechanisms in cathode materials of Li-ion batteries and opens new door for exploring new candidates for the cathode materials. More details of these research are given in the section 5.1.

As the Li^+ and O are removed, leaving vacancies in the lattice, especially at the surface of the particle, transition metal ions tend to migrate through the tetrahedral sites into the Li layer to balance the charge between cation and anion slabs[185]. Consequently, the structure rearrangement occurs[6,140,185,186]. As a result, the re-intercalation of Li^+ no longer happens in the identical structure as the origin, causing the voltage hysteresis between charging and discharging process[185,187-189]. Additionally, these transition metal

ions are trapped and inactive in the Li layer with each cycle, and consequently less sites in the Li layer are available for the subsequent Li^+ re-intercalation, causing the gradual capacity and voltage fading over long-term cycling[185,187-189].

Although significant research achievements have been made in understanding the underlying chemistry of these layered Li-rich transition metal oxides, problems and challenges remain due to the complexity of these materials and the limitation of characterization methodologies. Therefore, there still are a variety of research interests on these materials to be explored, so that their future application in next generation Li-ion batteries could be possible.

CHAPTER 2 Experimental Methodologies

2.1. Chemicals

All chemicals used for materials synthesis were purchased from Sigma-Aldrich and with a purity higher than 99%, unless otherwise specified in the experimental details in the following individual chapters. All reaction gases used for synthesis were ordered from BOC and with a purity higher than 99.5%. In addition, the gases were dried by flowing through a P_2O_5 containing dreschel bottle before going into the reaction furnace. The electrolytes used in electrochemical tests were 1M $LiPF_6$ in the binary solvents of EC:DMC (1:1, wt%) (Selectilyte Electrolytes™ LP30) or 1M $LiPF_6$ in the solvent of PC, both battery grade from BASF Catalysts.

2.2. Synthesis Methodologies

Different synthesis methodologies, which are briefly introduced as follow, were employed to prepare a variety of lithium transition metal oxides. The detail of the synthesis methodologies will be given in the experimental details in the relevant chapters.

2.2.1. Solid-State Synthesis

Solid state synthesis is the most well used method for synthesizing polycrystalline solids in inorganic chemistry[190]. The starting materials, in solid-state, are ground to a homogenous mixture and then pressed into a pellet. The resulting pellet is heated to a

high temperature for long time to provide suitable thermodynamics and kinetics conditions for reactions. Both the temperature and duration are highly depending on the precursors and reactions. In the case of my study on *3d* lithium transition metal oxides, it normally requires a temperature higher than 600 °C for no less than 15 hours. Besides, this process may also be repeated several times to ensure obtaining a single-phase material in the end. In some cases, reducing/oxidising gas atmosphere is necessary during the synthesis.

2.2.2. Co-precipitation Synthesis

The co-precipitation of metal cations as compounds (or "precursors") with extremely low solubility, such as hydroxides, carbonates, oxalates in aqueous solutions, is a common way of preparing crystalline oxides nanoparticles[191]. The co-precipitation generally involves the sequential nucleation, growth, and agglomeration processes.

For instance, the following reaction shows the precipitation of A_xB_y. which has a very low solubility constant K_{sp} in aqueous solution.

$$xA^{y+}(aq) + yB^{x-}(aq) \underset{}{\overset{precipitation}{\rightleftharpoons}} A_xB_y(s);\ K_{sp} = \alpha_A{}^x \alpha_B{}^y \quad \text{(Equation 2-1)}$$

Where the α_A and α_B are the activity of cation A^{y+} and anion B^{x-}.

For most cases, it is necessary for the above-mentioned precursors to go through subsequent calcination, decomposition and sintering processes to form a well-defined crystalline phase(s) of the target compound.

2.2.3. Sol-Gel Synthesis

The sol-gel synthesis applies the sol-gel process to prepare precursors, which are then calcinated and sintered at high temperatures (normally exceeding 600 °C) to form the target crystalline compounds. The early sol-gel process normally refers to the hydrolysis and poly-condensation of alkoxide or nitrate precursors, followed by a drying process to remove volatile solvents from the gel network, leaving a porous structure[191]. As the process gives highly homogenous element mixing and relatively uniform dispersion of particle size in the resulting precursors, it becomes very attractive and widely employed for many chemical synthesis, especially the synthesis of nanoparticles. By properly controlling conditions of the sol-gel process, precursors with desired particle sizes and morphologies could be obtained, so that it would benefit the following calcination and sintering process, and eventually, the target crystalline compounds.

2.3. Characterization Methodologies

2.3.1. Scanning Electron Microscope (SEM)

The Scanning Electron Microscope (SEM) is a microscope which uses electrons rather than light to form an image of the specimen. It has been widely used in many fields to observe the morphology of specimens at much higher magnification than the optical microscope.

In SEM, a high vacuum atmosphere is created during operating. An electron beam is

produced by an electron gun at the top of the microscope and accelerated by the electric field on the anode to form an electron beam. This beam vertically travels through a series of electromagnetic fields, which work as a “lens” for SEM and focus the beam towards the specimen (Figure 2-2(a)). Once the incident beam hits the specimen, X-rays, secondary electrons (SE), back-scattered electrons (BSE) and Auger electrons will be produced from the specimen (Figure 2-2(b)). The secondary electron detector and the back-scattered electron detector pick up SE and BSE, respectively, and convert signals into an image, which is projected onto the screen. The SE is emitted by atoms near the material surface and are more surface sensitive, while the BSE is more sensitive to the atomic mass of nuclei it scatters from. Therefore, the SE imaging gives higher resolution and normally used to get the topographic information of the specimen, while the BSE imaging normally used to get the elemental contrast.

The detail of SEM instrument used in the characterization will be given in the relevant chapters.

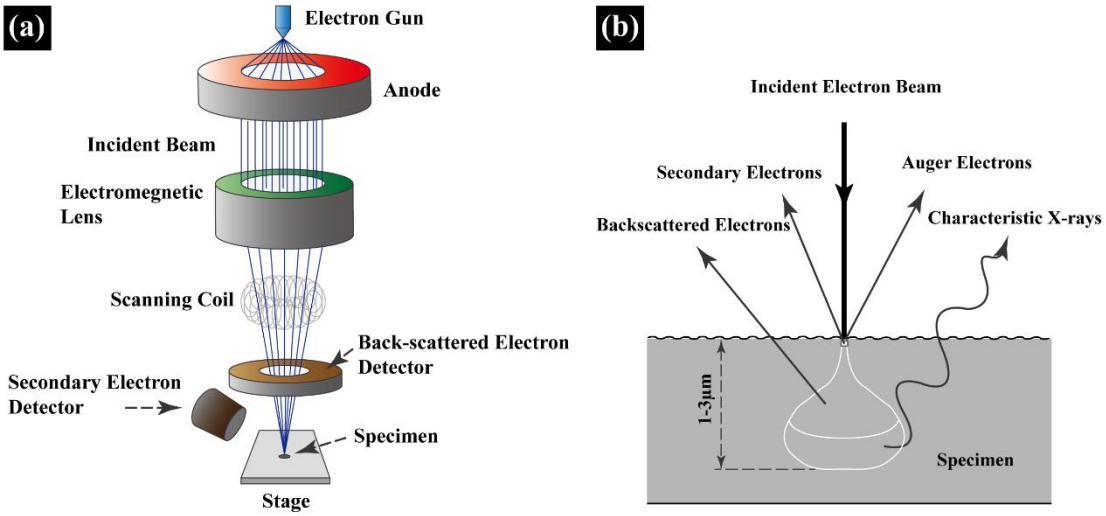

Figure 2-1 Schematic of (a) SEM; (b) the interaction between the Incident electron beam and specimen

2.3.2. Energy Dispersive X-Ray Spectrometry (EDX)[192]

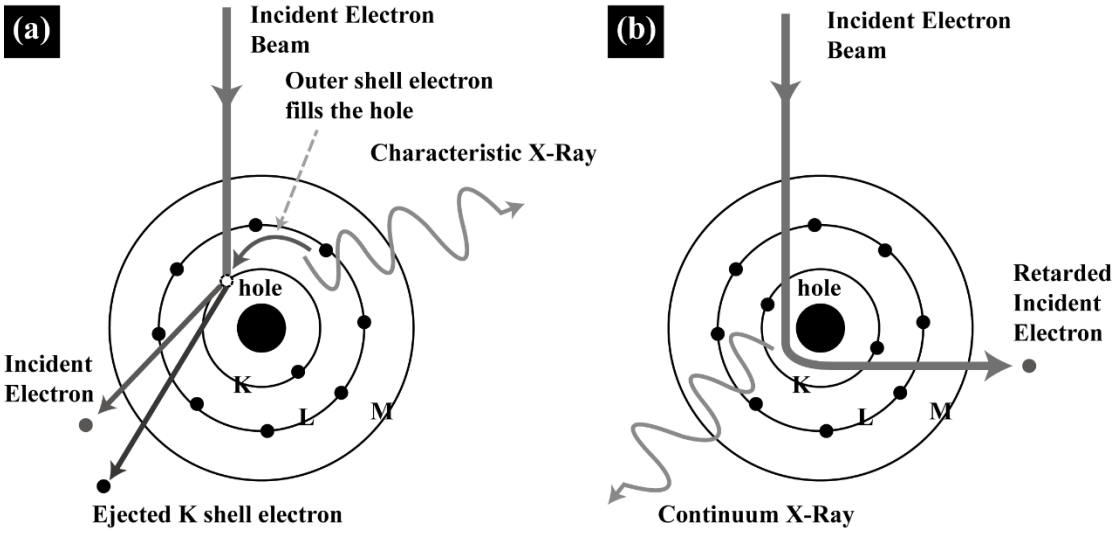

Figure 2-2 Schematic of the generation of (a) characteristic x-ray and (b) continuum x-ray from specimen atoms after hit by incident electron beam

The Energy Dispersive X-Ray Spectrometry (EDX), also known as EDS, is a microanalysis methodology for localized elemental analysis. Normally associated with SEM, it utilizes the characteristic X-rays emitted by the specimen when bombarded by the incident electron beam from the SEM (Figure 2-(b)). The incident electron transfers sufficient energy to an electron in one of the inner shells of a specimen atom, which excites it to leave the shell and the atom, leaving a vacancy in that shell. This is an unstable state for the atom, and an electron from outer shell transits back to fill the vacancy, accompanied by releasing energy in the form of X-rays. Since the energy difference is characteristic for different shells of different elements, this X-ray is also characteristic of the elements from which it originated. Thus, specific detectors of EDX can pick up elemental information such as the type and quantity of the element. Apart from the characteristic X-ray, the incident beam electron also is retarded by the electric field of those electrons around the nuclei of the atom, generating background and

continuum X-rays. It does not contain any information on element identity, however, its intensity is proportional to the total mass of the analysed volume of the specimen. Thus, it is also used for quantitive analysis. By scanning the incident beam, the EDX can get the elemental distribution information over a certain region, therefore, mapping out the elemental composition of the specimen.

The spatial resolution of the EDX is determined by the penetration of incident beam and thickness of the specimen. A thin specimen is preferred and the best resolution is achieved when the thickness of specimen is half of the penetration volume of the incident beam. The lowest concentration of an element for detection is in the order of mmol/kg, and the smallest amount is in the order of 10^{-18}g.

The detail of EDX instrument used in the characterization will be given in the relevant chapters.

2.3.3. Inductively Coupled Plasma Optical Emission Spectrometry (ICP-OES)[193]

The Inductively Coupled Plasma Optical Emission Spectrometry (ICP-OES) is an elemental analysis methodology that has been widely used in inorganic chemistry to determine trace levels of metal or a few non-metallic elements in a test sample. The test sample must be able to be solvated. The measurement sensitivity is in the range of $2*10^{-4}$ to 10^3 ppm.

The ICP-OES includes two parts - the ICP and the OES. In the ICP part, argon gas is ionized by high frequency current created electromagnetic field to generate high

electron density and temperature (about 10^4 K) plasma. The test sample is introduced into the plasma in an atomized state through a narrow tube, then atoms of different elements in the test sample are excited to high energy level. When these atoms fall back to the low energy state, the energy is emitted in the form of photons. For each element, there is a corresponding characteristic emission spectrometry. The detector in the OES part measures the photon wavelength and intensity to determine the type of elements and the corresponding quantity.

The elemental analysis using ICP-OES in this thesis was carried out by the Butterworth Laboratories, using the Perkin Elemer Optima 7300DV ICP-OES.

2.3.4. Powder X-Ray Diffraction (PXRD)

2.3.4.1. Basic Principle of X-Ray Diffraction (XRD)

X-Ray Diffraction (XRD) is a constructive diffraction methodology for the crystallographic analysis of solid crystalline materials. The constructive diffraction effect occurs when the electromagnetic radiation is scattered by a long-range ordered periodic structure that is of a similar length scale to the radiation wavelength[194]. The atoms in a crystal are arranged in periodic arrays and the distance between the atoms is similar to the wave length of the X-ray. Therefore, when a crystalline material is exposed to the X-ray, constructive interference at specific angles is observed, which contains crystallographic information of the material.

Both Laue conditions and the Bragg equations describe the condition for such constructive diffraction of X-ray.

Laue Condition[194-196]

$$\begin{aligned} \vec{a_1} \bullet (\vec{k_0}\text{-}\vec{k}_i) &= 2\pi h \\ \vec{a_2} \bullet (\vec{k_0}\text{-}\vec{k}_i) &= 2\pi k \\ \vec{a_3} \bullet (\vec{k_0}\text{-}\vec{k}_i) &= 2\pi l \end{aligned} \qquad \text{(Equation 2-2)}$$

Where$\{\vec{a}_i\}$ (i=1,2,3) is the primitive vector of the crystal lattice; $\vec{k_0}$ and $\vec{k}_i$ are the wave-vectors of the incident X-ray beam and diffracted X-ray beam, respectively; h,k,l are the Miller indices (integer values of a reflection's reciprocal lattice indices).

The Laue conditions describe the relation between the lattice primitive vector $\vec{a}_i$ and the scattering vector $\Delta\vec{k} = \vec{k_0}\text{-}\vec{k}_i$ for crystals of arbitrary symmetry at the position of constructive interference.

Bragg Equation[194-196]

$$n\lambda = 2d\sin\theta \qquad \text{(Equation 2-3)}$$

Where λ is the wavelength of the incident X-ray beam; *n* is integral; *d* is the spacing between the parallel plane of the scattering lattice; θ is the angel between the incident beam and the scattering plane.

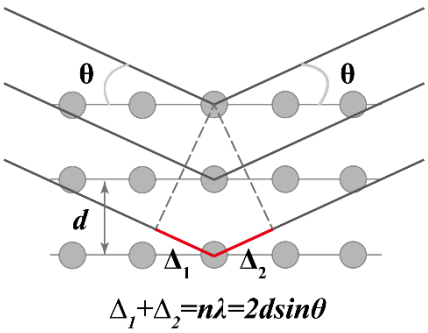

Figure 2-3 Schematic of the deduction of the Bragg Equation, reproduced from Ref.[194]

For different crystal systems, the *d*-spacing is dependent on the unit cell parameters (Detailed in Appx. 1). Thus, for a known incident wavelength λ, once the θ is measured, unit cell parameters of the crystalline material could be calculated.

2.3.4.2. Powder X-Ray Diffraction (PXRD)

Powder x-ray diffraction is precisely polycrystalline diffraction, as an ideal powder sample contains randomly oriented crystallites. The basic assumptions of PXRD are that (1) for every set of planes, there is an equal number of crystallites that satisfy the diffraction condition; and (2) there is a statistically relevant number of randomly oriented crystallites[194-196]. Therefore, in PXRD, (1) irradiating a large volume of sample could ensure that a statistically relevant number of crystallites contribute to the diffraction; (2) all possible diffraction peaks should be observed, excluding the extinction; (3) each diffraction peak is attributed to X-ray scattering from an equal number of crystallites[195].

The diffracted x-rays by randomly oriented crystallites in an ideal powder sample form Debye diffraction cones. The detector scans following an arc that intersects each Debye cones at a single point, giving discrete diffraction peaks (Figure 2-4(a)).

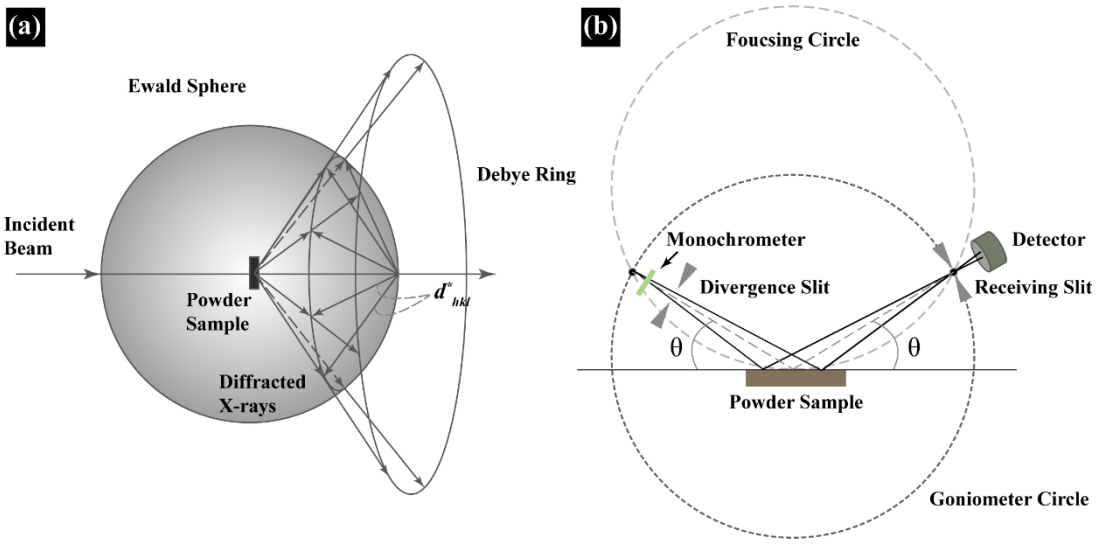

Figure 2-4 (a) The intersection of d^*_{hkl} vectors of the powder sample with the Ewald sphere to illustrate the generation of discrete powder diffraction peaks; (b) Schematic of the Bragg-Brentano geometry. Reproduced from Ref.[196].

Nowadays, the Bragg-Brentano geometry (Figure 2-4(b)) is most widely used for the laboratory PXRD diffractometers[196]. As for the anode material, which generates X-ray with fixed wavelength, a series of materials could be chosen, such as Cu, Fe, Co, Mo, W, and Rh. The selection of the anode material should consider the elements in the powder sample to avoid possible fluorescence[195], which will decrease the signal to noise ratio. Cu is the most widely used anode material and its wavelength for the K_α and K_β radiation are 1.54060 Å and 1.54443 Å, respectively; while $K_\alpha/K_\beta = 0.5$. In most cases, the Cu X-ray radiation is monochromatized and only the stronger K_α radiation is used for PXRD.

The detail of XRD diffractometer used in the characterization will be given in the relevant chapters.

2.3.4.3. Operando Powder X-Ray Diffraction (OPXRD)

Operando Powder X-Ray Diffraction (OPXRD) characterizes the powder sample by XRD in a fully operating device. In materials research for Li-ion batteries, OPXRD normally refers to XRD characterization of the electrode active material during electrochemical cycling. Commercial operando cell or in-house designed operando cell, which are actually close to the coin cell configuration (Figure 2-5), is used on a PXRD diffractometer with Bragg-Brentano geometry. The target electrode for characterization should be facing towards the incident X-rays and normally covered with X-ray transparent window such as beryllium or Kapton® film, which should ensure the isolation of the cell components from the atmosphere and enable the penetration of X-rays in the same time.

The key challenges for the OPXRD are (1) high angular resolution to detect subtle changes in the microstructure, which is reflected in small changes of the diffraction pattern; (2) fast data collection to reveal the time evolution of the diffraction pattern; (3) distinguishing the diffraction signal of the target powder sample from the rest of the components which may contribute to the diffraction pattern; (4) the successive data processing such as cell parameter calculation, phase determination and refinement[197].

The experimental detail of OPXRD used in the characterization will be given in the relevant chapters.

2.3.4.4. Rietveld Refinement of X-Ray Powder Diffraction Data

Rietveld Refinement is a well-established methodology for the analysis of powder diffraction data, proposed by Rietveld H. for the refinement of crystal structure from neutron powder diffraction data[198,199]. Later on, its application for analysing the PXRD data was published[200]. The principle of the Rietveld refinement is to calculate the diffraction pattern of a hypothetical structure, then compare to the measured diffraction pattern by the least square approach. This approach seeks the minimization of the squared sum of all differences between the observed (Y_{obs_i}) and calculated (Y_{calc_i}) step scan intensities in the powder pattern, which leads to the best agreement between the hypothetical structure model and the real data[194,196].

$$\text{Min}=\sum_{i=0}^{n-1}\left(w_i\left(Y_{obs_i}-Y_{calc_i}\right)^2\right) \qquad \text{(Equation 2-4)}$$

Where the index $i \in (0,1,2,...,n-1)$ stands for angular position in the step ($\Delta 2\theta$) scan powder diffraction pattern, as expressed below:

$$2\theta_i = 2\theta_{start} + i\Delta 2\theta \qquad \text{(Equation 2-5)}$$

The weight w_i is derived from the variance of Y_{obs_i}, assuming the covariance between different Y_{obs_i} to be zero.

The Rietveld refinement can be conducted by several softwares, such as Fullprof, GSAS, Topas and EXPO. In this thesis, Fullprof suite[201] is used and the detail of the Rietveld refinement used in the characterization will be given in the relevant chapters.

2.3.5. Electrochemical Measurements

2.3.5.1. Electrode Processing

As mentioned in section 1.1.3, for Li-ion batteries, both cathode and anode materials are mixed with conductive additives and binder, then processed into the form of electrodes before assembly in a battery. The most common electrode processing method is to cast the electrode slurry onto a piece of metal foil (aluminium foil for the cathode and copper foil for the anode); there are also several alternative ways including directly pressing the electrode mixture into pellets. Throughout this DPhil project, electrodes of cathode materials were processed mainly in two following methods, unless otherwise specified in individual chapters.

Casted Electrode

PVDF and Super P carbon were used as the binder and electronic conductivity additive for the casted electrode. PVDF (5 wt%) was dissolved in N-Methyl-2-pyrrolidone (NMP) (95 wt%) to form the binder solution. The electrode slurry was made by thoroughly mixing the cathode material, Super P carbon and PVDF binder solution in

a Retsch PM100 planetary ball mill, referring to the composition ratio of 80 wt%:10 wt%:10 wt% (for PVDF rather than the PVDF solution). Once mixed, the electrode slurry was cast onto an aluminium foil current collector (0.050 mm, Advent Research Material Ltd.) by a doctor blade and then dried at 120 °C to evaporate NMP. The resulting electrode film was then roll-pressed at 100 μm, which normally leading to an electrode thickness of 15~18 μm, and punched into electrodes with a 1.9 cm diameter and further dried at 80 °C under vacuum overnight before being assembled in an electrochemical cell.

Pellet Electrode

In this case, polytetrafluoroethylene (PTFE) was used as the binder, instead of PVDF. As PTFE is insoluble in both organic and inorganic solvent, the electrode processing of the pellet electrode follows a solvent-free process rather than casting, which resulting a pellet electrode film without attaching to a metallic correct collector. This is also the reason to call the obtained electrode as "pellet electrode".

The electrodes were made by thoroughly grinding the cathode materials (80 wt%), Super P carbon (10 wt%) and PTFE (10 wt%) in a mortar, and then adding a few drops of isopropanol to wet the mixture. The mixture was then gradually roll-pressed for several times to eventually reach a film with a thickness of 35 ~ 40 μm. The resulting electrode film was punched into 1.6 cm diameter electrodes and then dried at 80 ˚C under vacuum overnight before being assembled in an electrochemical cell.

2.3.5.2. Electrochemical Cells

For general electrochemical tests, the CR2325 type coin cell (National Research

Council Canada) was used (shown in the Figure 2-5), unless otherwise specified. Different electrochemical cells for specific electrochemical tests were specified in the corresponding chapters. Coin cells were assembled in an argon-filled glove box (Labmaster DP, MBRAUN) using lithium metal as counter/reference electrode, glass fiber separator (GE) and LP30 electrolyte (1 M $LiPF_6$ dissolved in 1:1 wt% Ethylene Carbonate (EC):Dimethyl Carbonate (DMC) solvent, BASF Selectilyte^{TM}).

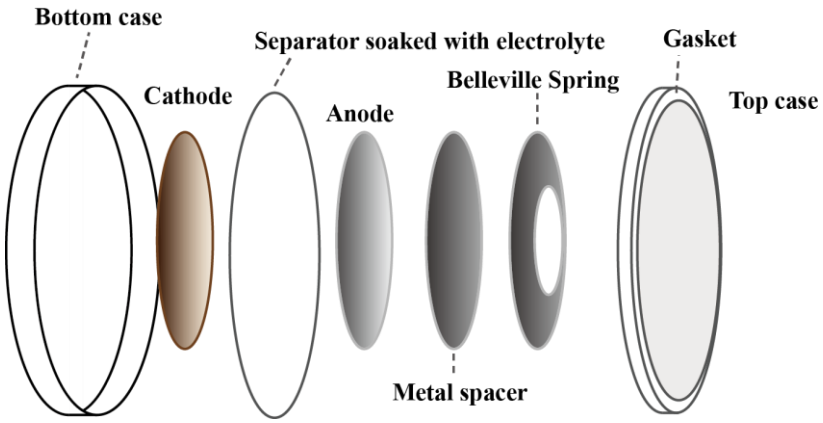

Figure 2-5 Schematic of the coin cell parts

2.3.5.3. Galvanostatic Cycling

The galvanostatic cycling test is a standard electrochemical test for battery electrode active materials, which can be used to obtain a variety of information such as the specific capacity/energy, cycling stability and average voltage evolution upon cycling. The obtained voltage profile can be used to characterize single/multi-step redox reaction(s) for the de-/intercalation process(es) of the active materials. In fact, the galvanostatic cycling is a constant current reversal and cyclic chronopotentiometry technique, in which electroactive species are oxidized/reduced at a constant rate by the constant anodic/cathodic current applied[202,203]. Depending on the electrode materials and test purposes, a certain voltage window is assigned to the tests. In this thesis,

voltages are given relative to the Li^+/Li redox couple, unless otherwise specified. These experimental details were specified in the following individual chapters.

2.3.6. Differential Electrochemical Mass Spectrometry (DEMS)

Differential Electrochemical Mass Spectrometry (DEMS) is an operando analytical methodology which combines an electrochemical cell with mass spectrometry to analyse any gaseous and/or volatile species during an electrochemical process[197,204].

An inert gas, such as Ar, flows through an operating electrochemical cell (Figure 2-6(a)) to carry any gaseous and volatile species generated during the ongoing electrochemical process to an enclosed ion source, where these species are ionized by the electron impact. The extraction lenses focus these ions into the quadrupole mass filter, which selects ions with a single mass/charge ratio at a time for the subsequent detector(s) (Figure 2-6(b)). The detection sensitivity can be a few parts per billion (ppb) to parts per million (ppm) and the response can be a few hundred milliseconds, depending on the inlet design, the pressure, the type of detectors, and instruments.

DEMS allows the operando, high resolution, mass-resolved detection of gaseous and volatile reactants, reaction intermediates and (by-)products of electrochemical process[197], which provides new perspective to understand electrochemical reactions happening in the cell.

The experimental detail of DEMS used in the characterization will be given in the relevant chapters.

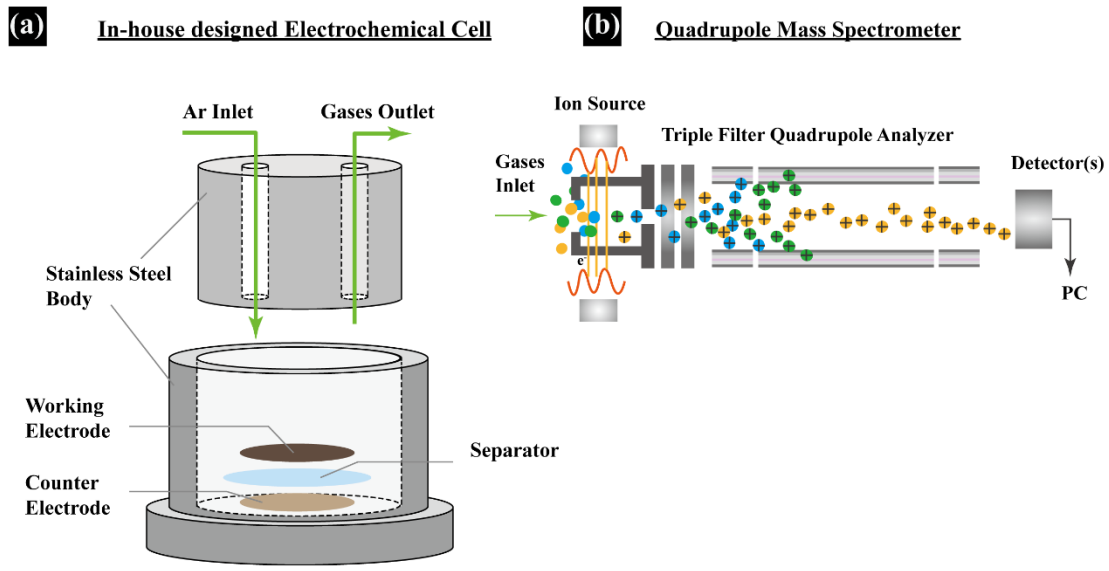

Figure 2-6 Schematic of (a) an in-house designed electrochemical cell for DEMS; (b) Quadrupole mass spectrometer

2.3.7. Raman Spectroscopy

Raman spectroscopy is a sensitive optical methodology to detect intrinsic vibrational frequency shifts in atoms or molecules upon their inelastic Raman scattering of monochromatic photons. As chemical bonds and functional groups scatter photon at different frequencies, Raman spectroscopy is employed as an effective tool in areas such as structural and compositional analysis, chemical fingerprinting and chemical imaging. As a vibrational spectroscopy, Raman spectroscopy is applicable to solid states, gaseous state and solution. This makes it a good complement for PXRD, which is only applicable for a traceable amount of crystalline materials.

Raman spectroscopy is based on Raman scattering. There are two scattering types for photons. Rayleigh scattering is a strong elastic scattering. Alternatively, Raman scattering, which only counts for about 10^{-5} of the incident beam, is an inelastic

scattering with modulated frequencies $\nu_0 \pm \nu_m$, where ν_0 is the frequency of incident photons and ν_m is the intrinsic vibration frequency of a molecule or atom[205]. The ν_0-ν_m and ν_0+ν_m are called *Stokes* and *Anti-Stokes*, respectively. It is worth noting that not all vibrations are Raman-active. Only when the change rate of polarizability (α) with respect to nuclei displacement q is not zero ($(\frac{\partial \alpha}{\partial q})_0 \neq 0$), can the vibration be Raman active[205].

In general, the vibrations of covalent bonds give strong Raman signals, whereas the vibrations of ionic bonds give strong Infrared (IR) signal. Therefore, Raman spectroscopy is effectively used to study metal oxygen bonds in solid-state chemistry[206-208] and lithium batteries (both Li-ion and lithium air batteries)[209], which have significant covalent character. One problem encountered in Raman spectroscopy is that the fluorescence emission from the sample or impurities, which could be as much as 10^4 times greater in intensity than the Raman signal, resulting in a broad, strong fluorescence band covering all the valuable Raman signals[205]. There are several ways to minimize the effect of fluorescence, such as Ultraviolet (UV)-Raman and Fourier Transform (FT)-Raman[205], which use excitation lasers at the UV and Near-Infrared (NIR) regions, respectively, rather than the visible region used in conventional Raman spectroscopy[210].

The experimental detail of Raman spectroscopy used in the characterization will be given in the relevant chapters

2.3.8. X-ray Absorption Near Edge Structure (XANES)

X-ray Absorption Near Edge Structure (XANES) is an inelastic X-ray absorption spectroscopy methodology widely used to study the atomic and electronic structure of materials[210-212]. It is also applicable for materials in gaseous, liquid and solid state, regardless of how ordered or disordered the materials are.

When X-ray photons are absorbed by atoms, the energy of the photons is transferred to the core-level electrons, exciting them to occupy a higher energy level. This phenomenon is localized and centred on the absorbing atoms. Thus, it is sensitive to the chemical bonding environment and valence state of the absorbing atoms[212]. The absorption only happens when the energy of photons equals to the energy difference of the unoccupied higher energy level and the core-level, as photons cannot be divided[210,212]. Meanwhile, each element corresponds to a characteristic energy level structure. Therefore, for each element, there are corresponding characteristic absorptions that can be studied separately. The absorption energies of elements can range from a few electron volts to 100 kilo electron volts. Thanks to the broadly tunable synchrotron X-ray source, it is practical to measure absorption energies of a variety of elements.

At the macroscopic level, for homogeneous isotropic materials, the transmission of X-ray follows the Beer-Lambert-type adsorption law[210,211].

$$\Delta I(\mathrm{E}) = -\mu(\mathrm{E}) I(\mathrm{E}) dx \qquad \text{(Equation 2-6)}$$

Where I is the intensity of X-ray, ΔI is the X-ray intensity loss after passing through a

thickness of *x*, and μ is the linear absorption coefficient. The integration of this equation gives the relation[210,211]:

$$I = I_0 e^{-\mu x} \quad \text{(Equation 2-7)}$$

Where I_0 is the intensity of the incident X-ray, and the x is the thickness of the sample. XANES measures μ by either transmission (for concentrated samples) or fluorescence mode (for diluted samples)[210-212] (Figure 2-7(a)), and a typical XANES spectrum is plotted as shown in Figure 2-7(b).

The label of the absorption edge refers to the first atomic quantum number *n*, with K, L, M, for *n* = 1, 2, 3. For example, the K edge adsorption corresponds to the excitation of *1s* level electrons to the lowest unoccupied *p* states[212]. The shift of absorption edges reveals the change of valence state of absorbing atoms. When the absorbing atoms are oxidized, the absorbing edges shift to higher energy[212]. For instance, it is a few eV per valence change for transition metal element K edges. The coordination environment of absorbing atoms also influence the position and intensity of absorbing edges[213].

The experimental detail of XANES used in the characterization will be given in the relevant chapters

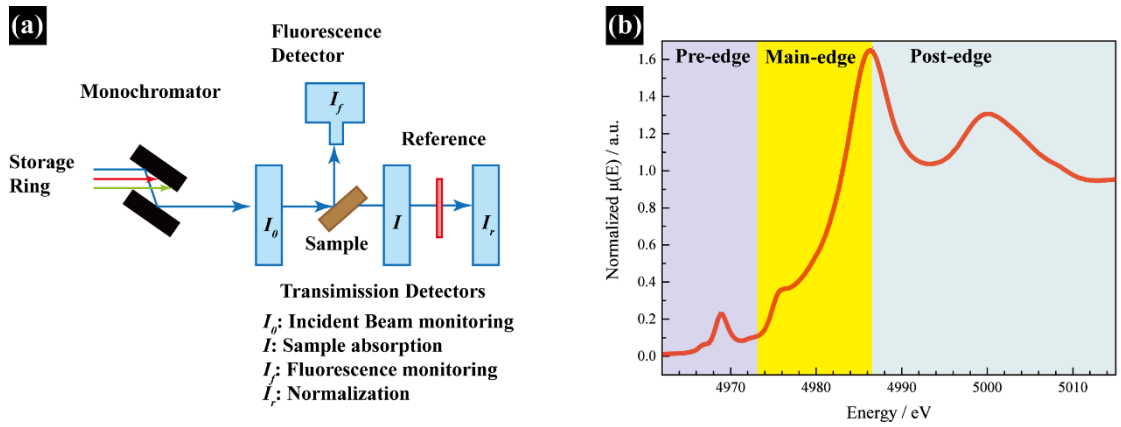

Figure 2-7 (a) Schematic of an X-ray absorption beamline in the traditional mode (with transmission and fluorescence detectors), reproduced from Ref.[210]; (b) A typical Ti K edge XANES spectroscopy at +4 valence state and 6-coordination environment.

2.3.9. Soft X-ray Absorption Spectroscopy (SXAS)

Soft X-ray Absorption Spectroscopy (SXAS) is an inelastic X-ray absorption spectroscopy methodology to study the electronic configurations of targeted elements[214-220]. In fact, SXAS is very similar to XANES, despite the energy of X-ray source and the way of data collection.

SXAS employs soft X-rays, normally in the energy range of 100 eV to 2500 eV, as the X-ray source for the absorption spectroscopy. This energy range covers the K edge absorption of most light elements and the L-edge absorption of the first row *3d* transition metals[214,215], which makes the direct study of valence electrons corresponding to these absorption possible[214,215,221]. The K edge adsorption of light elements is ideal for the understanding of their coordination symmetry and oxidation state. The L-edge absorption corresponds to the excitation of *2p* electrons to the unoccupied *3d* orbitals. Such transitions are sensitive to the local electronic structure, especially the changes on the *3d* orbitals. Furthermore, the $2p_{3/2}$ and $2p_{1/2}$ are separated by the core-hole spin-

orbital interaction, in which the core-hole lifetime broadening is small, resulting in sharp multiplet structures[214] (Figure 2-8(a)). Therefore, the study of L-edge absorption can reveal detailed electronic structures of *3d* transition metal elements.

The data collection of the SAXS is by measuring the electron yield (EY) and/or the fluorescence yield (FY) (Figure 2-8(b)). After a core-hole is created by excitation of the core-electron to higher energy level orbitals, the atom is at an unstable excited state and will relax back to a stable state by emission of fluorescence photons or by ejection of Auger electrons[221-224], which correspond to the FY and EY signals, respectively. By the nature of the fluorescence photons and the Auger electrons, the EY signals are mainly from the surface of sample, whereas the FY signals are relatively more bulk-sensitive[222,223].

The experimental detail of SXAS used in the characterization will be given in the relevant chapters.

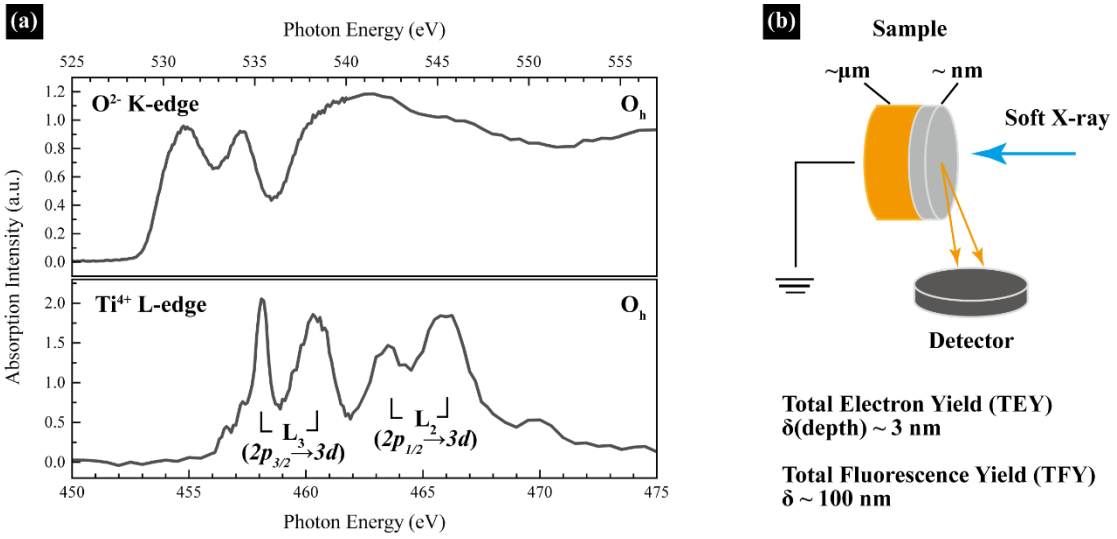

Figure 2-8 (a) Examples of the SXAS spectrum: O^{2-} K edge (top) and Ti^{4+} L-edge, both at O_h symmetry; (b) Schematic of the detection of SXAS experimental signals.

2.3.10. Resonant Inelastic X-Ray Scattering (RIXS)

Resonant Inelastic X-Ray Scattering (RIXS) is a photon-in photon-out inelastic X-ray spectroscopy methodology to study the low-energy intrinsic excitations of targeted atoms[225-229].

An incident photon excites an electron to a higher energy level and creates core-hole at the targeted atom, leaving the atom at the unstable excited state. The decay of the excite state happens normally within 1-2 fs, in which an electron refills the core-hole and emitting an Auger electron or a fluorescent photon. The Auger process is irradiative and has nothing to do with RIXS, whereas RIXS is directly relevant to the fluorescent decay[226]. The RIXS process can be either direct or indirect (Figure 2-9). In the direct RIXS process (Figure 2-9(a)), the core-hole is refilled by an electron from the occupied states while a photon is emitted[226]; in the indirect RIXS process (Figure 2-9(b)), the core electron is excited to an empty state a few electron volts above the Fermi level. At this intermediate state, another electron-hole excitation is created due to the strong coulomb interaction between the core-hole and the valence electron[226]. At the final state, the core-hole is refilled by the electron above the Fermi level and a photon is emitted, leaving the electron-hole excitation at the valence band[226]. The direct and indirect RIXS result in different cross-sections[230,231]. The measurement of RIXS spectrum is based on the measurement of the energy and momentum differences of the photons[225,227].

As an example, in the transition metal oxides, at the oxygen K edge, the core-hole is

created on the oxygen site and the photoelectron fills an oxygen *2p* hole, which is strongly hybridized with a metal *d* orbital. Then another O *2p* electron decays to fill the O *1s* core-hole. Therefore, it is a direct RIXS process[226].

RIXS benefits from the strong resonant enhancements at O K edge and *3d* transition metal $L_{2,3}$ edges, sometimes by many orders of magnitude[225]. Therefore, it is bulk sensitive and only requires a small volume of sample but offers a very sensitive way to probe the changes in energy, momentum, polarization of photons that are directly relevant to the intrinsic excitations of the targeted atoms. In fact, RIXS is even able to distinguish the same element at sites with inequivalent bonding, different valence state, or at inequivalent crystallographic sites if the corresponding X-ray adsorption edges in these cases are differentiable. By the nature of the photon-in photon-out process, RIXS is also element and orbital specific[226,227].

The experimental detail of RIXS used in the characterization will be given in the relevant chapters

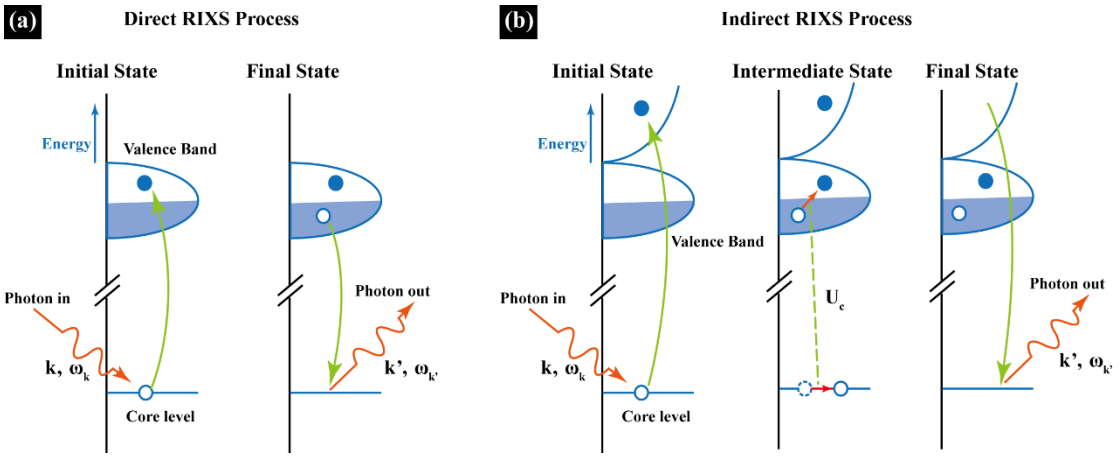

Figure 2-9 Schematic of (a) direct RIXS process and (b) indirect RIXS process. The momentum and energy differences between the initial (photon-in) and final (photon-out) states are $\hbar k - \hbar k'$ and $\hbar w_k - \hbar w_{k'}$, respectively.

CHAPTER 3 Preparation and Characterization of the Layered Li-rich Cathode Material

3.1. Background

The most commonly used methodologies to prepare the layered Li-rich cathode is the co-precipitation method[232-235]. It normally involves two steps: (a) preparation of transition metal hydroxides or carbonate precursors by co-precipitation, then thoroughly mixing the precursors with stoichiometric amount of Li salt(s), such as LiOH or Li_2CO_3; (b) calcination and sintering the mixture at an elevated temperature to form the targeted compounds. Li-rich cathode materials obtained by this method normally varies in electrochemical performance due to multiple reasons, including but not limited to the particle morphologies (size, shape, aggregation, porosity and surface area), composition gradient on surface and/or bulk of particles, and local structures of materials[236-238].

Alternative methodologies, such as sol-gel methods[180,239], could also be used and the resulting materials often exhibit different electrochemical performance. For better understanding of the electrochemical performance and correspondingly the underlying chemistry, we first need to establish a reliable synthesis method that could prepare layered Li-rich cathode materials in pure phase, controlled morphology, and optimized yet stable electrochemical behaviour.

3.2. Research Goal

In this chapter, the research goal is to prepare the $Li_{1.2}Ni_{0.13}Co_{0.13}Mn_{0.54}O_2$, an archetypal example of layered Li-rich cathode materials, by different methods; then to select the most promising one for the later fundamental research on the electrochemical reaction mechanism(s) of layered Li-rich cathode materials.

3.3. Experiment Details

3.3.1. Carbonate Co-precipitation Synthesis

The precursor was prepared by stirring stoichiometric amounts of lithium acetate dihydrate (reagent grade), nickel (II) acetate tetrahydrate, cobalt (II) acetate tetrahydrate (≥98%) and manganese (II) acetate tetrahydrate in the distilled water, then added into sodium carbonate solution to form transition metal carbonate precipitants, which were washed and dried to be used as the transition metal carbonate precursors for the following synthesis process (Figure 3-1).

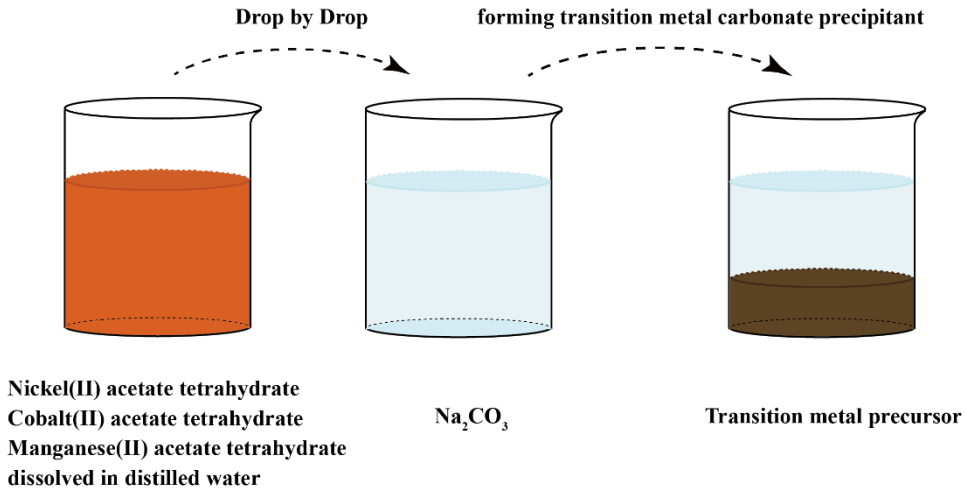

Figure 3-1 Schematic of preparing transition metal precursor by the carbonate co-precipitation

The resulting precursors and stoichiometric amount of lithium carbonate (Li_2CO_3) were mixed using a Retsch PM100 planetary ball miller. The mixture was calcined in an Al_2O_3 crucible (AI-24, Cylindrical, from the Alfa Aesar) at 900 ˚C for 15 hours under a normal atmosphere in a Lenton® AWF 13/12 furnace, then allowed to cool to the room temperature in the furnace. In this chapter, the material obtained in this route is referred as the "Carbonate co-precipitation" in figures and the "carbonate co-precipitated material" in the text.

3.3.2. Oxalate Co-precipitation Synthesis

Inspired by the work by Wei *et al.*[240], as well as the previous optimization work by our group[241], the oxalate co-precipitation synthesis of $Li_{1.2}Ni_{0.13}Co_{0.13}Mn_{0.54}O_2$ was carried out.

The precursors were prepared by stirring stoichiometric amounts of lithium acetate dihydrate (reagent grade), nickel (II) acetate tetrahydrate, cobalt (II) acetate tetrahydrate (≥98%) and manganese (II) acetate tetrahydrate in the distilled water, followed by the addition of acetic acid as an additive and 5 mol% excess lithium to compensate for lithium evaporation during heating. Oxalic acid is used as a precipitating agent. The precursors were pre-treated in poly(tetrafluoroethylene) (Teflon®) autoclave at 200 ˚C for 14 hours (Figure 3-2). The mixture was then heated and stirred until dry.

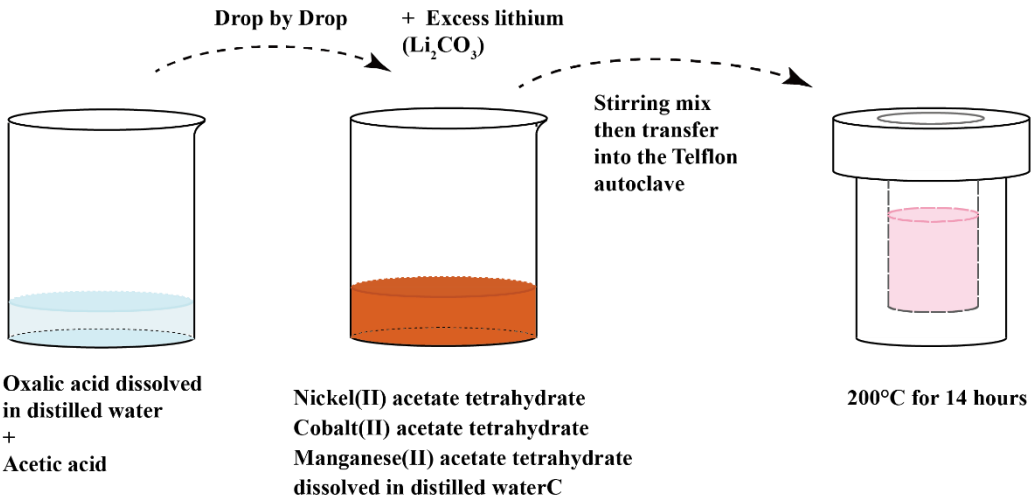

Figure 3-2 Schematic of preparing lithium transition metal precursor by the oxalate co-precipitation

The resulting powder was ground in a mortar and heated in an Al_2O_3 crucible at 450 ˚C for 5 hours ˚C in a Lenton® AWF 13/12 furnace. The obtained powder was re-ground and undergoes two 3-hours dwelling steps at 500 ˚C and 750 ˚C. Finally, it was heated at 900 ˚C for 8 hours, then allowed to cool to room temperature in the furnace. In this chapter, the material obtained by this route is referred as the "Oxalate co-precipitation" in figures and the "oxalate co-precipitated material" in the text.

3.3.3. Resorcinol - Formaldehyde Gel (R-F Gel) Synthesis

The R-F gel synthesis first involved a preparation process of two separated precursor solutions. For the clarification of description, the two precursor solutions were named "Precursor A" and "Precursor B". The Precursor A was prepared by stirring stoichiometric amounts of lithium acetate dihydrate (reagent grade), nickel (II) acetate tetrahydrate, cobalt (II) acetate tetrahydrate and manganese (II) acetate tetrahydrate in the distilled water. Precursor B was prepared by dissolving resorcinol (≥98%) in distilled water, then adding a formaldehyde-water solution (36.5%-38.0%) and 5 mol%

lithium carbonate as a catalyst for the gel formation, as well as compensation of lithium evaporation during calcination. Typically, for a 0.025 mol sample, 0.1 mol resorcinol and 0.15 mol formaldehyde were used.

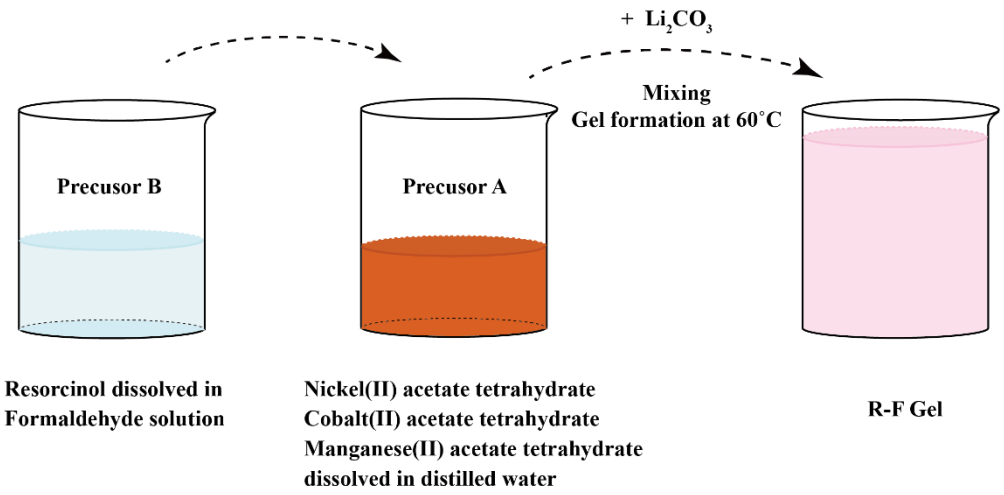

Figure 3-3 Schematic of preparing transition lithium metal precursor by the R-F gel synthesis

The two precursor solutions were mixed and stirred thoroughly, and then heated to 60 ˚C in an oil bath to form the gel (Figure 3-3). After aging for 2 hours, the gel was heated at 100 ˚C overnight for drying, and subsequently pre-treated at 300 ˚C for 4 hours in a Lenton® AWF 13/12 furnace to burn off all organic species. This formed a dark powder of porous metallic oxides. The resulting powder was ground and finally heated at 500 ˚C for 1 hour, then kept dwelling at 900 ˚C for 15 hours. Afterwards, it was allowed to cool to room temperature in the furnace. In this chapter, the material obtained by this route is referred as the “R-F Gel” in figures and the “R-F gel synthesized material” in the text.

3.3.4. Composition, Morphology and Structure Characterization

The ICP-OES was employed for the elemental analysis of the synthesized materials. It

was carried out by the Butterworth laboratories, using the Perkin Elmer Optima 7300DV ICP-OES.

The morphology of the synthesized materials was characterized by using a SEM. For the carbonate co-precipitated and the R-F gel synthesized material, the characterization was carried out on a Carl Zeiss Merlin SEM; for the oxalate co-precipitated material, it was conducted on a JSM 6700F FEG-SEM, operating at 5 kV, 10 μA.

The structure of the synthesized materials was characterized by the PXRD. For the carbonate co-precipitated and the R-F gel synthesized material, the PXRD analysis was carried out on a Rigaku Smartlab® 9KW diffractometer equipped with copper rotating anode (only Cu $K_{\alpha 1}$ emission was used) operating in reflection mode at 45 kV, 200 mA; for the oxalate co-precipitated material, the PXRD analysis was conducted on a STOE Stadi MP equipped with iron rotating anode (only Fe $K_{\alpha 1}$ emission was used) operating in a transition mode at 35 kV, 25 mA. The Rietveld structure refinement was carried out by using the Fullprof Suite programme[201]. The visualization of the refined structure was realized by using the VESTA programme[242,243].

3.3.5. Electrochemical Tests

The synthesized cathode materials ($Li_{1.2}Ni_{0.13}Co_{0.13}Mn_{0.54}O_2$) were made into pellet electrodes and then tested in coin cells to establish electrochemical behaviour. Electrodes and coin cells were made according to the methods described in the section 2.3.5 and section 2.3.5.2, respectively.

The galvanostatic cycling tests were done within the voltage window of 2 V to 4.8 V

versus Li^+/Li in a half-cell configuration at 50 mA g^{-1} or C/5 in C rate[vii]. The rate tests were performed with the same voltage window but at a series of different cycling rate. For the initial cycle, a constant current of 10 mA g^{-1} was applied for both the charge and discharge. For the subsequent cycles, a constant charge current of 50 mA g^{-1} (C/5) was applied, whereas in the discharge a series of currents of 50 mA g^{-1}, 100 mA g^{-1}, 200 mA g^{-1}, 300 mA g^{-1}, 500 mA g^{-1} (2C) and 1000 mA g^{-1} (4C) were applied respectively and repeated for 5 cycles for each of these discharge currents. Once completed, a galvanostatic cycling at 50 mA g^{-1} in the same voltage window was performed to check the capacity retention of the materials after being operated at high rates. All these electrochemical tests were done on a Biologic MPG-2 or Maccor Series 4000 battery tester and all the cells were kept at 30 °C in a Memmert ICP 600 laboratory incubator.

3.4. Results and Discussion

3.4.1. Compositions, Morphology and Crystallographic Structure

The elemental analysis of materials synthesized by different methods was done by ICP-OES measurement and the results were shown in Table 3-1. The results confirm that the compositions of these materials are in a close accordance with the targeted composition $Li_{1.2}Ni_{0.13}Co_{0.13}Mn_{0.54}O_2$.

[vii] In this chapter, 1C = 250 mA g^{-1} is defined

Table 3-1 ICP-OES measurement results of $Li_{1.2}Ni_{0.13}Co_{0.13}Mn_{0.54}O_2$ synthesized by different methods

Preparation Methods	Elemental Analysis Results (m/m %)				Corresponding contents (mol per mol of material)			
	Li	Ni	Co	Mn	Li	Ni	Co	Mn
Carbonate Co-precipitation	8.1	7.4	7.7	31	1.17	0.13	0.13	0.57
Oxalate Co-precipitation	8.3	7.3	8	31	1.20	0.12	0.14	0.57
R-F Gel	8.2	8	7.9	29	1.18	0.14	0.13	0.53

The Figure 3-4 shows the morphology of the materials synthesized by these three methods. For the carbonate co-precipitated $Li_{1.2}Ni_{0.13}Co_{0.13}Mn_{0.54}O_2$ (Figure 3-4(a)), the primary particles are in a size of 0.2 - 0.5 μm with pseudo-sphere like morphology, many of which aggregate to form larger secondary particles in a size of 1 - 3 μm. The oxalate co-precipitated $Li_{1.2}Ni_{0.13}Co_{0.13}Mn_{0.54}O_2$ (Figure 3-4(b)) has a plate-like morphology and its primary particles are in a size of 0.1 - 0.5 μm. Severe clusters of primary particles are observed. For the R-F Gel synthesized $Li_{1.2}Ni_{0.13}Co_{0.13}Mn_{0.54}O_2$ (Figure 3-4(c)), it presents desirable homogeneity in morphology and much less aggregation than the former two. The primary particles are in a size of 0.1 - 0.2 μm and the aggregated secondary particles are generally smaller than 0.5 μm.

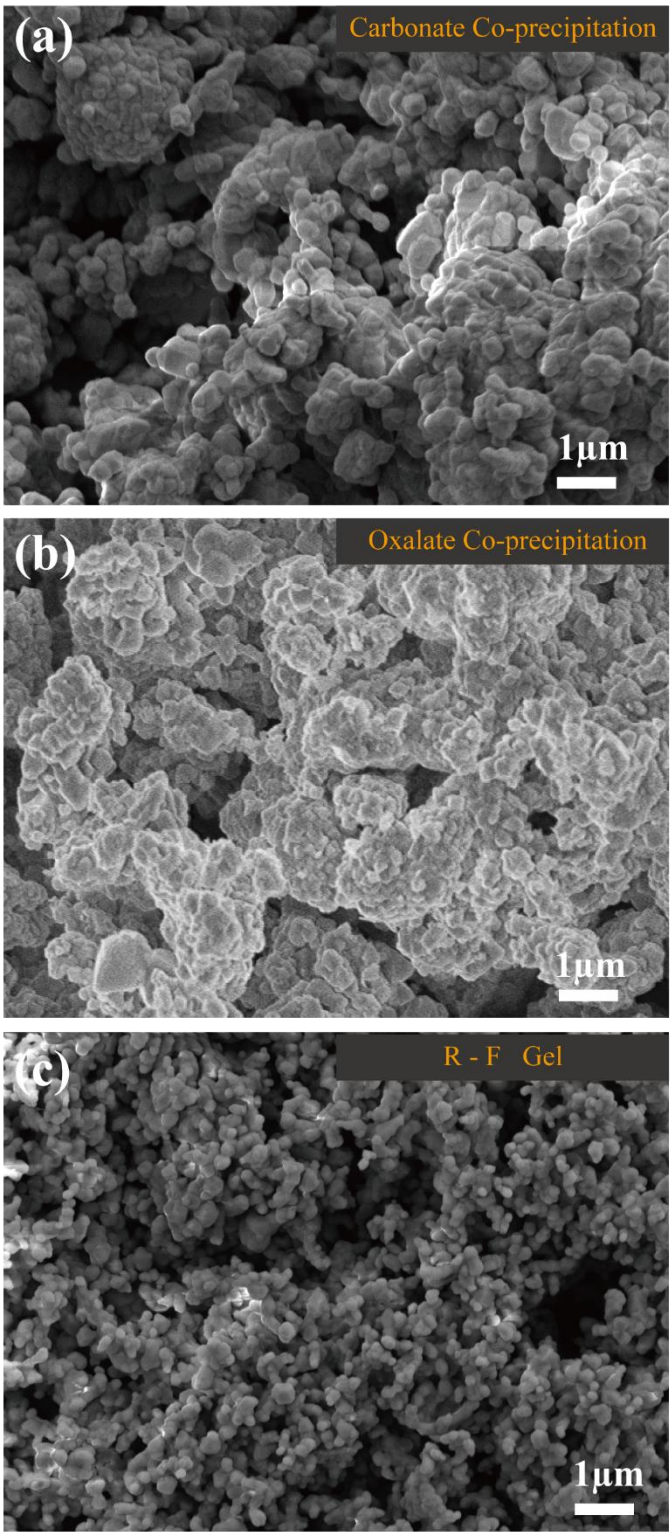

Figure 3-4 SEM images of the (a) carbonate co-precipitaiton, (b) oxalate co-precipitation, and (c) R-F gel synthesized mateirals. (a) & (c) were taken on a Carl Zeiss Merlin SEM and (b) was taken on a JSM 6700F FEG-SEM at 5 kV, 10 μA.

The comparison between the morphology of these materials suggests that the R-G gel synthesis forms the most homogenous and porous material. It has smaller particles size and less aggregation.

The diffraction data was collected in the two-theta region from 15° to 70° for the carbonate co-precipitation sample (Figure 3-5 (a)) and the R-F gel sample (Figure 3-5 (c)), and in the two-theta region from 15° to 88° for the oxalate co-precipitation sample (Figure 3-5 (b)), since the Fe X-ray source was used for this sample.

The diffraction data was then refined by the Rietveld refinement[199,244] using *R-3m* space group (#166). The two-theta regions highlighted by the dotted square was excluded in the Rietveld refinement, as these regions refer to superstructure peaks from *C2/m* space group (#12), which were attributed to the cation honeycomb-like ordering in the transition metal layers[173,245,246]. In detail, the atom position of oxygen, Li content, Li/Ni cation mixing, and unit cell parameters were refined, while the contents of transition metal elements (Ni, Co, and Mn) were taken from the ICP-OES results as being presented previously. Three factors for points with Bragg contributions for pattern, weight profile R value (R_{wp}), Bragg R-factor, and χ^2, were used to represent the reliability of refinement[244].

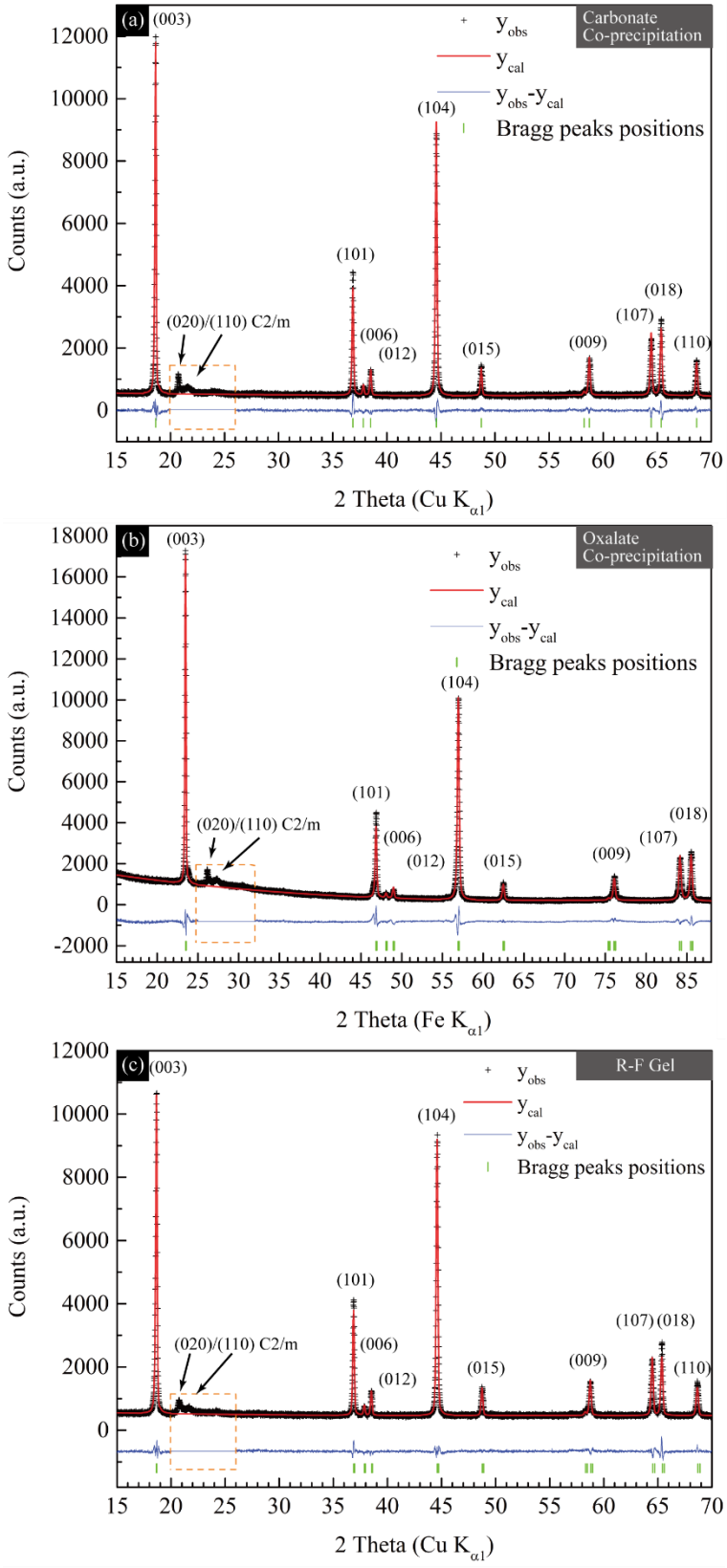

Figure 3-5 PXRD patterns of $Li_{1.2}Ni_{0.13}Co_{0.13}Mn_{0.54}O_2$ synthesized in three different methods, fitted using *R-3m* space group (#166). The "+" marks the observed data. The red and blue line represents the calculated diffraction profile and the difference between the observed and calculated profiles,

respectively. The green ticks mark the allowed Bragg peaks. The dashed square indicates the superstructure peaks of *C2/m* space group (#12). To be noticed, the PXRD pattern of the oxalate co-precipitation sample was collected by using a Fe X-ray source.

It exhibits a good accordance between the observed patterns and the calculated patterns for all three materials (Figure 3-5), indicating $Li_{1.2}Ni_{0.13}Co_{0.13}Mn_{0.54}O_2$ materials obtained by these methods are all formed in a pure *R-3m* phase with the desired structure. These PXRD patterns are also in agreement with the previous work[136,146,237,247].

The details of refinement of these diffraction data are given in the following Table 3-2.

Table 3-2 Crystallographic parameters of $Li_{1.2}Ni_{0.13}Co_{0.13}Mn_{0.54}O_2$ materials obtained by three syntheses

Synthesis Method		Carbonate Co-precipitation			
Atom	Wyckoff Position	Coordination			Occupancy
		x	y	z	
O(1)	6c	0.0000	0.0000	0.2407(5)	1.00
Li(2)/Ni(1)	3b	0.0000	0.0000	0.5000	0.21(1)/0.09(1)
Co(1)/Mn(1)	3b	0.0000	0.0000	0.5000	0.13/0.57
Li(1)/Ni(2)	3a	0.0000	0.0000	0.0000	0.96(1)/0.04(1)
``Cell Parameters	a = 2.8503(1) Å		c = 14.2319(5) Å		V = 100.130 (6) $Å^3$
R_{wp}: 11.6	Bragg R-Factor: 3.04				χ^2: 2.98

Synthesis Method		Oxalate Co-precipitation			
Atom	Wyckoff Position	Coordination			Occupancy
		x	y	z	
O(1)	6c	0.0000	0.0000	0.2420(5)	1.00
Li(2)/Ni(1)	3b	0.0000	0.0000	0.5000	0.20(2)/0.09(2)
Co(1)/Mn(1)	3b	0.0000	0.0000	0.5000	0.14/0.57
Li(1)/Ni(2)	3a	0.0000	0.0000	0.0000	0.97(2)/0.03(2)
Cell Parameters	a = 2.8523(5) Å		c = 14.2489(1) Å		V = 100.395 (3) $Å^3$
R_{wp}: 14.9	Bragg R-Factor: 3.46				χ^2: 6.43

Synthesis Method		R-F Gel			
Atom	Wyckoff Position	Coordination			Occupancy
		x	y	z	
O(1)	6c	0.0000	0.0000	0.2411(4)	1.00
Li(2)/Ni(1)	3b	0.0000	0.0000	0.5000	0.25(2)/0.09(2)
Co(1)/Mn(1)	3b	0.0000	0.0000	0.5000	0.13/0.53
Li(1)/Ni(2)	3a	0.0000	0.0000	0.0000	0.95(2)/0.05(2)
Cell Parameters	a = 2.8469(4) Å		c = 14.2050(7) Å		V = 99.706 (9) $Å^3$
R_{wp}: 12.2	Bragg R-Factor: 3.41				χ^2: 1.92

3.4.2. Electrochemistry

When being cycled in the voltage window from 2 V to 4.8 V, the $Li_{1.2}Ni_{0.13}Co_{0.13}Mn_{0.54}O_2$ generally shows a typical load curve[179] with a few key characters (Figure 3-6): (a) a curved region up to about 4.4 V, counting for a specific capacity of 122.5 mAh g^{-1} approximately, corresponds to the conventional transition metal oxidation ($Ni^{2+} \rightarrow Ni^{3+} \rightarrow Ni^{4+}$ and $Co^{3+} \rightarrow Co^{4+}$)[180]; (b) a plateau-like region and another subsequent curved region up to the 4.8 V cut-off, which are far beyond the limit of transition metal oxidation, corresponds to the oxidation of oxygen and the loss of oxygen from the lattice[76,184]; (c) an S-type discharge curve attributes to both the reduction of oxygen and transition metals[76,184]; (d) a significant irreversible capacity.

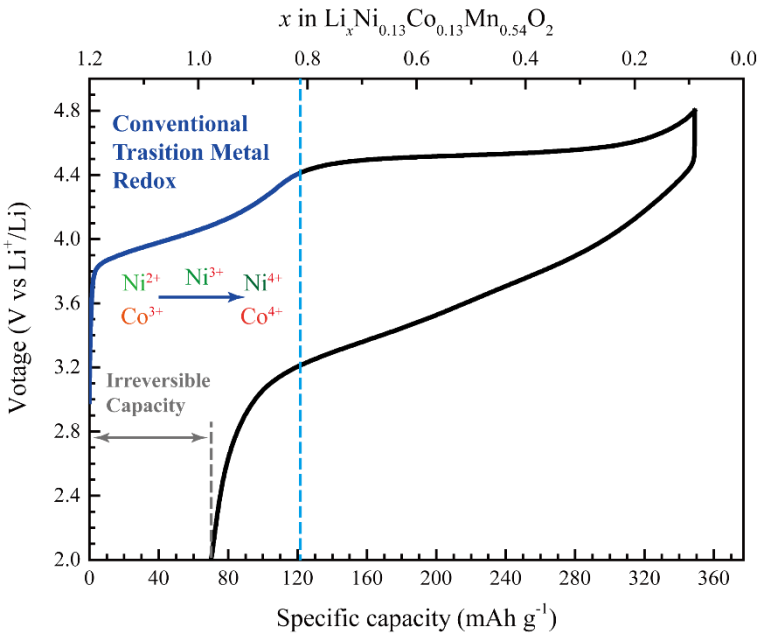

Figure 3-6 a typical load curve of $Li_{1.2}Ni_{0.13}Co_{0.13}Mn_{0.54}O_2$ when charged at 50 mA g^{-1} (C/5), at room temperature. The region corresponding to the conventional transition metal oxidation during charge is marked in dark blue.

The materials obtained from these three synthesis methodologies all present the typical load curve of the $Li_{1.2}Ni_{0.13}Co_{0.13}Mn_{0.54}O_2$ (Figure 3-7(a)), although the oxalate

synthesized material shows much less charge (280.6 mAh g^{-1}) and discharge capacities (219.3 mAh g^{-1}) than the others. The load curves of the carbonate co-precipitated and R-F gel synthesized materials are almost identical, with the specific charge capacities of 337.6 mAh g^{-1} and 348.8 mAh g^{-1}, respectively. The capacities up to 4.4 V of both are about 126 mAh g^{-1}, closely matching with the theoretical value (122.5 mAh g^{-1}) for the transition metal oxidation mentioned above. However, the same region for the oxalate co-precipitated material is far less than the theoretical value of the transition metal oxidation and only counts for 100 mAh g^{-1}. Considering the oxalate co-precipitated material has a larger particle size and wider particle size span than the others, it is likely the reason for the significant shortage of charge and discharge capacities for this material. Over 100 cycles, all materials share the similar trend of degradation on charge and discharge capacities (The Figure 3-7 (b) & (c)). In particular, the degradation appears to be faster in the first 10 cycles. It is interesting to notice that unlike the rest two materials, the carbonate co-precipitated material presents dramatic changes from the 2nd to the 4th cycle on both charge and discharge capacities. Similar behaviour is also observed for the hydroxide co-precipitated $Li_{1.2}Ni_{0.13}Co_{0.13}Mn_{0.54}O_2$ in the earlier work of our research group[241]. For both cases, the primary particles are severely aggregated and even with merged grain boundaries to form secondary particles with the size of a few micrometre. When cycling at a high rate, such morphology not only makes the core of secondary particles difficult being infiltrated by the electrolyte, but also extends the diffusion pass of Li^+ in these particles. It, therefore, hinders the kinetic capability of the material. Such dramatic changes on the charge and discharge

capacities for the carbonate co-precipitated material could possibly be attributed to the gradual activating process of secondary particles considering the morphology effects. In the subsequent cycles, the capacities degrade for the two co-precipitated materials following a quasi-linear trend, whereas the degradation of the R-F gel synthesized material is stabilized after about 40 cycles. At the 100th cycle, the specific discharge capacity of the carbonate co-precipitated and R-F gel synthesized materials are 230 mAh g^{-1} and 234 mAh g^{-1}, corresponding to 90% and 91% capacity retention (referring to the discharge capacity of the 10th cycle), respectively. The oxalate co-precipitated material shows much less discharge capacity of 176 mAh g^{-1} at 100th cycle, corresponding to only 83% capacity retention.

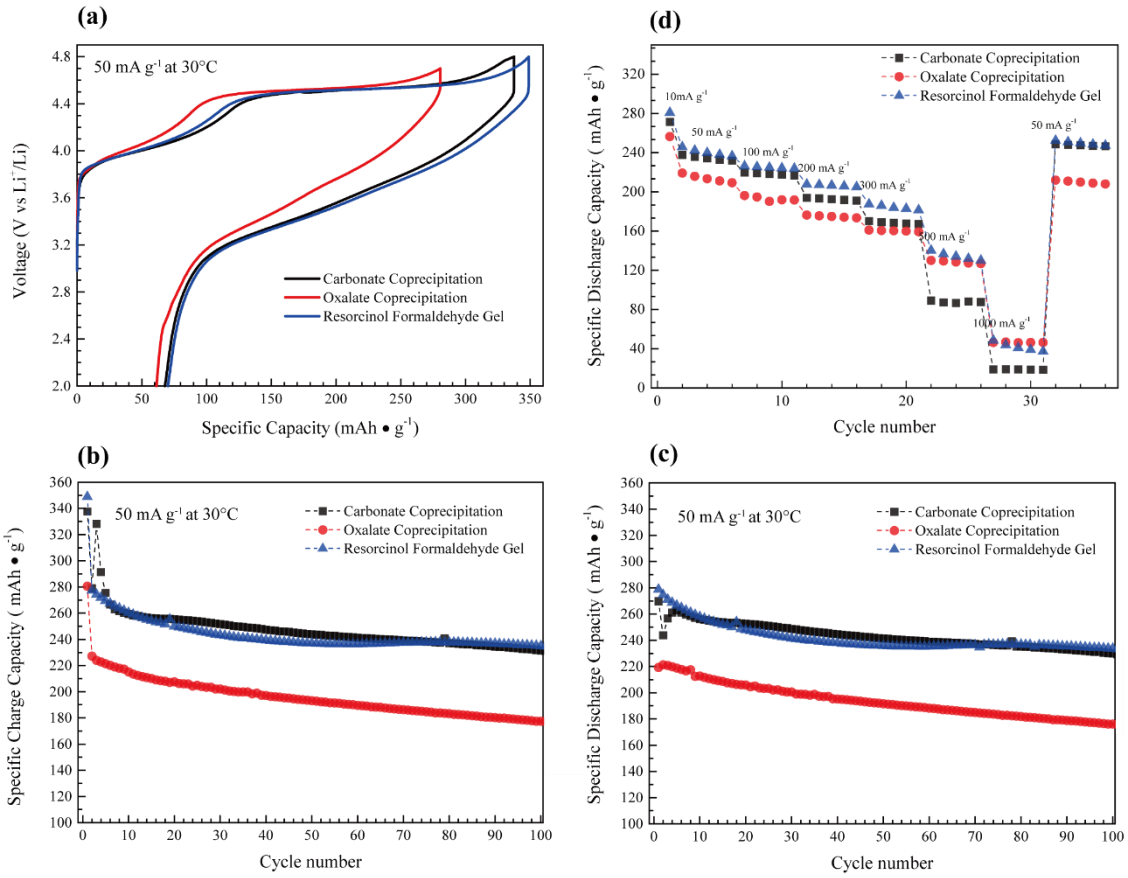

Figure 3-7 (a) the load curve, specific (b) charge and (c) discharge capacities versus cycle number plots and (d) discharge rate performance of $Li_{1.2}Ni_{0.13}Co_{0.13}Mn_{0.54}O_2$ synthesized by carbonate co-precipitation (in black), oxalate co-precipitation (in red) and R-F gel (in blue) methodologies.

The R-F gel synthesized material is also the most desirable one in terms of the discharge capacity at high rates among all three materials (Figure 3-7(d)). When discharged at 300 mA g^{-1} (1.2C, referring to 250 mA g^{-1} for 1C), the material is still capable of delivering a discharge capacity about 183 mAh g^{-1}. An accelerated discharge capacity degrading is noticed at higher rates for this material, and at 1000 mA g^{-1} the capacity even drops about 70% (from about 130 mAh g^{-1} to about 40 mAh g^{-1}) comparing with the capacity at 500 mA g^{-1}. This may due to the unstable surface of fine particles. At higher rates, radical electrochemical reactions require a stable solid-liquid interface for both the kinetics and preventing relevant side-reactions. As the R-F gel synthesized

material has the smallest primary and secondary particles, its particle surface is likely to be more reactive and support side reactions like electrolyte decomposition, which hindering the discharge.

The carbonate co-precipitated material shows desirable discharge capacity at lower rates, but its discharge capacity falls significantly comparing to the R-F gel synthesized material at higher rates ($\geqslant$200 mA g^{-1}) (Figure 3-7(d)). When it being discharged at 500 mA g^{-1} and 1000 mA g^{-1}, its discharge capacity becomes the worst among three materials. This could also be explained by the above-mentioned morphology effects. At higher rates, the severe aggregation and larger secondary particles become the limitation for the fast kinetics mainly due to the difficulty of electrolyte infiltration and Li^+ ion diffusion. On the contrary, the oxalate co-precipitated material shows a better rate stability at higher rates ($\geqslant$200 mA g^{-1}). At 500 mA g^{-1} and 1000 mA g^{-1}, it delivers similar capacity to the R-F gel synthesized material. After the rate variation, all these materials show promising capacity retention and remain the similar discharge capacities as compared with the 2nd to 6th cycles, when being discharged at 50 mA g^{-1} again.

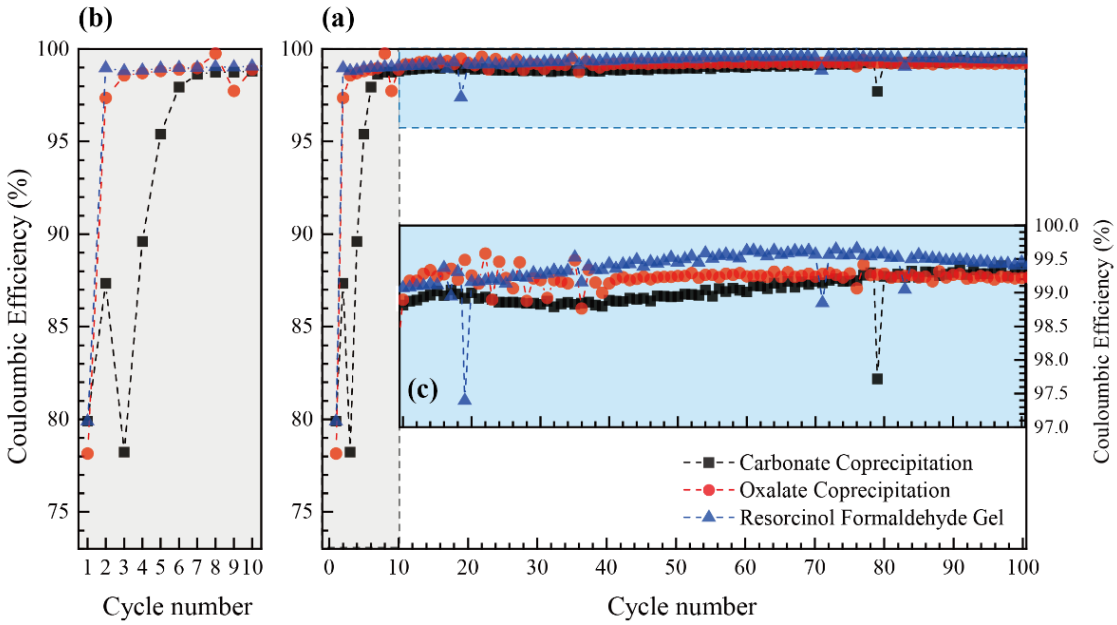

Figure 3-8 (a) Columbic efficiency versus cycle number plots of $Li_{1.2}Ni_{0.13}Co_{0.13}Mn_{0.54}O_2$ synthesized by carbonate co-precipitation (in black square), oxalate co-precipitation (in red dot) and R-F gel (in blue triangle) methodologies; (b) the initial 10 cycles (light gray region); (c) the subsequent 90 cycles (light blue region)

The couloumbic efficiency is essential for cathode materials of Li-ion batteries, since it is one of the direct factors to indicate the cycle life. In the laboratory characterizations of cathode materials, the half-cell setup is normally used, which takes lithium metal as the anode of the cell, providing unlimited Li^+ supply from the anode. However, in real Li-ion batteries, the anode materials are normally graphite, or silicon or lithium metal oxides in some cases, causing the limited supply of Li^+. Then, the cycle life of a battery is highly depended on the sustained Li^+ during cycling. Therefore, a long cycling-life Li-ion battery should ideally reach its highest coulombic efficiency in the earliest few cycles possible and keep operating at highest efficiency during cycling. The R-F gel synthesized material shows the most promising coulombic efficiency character among all these materials (Figure 3-8(a)). It establishes a significant high coulombic efficiency of 98.97% at the 2nd cycle and then reaches to 99.07% at the 10th cycle (Figure 3-8(b)).

Up to the 100th cycle, its coulombic efficiency is well above 99.2% (Figure 3-8(c)). The carbonate co-precipitated material shows a changing coulombic efficiency in the first 10 cycles and gradually stabilizes after then, but it does not reach 99% until the 56th cycle. The oxalate co-precipitated material also establishes high coulombic efficiency at an early stage of cycling (3rd cycle) but presents an unstable changing on the coulombic efficiency from 20th to 40th cycle and stabilizes afterwards.

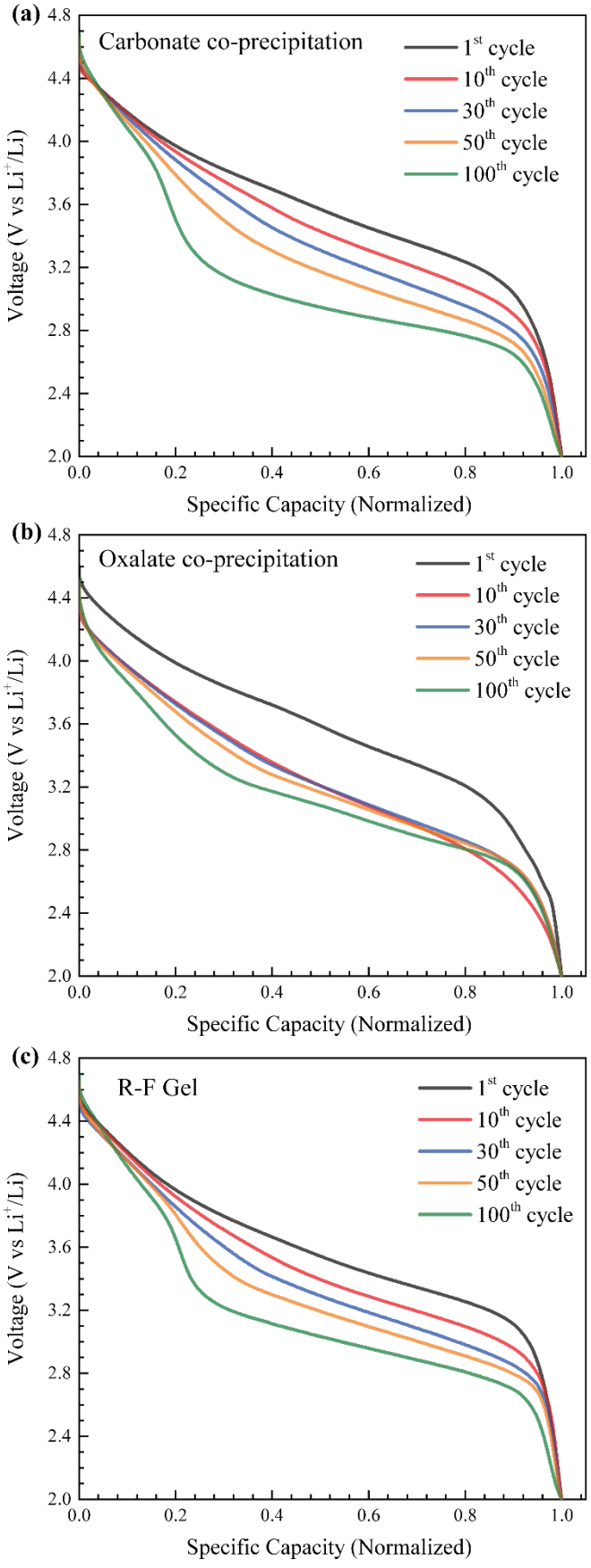

Figure 3-9 Normalized capacity discharge curves of $Li_{1.2}Ni_{0.13}Co_{0.13}Mn_{0.54}O_2$ synthesized by (a)

carbonate co-precipitation, (b) oxalate co-precipitation and (c) R-F gel methodologies. Only the data of 1st cycle, 10th cycle, 30th cycle, 50th cycle and 100th cycle are reported. The discharge capacity retention of these materials is shown in the Figure 3-7(c). The specific discharge capacities were normalized to the maximum discharge capacity of their corresponding cycles. This normalization method is as identical as reported[156].

As mentioned in the introduction, voltage fading remains one of the essential issues that hindering the Li-rich materials from applications. While cycling in long-term, the discharge voltage profile of the Li-rich materials fades gradually in each cycle, accompanied with capacity fading, which leads to a gradual fading of the energy density. This not only brings difficulties for the battery (pack) engineering but also shortens the cycle-life of a battery. The reason for the voltage fading is believed to be the structural rearrangement, which is attributed to both the cation migration and loss of oxygen from lattice during cycling[156,180,236,239,248]. The $Li_{1.2}Ni_{0.13}Co_{0.13}Mn_{0.54}O_2$ synthesized by these three methodologies present different degree of voltage fading from the 1st to the 100th cycle (Figure 3-9). For the carbonate co-precipitated (Figure 3-9(a)) and R-F gel synthesized sample (Figure 3-9(c)), the normalized discharge profiles show a gradual fading of voltage happening mainly in the low voltage region (<3.8V). The derivative curves of both also confirm that the two reduction peaks A & B in the 1st discharge are progressively shifting towards the lower voltage region over cycling. At the 100th cycle, the reduction peak B' has shifted about 570 mV and 350 mV (from B) for the carbonate co-precipitated (Figure 3-10(a)) and the R-F gel synthesized material (Figure 3-10(c)), respectively.

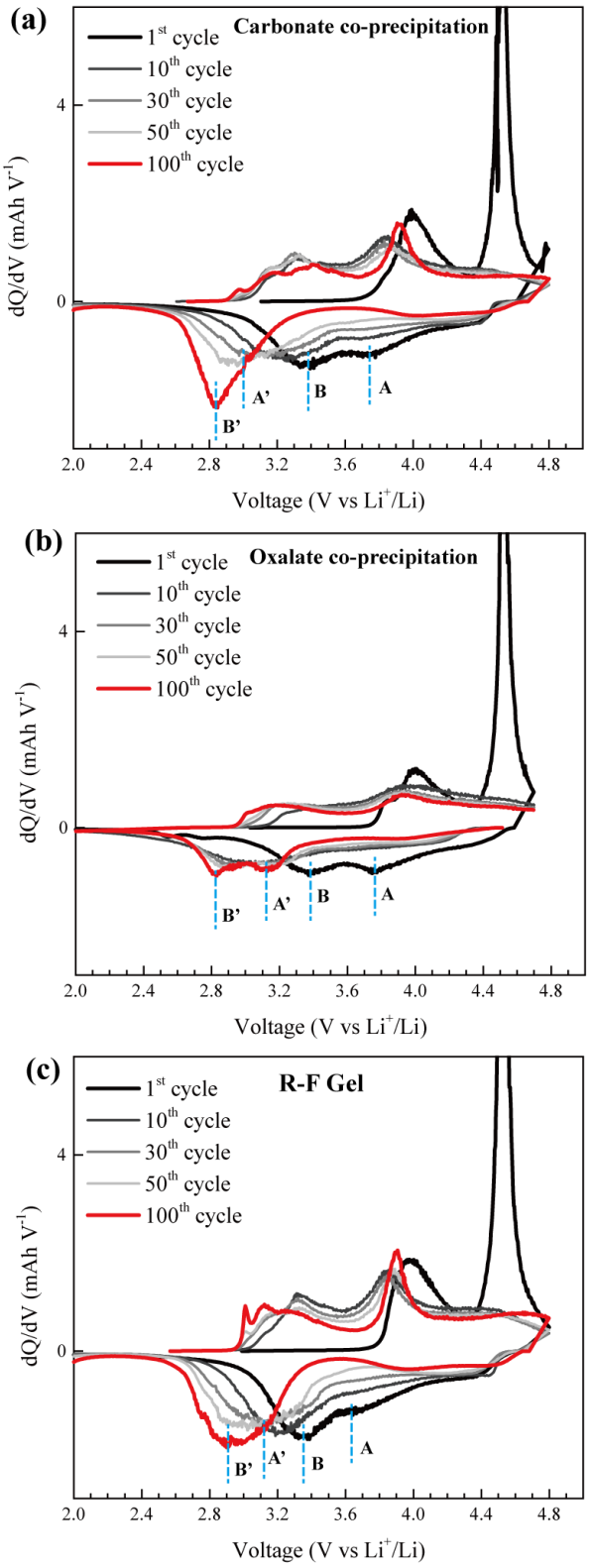

Figure 3-10 Capacity/voltage derivative versus voltage curves (dQ/dV versus V) from 1st (in black) to 100th (in red) cycle of the $Li_{1.2}Ni_{0.13}Co_{0.13}Mn_{0.54}O_2$ synthesized by (a) carbonate co-precipitation, (b) oxalate co-precipitation and (c) R-F gel methodologies. Only the data of 1st cycle, 10th cycle, 30th cycle, 50th cycle and 100th cycle are reported.

For the oxalate co-precipitated material, the major voltage fading happens in the initial 10 cycles and then becomes relatively steady (Figure 3-9(b)), instead of gradual fading over cycling like the other cases. The derivative curve also confirms the significant shift of the reduction peaks A & B happens during the transition from the 1st to 10th cycle, whereas from the 10th to 100th cycle, minor shift of the reduction peaks is observed (Figure 3-10(b)). At the 100th cycle, the voltage fading of the reduction peak B' is about 590 mV, close to the case of the carbonate co-precipitated material. Therefore, the R-F gel synthesized material presents the least voltage fading over 100 cycles among these three materials.

3.5. Conclusion

In this chapter, three synthesis methodologies are introduced and employed to prepare an archetypal Li-rich material - $Li_{1.2}Ni_{0.13}Co_{0.13}Mn_{0.54}O_2$. The crystallographic structure characterization of these materials confirms that obtained materials are in a layered single phase with honeycomb interlayer ordering. The detailed crystallographic parameters are given by applying the Rietveld structure refinement following the *R-3m* space group.

The elemental analysis confirms that the compositions of these materials are in good accordance with the targeted chemical formula. The morphology of these materials, however, significantly differs from each other. The R-F gel synthesized material shows the most homogeneous and porous morphology with smallest particle size and less aggregation. The galvanostatic cycling test shows that both the carbonate co-

precipitated and R-F gel synthesized materials can deliver very high capacity, whereas the capacity of the oxalate co-precipitated material is not ideal. The rate test demonstrates good rate performance obtained from the oxalate co-precipitated and R-F gel synthesized materials but dramatic capacity drops for the carbonate co-precipitated material. These observed electrochemical behaviours could be explained associated with the morphology of these materials. In addition, the study on discharge curves and its derivative curves of these materials over 100 cycles demonstrates that all these materials suffer voltage fading over the long-term cycling, which is a typical but problematic issue for Li-rich materials. Relatively, the R-F gel synthesized material shows less voltage fading over 100 cycles.

Considering its less complicated protocol, accurate composition, controlled morphology, and excellent yet stable electrochemical performance, the R-G gel synthesis is regarded as an ideal one among these synthesis methodologies. Therefore, it is selected for the preparation of $Li_{1.2}Ni_{0.13}Co_{0.13}Mn_{0.54}O_2$ in all the relevant mechanism studies afterwards.

CHAPTER 4 Binder Effects on The Electrochemical Performance of Li-rich Cathode Material

4.1. Background

As being mentioned in section 1.1.3.3, PVDF is the most widely used binder in commercial Li-ion batteries. This is mainly due to its wide electrochemical stability window and good adhesion to electrodes[78]. However, PVDF binder also has some disadvantages including that (1) its interaction with the electrode material is based on a weak Van der Waals force[84], resulting in poor binding strength, especially for long-term cycling; (2) the processing of PVDF binder based electrode involves volatile and toxic organic solvents such as NMP or Tetrahydrofuran (THF), thus it is neither cost-efficient nor environmental friendly[78,87,249].

Finding the most suitable binder is very important and intensive work goes on optimizing electrodes of Li-ion batteries. So far, most academic research has focused on new binders for anode[78,87,250,251], particularly for the Si-based composite electrode[79-81,83,252-254]. This is due to the critical need to accommodate an enormous volume expansion/contraction[35,36] of silicon during lithiation/delithiaion. Much less research focuses on binders for cathodes and it normally targets conventional cathode materials such as $LiCoO_2$, $LiFePO_4$ and NMC materials. However, for the high energy density cathode materials, such as layered Li-rich materials, relevant binder research is rare. In section 1.3, the issues which inhibit the commercialization of the Li-rich materials were

discussed. This included the low 1st cycle coulombic efficiency[154,155], the capacity and voltage fading in long-term cycling[6,140,156,157], the stability of electrolyte at higher operating voltage window and the corresponding harsh chemical and electrochemical environment[77]. In addition, the Li-rich materials normally show oxygen redox and release during cycling, which is discussed in the following CHAPTER 5. These issues enhance the significance of binder and a new focus on electrode composition is required. Therefore, exploring alternative binders which are specifically suitable for the Li-rich materials is critical for elevating its electrode performances.

Additionally, as discussed in section 1.3, the Li-rich materials are potential candidates for next generation EVs and would be manufactured in ultra-large scale once commercialized. Therefore, from the application perspective, it is essential to investigate the water-soluble binders for Li-rich materials, following the trend of cost-efficient and eco-friendly large scale manufacture of Li-ion batteries.

4.2. Research Goal

In this chapter, the research goal is to explore the effects of PTFE and Sodium Carboxymethyl Cellulose (CMC-Na) as alternative binders for the Li-rich materials.

The PTFE binder is chosen because that all carbons in PTFE are fully fluorinated. Consequently, PTFE binder is expected to be more chemically and electrochemically stable compared with conventional PVDF binder. However, to the best of my knowledge, the effects of PTFE binder on the Li-rich materials has not been studied, although PTFE has served as the binder in many published researches on Li-rich

materials[255-257].

The CMC-Na is reported as a good binder for the Si anode[78,252,258,259], as it exhibits a high tolerance towards the volume expansion of Si[79,80]. Since the layered Li-rich materials also present volume variation during cycling, CMC-Na is proposed to enhance cycling performance of the Li-rich materials based electrodes.

4.3. Experiment Details

4.3.1. Electrode Processing

Pellet electrodes and two different casted electrodes were made for studying the binder effects. The pellet electrode with PTFE binder and the casted electrode with PVDF binder were made as described in section 2.3.5. For the processing of the casted electrode with CMC-Na binder, CMC-Na (10 wt%) was dissolved in deionized water (90 wt%) to form the aqueous binder solution, as it is insoluble in organic solvent. The electrode slurry was made by thoroughly mixing the cathode material, Super P carbon and CMC-Na binder solution in a Retsch PM100 planetary ball mill, referring to the composition ratio of 80 wt%:10 wt%:10 wt% (for CMC-Na rather than the CMC-Na binder solution). Once mixed, the electrode slurry was cast onto an aluminium foil current collector (0.050 mm, Advent Research Material Ltd.) by a doctor blade and then dried at 100 °C to evaporate the water. The resulting electrode film was then roll-pressed at 100 μm, which normally leading to an electrode thickness of 15~18 μm, and punched into electrodes with a diameter of 1.9 cm then further dried at 80 °C under vacuum overnight before being assembled in an electrochemical cell.

A detailed summary of electrodes with different binders and their processing are given in the Table 4-1.

Table 4-1 Summary of electrodes with different binders and their processing

Processing Category	Pellet Electrode	Casted Electrode	
Electrode Name	PTFE Binder Based Electrode	PVDF Binder Based Electrode	CMC-Na Binder Based Electrode
Active Material (80 wt%)	$Li_{1.2}Ni_{0.13}Co_{0.13}Mn_{0.54}O_2$		
Conductive Additive (10 wt%)	Carbon Super P		
Binder (10 wt%)	PTFE	PVDF	CMC-Na
Binder Solution	-	PVDF (5 wt%) in NMP (95 wt%)	CMC-Na (10 wt%) in deionized water (90 wt%)
Drying Temperature (Solvent evaporation) (Electrode Drying)	- 80 °C	120 °C 80 °C	100 °C 80 °C
Pellet Size (Diameter)	1.6 cm	1.9 cm	
Electrode Thickness	35~40 μm	15~18 μm	

In the following text, the pellet electrode is named “PTFE binder electrode”, while the electrode with PVDF binder is named “PVDF binder electrode”. In the following figures, the PTFE electrode and the PVDF electrode are labelled “PTFE” and “PVDF”, respectively. For all the binder effects study, the R-F gel synthesized $Li_{1.2}Ni_{0.13}Co_{0.13}Mn_{0.54}O_2$ was used as the active material.

4.3.2. Electrochemical Tests

All of the electrodes were tested by galvanostatic cycling in coin cells to characterize the binder effects on the electrochemical performance of electrodes. Coin cells were made according to the methods described in section 2.3.5.2.

The galvanostatic cycling tests were done within the voltage window of 2 V to 4.8 V versus Li^+/Li in a half-cell configuration at 50 mA g^{-1}. All these electrochemical tests were done on a Biologic MPG-2 or Maccor Series 4000 battery tester. During cycling, all the cells were kept at 30 °C in a Memmert ICP 600 Laboratory Incubator. After 100 cycles, the coin cells with PVDF and PTFE electrodes were disassembled and washed with DMC. Once being dried under vacuum overnight, they were taken for further topography and elemental distribution analysis.

4.3.3. Topography and Elemental Distribution Characterization

The topography of electrodes, both top-view and cross-section view, was investigated by a Carl Zeiss Merlin SEM. The EDX microanalysis was employed to map the elemental distribution of the electrodes, using the X-Max^N Silicon Drift Detector (Oxford Instruments) associated with the Carl Zeiss Merlin SEM. Before transference into the SEM vacuum chamber, electrodes for the cross-section investigation were glued onto a special metallic blade by conductive silver paint, then polished using a Gatan PECS II Instrument.

The experimental idea of these characterization and the operation of Gatan PECS II instrument was attributed to the author of this thesis, while the SEM and EDX instrument were operated by Dr Andrew Naylor from our research group.

4.4. Results and Discussion

4.4.1. PTFE Binder Effects

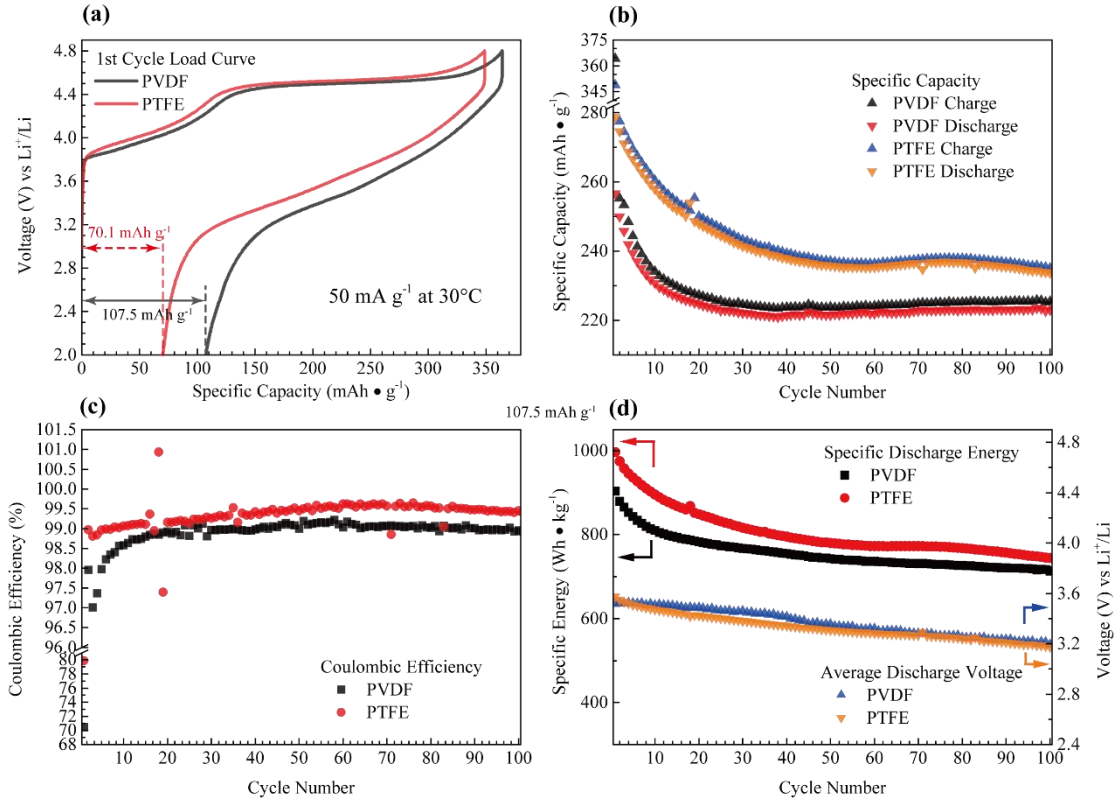

Figure 4-1 The electrochemical behaviour comparison of the PVDF and PTFE binder electrodes at the cycling rate of 50 mA g^{-1} at 30 °C. (a) 1st cycle load curve; (b) charge (up-triangle) and discharge (down-triangle) capacity over 100 cycles; (c) coulombic efficiency over 100 cycles; (d) specific discharge energy (in square and circle) and average discharge voltage (in up-/down-triangles) over 100 cycles. Additionally, the 1st cycle irreversible capacities of both binder electrodes have been annotated.

Figure 4-1 indicates that the PVDF and PTFE binder electrodes exhibit clear differences in performance even at the very early stage of cycling. Although both electrodes present a typical 1st cycle load curve for $Li_{1.2}Ni_{0.13}Co_{0.13}Mn_{0.54}O_2$, it is obvious that the PTFE binder electrode has much less 1st cycle irreversible capacity (Figure 4-1(a)), resulting in an excellent first cycle coulombic efficiency of 79.9% (Figure 4-1(c)), while most of the reported values for Li-rich materials are around 75%[6,136,140]. Over the 100 cycles,

the PTFE binder electrode outperforms the PVDF binder electrode, as it demonstrates significantly higher specific capacities (about 20 mAh g^{-1}) in both charge and discharge (Figure 4-(b)). In general, the PTFE binder electrode achieves an extremely high coulombic efficiency over 99% from the 2nd cycle and improves further in the subsequent cycles, whereas it takes more than 10 cycles for the PVDF binder electrode to reach a relatively high level of coulombic efficiency over 98.5%, which is maintained at about 98.7% throughout the 100 cycles. This is about 0.5% less than the case for the PTFE binder electrode. Considering a full-cell configuration, in which the anode cannot provide unlimited Li^+ ions as in a Li half-cell, the 0.5% difference in coulombic efficiency is significant, as every cycle the PVDF binder electrode would lose 0.5% more Li^+ ions, resulting in a poor cycling life of the entire cell compared with the PTFE binder electrode.

To the best of my knowledge, the superior cycling performance of the PTFE binder electrode over the conventional PVDF binder electrode has not been studied, although PTFE is not a new binder for Li-ion batteries[255-257,260,261]. A combined cross-section XRD and EDX study is done to understand the source of the enhanced cycling performance of the PTFE binder electrode.

4.4.1.1. Pristine Electrodes Studies

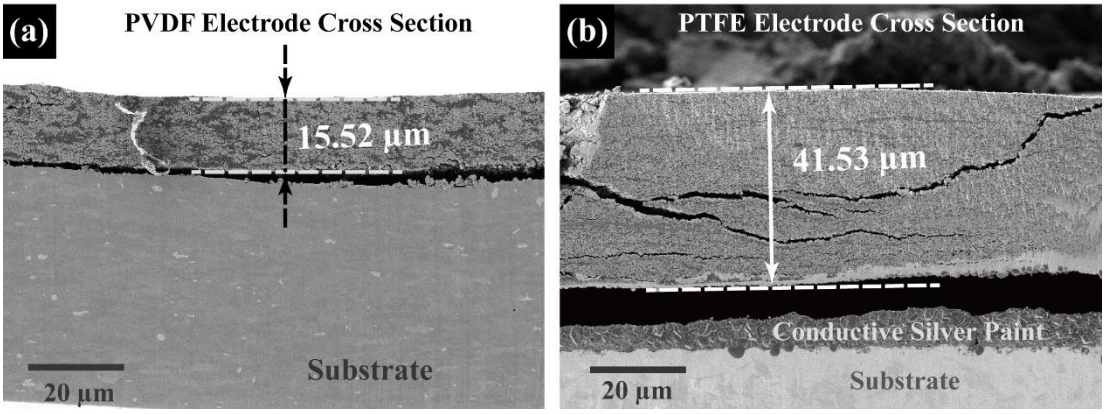

Figure 4-2 Cross section SEM view of the electrodes with PVDF (a) and PTFE (b) binder, respectively. Both images were generated from the secondary electron signals.

A cross-section view (Figure 4-2) of both pristine electrodes shows that the PVDF binder electrode is 15.52 µm in thickness, while the PTFE binder electrode is 41.53 µm in thickness. Visible cracks appear on the PTFE binder electrode cross-section, which is a lamella structure and likely resulting from the pellet electrode processing steps. They also appear in the Figure 4-4(b)&(d). It is worth noting that in the cross-section view of the PVDF binder electrode, there are multiple regions showing lower contrast, which may suggest that mixing of the electrode components is not homogenous in the PVDF binder electrode. To verify such assumption, EDX analysis at a higher magnification on both electrodes is carried out.

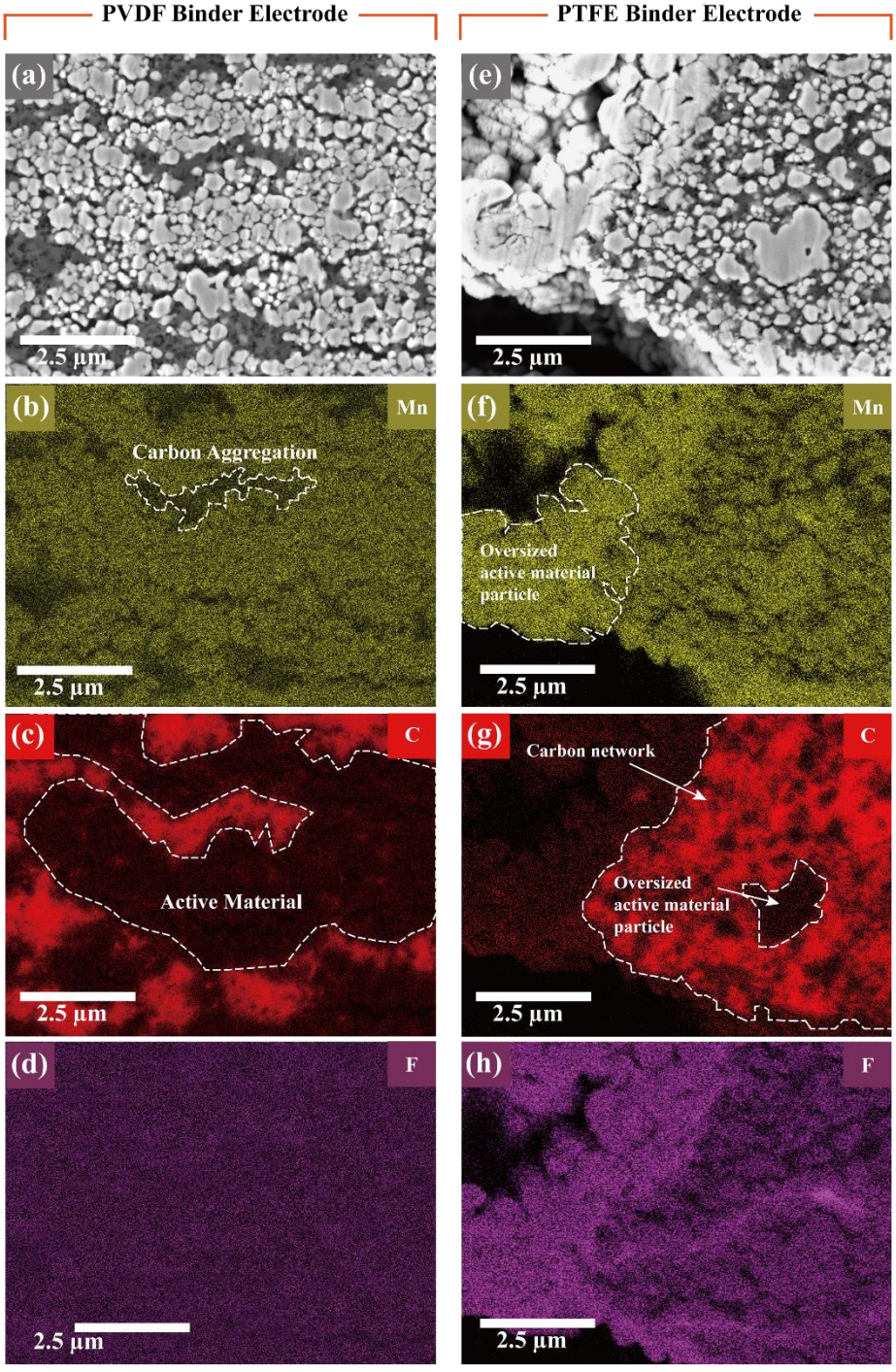

Figure 4-3 Cross section SEM images and the EDX element labelled views of the PVDF (the left column) and PTFE (the right column) binder electrodes: (a) & (e) SEM images generated from the secondary electron signals, and the EDX element labelled views on (b) & (f) Manganese, (c) & (g) carbon, and (d) & (h) fluorine.

In Figure 4-3(a), a SEM image of the PVDF binder electrode at a higher magnification clearly presents the contrast differences among regions of the electrode. The EDX elemental mapping distinguishes the elemental distribution of manganese (Figure 4-3(b)), carbon (Figure 4-3(c)) and fluorine (Figure 4-3(d)) in the same image. They represent $Li_{1.2}Ni_{0.13}Co_{0.13}Mn_{0.54}O_2$ (active material), carbon SP (conductive additive) and PVDF binder, respectively. A higher saturation of the colour stands for a higher concentration of elements, or equivalently higher content of a certain composition. As expected, the PVDF binder evenly distributes over the electrode since it is dissolved in NMP for the electrode processing. However, the concentration gradient of Mn and C indicates $Li_{1.2}Ni_{0.13}Co_{0.13}Mn_{0.54}O_2$ and carbon SP are not homogeneously mixed in the PVDF electrode. In fact, the Mn and C contents on Figure 4-3(b) & (c) are complementary to each other, suggesting there are $Li_{1.2}Ni_{0.13}Co_{0.13}Mn_{0.54}O_2$ and carbon SP aggregation regions of the PVDF electrode. Combining with the contrast differences of the SEM image, it is confirmed that in Figure 4-3(a) the dark gray regions are carbon SP aggregations, while the light gray regions are $Li_{1.2}Ni_{0.13}Co_{0.13}Mn_{0.54}O_2$ aggregations. Between the $Li_{1.2}Ni_{0.13}Co_{0.13}Mn_{0.54}O_2$ particles, there are much less or even no carbon SP particles.

The EDX analysis on the PTFE binder electrode suggests that no large aggregations of $Li_{1.2}Ni_{0.13}Co_{0.13}Mn_{0.54}O_2$ and carbon SP are presented and a homogenous mixture of both particles is obtained. A well-connected carbon SP network is presented when the carbon is mapped over the entire view (Figure 4-3(g)). Combining with the Mn element mapping (Figure 4-3(f)), it is clear that carbon SP network is established around the

$Li_{1.2}Ni_{0.13}Co_{0.13}Mn_{0.54}O_2$ particles providing good contact. Meanwhile, unlike the PVDF binder electrode case, the F element mapping (Figure 4-3(h)) shows an almost identical distribution as the Mn element, which indicates that the majority of PTFE binder binds to $Li_{1.2}Ni_{0.13}Co_{0.13}Mn_{0.54}O_2$ particles providing well-bound active material particles. It should be noted that there are regions showing very little or even no signal of Mn, C, and F on the element mapping views, as there is no sample on the focused plane of the EDX detector.

The above-mentioned topography could explain the difference in electrochemical behaviour between both electrodes. For the PVDF binder electrode, due to the segregation of the active material and carbon SP particles, the electronic conductivity between particles is not homogenous, resulting in lower charge & discharge capacities. It also leads to a longer activation process for the $Li_{1.2}Ni_{0.13}Co_{0.13}Mn_{0.54}O_2$ particles, which presents as a lower coulombic efficiency for the initial cycles and then a gradual increase of the coulombic efficiency in the subsequent cycles. In contrast, for the PTFE binder electrode, the well-distributed carbon SP network enables fast charge transfer kinetics. Therefore, it achieves a high level of coulombic efficiency at about 99% right after the 1st cycle and maintains higher charge & discharge capacities and coulombic efficiency afterwards.

4.4.1.2. Multi-cycled Electrode Studies

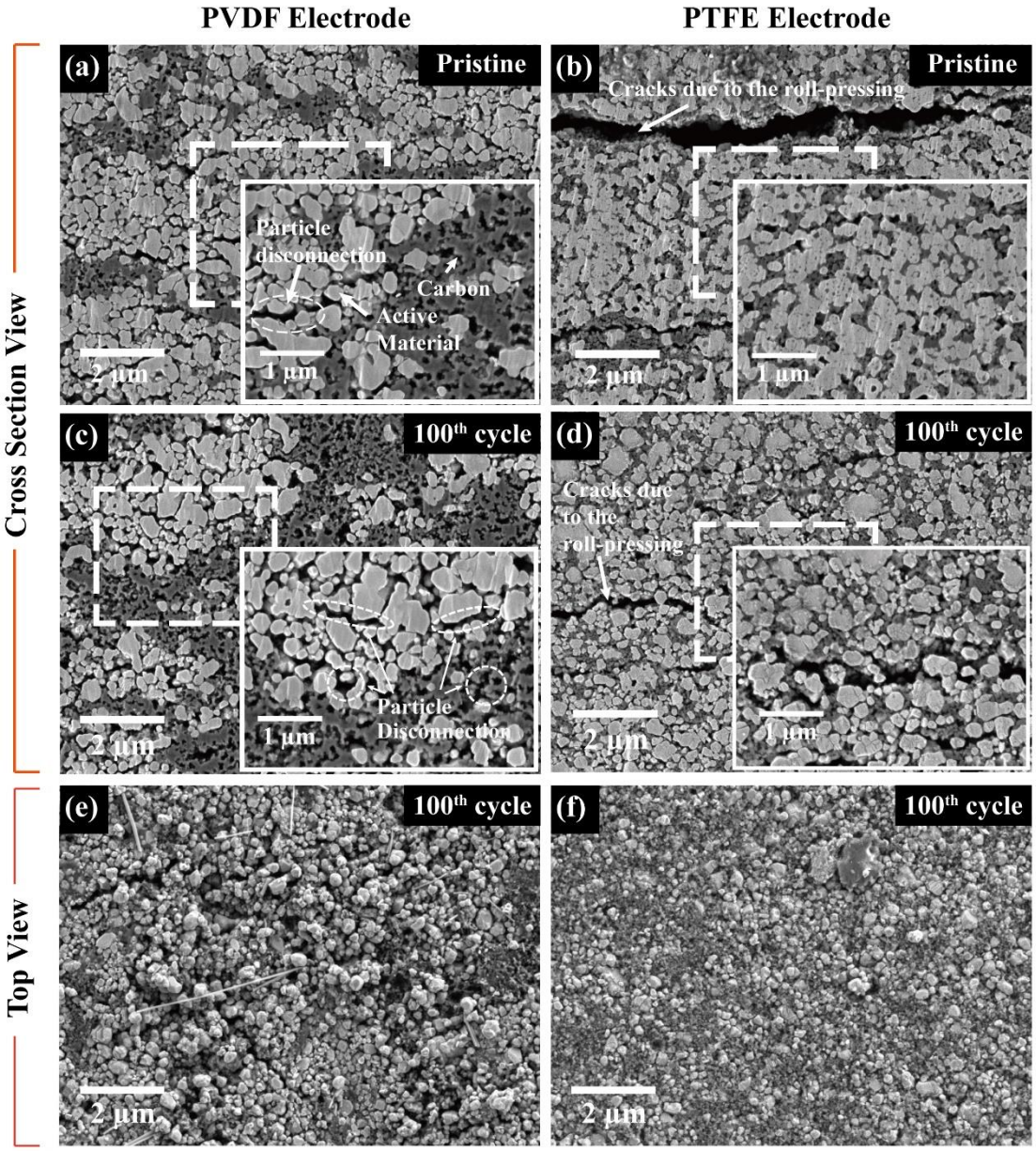

Figure 4-4 SEM fine-view comparison on the PVDF (left column) and PTFE electrodes (right column). (a) & (b) cross-section view on pristine electrodes; (c) & (d) cross-section views and (e) & (f) top-views on electrodes after 100 cycles. These images were generated from the secondary electron signals.

Further comparison of the topography of the two binder electrodes after 100 cycles illustrates a better binding property of PTFE binder over the PVDF binder. The pristine PVDF binder electrode (Figure 4-4(a)) not only shows segregations of the active material particles and the carbon SP particles, but also presents a few disconnected

active material particles, whereas the pristine PTFE binder electrode (Figure 4-4(b)) shows a dense packing of compositions. After 100 cycles, for the PVDF binder electrode (Figure 4-4(c)), cracks between active material particles becomes obvious and more disconnected particles appear, whereas the PTFE binder electrode (Figure 4-4(d)) remains tightly bound and no significant differences are found comparing with the pristine electrode. The top-view of both electrodes (Figure 4-4(e)&(f)) also confirms such changes: for the PVDF electrode, a significant number of disconnected particles could be observed and the electrode construction appears to be loose; in contrast, the PTFE binder electrode preserves a dense construction and disconnected particles are rarely found. As a result, the PTFE binder electrode maintains higher charge and discharge capacities and excellent coulombic efficiency of over 99% during the first 100 cycles, whereas the PVDF binder electrode delivers much lower capacities and coulombic efficiency. Presumably, the PVDF binder electrode would face severer capacity fading and lower coulombic efficiency in longer term cycling. In fact, the binding strength issue of PVDF binder has also been reported in the Si based anode electrode[253], in which it influences significantly due to the volume expansion of Si-based composite anode. As reported[262,263], the PVDF binder suffers from swelling when exposed to carbonates based electrolytes, and failed to maintain its mechanical property as a result.

To summarize, the homogeneously mixed electrode compositions and a better binding property of the PTFE binder enable advantages on electrochemical performance when it is used. However, besides this finding, there could be other factors that are responsible

for the electrochemical performance differences of both binders.

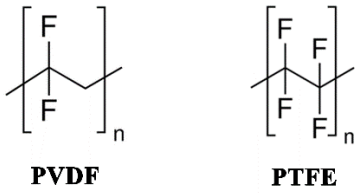

Figure 4-5 Structure of PVDF and PTFE

One such factor could be the chemical and electrochemical stability differences between PVDF and PTFE. When used as the binder for Li-rich materials, they face more critical challenges, as being discussed in section 1.3 and 4. Particularly, their binding properties could be influenced by (1) radical oxygen species generated from the oxygen redox and release process of Li-rich materials[76,184] and (2) a high operation voltage window of the electrode. In fact, according to Nazar *et al.*[264], the O_2^- ion reacts with PVDF and subtracts hydrogen, resulting in the decomposition of PVDF. Thus, the chemical and electrochemical stability of a binder is essential for the Li-rich cathode. Considering PTFE is fully fluorinated, and its C-F bond provides much stronger interaction than the C-H bond (Figure 4-5), it is expected to be chemically and electrochemically more stable than PVDF. Consequently, PTFE would maintain its properties better when used as the binder for Li-rich materials, whereas the conventional PVDF binder fails to preserve electrochemical performance of the electrode. The stability of PVDF and PTFE binders and how it would influence the electrode performance need to be further investigated and is not discussed in this thesis.

4.4.2. CMC-Na Binder Effects

As the PTFE binder electrode outperforms the PVDF binder electrode, the CMC-Na

binder electrode is compared directly with the PTFE binder electrode in electrochemical performance.

The 1st cycle load curves (Figure 4-6(a)) of the PTFE and CMC-Na binder electrodes almost overlay completely during charge, but their discharge curves present small differences in shape. The CMC-Na binder electrode also shows a 10 mAh g^{-1} lower irreversible capacity than the PTFE binder electrode, resulting in an even higher first cycle coulombic efficiency of 82.4%. This is rare to see for $Li_{1.2}Ni_{0.13}Co_{0.13}Mn_{0.54}O_2$. In the first 30 cycles, the CMC-Na electrode has clear advantages on charge & discharge capacities over the PTFE binder electrode (Figure 4-6(b)). However, the capacity fades more rapidly and drops below those of the PTFE binder electrode after 28 cycles. Furthermore, the CMC-Na binder electrode fails to show a high and stable coulombic efficiency (Figure 4-6(c)), whereas the PTFE binder electrode preserves excellent coulombic efficiency during cycling. In fact, the coulombic efficiency of the CMC-Na binder electrode is at the same level as the PVDF binder electrode over 100 cycles (around 98.7%, shown in the Figure 4-(c)).

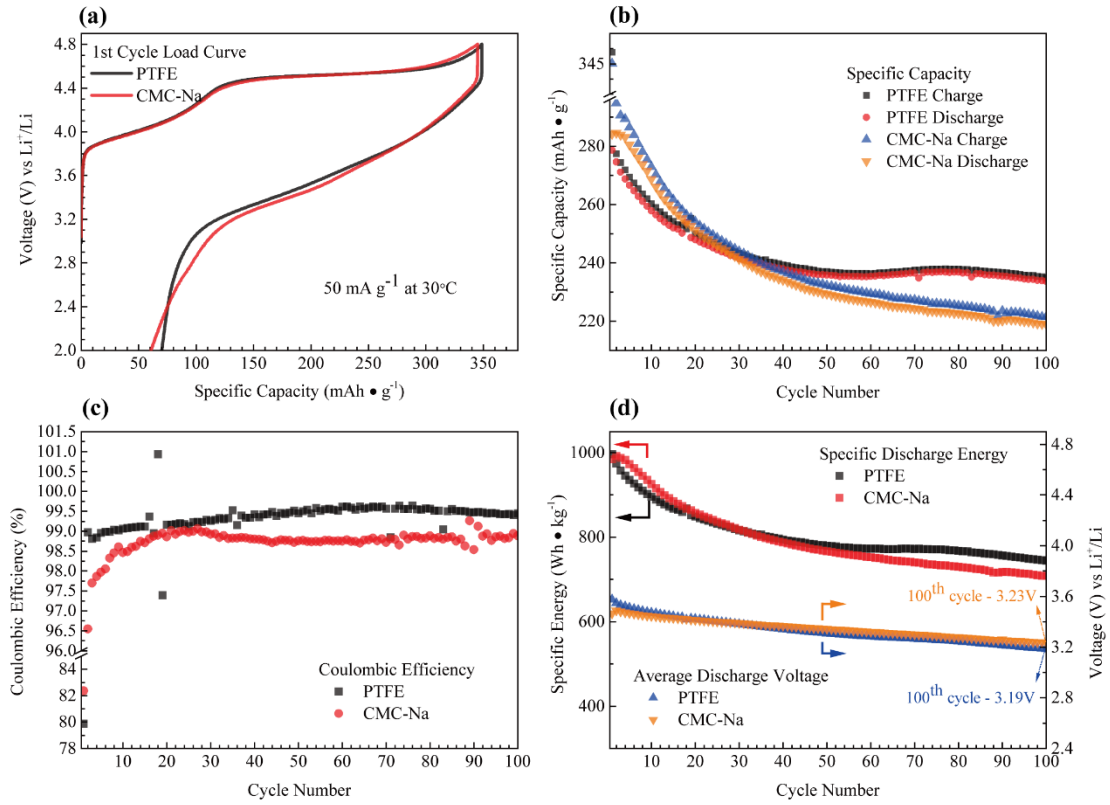

Figure 4-6 the electrochemical behaviour comparison of electrodes using the PTFE and CMC-Na binder, respectively. (a) 1st cycle load curve; (b) charge (up-triangle) and discharge (down-triangle) capacity over 100 cycles; (c) coulombic efficiency over 100 cycles; (d) specific discharge energy (in square and circle) and average discharge voltage (in up-/down-triangles) over 100 cycles.

Interestingly, although the specific energies of both electrodes behave similarly to the charge & discharge capacity, their average voltages behave contrarily (Figure 4-6(d)). The average voltage of the CMC-Na binder electrode is steadier and takes over the lead from the PTFE binder electrode after 28 cycles. At the 100th cycle, the average voltage of the CMC-Na and PTFE binder electrodes are 3.23 V and 3.19 V, respectively. This could imply that the CMC-Na binder has a positive impact on suppressing the voltage fade of the Li-rich materials during cycling. To investigate this, further investigation is carried out on the discharge curves and corresponding capacity/voltage derivative curves of both binder electrodes in 100 cycles (Figure 4-7).

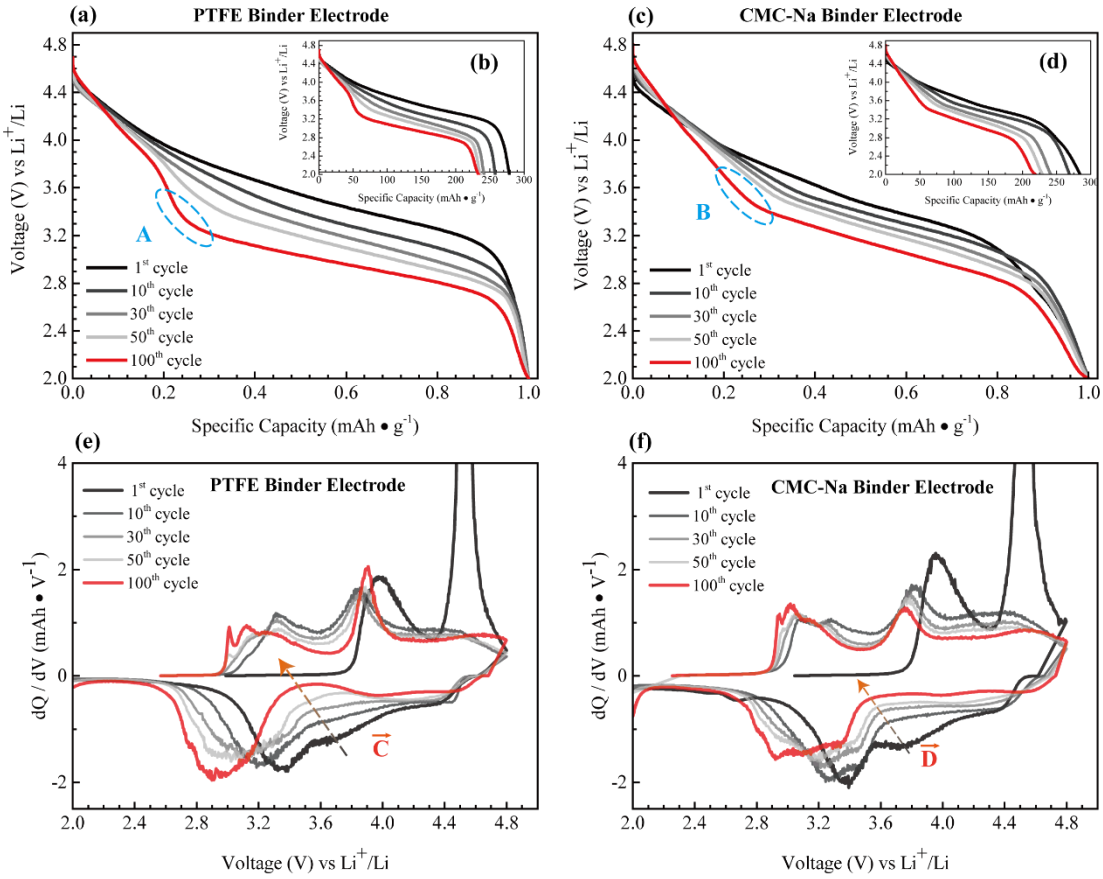

Figure 4-7 (a) - (d) Normalized and original specific discharge curves of electrodes with PTFE and CMC-Na binder, respectively; (e) & (f) capacity/voltage derivative versus voltage curves (dQ/dV versus V) from 1st (in black) to 100th (in red) cycle of electrodes with PTFE and CMC-Na binder, respectively. Only the data of 1st cycle, 10th cycle, 30th cycle, 50th cycle and 100th cycle are reported. The specific discharge capacities were normalized to the maximum discharge capacity of their corresponding cycles, following the reported method[156].

During the 100 cycles, both binder electrodes present voltage fading on discharge curves (Figure 4-7(b) &(d)). The accompanied discharge capacity fading makes the direct comparison of voltage fading confusing, thus the discharge curves of both electrodes are normalized to their corresponding 1st cycle capacities (Figure 4-7(a) &(c)). For both electrodes, the voltage fading happens at the region under 3.8 V. However, it is obvious that the discharge curves of CMC-Na binder electrode shift less towards the lower voltage direction. Particularly, at the 100th cycle, the turning region B (for the CMC-Na binder electrode) locates at about 200 mV higher than the turning

region A (for the PTFE binder electrode). This feature is better pronounced in the capacity/voltage derivative ((Figure 4-7(e) &(f))), as the evolution of derivative curves (shown as vector D) for the CMC-Na binder electrode is less significant than the one (shown as vector C) for the PTFE binder electrode. Therefore, it clearly demonstrates the effect of CMC-Na binder to suppress the electrode voltage fading.

In fact, a few studies have reported the CMC-Na as a binder for cathode materials[265-268], but most of them only focus on its advantage on discharge capacity to the PVDF binder. The effect to suppress the electrode voltage fading is not mentioned until a very recent publication[269]. Despite the fact that the CMC-Na has advanced physical properties such as stronger adhesion, negligible swelling and stable mechanical properties, the effect is explained by (1) Na^+ exchange between the binder and the active material, resulting in suppressed transition metal migration and preserved crystallographic structure; (2) inhibited dissolution of transition metal elements. However, no direct evidence of Na^+ presence in the lithium layer is presented. Besides, the stability of Li-rich materials in the aqueous solution should also be questioned, as previous studies show that when processed with CMC-Na aqueous solution, cathode materials present structural and composition changes due to proton/Li^+ exchange[267,270]. In addition, it is also essential to carefully study the stability of CMC-Na towards radical oxygen species, considering the oxygen redox and release feature of the Li-rich materials.

To summarize, the effect of CMC-Na binder to suppress voltage fading of $Li_{1.2}Ni_{0.13}Co_{0.13}Mn_{0.54}O_2$ is discovered from electrochemical tests. However, the

reasons remain uncertain and further studies should be done to fully understand the underlying chemistry.

4.5. Conclusion

In this chapter, the PTFE and CMC-Na are chosen as alternative binders for the Li-rich cathode materials based electrode and the corresponding effects of both binders are studied. It is found that the PTFE binder electrode outperforms the PVDF binder in all electrochemical aspects, mainly due to the homogeneously mixed electrode composition and the superior binding property of PTFE. It is worth noting that the intrinsic effect of the binder on the mixing of electrode compositions is difficult to compare between PTFE and PVDF binder, since the processing is so different. Other factors, such as the chemical and electrochemical stability of PTFE binders, may also influence the electrode behaviours but have not been studied yet. Meanwhile, the CMC-Na binder is demonstrated to have the effect to suppress the voltage fading of the Li-rich materials, although the CMC-Na binder electrode fails to compete with the PTFE binder electrode in terms of other electrochemical performance. Up to this point, the chemical mechanism of such effect has not been well understood yet.

The study of this chapter clearly suggests that the research on binder effects towards the Li-rich materials is critical and provides a new perspective to elevate their electrochemical performance, although the binder only counts for a small percentage of the electrode composition. Further research needs to be done to better understand the binder effects from the fundamental aspect. Moreover, transforming to the water-

soluble binder based electrode system may be an ideal future option, as it matches with the goal towards the cost-efficient and eco-friendly large scale manufacture of Li-ion batteries. Yet the challenges remain in many aspects since little research has been done, which leaves researchers a field of opportunities to explore.

CHAPTER 5 Oxygen Redox in the Layered Li-rich Cathode Material

5.1. Background

The cathode materials for Li-ion batteries are generally lithium transition metal oxides ($Li_xTM_yO_z$). During cycling, the Li-ions are de-/intercalated from the $Li_xTM_yO_z$ and the charge is compensated by the oxidation/reduction of transition metal ion(s)[3,4,13,99,271].

$$Li_xTM_y^{\beta+}O_z \underset{\text{Discharge/Lithiation/Reduction}}{\overset{\text{Charge/Delithiation/Oxidation}}{\rightleftharpoons}} \alpha Li^+ + Li_{x-\alpha}TM_y^{(\beta+\alpha)+}O_z + \alpha e^- \quad \text{(Equation 5-1)}$$

Where $\beta+$ *and* $(\beta+\alpha)+$ are the oxidation states of the transition metal ion in the pristine material and in the charged material after the de-intercalation of α Li^+, respectively.

The charge stored in the cathode material is depending on the redox capacity of the transition metal ion(s). Currently, the specific capacity of a commercial cathode material can be as high as about 190 mAh g^{-1} by $LiNi_xCo_yAl_zO_2$ (NCA)[97,98]. If the redox activity of both transition metal ion(s) and oxygen can be activated, it will release the full capacity potential of the cathode material and lead to cathode materials with significant higher capacity.

The layered Li-rich cathode materials, such as $Li_{1.2}Ni_{0.13}Co_{0.13}Mn_{0.54}O_2$, can deliver a specific capacity about 230-250 mAh g^{-1} or even higher. Early research on Li-rich materials has proposed a variety of mechanisms to explain the enormous capacity. Dahn *et al.*[138] and Thackeray *et al.*[171] proposed that the simultaneous removal of Li^+ and O from lattice happens beyond the conventional transition metal oxidation; O_2 gas

evolution has been directly observed by Armstrong *et al.*[176] and Novak *et al.*[172] but not by the others[177]. Additionally, complex reaction mechanisms of formation and decomposition of CO_2 and carbonates also been proposed by different authors[172-175].

The solid-state redox activity of oxygen is not well understood in transition metal oxides, although it has been proposed in a few publications[139,146,156,179,180,182,183,272,273]. Delmas and co-workers proposed the irreversible oxygen redox mechanism in a core-shell structure, in which the bulk undergoes the irreversible oxygen redox without oxygen loss or structure change, while oxygen loss happens at the surface associating with densification[146,179,180]. Tarascon and co-workers studied oxides with *4d* and *5d* transition metal ions and demonstrated the anionic redox activity in these compounds[139,156,181-183]. Additionally, they observed $(O_2)^{n-}$ dimmers (O-O ~2.4 Å) as the result of oxidation of oxygen[182].

The deeper understanding on the origin of the extra capacity of the layered Li-rich materials and the oxygen redox mechanism in these lithium transition metal oxides is essential to unlock the potential capacity of both cationic and anionic redox so to achieve cathode materials of significant capacity.

5.2. Research Goal

The research goal in this chapter is to explore the origin of the enormous capacity of the layered Li-rich materials and to understand the oxygen redox mechanism in Li-rich *3d* transition metal oxides. $Li_{1.2}Ni_{0.13}Co_{0.13}Mn_{0.54}O_2$ is taken as the example, as it is the most recognized model for the layered structure in Li-rich *3d* transition metal oxides.

5.3. Experimental Detail

5.3.1. Synthesis and Basic Characterizations

The R-F gel synthesis of $Li_{1.2}Ni_{0.13}Co_{0.13}Mn_{0.54}O_2$ was referred to section 3.3.3; the experimental details of morphology, elemental and structural characterization, as well as the basic electrochemistry were referred to section 3.3.4; section 3.3.5, respectively.

5.3.2. Operando DEMS

The operando DEMS system consisted of three components: a commercial quadrupole mass spectrometer (Thermo Scientific Prolab Benchtop Gas Analysis Mass Spectrometer), a turbo-molecular pump (Pfeiffer Vaccuum) and an in-house designed Swagelok electrochemical cell (Figure 2-6(a)). The cell was assembled using the lithium metal as a counter/reference electrode, glass fiber separator (GE), 1M $LiPF_6$ in PC as the electrolyte, and the $Li_{1.2}Ni_{0.13}Co_{0.13}Mn_{0.54}O_2$ pellet electrode (section 2.3.5) as the working electrode. The configuration and calibration of the operando DEMS system were based on the previous work from our research group[274,275].

5.3.3. XANES

The Ni, Co and Mn XANES spectroscopy were measured at the *B18* Beamline at the Diamond Light Source, Harewell, U.K. It covers the energy range of 2.05 – 35 keV. Its monochromator is equipped with two sets of crystal, Si (111) for 2.05-20 keV and Si (311) for 4-35 keV. The spectra were collected in the transition mode[276]. Two or three scans were collected for each sample, then the data was summed up, calibrated by a

reference signal, background subtracted and eventually normalized by using the Athena programme[87]. The XANES Spectra of Mn_2O_3, MnO_2, $LiCoO_2$, NiO and $LiNiO_2$ were also collected as references for the data interpretation.

5.3.4. SXAS and RIXS

The SXAS and RIXS were measured at the Beamline 8.0.1 at the Advanced Light Source (ALS), Lawrence Berkeley National Laboratory, U.S.A. This beamline covers the energy range of 80 - 1250 eV. For the O K edge SXAS, the Total Fluorescence Yield (TFY) signal was recorded from 520 eV to 562 eV. The normalization followed the established procedure[277] below: (1) I_0-based normalization: the sample signal is divided by the incident intensity I_0; (2) pre-edge line was fit to the flat low energy region (520 – 524 eV), which is way below the O K edge absorption, to remove a linear sloping background; (3) The Spectra were normalized by setting the pre-edge line to zero and the post-edge to unity. The energy selected for the post-edge was 560 eV, which was beyond the region of any O K edge absorption. The excitation energy for the RIXS was 529.5 eV.

5.3.5. Raman Spectroscopy

The raman spectra of the materials at different charge/discharge states were collected by the RENiSHAW inVia Raman spectrometer. The monochromatic photon resource was a diode laser (λ = 785nm). The pellet electrodes were recovered from the cycled coin cells in an argon-filled glove box (Labmaster DP, MBRAUN) and sealed in an in-

house made airtight glassware for the Raman spectroscopy characterization.

5.4. Results and Discussion

The typical 1st cycle load curve of the $Li_{1.2}Ni_{0.13}Co_{0.13}Mn_{0.54}O_2$ is shown in Figure 5-1. For the convenience of discussion in this chapter, the charge curve is divided into three regions: (1) Sloping region "S": the sloping charge region up to about 4.4 V, which has been traditionally assigned to conventional transition metal oxidation ($Ni^{2+} \rightarrow Ni^{3+} \rightarrow Ni^{4+}$, and $Co^{3+} \rightarrow Co^{4+}$)[180] and counts for about 120 mAh g^{-1}on the charge curve (theoretically, 122.5 mA g^{-1}); (2) Plateau-like region "P": a relatively flat region above 4.4 V on charge; (3) Tail-like region "T": a sloping region at the end of charge. The sum of the region "P" and "T" corresponds to the extra charge capacity above the conventional transition metal oxidation region.

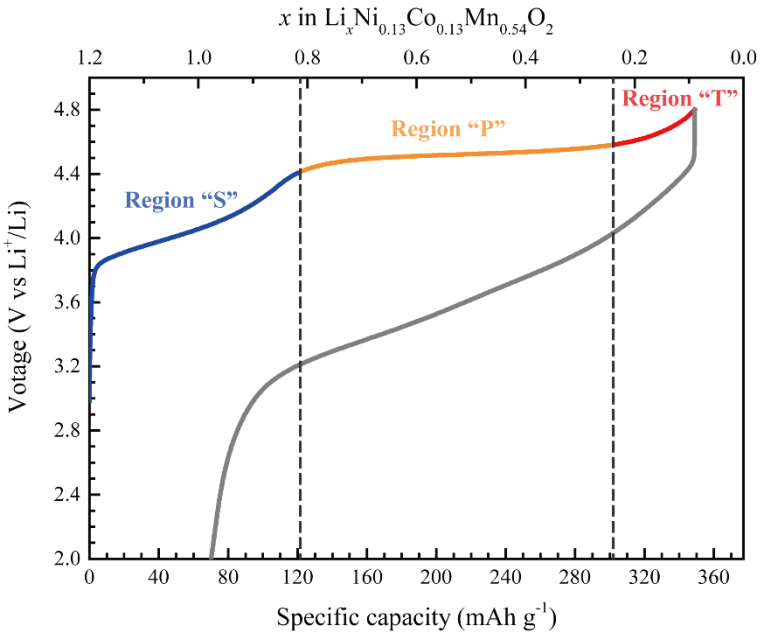

Figure 5-1 A typical 1st cycle load curve of the $Li_{1.2}Ni_{0.13}Co_{0.13}Mn_{0.54}O_2$. For the convenience of discussion in this chapter, the regions are labelled as "S" (Sloppy, in blue), "P" (Plateau-like, in orange) and "T" (Tail-like, in Red), respectively.

5.4.1. Oxygen Loss on Charge

By the operando DEMS using ^{18}O-labelled $Li_{1.2}Ni_{0.13}Co_{0.13}Mn_{0.54}O_2$ (detailed synthesis in Appx. 2), the gas evolution during the 1st cycle was probed to investigate directly if the O is extracted beyond the transition metal oxidation (Figure 5-2). The time-of-flight secondary ion mass spectrometry (ToF-SIMS) confirms the presence of ^{18}O in the material with the ratio $^{18}O/^{16}O$ = 15%/85% (detailed in Appx. 2). Thus, O extracted from the lattice, if there will be any, should be a combination of ^{18}O and ^{16}O. Besides, it is worth noting that the nature abundance of ^{18}O is 0.20%, which is comparably negligible. Thus, any ^{18}O detected, if there will be any, should originated from the ^{18}O-labelled $Li_{1.2}Ni_{0.13}Co_{0.13}Mn_{0.54}O_2$.

Neither O_2 nor CO_2 is observed in the region "S"; CO_2 starts to present at the beginning of the region "P" and continuously in the region "T"; O_2 is only observed in the region "T" (Figure 5-2(b)). The presence of ^{18}O is detected in O_2 in the region "T", and in CO_2 in the region "P" & "T"(Figure 5-2(c)). This clearly demonstrates that there is O extracted above the transition metal ion oxidation region.

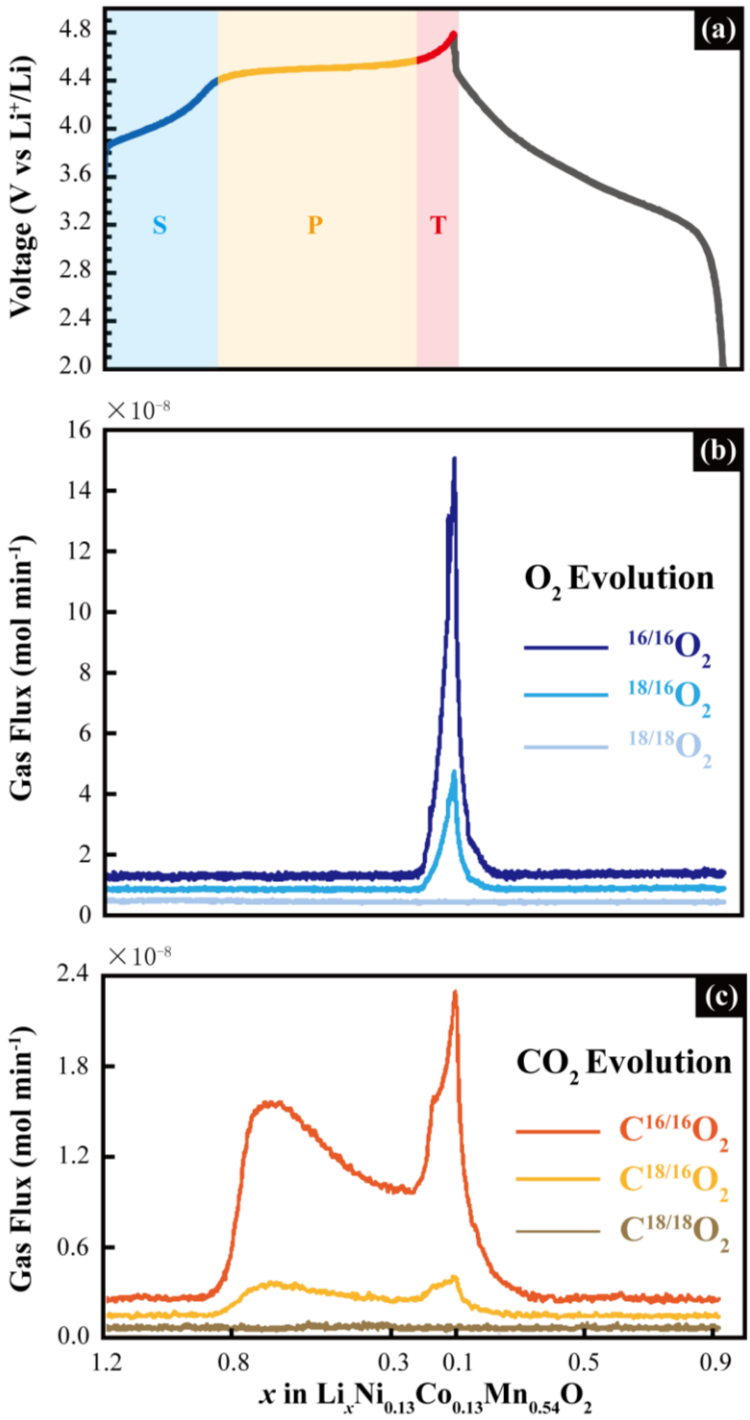

Figure 5-2 Operando DEMS of ^{18}O-labelled $Li_{1.2}Ni_{0.13}Co_{0.13}Mn_{0.54}O_2$ cathode in the 1st cycle. (a) electrochemical curve of the operando DEMS cell; (b) O_2 and (c) CO_2 evolution plot as a function of the state of charge. For clarity purpose, the plots of O_2 and CO_2 evolution are plotted separately along y-axis.

The integrated area of the gas evolution curve corresponds to the quantity of a certain gaseous specie (in mol). A comparison on the theoretical and experimental values (in percentage) of gaseous species is given in the Table 5-1 (detailed calculation in Appx. 3).

Table 5-1 Theoretical and experimental values of gas evolution in percentage, detailed calculation is given in Appx. 3.

Gas Evolution		Predicted (%)	Experimental (%)
O_2	$^{16/16}O_2$	72.25	77
	$^{18/16}O_2$	25.5	23
	$^{18/18}O_2$	2.25	0
CO_2	$C^{16/16}O_2$	79.37	87
	$C^{18/16}O_2$	19.44	13
	$C^{18/18}O_2$	1.19	0

For the O_2 evolution, assuming that it all comes from the O extraction from lattice, then the percentage of $^{16/16}O_2$, $^{18/16}O_2$, and $^{18/18}O_2$ can be estimated as shown in Table 5-1. The experimental values from the gas evolution curve integration closely match with the estimated values. The slightly higher/lower percentage of $^{16/16}O_2$/$^{18/16}O_2$ could be explained by the concentration gradient of ^{18}O across the depth of the ^{18}O-labeled $Li_{1.2}Ni_{0.13}Co_{0.13}Mn_{0.54}O_2$. The concentration of ^{18}O close to the particle surface is 15% as identified by the TOF-SIMS, whereas the ^{18}O concentration in core could be less than 15%, given the mechanism used for ^{18}O labelling. Thus, as the O extraction goes deeper into the particle, less ^{18}O presence is expected, resulting in a lower percentage of $^{18/16}O_2$ in the O_2 evolution. The quantity of $^{18/18}O_2$ is likely below the detection limit of the instrument. In all, the good agreement of the theoretical and experimental value suggests that the hypothesis is correct and the O_2 evolution during the 1st charge is attributed to the direct O extraction from the lattice.

For the CO_2 evolution, the presence of $C^{18/16}O_2$ suggests that the electrolyte must react with O extracted from the material lattice in some ways to decompose. It has been discussed previously in the research of Li-O_2 batteries that the reduced O species attacks the carbonate solvent resulting in decomposition[65,278,279]. Assuming the PC decomposition is mainly initiated by the O extracted from the lattice, based on the previous decomposition mechanism proposed by our research group, the simplest decomposition model is given in Appx. 3, according to which the percentage of $C^{16/16}O_2$, $C^{18/16}O_2$, and $C^{18/18}O_2$ is estimated as shown in Table 5-1. Experimentally, the detected percentages are slightly different from the estimated values. This could be explained from at least three aspects: (1) the ^{18}O concentration gradient across the depth as being explained in the case of O_2 evolution; (2) the propagating reactions of the decomposition could possibly generate more $C^{16/16}O_2$ than the estimated quantity based on the proposed model; (3) the decomposition of surface carbonates residuals, which was formed during the synthesis. The quantity of $C^{18/18}O_2$ is also too small to be detected. Further operando DEMS experiment using ^{18}O-labelled $LiNi^{II}_{0.5}Mn^{IV}_{1.5}O_4$ high-voltage spinel have also been performed to carefully consider the possibility of direct electrolyte oxidation (detailed in Appx. 4). The result indicates that the direct oxidation of PC is in a negligible quantity up to 4.8 V. It, therefore, could be concluded that the majority of CO_2 released on charge is originated from the decomposition of the electrolyte as being attacked by O extracted from the material lattice.

The charge (Q_g) transferred to form the O_2 and CO_2 could be calculated based on the mechanism proposed in Appx. 3. In Table 5-2, it is compared with its electrochemically

recorded equivalents (Q_e).

Table 5-2 A comparison between the charge transfer (Q_g) corresponding to the gas evolution and the electrochemically recorded equivalents (Q_e)

Region	Q_g (e^- per formula unit)	Specifc Charge Capacity (mAh g^{-1})	Q_e (e^- per formula unit)	Percentage (%) (Q_g/Q_e)
Region "P"	0.05	180.32	0.57	9
Region "T"	0.12	45.64	0.14	86

Although direct gas evolution is detected in both the region “P” and “T”, the total Q_g only accounts for 0.17 e^- in total, which is significantly less than the total Q_e (0.71 e^-). Particularly, in the region “P”, the gas evolution only contributes for 9% of the charge capacity. Therefore, it could be concluded that the extra capacity above the transition metal oxidation on charge is not dominantly from gas evolution but by the formation of electron-holes on oxygen. Further discussion will be given in the following sections.

5.4.2. The Hole States Oxidation

Multiple spectroscopy methodologies, including XANES, SXAS, RIXS and Raman, were employed to carefully study the oxidation of $Li_{1.2}Ni_{0.13}Co_{0.13}Mn_{0.54}O_2$ during charge.

5.4.2.1. Region “S”

On charging across this region, Li^+ is extracted from the $Li_{1.2}Ni_{0.13}Co_{0.13}Mn_{0.54}O_2$ and the charge compensation is achieved by the continuous oxidation of Ni^{2+} and Co^{3+} to their highest oxidation states (Ni^{4+} and Co^{4+}), which corresponds to about 0.4 e^- charge transfer per formula unit. The Ni and Co K edges on XANES (Figure 5-3 (b) & (c)) shift to higher energy as the evidence for the oxidation[180,280,281]. The Mn K edge (Figure 5-3(d)), however, appears to change its shape and shift slightly, which is in accordance

with literatures[180,282,283] and is attributed to the change of the Mn coordination environment rather than the oxidation of Mn^{4+} to Mn^{5+} [180,282]. The oxidation of Ni^{2+} and Co^{3+} generates extra unoccupied states on the transition metal *d* orbitals, which are hybridized with the O *2p* orbitals. Thus, the change of unoccupied states could be reflected by probing the O K edge using SXAS.

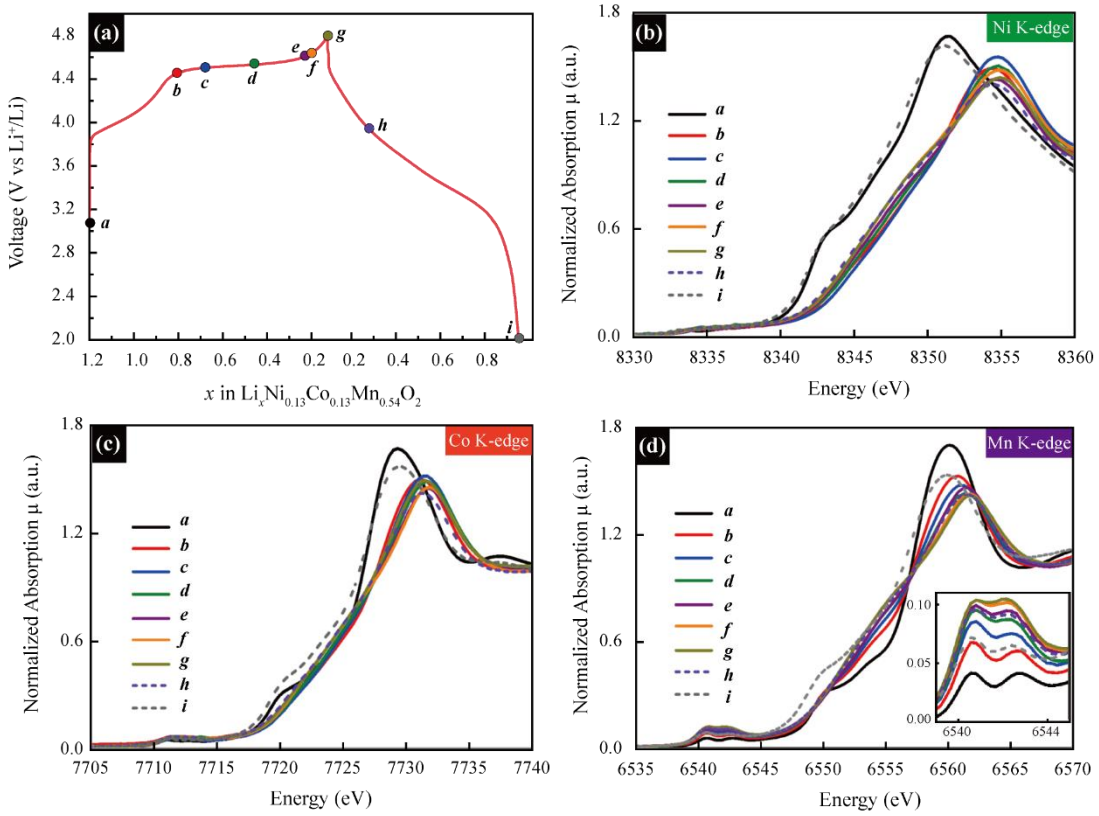

Figure 5-3 Transition metal ((b) Ni, (c) Co, (d) Mn) K edge XANES spectra on different state of charge during the 1st cycle. (a) The corresponding state of charge of the measured samples is projected on the electrochemical profile, in which the voltage is plotted versus the lithium content of the cathode material.

The SXAS spectrum of O K edge (Figure 5-4) consists of two regions: a high-energy region ($\gtrsim$ 535 eV) corresponding to the electron excitation from O *1s* to the unoccupied O *2p* hybridized with the transition metal *4sp*; a low-energy region ($\lesssim$ 535 eV) corresponding to the electron excitation from O *1s* to the unoccupied O *2p* hybridized with the transition metal *3d*. Therefore, attentions should be paid on the low-energy

region.

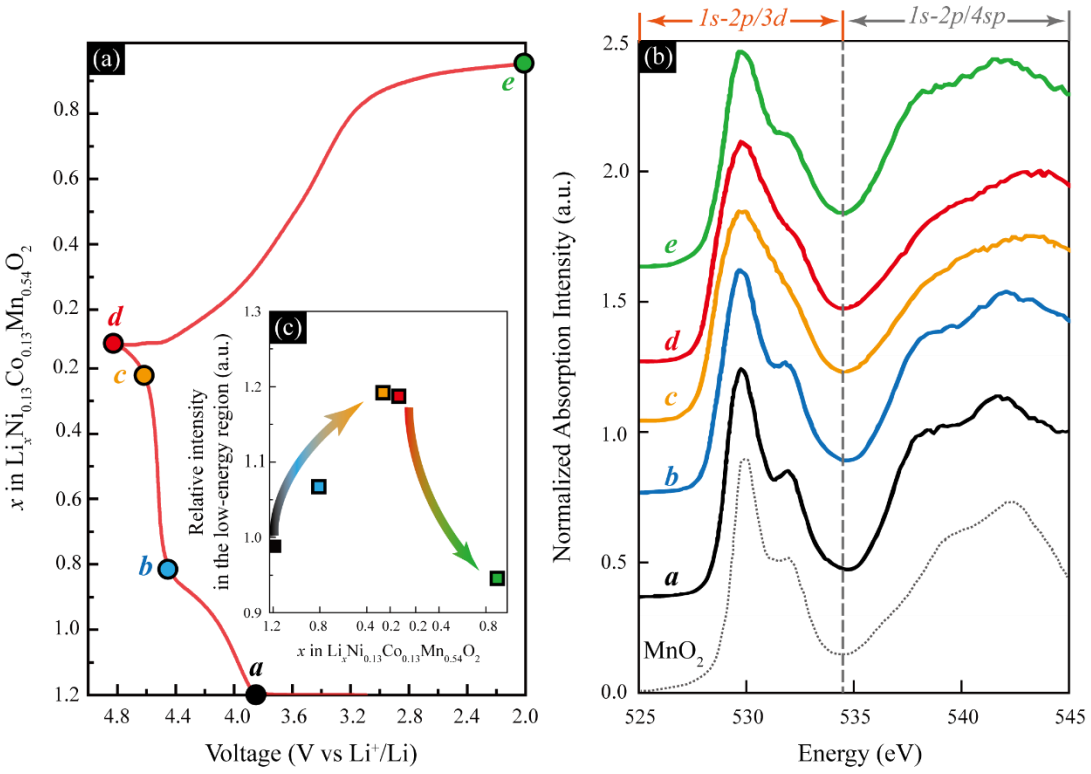

Figure 5-4 Oxygen K edge SXAS spectra at different state of charge in the 1st cycle. A spectrum of MnO_2 (reproduced from Ref.[284]) is taken as the reference. The vibration of integrated intensity in the low-energy region (shown in (b)) of the SXAS spectra is plotted versus the state of charge in (c).

The SXAS Oxygen K edge spectra (Figure 5-4) at the beginning (spectrum *a*) and end (spectrum *b*) of region "S" shows almost identical shape. This is due to the minority presence of these two elements in the chemical composition and the spectrum is dominant by Mn (Appx. 5). Nevertheless, the integrated area under the spectrum *b* increases by about 8% (Figure 5-4(c)) compared by the integrated area under the spectrum *a*. In fact, the differences on the integrated areas indicates the additional unoccupied states created during oxidation, which is in good agreement with the estimated value (8.5%). The estimation is demonstrated in detail in Appx. 5.

5.4.2.2. Region “P”

On charging across the region “P”, the Ni and Co K edges show almost no change indicating of no further oxidation on both. Although there are change in shape on the Mn K edge (Figure 5-3(d)), it only reveals the continuous change on Mn coordination environment due to the MnO_6 octahedra distortion[180,282,283], as being discussed above. Therefore, there is no evidence of further oxidation of transition metal ions over 4+ oxidation state, which is in accordance with the previous research[173,180].

On the SXAS O K edge spectrum *c* at the end of the region “P”, there is an obvious increase on the intensity in the low-energy region, which accounts for about 10% increase in the integrated area compared with the spectrum *b* at the beginning of the region “P” (Figure 5-4(c)). As there is no further oxidation of transition metal ions and Ni^{4+} and Co^{4+} are known to be pinned at the top of the O valence band[4], this increase of the integrated area (extra unoccupied states) should be attributed to electron-holes primarily in the O *2p* orbitals.

Considering that about 8% increase of the integrated area corresponds to about 0.4 e^- per formula unit, it can be calculated that the 10% increase of unoccupied states corresponds to about 0.5 e^- per formula unit. Additionally, there is 0.05 e^- per formula unit associated with the O loss in this region. In total, the oxygen redox and O loss account for 0.55 e^- per formula unit, which is in good agreement with the 0.57 e^- per formula unit extracted electrochemically. Therefore, the anion (O) redox is dominant in the region “P” in this material.

5.4.2.3. Region “T”

On charging across the region “T”, the XANES spectra of the transition metal ions K edges (Figure 5-3) indicate the same information as in the region “P”. The SXAS O K edge spectrum *d* at the end the region “T”, however, is very similar to the spectrum *c* at the end the region “P”. This can be explained as the charge corresponding to the O loss (0.12 e^- per formula unit) almost accounts for all the charge (0.14 e^- per formula unit) extracted electrochemically. Therefore, the dominant process in this region is O loss rather than the oxygen redox.

Eventually, the SXAS O K edge spectrum *e* at the end of the 1st discharge recovers the shape, as compared with the spectrum *a* for the pristine material. It demonstrates the reversible nature of the oxygen redox.

5.4.3. Nature of the Holes on Oxygen

Up to this point, it is clear that electron-holes are created on oxygen on charging of the $Li_{1.2}Ni_{0.13}Co_{0.13}Mn_{0.54}O_2$ beyond the conventional transition metal oxidation up to 4.8 V. To better understand this oxygen redox process, the nature of the electron-holes on oxygen needs to be understood.

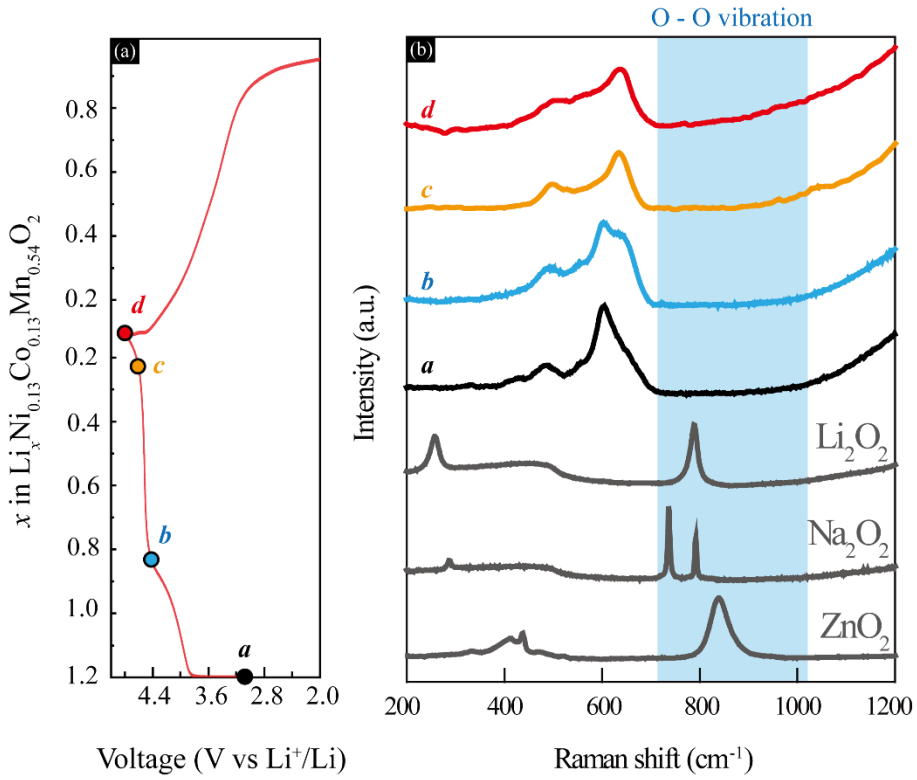

Figure 5-5 (b) Raman spectra at (a) different state of charge. The spectra of three reference samples (in grey), Li_2O_2, Na_2O_2, ZnO_2 (Alfa Aesar, approximately 50% ZnO_2 in ZnO), refine the region of O-O vibrations.

Raman spectroscopy (Figure 5-5) was employed to investigate if the O_2^{2-} (O-O ~ 1.45 Å) is formed in the *3d* transition metal oxide, as it is very sensitive to the O-O peroxo vibrations. Three peroxo compounds, Li_2O_2, Na_2O_2 and ZnO_2, are picked as references of the O-O peroxo vibrations. The shape and relative intensity changes are observed on the peaks centered around 630 cm^{-1}, which are in accordance with the previous research[178,285,286] and known to correspond to the metal-O vibration[178,285,286]. However, in the region anticipated for the O-O peroxo vibrations, there is no clue of peaks appearing, suggesting that the true O-O peroxo species are not formed in the *3d* transition metal oxides. In the *4d* and *5d* transition metal oxides, however, the formation of peroxo-like $(O_2)^{n-}$ dimers (O-O ~2.4 Å) is reported[182], as the holes are created on O^{2-} on charge.

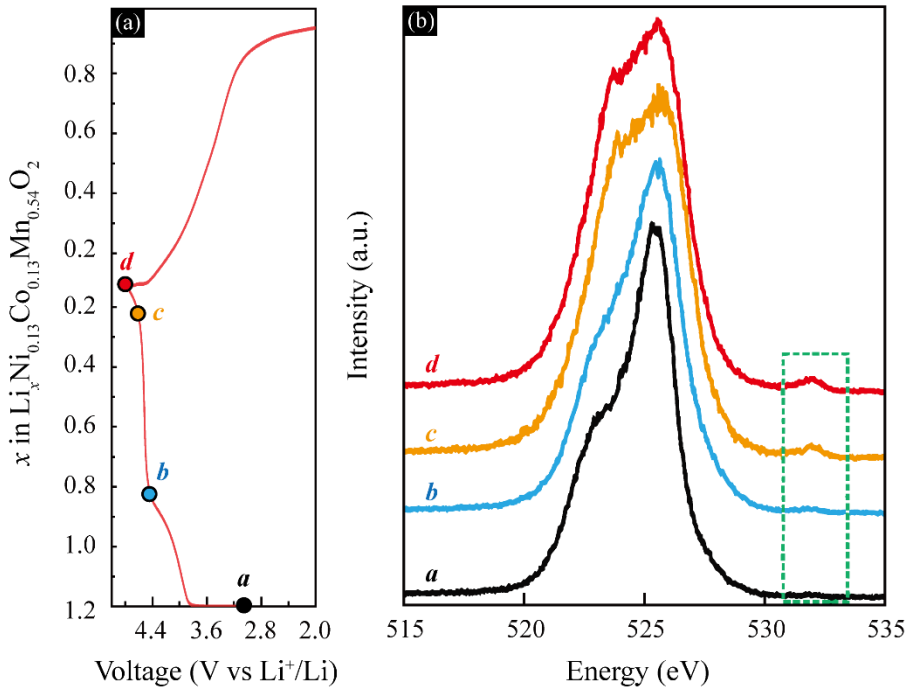

Figure 5-6 (b) Oxygen K edge RIXS spectra with excitation energy of 531.8 eV at (a) different state of charge.

Further characterization on the electron-hole on O is done by the O K edge RIXS spectra at different state of charge (Figure 5-6). The RIXS directly probes on the electron-holes on O, as the spectrum of the O K edge RIXS is dominant by the resonant emission of photons from O *2p* to O *1s* electron transition. The spectrum *b* at the end of the region "S" remains unchanged in general, as there is no oxygen redox in this region. However, when it comes to the end of region "P", the spectrum *c* experiences considerable broadening and weight rearrangement around the main peak. This suggests a significant electronic reconfiguration around the O, such as the electron negativity change of oxygen anion[287-290]. The spectrum *d* at the end of the charge remains almost identical compared with the spectrum *c*, as the oxygen loss, rather than the oxygen redox, is dominant in the region "T". Moreover, it is observed that the elastic peak around 532 eV is enhanced as the charge goes on, which suggests the localized

character of O excitation state[289]. Overall, it can be concluded that the localized electron-holes are formed on oxygen on charging.

Associated with the XANES spectrum of transition metal ions, the exact transition metal ion(s) that directly interacts with the electron-holes on O can be identified. As being mentioned above, the Ni^{2+} and Co^{3+} are oxidized in the region "S" then stays at their highest oxidation states till the 4.8 V cut-off. By extracting the Ni and Co K edge *1s-4p* adsorption peak energy and plotting it against the different state of charge, the plots reveal the same information (Figure 5-7). The Ni K edge *1s-4p* adsorption peak energy shows almost no change in region "P", where the electron-holes are primarily generated. It is the same case for Co. It indicates that both Ni and Co do not directly interact with the electron-holes on oxygen. After discharge to 2 V, the Ni and Co K edge *1s-4p* adsorption peak energy falls back to the same level as that of the pristine material, suggesting that both Ni and Co are reduced from 4+ to their original oxidation state (Ni^{2+} and Co^{3+}, respectively). The Mn K edge *1s-4p* adsorption peak energy, however, shows gradual shift (< 2 eV) to higher energy, which is attributed to the coordination environment change and the distortion of MnO_6 octahedra[180,282,283], as being discussed in section 5.4.2.1. This indicates that Mn directly interact with the electron-holes on oxygen. On discharge back to 2 V, the Mn K edge *1s-4p* adsorption peak energy does not match with that of the pristine materials, which is anticipated as the discharged material is no longer identical with the pristine material[180,245,272], both structurally and chemically. For example, both structure rearrangement and O loss have happened, and there is a significant irreversible capacity indicating the much less Li

content in the discharge material. A minor Mn^{3+} feature (small shift of the pre-edge) is observed at the end of discharge, as also being seen in the previous research[180] and explained by a net change in the structure[180,272].

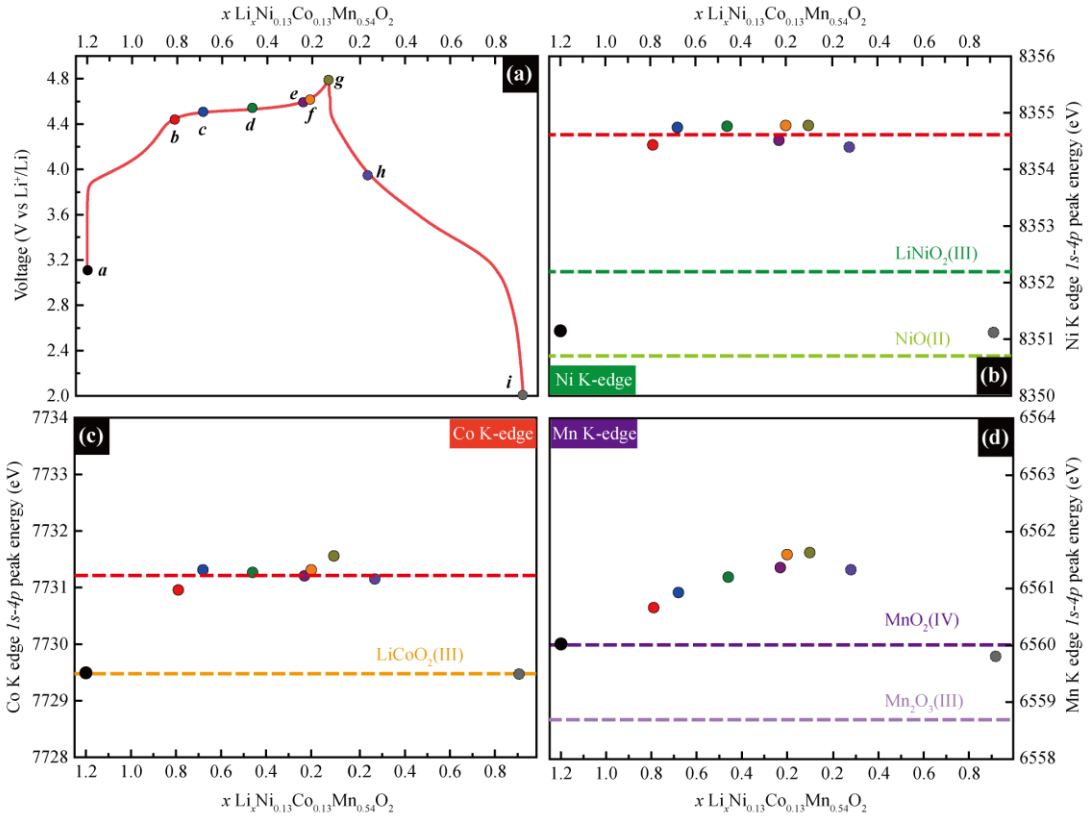

Figure 5-7 Transition metal ((b) Ni, (c) Co, (d) Mn) K edge *1s-4p* peak energy plots against different state of charge in the 1st cycle. (a) The corresponding state of charge of the measured samples is projected on the electrochemical profile, in which the voltage is plotted versus the lithium content of the cathode material.

5.4.4. Model for the Formation of Electron-hole States on Oxygen

Summarizing all the results above, it leads to a complete model for the formation of electron-hole states on oxygen. In the transition metal layer of $Li_{1.2}Ni_{0.13}Co_{0.13}Mn_{0.54}O_2$, transition metal ions and Li ion ($[Li_{0.2}Ni_{0.13}Co_{0.13}Mn_{0.54}]$) are in a honeycomb-like ordering, as being indicated by the broad peak feature in the 2θ range of 20°-26° on the powder diffraction pattern[146,245,246] (Figure 3-5). Each O is surrounded by six cations,

among which three are Li^+ from alkaline layer and the others from the transition metal layer. Therefore, the coordination environment of O is not always the same, as coordinating with different metal ion ternaries in the transition metal layer.

On charging into the region "P" and "T", with transition metal ions all in 4+ oxidation states, the hybridization between O^{2-} *2p* and Ni^{4+}/Co^{4+} *3d* (*d-p* mixing) tends to have relatively more covalent character, whereas the hybridization between O^{2-} *2p* and Mn^{4+} *3d* / Li^+ *2s* tends to have relatively more ionic character. According to the molecular orbital theory, a series of hybridized molecular orbitals are generated from the *d-p* mixing, except that the transition metal *3d*(t_{2g}) orbitals remain non-bonding due to the non-overlapping between the transition metal *3d*(t_{2g}) orbitals and O^{2-} *2p* orbital. Thus, the electrons interested are those lying in the transition metal *3d*(e_g)-O^{2-}(*2p*) hybridized orbitals. The more ionic character of Mn^{4+} *3d* - O^{2-}(*2p*) hybridization rises the energy level of Mn^{4+} *3d*(e_g)-O^{2-}(*2p*) hybridized orbitals to the top of the O^{2-} valence band, which makes the electrons in Mn^{4+} *3d*(e_g)-O^{2-}(*2p*) hybridized orbitals possible to be accessed for further oxidation beyond the transition metal oxidation within the stability window of electrolyte. Since the O^{2-} *2p* - Li^+ *2s* hybridization is an extreme case of ionic character, it is also likely to promote the activation of electrons on O^{2-} *2p* orbitals.

Therefore, those oxygens surrounded by Mn^{4+}/Li^+ are expected to form localized electron-holes states near the top of the O^{2-} valence band. As the Mn^{4+} and Li^+ in the transition metal layer are in the same coordination shell around O^{2-}, it is those O^{2-} which forms localized electron-holes during the region "P" and "T". Relatively, the Li^+-O interaction is more ionic than the Mn^{4+} interaction, thus it is probably more effective in

forming the localized electron-holes on oxygen surrounded by Mn^{4+} and Li^{+}.

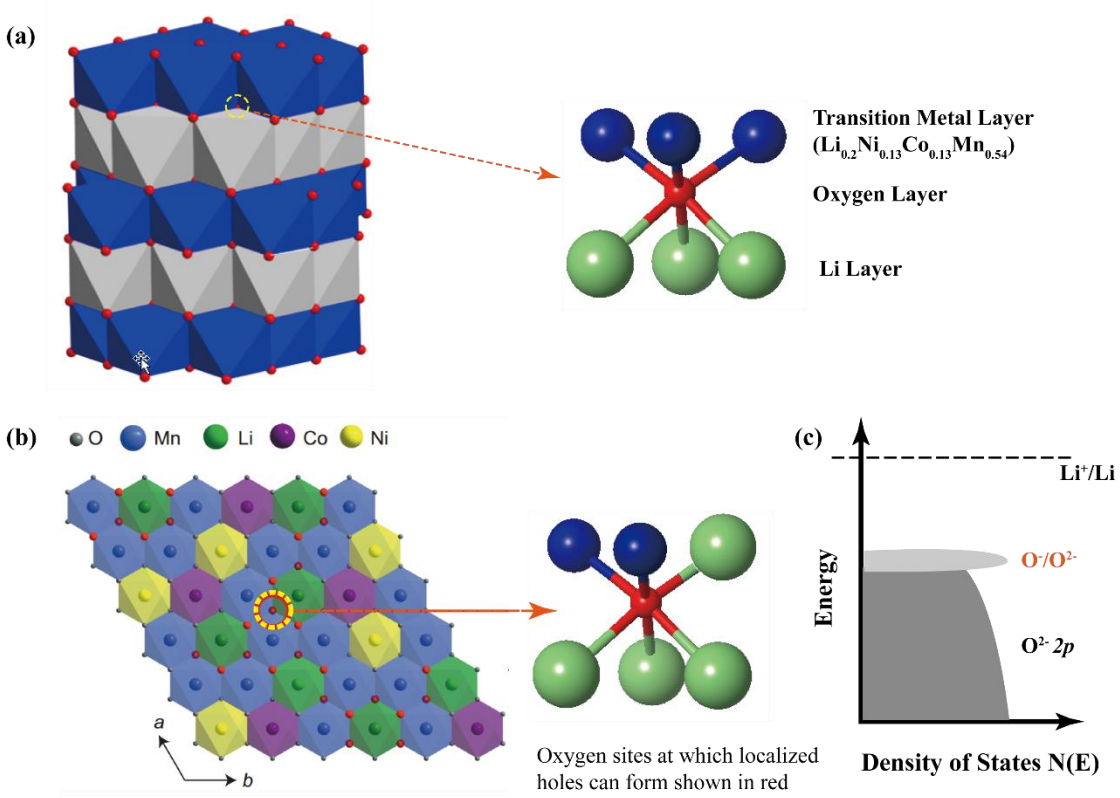

Figure 5-8 Schematic of the model for the formation of electron-hole states on oxygen. (a) oxygen coordination environment in $Li_{1.2}Ni_{0.13}Co_{0.13}Mn_{0.54}O_2$; (b) honeycomb-type cation ordering in the transition metal layer, view from ***c*** axis. The oxygen sites at which localized holes can form shown in red spheres; (c) schematic to show the position of the O^{-}/O^{2-} redox couple

5.5. Conclusion

For $Li_{1.2}Ni_{0.13}Co_{0.13}Mn_{0.54}O_2$, the O loss is proved to start happening on charging over about 4.4 V (region "P"), even though no direct O_2 gas evolution is observed in this region. The O extracted from the lattice only accounts for 0.17 e^{-} charge-transfer on charging over about 4.4 V to 4.8 V cut-off, the rest enormous capacity is attributed to the formation of electron-holes on O. The formation of true O_2^{2-} (O-O ~ 1.45 Å) is not observed as there is no peak appearing on the Raman region for the O-O vibration (~ 1.45 Å). Instead, multiply spectroscopy methodologies have proved that (1) the

electron-holes on O are localized; (2) the localized electron-holes are formed on those oxygen surrounded by Mn^{4+} and Li^{+}, as the O- Mn^{4+}/Li^{+} interaction tends to be relatively more ionic than the O-Ni^{4+}/Co^{4+} interaction (more covalent), therefore, rising the energy of hybridization and form the localized electron-holes states near the top of the O^{2-} valence band.

The results reveal the role of Mn in the first row transition metal elements, which promotes the oxygen redox chemistry - the formation of electron-holes localized on O. The critical challenge is to find a good balance of the ionicity and covalency of the TM-O interaction, which determines the boundary between the oxygen loss and the oxygen redox; or even further, to suppress the oxygen loss but promote the oxygen redox. Therefore, guided by the proposed model, the attempts to explore new structures and different elements other than Mn will be significant to release the potential of the oxygen redox, and consequently to achieve high-capacity cathode materials for the future Li-ion batteries.

CHAPTER 6 Oxygen Redox in a Novel Cation Disordered Rock-Salt Li-rich Material

6.1. Background

The study of Li-rich layered transition metal oxides has demonstrated that both the conventional transition metal redox and oxygen redox contribute to the enormous capacity of these layered oxides[76,139,180-184,291,292]. Despite the fact that majority of research of Li-rich materials focuses on the layered transition metal oxides, it remains unclear whether or not the layered structure is necessary for activating oxygen redox. In fact, in some early study of the cation disordered rock-salt Li-rich transition metal oxides[293,294], extra capacity beyond the transition metal redox has been observed and anticipated as the oxidation of oxygen, although such anticipation lacked of experimental evidence.

Historically, the cation disordered rock-salt materials were generally disregarded as cathode materials due to their poor electrochemical performance[295-297]. Some studies[281,297-301] suggest that enriching the Li content in these materials establishes a Li percolating network, which could contribute to a relatively facile Li^+ diffusion in these materials and consequently improve the electrochemical performance. Recently, a series of cation disordered rock-salt Li-rich transition metal oxides, mainly involving a mix of *4d* and *3d* transition metals, have been reported to have extra capacity during cycling[281,297,301-303]. The evidence of the oxygen redox contributing to the extra capacity

is discussed by employing advanced characterization methodologies[281,297,302,303], such as SXAS, Electron Energy Loss Spectroscopy (EELS) and theoretical modeling[281]. These researches appear to be interesting, as the oxygen redox also occurs in the cation disordered Li-rich transition metal oxides. It suggests that the layered structure might not be a necessary condition for activation of oxygen redox and that alternative structures could also open doors for exploring new candidate oxides for oxygen redox. There is one thing in common, Li enrichment, for both the layered and cation disordered rock-salt materials showing oxygen redox. To the best of my knowledge, the oxygen redox has not been seen in the Li stoichiometric compounds.

Exploring cation-disordered rock-salt Li-rich transition metal oxides is valuable for a broader and better understanding of the oxygen redox phenomenon in oxides with different structures, so that we can ultimately unlock the full capacity potential of the Li-rich transition metal oxides by utilizing oxygen redox. Moreover, it is also a highly interesting study from a more general solid-state chemistry perspective. As mentioned in CHAPTER 5, the primary target is to explore *3d* transition metal oxides rather than *4d* or *5d*, bearing in mind the nature abundance of elements and the price of the resources. According to the proposed model in CHAPTER 5, a more ionic transition metal - oxygen interaction, like Mn-O interaction in the layered case, is potentially more effective in promoting the formation of the electron-holes on oxygen, than a covalent TM-O bond. Thus, *3d* elements that are more ionic than Mn are considered when identifying candidates. Ti is interesting as lithium titaniunm oxides, Li_2TiO_3, has a stable polymorph in the disordered rock-salt structure (γ-Li_2TiO_3)[304,305], which could

be used as the host structure like Li_2MnO_3 in the layered structure case. Moreover, in early[294,306] and recent[302,307] studies, a few Ti based Li-rich rock-salt transition metal oxides have been reported to be electrochemically active and have extra capacity.

In Li_2TiO_3, Ti^{4+} has a $3d^0$ electron configuration (no electrons in the conduction band), resulting a poor electronic conductivity of Li_2TiO_3. This is similar to the situation of Li_3NbO_4, in which Nb^{5+} is in $4d^0$ electron configuration[281]. It was reported[281] that partial substitution of Nb by Mn^{3+}, whose ionic radius lays between Li^+ (0.76Å) and Nb^{5+}(0.67Å), forms $Li_{1.3}Nb_{0.3}Mn_{0.4}O_2$ (or 0.43 Li_3NbO_4-0.57 $LiMnO_2$) in a cation disordered rock-salt structure. $Li_{1.3}Nb_{0.3}Mn_{0.4}O_2$ was reported to have extra capacity beyond the Mn^{3+}/ Mn^{4+} redox, which was speculated to be from oxygen redox[281]. By employing the same idea, my attempt was to partially substitute Ti^{4+} in γ-Li_2TiO_3 by Mn^{3+}, aiming to synthesize and characterize $Li_{1.2}Mn_{0.4}Ti_{0.4}O_2$ (or 0.5 Li_2TiO_3-0.5 $LiMnO_2$) in a cation disordered rock-salt structure, which utilizes Mn^{3+}/Mn^{4+} redox couple in a lower voltage region and could potentially be oxygen redox active beyond the transition metal redox.

6.2. Research Goal

The research goal in this chapter is to explore the oxygen redox phenomenon in a rock-salt Li-rich *3d* transition metal oxide. For this purpose, $Li_{1.2}Mn_{0.4}Ti_{0.4}O_2$, expected in a cation disordered rock-salt structure, was proposed and synthesized. The goal to broaden the understanding of oxygen redox in the context of Li-rich *3d* transition metal oxides is approached by carefully studying the electrochemistry of $Li_{1.2}Mn_{0.4}Ti_{0.4}O_2$ and

its corresponding reaction mechanism(s) and structure evolution mainly in the 1st cycle.

6.3. Experiment Details

6.3.1. Solid-state Synthesis

Stoichiometric amount of lithium carbonate, manganese (III) oxide, and titanium (IV) oxide were ball-milled together to form the precursor mixture. The resulting precursor mixture was pressed into 13 mm diameter pellets and preheated at 600 °C for a few hours in a Lenton CSC 12/90/300H split tube furnace, then reground thoroughly and pressed into a pellet again. The final calcination was carried out at a temperature above 900 °C for 12 to 15 hours, followed by cooling to room temperature in the furnace. The entire process was done in an argon atmosphere to prevent manganese (III) oxidation to a higher oxidation state(s).

6.3.2. Basic Characterizations

The experimental details of morphology, elemental and structural characterization of the synthesized $Li_{1.2}Mn_{0.4}Ti_{0.4}O_2$ were referred to section 3.3.4. For PXRD in particular, both Cu $K_{\alpha1}$ and $K_{\alpha2}$ emission were used, in order to maximize the brightness of the incident X-ray beam. Before being made into pellet electrodes, the as-prepared material was ball-milled in a zirconium oxide milling jar by a Fritsch PULVERISETTE 7 planetary ball-milling machine. The PXRD measurement was carried out before and after the milling to confirm the crystallographic consistency (Appx. 6). Electrodes and coin cells were made as the methods described in section 2.3.4.1 and 2.3.4.2,

respectively. A minor difference was that the weight ratio of the active material ($Li_{1.2}Mn_{0.4}Ti_{0.4}O_2$), carbon super P, and PTFE binder was 7:2:1 in this case. The basic electrochemistry test was referred to section 3.3.5. In particular, a current of 5 mA g^{-1} were applied in the galvanostatic cycling tests at 30 °C.

6.3.3. Operando PXRD (OPXRD)

The OPXRD was carried out by jointly using a Rigaku Smartlab® 9KW diffractometer and a Biologic VMP-3 battery tester. The diffractometer was equipped with copper rotating anode operating in reflection mode at 45 kV and 200 mA. The operando electrochemical cell was a commercial product from Rigaku, which was equipped with an X-ray transparent beryllium window to allow the penetration of the incident and refection X-ray. The electrochemical cell was configured as a half-cell and was assembled in an argon-filled glove box (Labmaster DP, MBRAUN) using a $Li_{1.2}Mn_{0.4}Ti_{0.4}O_2$ pellet electrode as the cathode, lithium metal as counter/reference electrode, glass fiber separator (GE) and LP30 electrolyte (1 M $LiPF_6$ dissolved in 1:1 wt% Ethylene Carbonate (EC)/ Dimethyl Carbonate (DMC) solvent, BASF Selectilyte^{TM}). A 0.0125 mm thick aluminium foil was placed in between the $Li_{1.2}Mn_{0.4}Ti_{0.4}O_2$ pellet electrode and the beryllium window as a well-conductive current collect. A constant current of 5 mA g^{-1} was applied to the cell at room temperature to cycle it in the voltage window of 2 V to 4.8 V versus Li^+/Li. The diffraction patterns were collected continuously, and each scan took 1 hour.

6.3.4. Operando DEMS, Raman Spectroscopy and XANES

Details of the operando DEMS experiment was referred to in section 5.3.2. Minor differences include (1) a current of 5 mA g^{-1} was applied in the galvanostatic cycling of the DEMS cells; (2) the pellet electrode used for this experiment was in a weight ratio of 7:2:1 for the active material ($Li_{1.2}Mn_{0.4}Ti_{0.4}O_2$), carbon super P, and PTFE binder.

The Raman Spectra of the materials at different charge/discharge states were collected following the same experimental details as mentioned in section 5.3.5.

The Mn and Ti XANES spectroscopy were measured at the *B18* Beamline at the Diamond Light Source, Harewell, U.K. The XANES spectra of Mn_2O_3, MnO_2, and Li_2TiO_3 were also collected as references for the data interpretation. The detail was referred to section 5.3.3.

6.3.5. SXAS and RIXS

The SXAS and RIXS were measured at the Beamline BL27SU, RIKEN Spring-8 Synchrotron Facility, Japan. This beamline consisted of two branches that covers both the higher-energy region (2.1-3.3 KeV) and the lower-energy region (0.17-2.2 KeV). The SXAS of O K edge, Ti L edge and Mn L edge were measured. For both the Partial Fluorescence Yield (PFY) signal and the TEY signal, the normalization followed an established procedure[277], which has been discussed in section 5.3.4. The energy region of data collection and normalization for these three elements were listed below (Table

6-1). The emission energy of RIXS mapping was in the region of 427 - 949 eV, in which the RIXS spectra at the excitation energy of 531.5 eV were taken for analysis.

Table 6-1 The energy region of data collection and normalization for O K edge, Ti L edge and Mn L edge SXAS

SXAS	Data Collected (eV)	Pre-edge Line Fitted region (eV)	Post-edge Line Fitted Region (eV)
O K edge	515 - 580	516 - 523	555 - 577
Ti L edge	450 - 485	450 - 455	480 - 485
Mn L edge	620 - 670	620 - 638	660 - 670

6.4. Results and Discussion

6.4.1. Disordered Rock-Salt Li-rich Material

6.4.1.1. Composition, Morphology and Crystallographic Structure

The synthesized material shows polyhedral-like morphology and a wide particle size distribution in the range of 0.1~2 μm, in which most primary particles are in a size about 1~2 μm. Its elemental contents are in a good agreement with the proposed chemical composition, as confirmed by ICP-OES (Table 6-2).

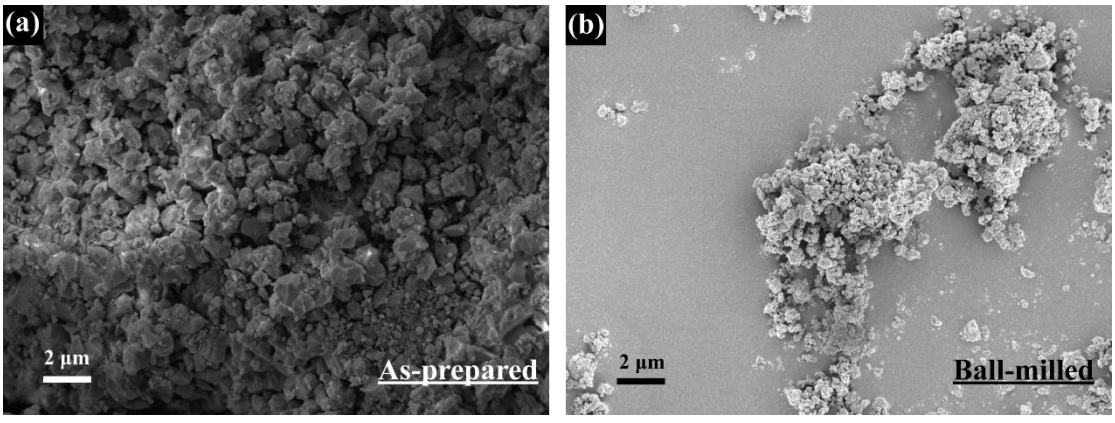

Figure 6-1 SEM images of (a) the as-prepared material and (b) the material after ball-milling

Table 6-2 Result of the ICP-OES

Elemental Analysis Results (m/m%)			Corresponding Contents (mol per mol of material)			Expected Contents (mol per mol of material)		
Li	Mn	Ti	Li	Mn	Ti	Li	Mn	Ti
8.41	22.1	18.9	1.21	0.40	0.39	1.20	0.40	0.40

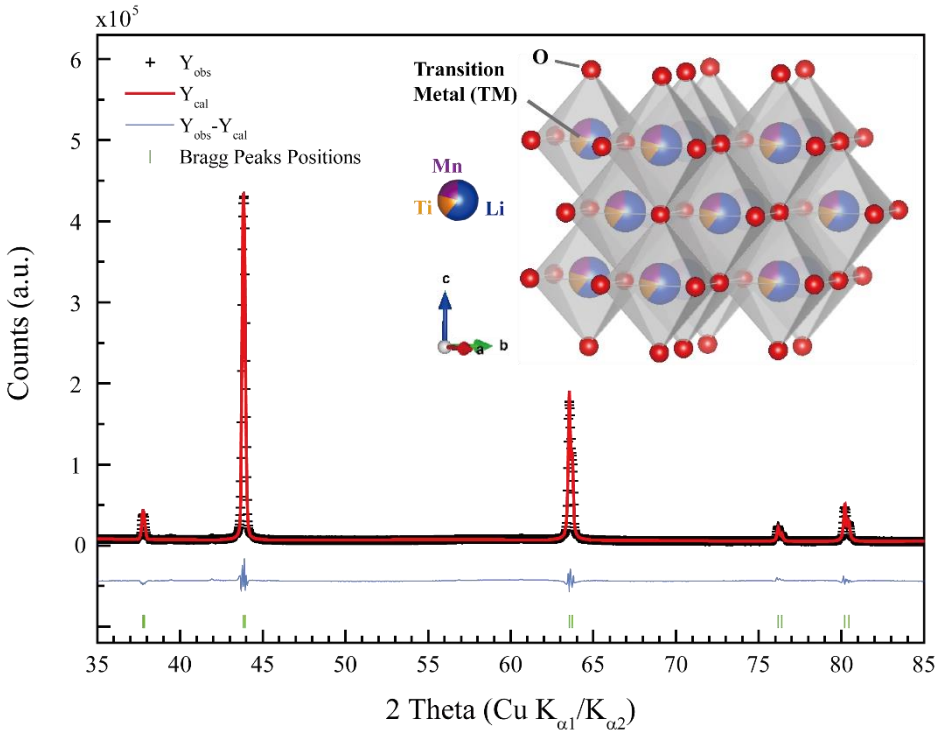

Figure 6-2 The refined PXRD pattern (in *Fm-3m* space group) of the solid-state synthesized $Li_{1.2}Mn_{0.4}Ti_{0.4}O_2$. The "+" marks the observed data. The red and blue line represent the calculated diffraction profile and the difference between the observed and calculated profiles, respectively. The green ticks mark the allowed Bragg peaks. The schematic of the refined structure is also presented in a polyhedral view. The transition metal sphere consists of three colours (blue-Li, orange-Ti, and purple-Mn), in which the ratio of coloured area corresponds to the occupancies of transition metal ions at the crystallographic site *4a*.

The PXRD data was collected in the two-theta region from 35° to 85°. Clear and sharp diffraction peaks are observed, indicating the good crystallinity of the synthesized material. The Rietveld refinement[199,244] of the PXRD data in the *Fm-3m* (#225) space group was carried out by using the Fullprof suite programme[201]. It shows that the observed pattern is in a good accordance with the calculated one, indicating the

formation of a pure phase cation-disordered rock-salt $Li_{1.2}Mn_{0.4}Ti_{0.4}O_2$. Only the unit cell parameters are refined, while the transition metal and alkali ions are considered randomly distributed at the crystallographic site *4a*, and their occupancies are fixed according to their chemical contents obtained from the ICP-OES elemental analysis. Three factors for points with Bragg contributions for pattern, weight profile R value (R_{wp}), Bragg R-factor, and χ^2, were used to represent the reliability of refinement[244].

The details of the crystallographic parameters are listed in the Table 6-3.

Table 6-3 The crystallographic parameters for the $Li_{1.2}Mn_{0.4}Ti_{0.4}O_2$

Atom	Wyckoff Position	Coordination			Occupancy
		x	y	z	
O	*4b*	0.5000	0.5000	0.5000	1.000
Li	*4a*	0.0000	0.0000	0.0000	0.605
Mn	*4a*	0.0000	0.0000	0.0000	0.200
Ti	*4a*	0.0000	0.0000	0.0000	0.195
Cell Parameters	a = b = c = 4.1543(5)		V = 71.699(5)		
R_{wp}: 8.60		Bragg R-Factor: 3.03		χ^2: 2.98	

6.4.1.2. General Electrochemistry at Room Temperature

The typical 1st cycle load curve (Figure 6-3(a)) of the $Li_{1.2}Mn_{0.4}Ti_{0.4}O_2$ shows a very similar shape and layout to layered Li-rich materials, which was discussed in the CHAPTER 5 (Figure 5-1). For the convenience of the discussion in this chapter, the charge curve is divided into three regions: (1) Sloping region "S": the sloping charge region up to about 4.32 V, which counts for about 130 mAh g^{-1} on the charge curve and is in consistent with the conventional manganese oxidation ($Mn^{3+} \rightarrow Mn^{4+}$, theoretically, 131.6 mA g^{-1}); (2) Plateau-like region "P": a relatively flat region above 4.32 V on charge; (3) Tail-like region "T": a sloping region at the end charge. The sum

of the region "P" and "T" corresponds to the extra charge capacity beyond the $Mn^{3+} \rightarrow Mn^{4+}$ oxidation. In the subsequent cycles (up to 32 cycles), despite the gradual capacity fading, both the charge and discharge capacity of the $Li_{1.2}Mn_{0.4}Ti_{0.4}O_2$ still remain well-above the theoretical capacity of Mn^{3+}/Mn^{4+} redox reaction (Figure 6-3(b)). After 15 cycles, the coulombic efficiency of the $Li_{1.2}Mn_{0.4}Ti_{0.4}O_2$ stabilizes at about 98%, which is about 1.5% less compared to the layered Li-rich material (the RF-gel synthesized $Li_{1.2}Ni_{0.13}Co_{0.13}Mn_{0.54}O_2$, as being discussed in section 3.4.2)

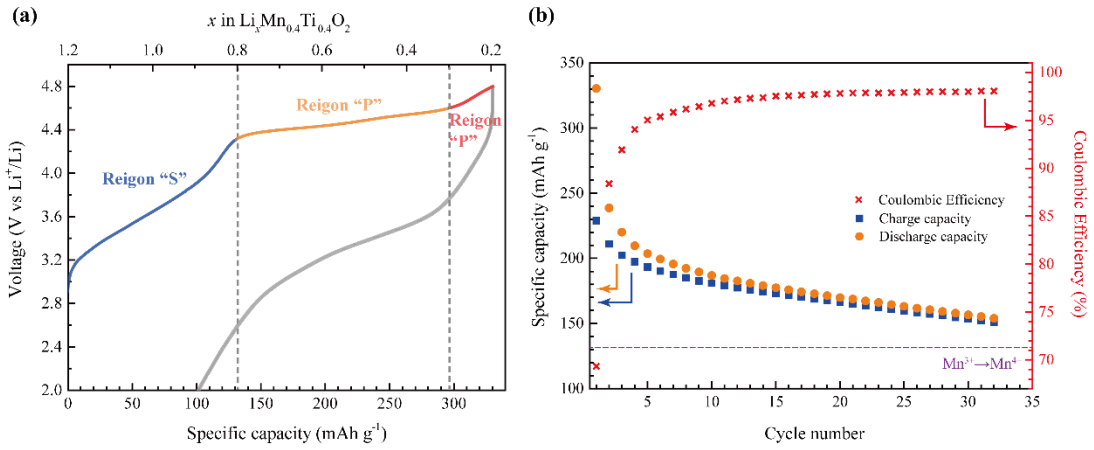

Figure 6-3 (a) A typical 1st cycle load curve of the $Li_{1.2}Mn_{0.4}Ti_{0.4}O_2$ at the room temperature. For the convenience of the discussion in this chapter, the regions are labelled as "S" (Sloppy, in blue), "P" (Plateau-like, in orange) and "T" (Tail-like, in Red), respectively; (b) Specific charge (orange dot, left y axis) and discharge capacities (blue square, left y axis) and coulombic efficiency (red cross, right y axis) in 32 cycles.

6.4.2. Gas Evolution on Charge

The capacity of $Li_{1.2}Mn_{0.4}Ti_{0.4}O_2$ when charged to a 4.8 V cut-off is well beyond the limit of the $Mn^{3+} \rightarrow Mn^{4+}$ oxidation and its load curve shares many features with $Li_{1.2}Ni_{0.13}Co_{0.13}Mn_{0.54}O_2$. To investigate if oxygen loss plays a role as discussed in the earlier chapter, the operando DEMS was used. Here, the operando DEMS was used to measure the quantity of the gas evolved during the 1st cycle, which can be used to

calculate the corresponding charge transfer (Q_g) and compared to the electrochemically record equivalent (Q_e), based on the model used in section 5.4.1 and Appx. 3.

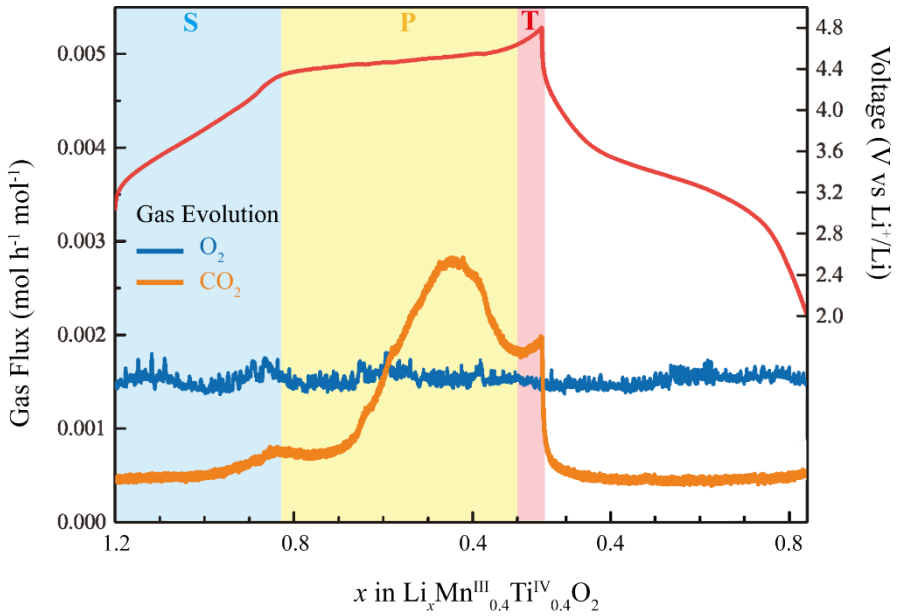

Figure 6-4 Operando DEMS of $Li_{1.2}Mn^{III}_{0.4}Ti^{IV}_{0.4}O_2$ cathode in the 1st cycle. The electrochemical curve of the operando DEMS cell (in red, refers to the right y-axis), O_2 (in blue) and CO_2 (in orange) evolution (gas in mol per hour, per mol of cathode material, refers to the left y-axis) plot as a function of the state of charge.

Throughout the entire 1st cycle, only CO_2 evolution is observed. In region "S", the trace of significant CO_2 evolution is not observed, although the minor flux rise of CO_2 appears close to the end of the region, which may indicate that minor decomposition of PC electrolyte happens slight before the high-voltage region. Nevertheless, the rise of the CO_2 flux is still insignificant compared with the dominant CO_2 evolution in the high-voltage regions afterwards. In region "P", considerable amount of CO_2 evolution is observed and reaches its maximum at the second-half of the region. The integrated area of the CO_2 in this region equals to 0.05336 mol CO_2 per mol of cathode material, which corresponds to 0.05336 mol e^- transferred or 17.56 mAh g^{-1} in specific capacity, based on the model described in Appx. 3. In region "T", continuous evolution of CO_2 is clearly

probed and the integrated area equals to 0.00958 mol CO_2 per mol of cathode material, corresponding to 0.00958 mol e^- transferred or 3.15 mAh g^{-1} The comparison of the gas evolution corresponded charge transfer with the actual charge transfer from the electrochemistry is detailed in Table 6-4.

For the O_2, there is no clear trace of O_2 evolution observed during the 1st cycle, although minor wobble of the signal appears. Nevertheless, considering the integrated area of the wobbled signal is below 1 mAh g^{-1}, the contribution on capacity from the O_2 evolution is negligible.

Table 6-4 A comparison between the charge transfer (Q_g) corresponding to the CO_2 evolution and the electrochemically recorded equivalents (Q_e)

Region	Q_g (e^- per formula unit)	Specifc Charge Capacity (mAh g^{-1})	Q_e (e^- per formula unit)	Percentage (%) (Q_g/Q_e)
Region "P"	0.053	119.013	0.362	14.8
Region "T"	0.010	18.944	0.058	16.6
Total	0.063	137.958	0.419	15.0

In the high-voltage region (region “P” & “T”) during the 1st charge, the charge transfer corresponded to the gas (CO_2) evolution only contributes about 15% of the electrochemical capacity (Table 6-4). Assuming the CO_2 mainly formed by decomposition of the PC electrolyte under the attack of O extracted from the lattice of $Li_{1.2}Mn_{0.4}Ti_{0.4}O_2$, as the model being proposed in Appx. 3, such result suggests that there should be other dominant mechanism(s) responsible for the extra capacity on charge in the high-voltage region, rather than the gas evolution. Further discussion will be given in the following contents.

6.4.3. The Hole States Redox

Multiple spectroscopy methodologies, including SXAS, RIXS, XANES[viii] and Raman, were employed to carefully study the redox, mainly oxidation, of $Li_{1.2}Mn_{0.4}Ti_{0.4}O_2$ during cycling.

6.4.3.1. Region "S"

The capacity in this region is attributed to the oxidation of Mn. To confirm this, the oxidation states of Mn is checked using the Mn L edge SXAS. The Mn L edge SXAS corresponds to the excitation of Mn *2p* electrons to the unoccupied *3d* state. Such transition is sensitive to the Mn local electronic structure (more sensitive than Mn K edge (*1s* to unoccupied *4p* transition)), especially the changes on the *3d* states, making it ideal for probing the Mn oxidation state variation. In particular, the spectra collected using the inverse PFY (iPFY) mode are bulk sensitive while the spectra at TEY mode are surface sensitive, as already being explained in section 2.3.9. Moreover, the Mn L_3 ($2p_{3/2}$) edge and L_2 edge ($2p_{1/2}$) are separated by the core-hole spin-orbital interaction, in which the core-hole lifetime broadening is relatively smaller for L_3 edge, resulting in better pronounced multiplet feature[214]. Therefore, the changes of Mn L_3 edge SXAS spectra are mainly compared when investigating the Mn oxidation state variation.

In fact, the Mn L edge SXAS spectrum collected using iPFY mode (Figure 6-5(b)-Spectrum *a*) indicates that the majority of Mn is in +3 oxidation state in the bulk of the pristine $Li_{1.2}Mn_{0.4}Ti_{0.4}O_2$. In addition, a minor presence of a Mn^{4+} feature is also

[viii] The Mn and Ti K edge XANES spectroscopy is discussed in the Appx. 7.

observed. Further investigation of the Mn L edge SXAS TEY spectrum *a* (Figure 6-5(c)) confirms the co-existence of Mn^{2+} and Mn^{4+} on the surface of the pristine material. The presence of Mn^{2+} and Mn^{4+} in the pristine material could be explained by the disproportionation reaction[ix] of Mn^{3+} to form Mn^{2+} and Mn^{4+}, which has been well recognized in the previous study of $LiNi_{0.5}Mn_{1.5}O_4$[308-310] and $LiMn_2O_4$[311-313] spinel cathode materials.

On charging to the end of region "S", Mn^{3+}, both in bulk and on surface, and majority of Mn^{2+} are oxidized to Mn^{4+}, although Mn^{2+} trace is still presented on the TEY spectrum (Figure 6-5(c)-Spectrum *b*), which may indicate a small quantity of Mn^{2+} existing at the surface of the material. In addition, the investigation on the O K edge SXAS spectra (Figure 6-7(b), spectrum *b*) identifies a clear spectral feature (peak A) of O *2p* in hybridization with *3d* state of Mn^{4+}, which also indicates the +4 oxidation state of Mn at the end of region "S".

[ix] $2Mn^{3+} \rightarrow Mn^{2+} + Mn^{4+}$

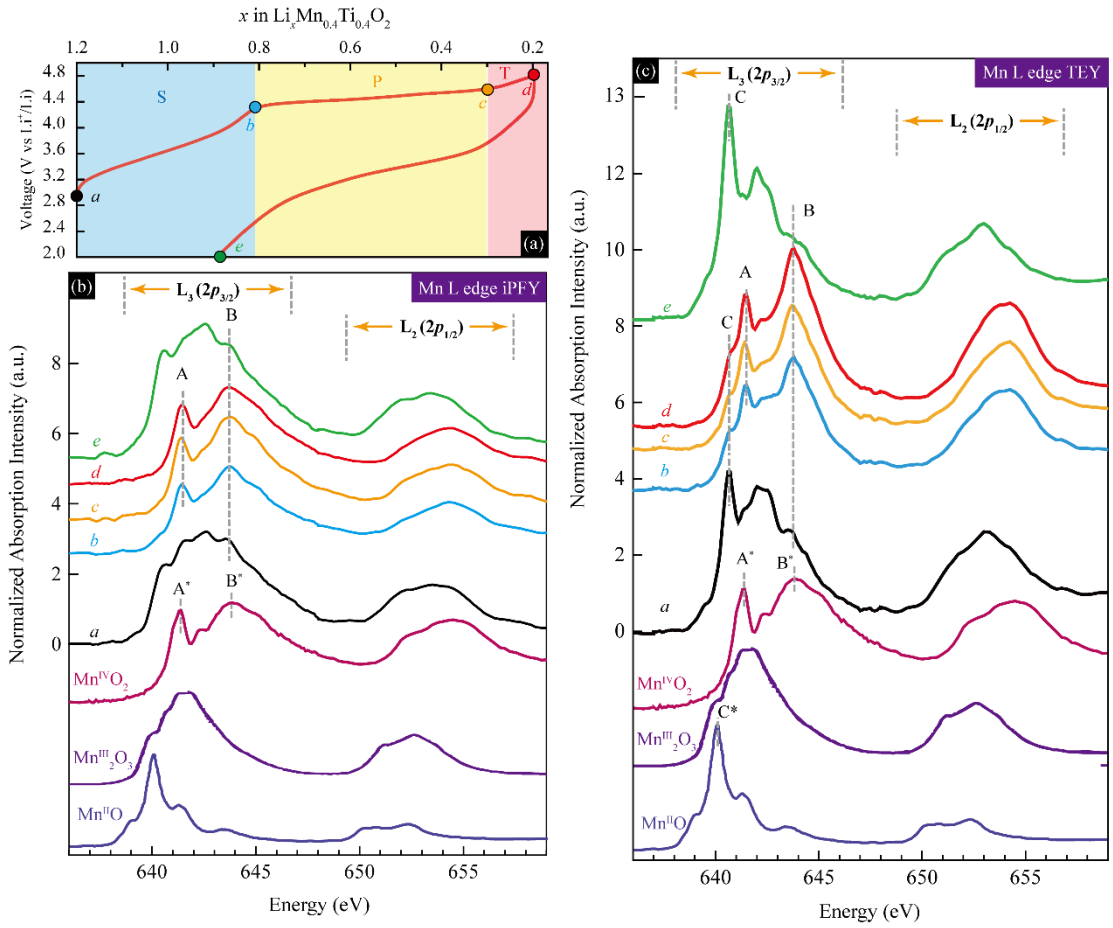

Figure 6-5 The ex-situ Mn L edge SXAS spectra at different state of charge: (a) the corresponding state of charge on load curve for ex-situ samples; (b) Mn L edge SXAS spectra at iPFY mode; (c) Mn L edge SXAS spectra at TFY mode. The peak A, B, and C correspond to the characteristic peaks of Mn^{4+} (A^* & B^*) and Mn^{2+} (C^*), in $Mn^{IV}O_2$ and $Mn^{II}O$, respectively. The $Mn^{II}O$, $Mn^{III}_2O_3$, and $Mn^{IV}O_2$ reference spectra are reproduced from Ref.[314], by the permission from Elsevier: Current Applied Physics 13, 544-548, copyright 2013.

For the Ti, the L edge SXAS PFY spectrum *a* (Figure 6-6) confirms that it is in +4 oxidation state in the pristine material, as expected. Since at its highest and most stable oxidation state, Ti remains in +4 oxidation state on charging to the end of region "S" (Figure 6-6, spectrum *b*). In fact, there is no redox activity of Ti in the 1st cycle of $Li_{1.2}Mn_{0.4}Ti_{0.4}O_2$, as demonstrated by the identical Ti^{4+} features on all Ti L edge PFY spectra throughout the 1st cycle, although the variation of spectra intensity suggests that the distortion of TiO_6 octahedra occurs at different state of charge. This is also discussed

in Appx. 7 using the Ti K edge XANES spectroscopy.

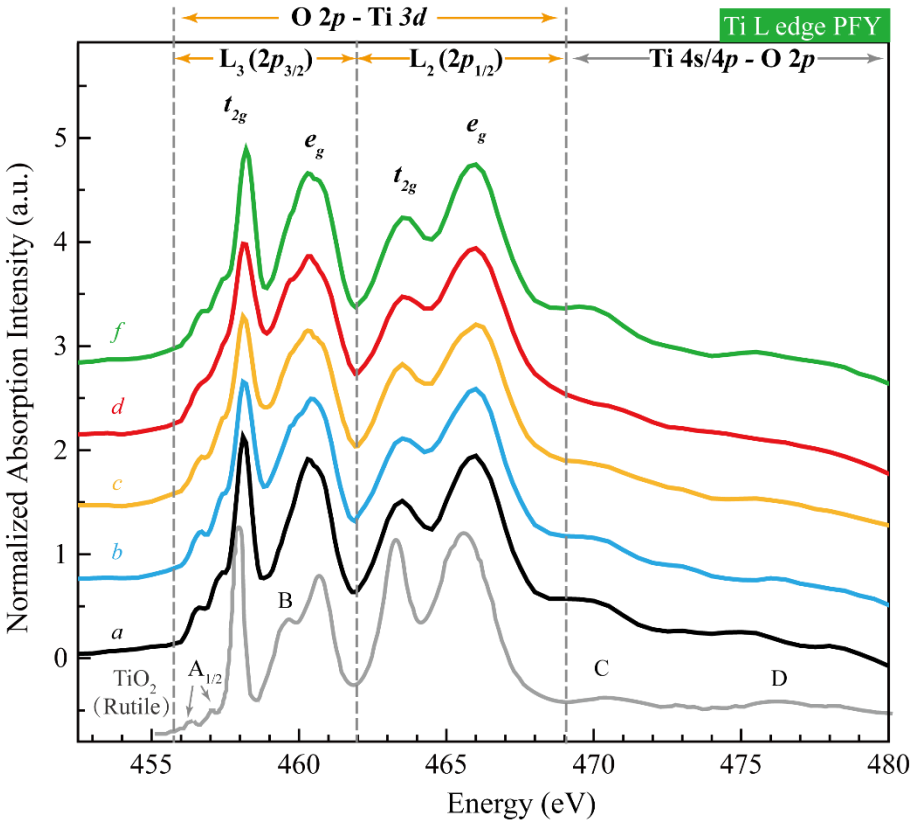

Figure 6-6 The ex-situ Ti L edge SXAS spectra at PFY mode at different state of charge. The corresponding state of charge is identical as the Figure 6-5(a). The reference spectra of TiO_2 (Rutile) reproduced from the Ref[315]; the weak peak A_1 & A_2 are the pre-edge resonance and the shoulder B is the fingerprint of rutile structure of TiO_2[316,317]; the two weak peaks C & D are due to the Ti 2p, 4s and 4p states coupled with O 2p states[315,318].

The oxidation of Mn^{3+} generates extra unoccupied states on its *d* orbitals, which are hybridized with the O *2p* orbitals. Thus, the change of unoccupied states could be reflected by probing the O K edge using SXAS.

The low-energy region (≤ 535 eV) of O SXAS K edge PFY spectra corresponds to the electron excitation from O *1s* to the unoccupied O *2p* orbitals hybridized with the transition metal *3d* orbitals, which is mainly discussed. The spectra show combined features of O *2p* orbitals hybridized with both Mn and Ti *3d* orbitals (Figure 6-7(b)). This is due to the equal presence of Mn and Ti in the chemical composition. For the

pristine material (spectrum *a*), the broad peak at 531.2 eV corresponds to a combined feature of O *2p* - Mn^{3+} *3d* hybridization (peak D^{*}) and O *2p* - Ti *3d* hybridization (peak B^{*}). On charging across the region "S", the O K edge SXAS spectrum *b* changes substantially. The splitting of multiplet shows clear features of O *2p* hybridized with the Mn^{4+} *3d* (peak A) and O *2p* hybridized with the Ti^{4+} *3d* (peak B & C). The increased integrated area underneath of spectrum *b* corresponds to the additional unoccupied states created during oxidation of Mn^{3+} into Mn^{4+}.

6.4.3.2. Region "P"

On charging across the region "P", Mn L edge SXAS spectra shows almost no change, regardless the bulk (iPFY) or surface (TEY), indicating no further oxidation of Mn. Meanwhile, Ti remains at its highest oxidation state and cannot be further oxidized. Thus, the possibility of the further oxidation of transition metal can be excluded, leaving the oxidation of O as the only possibility.

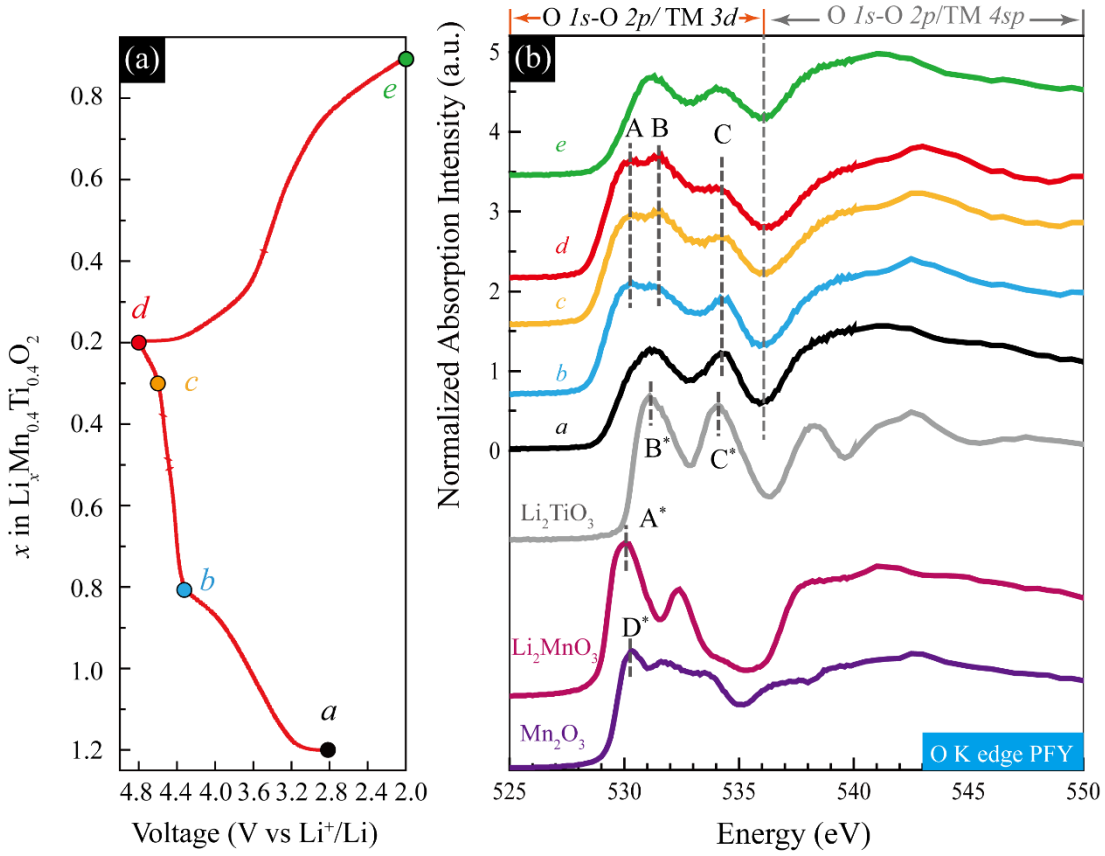

Figure 6-7 (b) The ex-situ O K edge SXAS spectra on PFY mode at (a) different state of charge. The O K edge SXAS spectra of Li_2TiO_3, Li_2MnO_3 and Mn_2O_3 are collected as reference.

The O K edge SXAS PFY spectrum *c* (Figure 6-7) at the end of the region "P" appears identical in shape to the spectrum *b* at the start of this region, whereas its integrated area underneath in the low-energy region (525 eV-536 eV) increases by about 10% compared with the spectra *b*. The integrated area increase is corresponding to extra unoccupied states created through the oxidation of O. Thus, it should be attributed to the formation of electron-holes primarily in the O *2p* states.

Therefore, as being discussed in section 6.4.2, the CO_2 evolution in this region only counts for about 14.8% of the extra capacity, leaving the formation of electron-holes being responsible for the majority of extra capacity in this region.

6.4.3.3. Region "T"

On charge across the region "T" to the 4.8V cut-off, the transition metal (Mn & Ti) L edge SXAS spectra remain as they were at the end of region "P". The O K edge SXAS PFY spectrum *d* at the end of this region has no change in shape compared with the spectrum *c* at the beginning of this region, although the integrated area at the low-energy region increases by about 2%, which can be explained by the continuous creation of electron-holes on O (oxidizing O) during charge. As the operando DEMS result shows no O_2 gas evolution (Figure 6-4) and the CO_2 evolution only counts for about 16.6% of the extra capacity (Table 6-4) in this region, the creation of electron-holes on O is still the dominant contributor for the extra capacity in this region.

6.4.3.4. End of the 1st cycle

When discharged back to 2 V, the Mn L edge SXAS iPFY spectrum *e* returns to almost the same feature as the spectrum *a* for the pristine material and the minor presence of Mn^{4+} retains as it is in the spectrum *a* (Figure 6-5(b)). A similar recovery on the spectral feature is also observed on the Mn L edge SXAS TEY spectrum *e*. In particular, the Mn^{2+} feature (peak C) on spectrum *e* develops to a higher intensity (Figure 6-5(c)). The Mn L edge SXAS spectra suggest that when fully discharged to a 2 V cut-off, Mn in the bulk of material is mostly reduced to +3 oxidation state, while a small quantity remained +4 oxidation state. For the Mn at the material surface, upon the reduction to +3 oxidation state, a possible disproportionation reaction may happen, causing the presence of +2 and +4 oxidation states. The presence of Mn^{2+} feature may also attribute to the over reduction of Mn for charge balance.

The O K edge SXAS PFY spectrum *e* at the end of 1st discharge also recovers the shape, as compared with the spectrum *a* for the pristine materials, which demonstrates the reversible nature of the oxygen redox. It will be further discussed in the later section. The integrated area in low-energy region of spectrum *e* is about 6% less as compared with the spectrum *a*. It can be considered as the indirect evidence of the O extraction from the lattice, which then attacks and decomposes the PC electrolyte to generate CO_2 gas, as being measured by the operando DEMS.

6.4.4. Nature of the Holes on Oxygen

According to the above discussion, it is clear that oxygen redox happens on charging the $Li_{1.2}Mn_{0.4}Ti_{0.4}O_2$ beyond the Mn oxidation up to the 4.8 V cut-off and on discharging it to a 2 V cut-off. Investigation on the nature of the electron-holes would bring better understanding of this oxygen redox process.

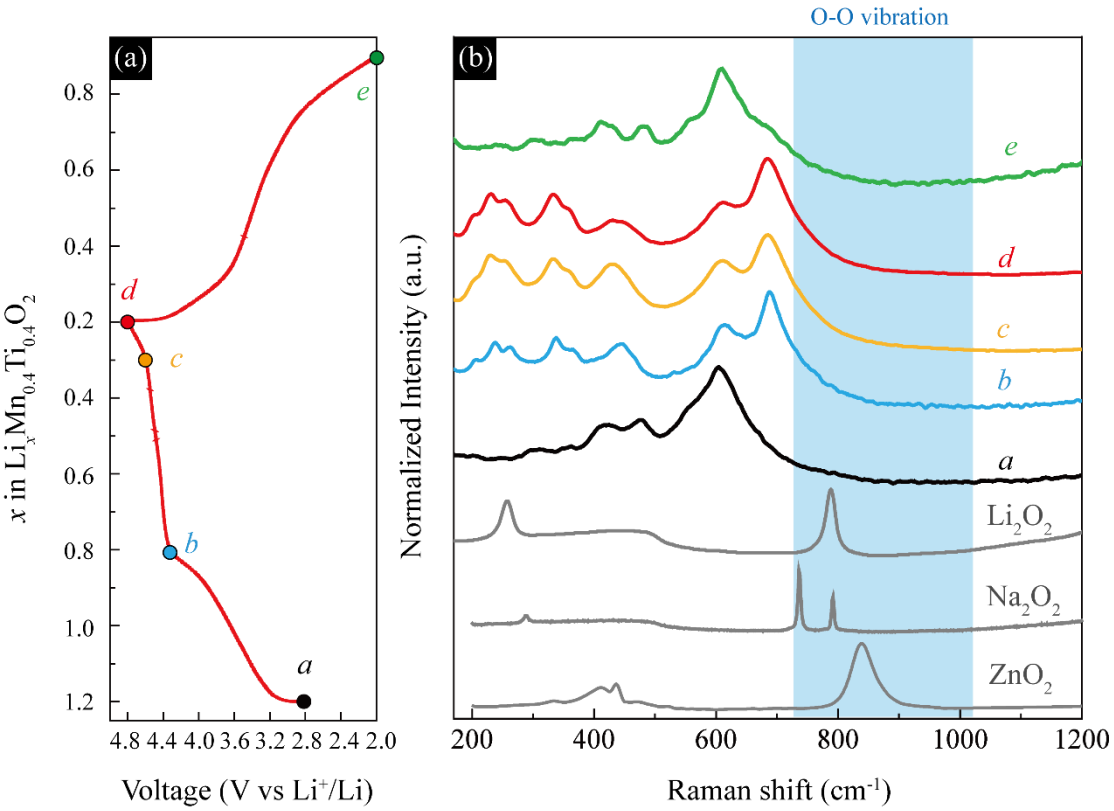

Figure 6-8 (b) Raman spectra at (a) different state of charge. The spectra of three reference samples (in grey), Li_2O_2, Na_2O_2, ZnO_2 (Alfa Aesar, approximately 50% ZnO_2 in ZnO), refine the region of O-O vibrations.

Ex-situ Raman spectra of the material at different state of charge were collected to investigate whether the peroxide species, O_2^{2-} (O-O ~ 1.45 Å) is formed as the result of the O oxidation, since the Raman spectroscopy is sensitive to the O-O peroxo vibrations. Three peroxo compounds, Li_2O_2, Na_2O_2 and ZnO_2, are selected as references of the O-O peroxo vibrations. The low Raman shift region (≤ 720 cm^{-1}) is known to correspond to the metal-O vibrations[178,285,286]. The nearly identical spectra in region "P" & "T" (spectrum *b*, *c* & *d*) and the recovery of spectrum *e* at the end of discharge suggest the same information as the other spectroscopy results. In the region anticipated for the O-O peroxo vibrations, there is no clue of peaks appearing, indicating that the true O-O peroxo species are not formed in this cation disordered rock-salt Li-rich *3d* transition

metal oxide, whereas the formation of peroxo-like $(O_2)^{n-}$ dimers (O-O ~ 2.4 Å) is reported in the layered Li-rich *4d* and *5d* transition metal oxides, while the electron-holes are created on O^{2-} on charge.

Direct probing on the electron-holes on O is realized by using the ex-situ O K edge RIXS spectrum at different state of charge (Figure 6-9), as the spectrum records the resonant emission of photons from O *2p* to O *1s* electron transition, which is highly sensitive to the electronic configuration of the O. The spectrum *b* at the end of region "S" retains the same shape as the spectrum *a* in general, due to no oxygen redox activity in this region. The broadening of spectrum *b* is observed. It may be due to the geometry change of MnO_6 octahedra, since the MnO_6 octahedra is not anticipated to have Jahn-Teller distortion once Mn^{3+} being oxidized to Mn^{4+}, other than it was in the pristine material when Mn is at +3 oxidation state. However, at the end of region "P", the spectrum *c* shows new peak feature at about 524 eV and rearrangement of the weight of peaks. This indicates a significant electronic reconfiguration around O, which may be due to the electron negativity change of O as it is oxidized in the region "P". At the end of charge, the spectrum *d* presents better developed peak features and substantial intensity increase for both peaks, as the consequences of both O oxidation (major) and O loss (minor) in the region "T". Particularly, the elastic peak presented at 531.5 eV increases in intensity as the material is charged through regions "P" & "T". This again, indicates the localized character of O excitation state[289].

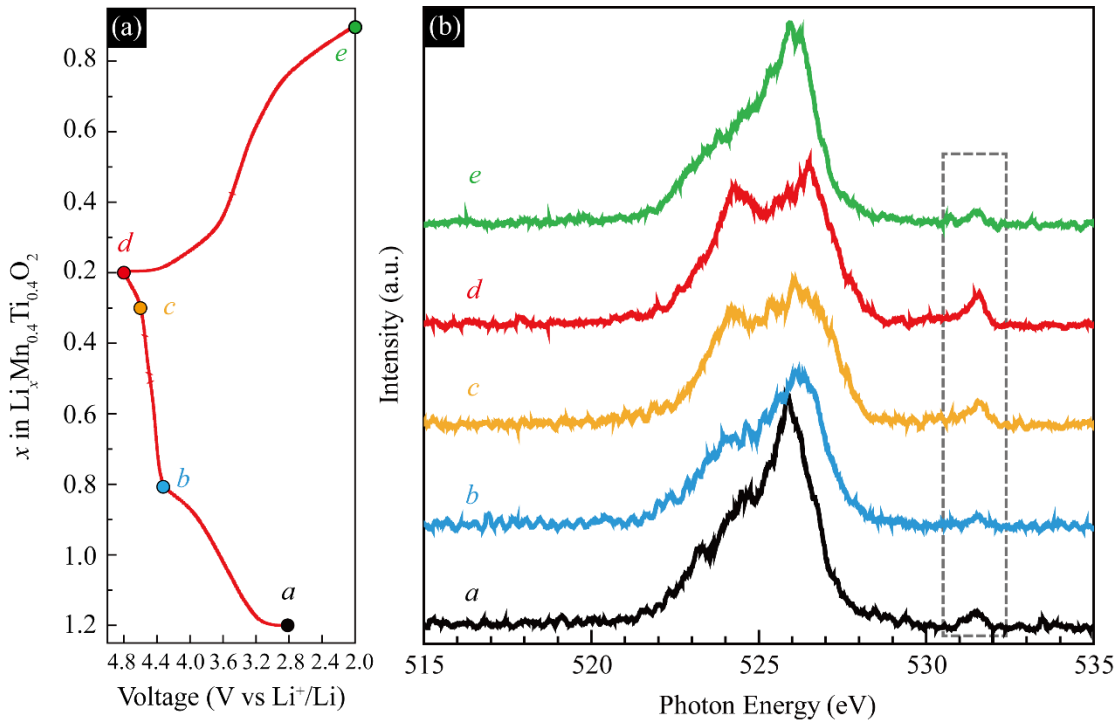

Figure 6-9 (b) Oxygen K edge RIXS spectra with excitation energy of 531.5 eV at (a) different state of charge.

Eventually, on fully discharge to a 2 V cut-off, the spectrum *e* recovers to almost identical shape as the spectrum *a*, which also demonstrates the reversible nature of the oxygen redox. The slight difference on intensity is attributed to the O loss on charging across the regions “P” & “T”.

6.4.5. Reversibility of Oxygen Redox and Structure Revolution

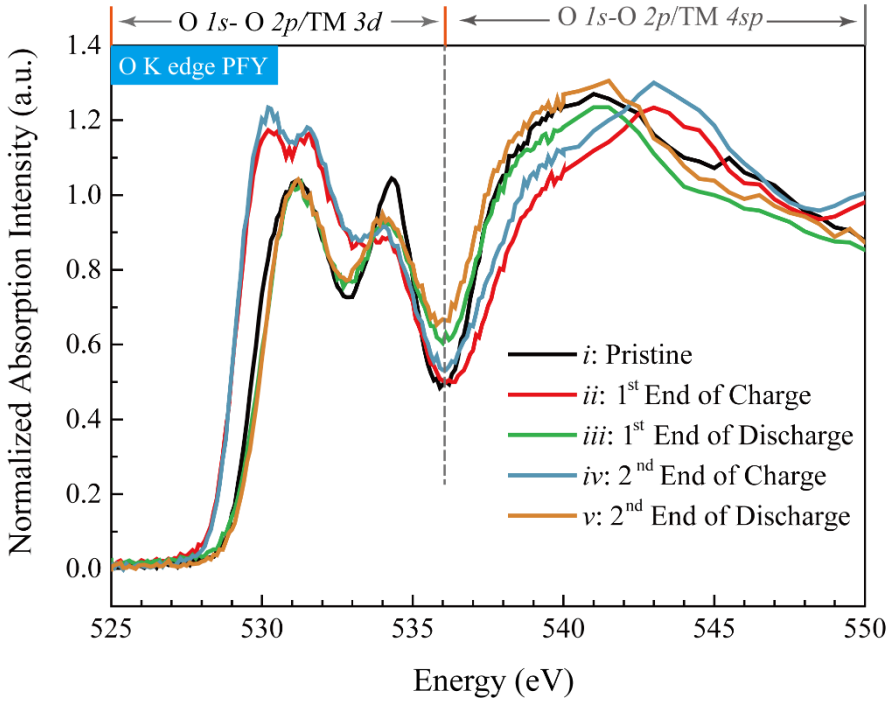

Figure 6-10 The ex-situ O K edge SXAS spectra at PFY mode for the pristine material (in black), at the 1st cycle end of charge (in red) and discharge (in green), and the 2nd cycle end of charge (in blue) and discharge (in light brown).

The reversible nature of the oxygen redox has been investigated and demonstrated by using the SAXS and RIXS to probe the O K edge at different state of charge in the 1st cycle of $Li_{1.2}Mn_{0.4}Ti_{0.4}O_2$. Further investigation on the reversibility of oxygen redox is also done by directly probing the O K edge using SAXS particularly, at the end of charge and discharge of the 2nd cycle (Figure 6-10).

In the low-energy region (≤ 535 eV) corresponding to the excitation of O *1s* to hybridized states of O *2p* and transition metal *3d*, the spectrum *iv* at the end of 2nd charge almost overlaps with the spectrum *ii* at the end of 1st charge, indicating the continuation of oxidation of O in the 2nd cycle. In fact, the intensity of the spectrum *iv* is slightly higher than the spectrum *ii*, which could be attributed to the generation of

electron-holes on more O after the O loss from the lattice in the 1st charge. At the end of 2nd discharge, the spectrum *v* overlaps with the spectrum *iii* for the end of 1st discharge, clearly demonstrating the reversible nature of the oxygen redox of the 2nd cycle.

In addition, the peak at around 534 eV for both spectrum *iii* and *v* show lower intensity, as compared with the spectrum *i* for the pristine material. This peak corresponds to the O *2p* hybridized with Ti *3d* states, as being presented in Figure 6-7. It indicates a decrease of the amount of the unoccupied states in the O *2p* - Ti *3d* hybridization. This could also be anticipated by the O loss in the 1st cycle, which results in relatively less O presence in the lattice. However, the peak at around 531 eV, corresponding to the O *2p* hybridized with Mn *3d* states, shows identical intensity and shape. It suggests that the unoccupied states in the O *2p* - Mn *3d* hybridization have not changed for both discharge materials in the 1st and 2nd cycles, although the O loss happens in the extra capacity region (region "P" & "T") in the 1st charge. Combining above clues, it may imply that the O loss prefers to happen on those O associated with Ti rather than Mn.

Meanwhile, it is also in a good accordance with the proposed oxygen redox mechanism of layered Li-rich cathode materials. In the previous case, those oxygens surrounded by Mn^{4+}/Li^{+} are expected to form localized electron-holes states near the top of the O^{2-} valence band, as the hybridization between O^{2-} *2p* and Mn^{4+} *3d* (*d-p* mixing) / Li *2s* tends to be relatively more ionic than the O^{2-} *2p* and Ni^{4+}/Co^{4+} *3d* (*d-p* hybridization. Thus, it tends to lie higher in energy to activate the oxygen redox. In the $Li_{1.2}Mn_{0.4}Ti_{0.4}O_2$ case, the O^{2-} *2p* and Ti^{4+} *3d*/ Li *2s* hybridization tends to be relatively

more ionic. Therefore, those O surrounded by Ti and Li would potentially be more accessible for oxygen redox.

However, in the cation disordered rock-salt structure, all the cation (Li, Ti and Mn) randomly occupy the same crystallographic site *4a*, and Mn & Ti share the identical chemical contents per formula unit, thus there should be equivalent possibility for Mn and Ti to present in the metal - O octahedra (MO_6). Therefore, the previous implication, which the O loss preferably happens on those O associated with Ti and Li, could only be valid if there would be cation local ordering within the structure. Such anticipation leads to a clear direction for further in-depth investigation on the oxygen redox mechanism for $Li_{1.2}Mn_{0.4}Ti_{0.4}O_2$.

The structural reversibility of the $Li_{1.2}Mn_{0.4}Ti_{0.4}O_2$ in the 1st cycle is also investigated by using the OPXRD (Figure 6-11). As the Al foil used in the OPXRD cell configuration diffracts the incident X-ray beam as well, the actual incident beam for the electrode is weak in intensity, resulting in a weak intensity for diffraction patterns of the electrode. Besides, the Al shares the same *Fm-3m* space group (#225) with $Li_{1.2}Mn_{0.4}Ti_{0.4}O_2$, which leads to conflict of diffraction peaks between both. In fact, only the 1st and 2nd most intensive peaks (peak A and B) and their corresponding evolutions are observed in a reasonable quality on the OPXRD patterns, therefore, the discussion is based on the evolution of Peak A and B.

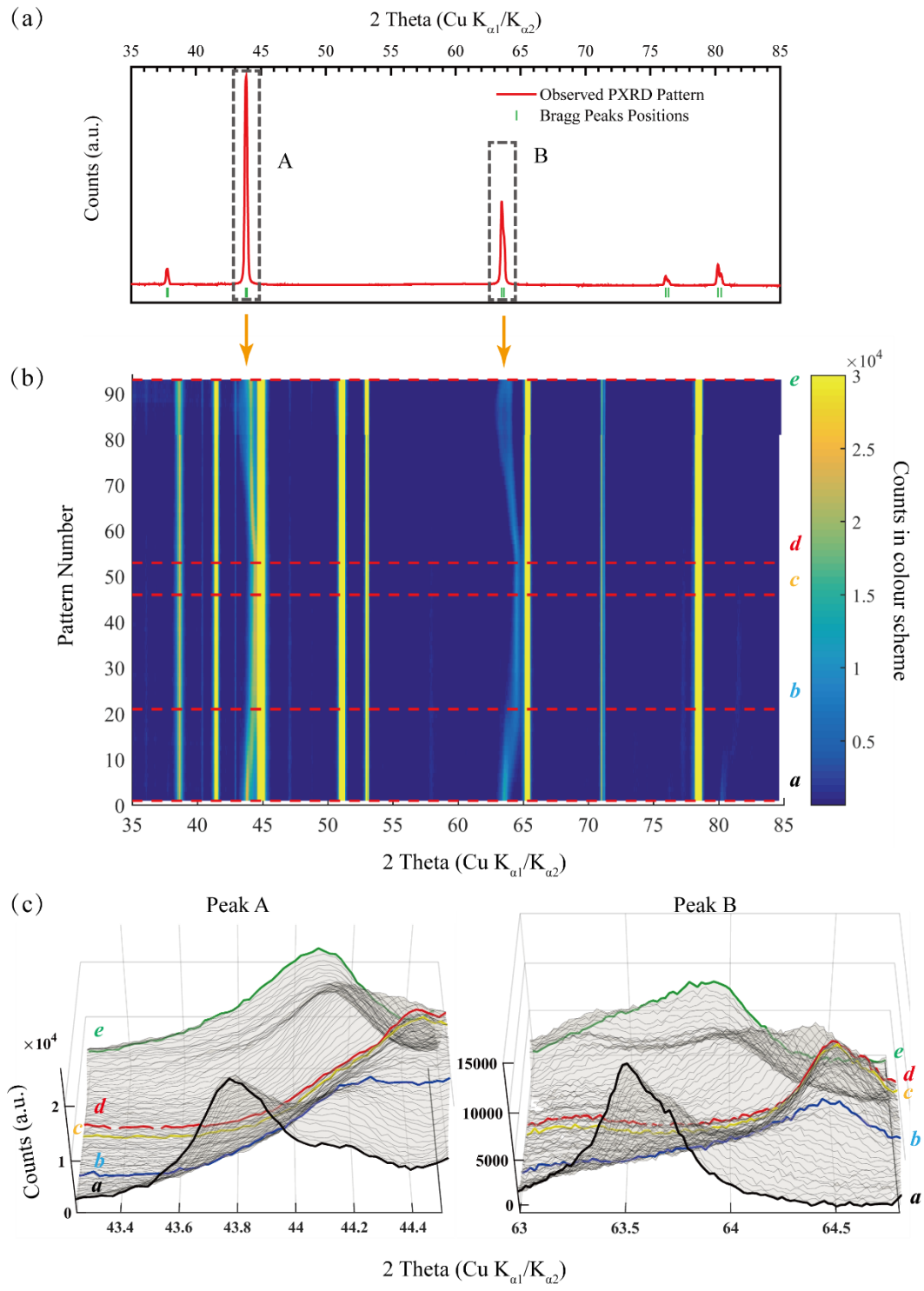

Figure 6-11 (b) The OPXRD patterns of $Li_{1.2}Mn_{0.4}Ti_{0.4}O_2$ in its 1st cycle. (c) The 1st and 2nd most intensive peaks in the OPXRD patterns are enlarged for clarity and convenience of discussion. As a comparison, (a) the powder diffraction pattern of the pristine material is presented. The notation *a*, *b*, *c*, *d*, and *e* correspond to the diffraction patterns of the electrode at beginning of charge (in black), end of region "S" (in blue), end of region "P" (in yellow), end of region "T" (in red), and end of discharge (in green), respectively.

In general, both diffraction peaks shift towards higher angle on charging to the 4.8 V cut-off, indicating a shrink of lattice parameter ***a*** for *Fm-3m* space group (cubic crystal system). This could be anticipated by the combined contribution from the continuous extraction of Li^+ (less cation in structure) during charging, oxidation of Mn (shortening of Mn-O bond) in region "S" and loss of O (less anion in structure) in region "P" and "T". Especially, the peak shift in region "S" is relatively more significant than the peak shift in both region "P" and "T". It indicates that for the $Li_{1.2}Mn_{0.4}Ti_{0.4}O_2$, the Mn-O bond shortening gives more influence on the lattice parameter ***a*** than the loss of O, considering that the O extraction from lattice is not dominant in region "P" and "T". In fact, as mentioned in section 6.4.4, the Mn^{3+} is anticipated to have Jahn-Teller distortion, leading a highly distorted MnO_6 octahedra. Once being oxidized to Mn^{4+}, the MnO_6 recovers from the distortion, which potentially bring substantial impact on the lattice parameter ***a***.

On discharge, both diffraction peaks shift back to lower angle but not the identical two theta angle as the pristine electrode, indicating a partial recovering of lattice parameter ***a***. This could be attributed to both the re-intercalation of Li^+ and the reduction of Mn^{4+} mainly to Mn^{3+} (lengthening Mn-O bond and introducing Jahn-Teller distortion). As not all the Li^+ can be re-intercalated and O vacancies are expected in lattice due to the O loss on charge, the diffraction peaks are not expected to be fully recovered. To be noticed, the peak broadening of both peak A and B is observed. However, based on the limited data resolution (in terms of the number of observable diffraction peaks and their corresponding intensity), it is not compelling to further interpret the sources of peak

broadening and further investigation is needed.

Nevertheless, based on the reversible shifts of peak A and B, it could indicate that for the cation disordered rock-salt $Li_{1.2}Mn_{0.4}Ti_{0.4}O_2$, the structure remains stable in *Fm-3m* space group during the 1st cycle. Such structure retention is also observed in the study of other Li-rich cation disordered rock-salt materials[297,301,303]. This is significantly different from layered Li-rich cathode materials, for which the dramatic structure rearrangement happens during the 1st cycle[154,155], and it then triggers problematic issues such as capacity fading and voltage decay[6,140,156,157] in subsequent cycles. The structure stability of the cation disordered rock-salt $Li_{1.2}Mn_{0.4}Ti_{0.4}O_2$ may illustrate a way to tackle the capacity fading and voltage decay problems for Li-rich cathode materials, and may even provide a stable structure frame for continuous oxygen redox in long-term cycling, which is the key to realize higher capacity Li-ion cathode materials.

6.5. Conclusion

The $Li_{1.2}Mn_{0.4}Ti_{0.4}O_2$ is obtained by solid-state synthesis under Argon atmosphere. Its chemical composition is in a good accordance with the proposed composition. The obtained material is confirmed in a pure phase cation disordered rock-salt structure by applying the Rietveld refinement using *Fm-3m* (#225) space group. The $Li_{1.2}Mn_{0.4}Ti_{0.4}O_2$ presents a very similar shape and layout on its 1st cycle electrochemistry behaviour to layered Li-rich materials, in which the extra capacity beyond the capacity of the Mn^{3+}/Mn^{4+} redox couple is observed for both charge and discharge process for more than 30 cycles, although capacity fading is severe and the

coulombic efficiency is not ideal.

A variety of characterization methodologies is employed for the in-depth investigation on the charge compensation mechanism(s) of $Li_{1.2}Mn_{0.4}Ti_{0.4}O_2$ in the 1st cycle. The Mn L edge SXAS confirms the Mn mainly exists in +3 oxidation state both in the core and on the surface of pristine $Li_{1.2}Mn_{0.4}Ti_{0.4}O_2$, whereas minor presence of Mn^{2+} (surface) and Mn^{4+} (core and surface) are also observed, which is possibly due to the disproportionation of Mn^{3+}. On charging in the normal capacity region, Mn is oxidized to +4 oxidation state while Li^+ is extracted from the lattice; in the extra capacity region, Mn remains in the +4 oxidation state without further oxidation, yet the distortion of MnO_6 octahedra occurs. Furthermore, CO_2, but no O_2, is observed in the extra capacity region by using operando DEMS. However, the gas evolution is not the dominant contributor for the extra capacity. By using SXAS and RIXS probing on O K edge, it is confirmed that localized electron-holes are formed on O (Oxidation of O), which should be the dominant contributor for the extra capacity. The Raman spectra show that there is no clue of the formation of true O_2^{2-} (O-O ~ 1.45 Å) during the O oxidation. On discharge to the 2 V cut-off, the capacity should be attributed to the reduction of both Mn and O. In addition, further reduction of surface Mn to +2 oxidation state cannot be excluded. Throughout the entire 1st cycle, the oxidation state of Ti stays unchanged at +4 oxidation state, but the TiO_6 octahedra distorts in the extra capacity region associate with the oxidation of O. All the changes on oxidation states and coordination environment of the *3d* transition metals have been confirmed by using SXAS and XANES to probe on the L edge and K edge of the corresponding transition metals,

respectively.

Further probing the O K edge of the material at the end of the 2nd charge and discharge revealed the reversible nature of oxygen redox in 2nd cycles. Moreover, the decrease of unoccupied states on O *2p* - Ti *3d* hybridization and almost unchanged unoccupied states on O *2p* - Mn *3d* hybridization may imply the electron-holes formation preferably happens on those O surrounded by Ti and Li, as the O^{2-} *2p* and Ti^{4+} *3d*/ Li *2s* hybridization tends to be relatively more ionic. This is also in a good accordance with the proposed oxygen redox mechanism in layered Li-rich cathode materials.

Moreover, the OPXRD patterns of $Li_{1.2}Mn_{0.4}Ti_{0.4}O_2$ in its first cycle shows that the rock-salt structure remains stable in the 1st cycle, which may suppress the capacity fading and voltage decay in the long-term cycling as shown in the case of layered Li-rich cathode materials. More importantly, the stable structure frame may even potentially promote the continuous oxygen redox in long-term cycling, which is the key to release the full capacity potential of Li-ion cathode materials.

To summarize, rather than the classic layered structure, the cation disordered rock-salt $Li_{1.2}Mn_{0.4}Ti_{0.4}O_2$ establishes a new structure possibility for the oxygen redox in *3d*-transition-metal based Li-rich cathode materials. Although at the moment its electrochemical performance has not yet been optimized, it still brings a new perspective for the study of oxygen redox in Li-rich cathode materials, as well as the general interests of solid-state chemistry. Further study of this material or this category of materials remains attractive and more investigations should be done to eventually

take advantages of the enormous extra capacity (oxygen redox) of Li-rich cathode materials.

CHAPTER 7 General Conclusions and Future Work

The main goal of this D.Phil. project is to investigate the underlying chemistry of layered Li-rich cathode materials and to further explore new Li-rich materials that are potential cathode candidates for future high capacity Li-ion batteries.

The thesis presents results showing the development of a reliable methodology to synthesize conventional Li-rich cathode materials. The electrode formulation for this material was then optimized for the state of the art electrochemical performance. Using this material, a fundamental study of the solid-state oxygen redox phenomenon in these materials was presented. Informed by the findings, the oxygen redox behaviour in the new rock salt $Li_{1.2}Mn_{0.4}Ti_{0.4}O_2$ was then studied.

In the following pages some general conclusions, which have come out of this work, will be presented with a discussion on what future work is required.

7.1. General Conclusions

Of the three preparative routes used (carbonate co-precipitation, oxalate co-precipitation, and R-F gel synthesis) to prepare $Li_{1.2}Ni_{0.13}Co_{0.13}Mn_{0.54}O_2$, the R-F gel synthesis was identified as resulting in the best electrochemical performance. When this material was combined with a variety of binders, it was found that the electrochemical behaviour would vary significantly, particularly in the case of PTFE and PVDF. The study on the corresponding effects of both binders shows that (1) the PTFE binder electrode outperforms the conventional PVDF binder from all electrochemical aspects;

and (2) the CMC-Na binder has the effect to suppress the voltage fading of Li-rich materials. The work clearly suggests that choosing an appropriate binder is critical for these Li-rich cathodes to obtain optimized electrochemical performance. For all future work presented in the thesis, it was determined that a PTFE binder was the most reliable for future work. Using this preparation and electrode formulation, a careful study of the $Li_{1.2}Ni_{0.13}Co_{0.13}Mn_{0.54}O_2$ charge compensation mechanism was then performed. This suggested that the charge compensation could be accounted through a combination of oxidation of the transition metal ions (Ni and Co), oxygen ion oxidation and oxygen evolution from the lattice. The oxygen loss is initially in the form of CO_2 loss and occurs from the beginning of the plateau region and direct O_2 gas evolution is only observed at the end of charge. However, the dominant source for extra capacity is not the oxygen loss but the formation of localized electron-holes on those oxygen surrounded by Mn^{4+} and Li^+. This work indicates that the critical point for reversible oxygen redox is to find a good balance between the ionicity and covalency of the TM-O interaction, which determines the boundary between the oxygen loss and the oxygen redox. Bearing this in mind, the further exploration of new structures and compositions would be significant to release the full potential of the oxygen redox in Li-rich cathode materials, so that both transition metal redox and oxygen redox could be activated and reversible to achieve much higher capacity than the currently available cathode materials.

The cation disordered rock-salt $Li_{1.2}Mn_{0.4}Ti_{0.4}O_2$, which was obtained by solid-state synthesis, exhibits a very similar shape and layout on its 1st cycle electrochemical behaviour to layered Li-rich cathode materials. A detailed study of this material

indicates its enormous capacity is attributed to the redox activity of Mn and oxygen, while Ti remains electrochemically inactive. The oxygen redox process in this cation disordered rock-salt structure is achieved by reversibly forming localized electron-holes on oxygen, which is more likely to be those surrounded by Ti and Li. This is in a good accordance with the proposed mechanism of layered Li-rich cathode materials. Additionally, the rock-salt structure of $Li_{1.2}Mn_{0.4}Ti_{0.4}O_2$ was found to be stable in the 1st cycle and would potentially promote a continuous O redox in long-term cycling. This work brings new structure and composition possibilities for the oxygen redox in *3d*-transition-metal based Li-rich cathode materials, which is significant for the understanding of solid-state oxygen redox phenomenon in these materials.

7.2. Future Work

An industrial perspective suggests that the R-F gel synthesis is still not the best option, as (1) the synthesis process involves organic compounds which increases the cost; (2) the obtained layered Li-rich cathode materials have a relatively low tap density, which reduces the mass loading of the electrode. Therefore, optimizing the existing synthesis methods like co-precipitation and exploring new synthesis methods would be essential for further development of layered Li-rich cathode materials.

Finding appropriate binders and the corresponding processing methods for these Li-rich cathode materials is another direction worthy to explore, as it significantly influences the electrode performance. Meanwhile, the investigation on the water-soluble binder based electrode system is interesting to conduct, as it matches with the

goal towards the cost-efficient and eco-friendly large-scale manufacture of Li-ion batteries. It is also exciting to realize that intensive research work is demanded in the fundamental understanding of binder effects, as little research has been done so far.

Finally, although significant progress has been made in understanding the solid-state oxygen redox phenomenon in Li-rich cathode materials, many questions remain to be understood. For example, it would be interesting to investigate if the capacity and voltage fading correspond to structural evolution over long-term cycling. Ultimately, it would be extremely inspiring to solve the key structural and compositional requirements for achieving a continuously reversible oxygen redox, so that it can be used to guide the exploration of high capacity cathode materials for the future Li-ion batteries. Additionally, most of the advanced characterization methodologies, such as SXAS, RIXS, XANES, are still performed in an ex-situ way. Developing in-situ or even operando characterization methodologies would be crucial for a better understanding of the mechanisms of chemical and electrochemical processes happening in Li-ion batteries.

APPENDIX

Appx. 1. Unit Cell Parameters and d-Spacing of Crystal Systems

Table Appx.1-1 Crystal systems and corresponding parameters and d-spacing

Crystal System	Axial's Length and Angles	d-spacing (d_{hkl})
Triclinic	$a \neq b \neq c$ $\alpha \neq \beta \neq \gamma \neq 90°$	$\frac{1}{d^2} = \left[\begin{array}{l} \frac{h^2}{a^2 \sin^2 \alpha} + \frac{2kl}{bc}(\cos\beta\cos\gamma - \cos\alpha) \\ + \frac{k^2}{b^2 \sin^2 \beta} + \frac{2hl}{ac}(\cos\alpha\cos\gamma - \cos\beta) \\ + \frac{l^2}{c^2 \sin^2 \gamma} + \frac{2hk}{ab}(\cos\alpha\cos\beta - \cos\gamma) \end{array} \right] (1 - \cos^2\alpha - \cos^2\beta - \cos^2\gamma + 2\cos\alpha\cos\beta\cos\gamma)$
Monoclinic	$a = b \neq c$ $\alpha = \gamma = 90°,\ \beta \neq 90°$	$\frac{1}{d^2} = \frac{h^2}{a^2 \sin^2\beta} + \frac{k^2}{b^2} + \frac{l^2}{c^2 \sin^2\beta} + \frac{2hl\cos\beta}{ac\sin^2\beta}$
Orthorhombic	$a \neq b \neq c$ $\alpha = \beta = \gamma = 90°$	$\frac{1}{d^2} = \frac{h^2}{a^2} + \frac{k^2}{b^2} + \frac{l^2}{c^2}$
Rhombohedral	$a = b = c$ $\alpha = \beta = \gamma \neq 90°$	$\frac{1}{d^2} = \frac{1}{a^2} \frac{(h^2 + k^2 + l^2)\sin^2\alpha + 2(hk + kl + lh)(\cos^2\alpha - \cos\alpha)}{1 + 2\cos^3\alpha - 3\cos^2\alpha}$
Hexagonal	$a = b \neq c$ $\alpha = \beta = 90°,\ \gamma = 120°$	$\frac{1}{d^2} = \frac{4}{3}\frac{h^2 + hk + k^2}{a^2} + \frac{l^2}{c^2}$
Tetragonal	$a = b \neq c$ $\alpha = \beta = \gamma = 90°$	$\frac{1}{d^2} = \frac{h^2 + k^2}{a^2} + \frac{l^2}{c^2}$
Cubic	$a = b = c$ $\alpha = \beta = \gamma = 90°$	$\frac{1}{d^2} = \frac{h^2 + k^2 + l^2}{a^2}$

Appx. 2. Synthesis of ^{18}O-labelled $Li_{1.2}Ni_{0.13}Co_{0.13}Mn_{0.54}O_2$

The synthesis of ^{18}O-labelled $Li_{1.2}Ni_{0.13}^{II}Co_{0.13}^{III}Mn_{0.54}^{IV}O_2$ started with the R-F gel synthesized $Li_{1.2}Ni_{0.13}^{II}Co_{0.13}^{III}Mn_{0.54}^{IV}O_2$. The as-prepared material was heated in powder form in an ^{18}O containing atmosphere (a mixture of 22 vol% $^{18}O_2$ (>95% atom%, 99.9%) and 78 vol% N_2 (99.999%), BOC, U.K.) at 800 °C for 8 hours. Such atmosphere simulates the ambient atmosphere for the normal preparation of this material, providing the closest oxidation condition to ensure the targeted material is formed.

Negative ion Time of Flight Secondary Ion Mass Spectrometry (ToF-SIMS) was employed to identify the amount of ^{18}O in the labelled sample. It was measured by an ION-ToF GmbH instrument using 25 kV Bi_3^+ primary ion source. The data was collected from a relatively large area (50 μm * 50 μm) by a stage scanning function, which was capable of 20 shots per pixel at a resolution of 256 pixels/mm. The ToF-SIMS confirms that the ration of ^{18}O and ^{16}O at or near the surface of the ^{18}O-labelled $Li_{1.2}Ni_{0.13}^{2+}Co_{0.13}^{3+}Mn_{0.54}^{4+}O_2$ sample is $^{18}O/^{16}O$ = 15%/85%.

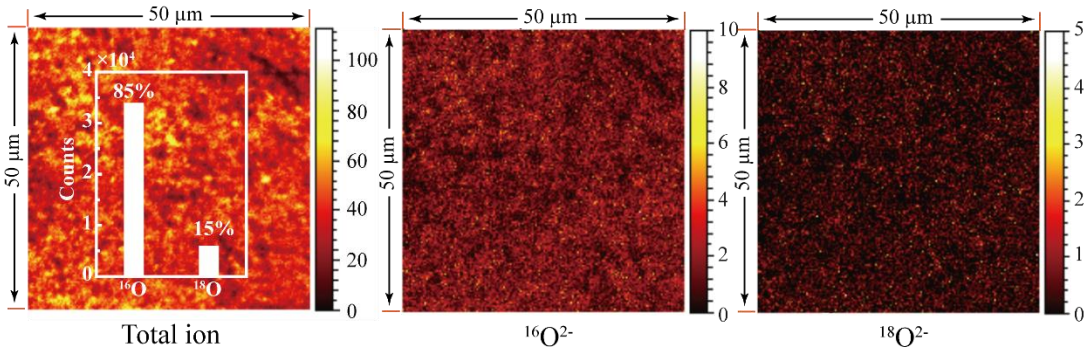

Figure Appx.2-1 ToF-SIMS images of the as-prepared ^{18}O-labelled $Li_{1.2}Ni_{0.13}^{2+}Co_{0.13}^{3+}Mn_{0.54}^{4+}O_2$ material.

Appx. 3. Possibility on the Formation of ^{18}O-labelled O_2 and CO_2

As the $^{18}O/^{16}O$ = 15%/85% at or near the surface of the ^{18}O-labelled $Li_{1.2}Ni_{0.13}^{2+}Co_{0.13}^{3+}Mn_{0.54}^{4+}O_2$, the presence possibility of ^{18}O and ^{16}O are 0.15 and 0.18, respectively.

Then, the formation possibility of $^{16/16}O_2$, $^{18/16}O_2$, $^{18/16}O_2$ can be calculated as:

$$p_{^{16/16}O_2} = p_{^{16}O} \times p_{^{16}O} = 0.85 \times 0.85 = 0.7225$$
$$p_{^{18/16}O_2} = A_2^1 \times p_{^{18}O} \times p_{^{16}O} = 2 \times 0.15 \times 0.85 = 0.255$$
$$p_{^{18/18}O_2} = p_{^{18}O} \times p_{^{18}O} = 0.15 \times 0.15 = 0.0225$$

The presence of ^{18}O in CO_2 should rise from the decomposition of electrolyte solvent under the attack of oxygen species extracted from the lattice. The assumption is made that the oxygen is in a reduced state, possibly as O_2^-. Our group has proposed a mechanism for the decomposition of PC under the presence of O_2^- in the Li-O_2 battery research[279], according to which the decomposition undergoes a series of chain reaction but does not involve O_2 release. Eventually, the intermediate products decompose to form CO_2 and H_2O at high voltage (> 4 V). Therefore, a simplified decomposition equation is proposed as:

$$CH_3C_2H_3O_2CO + 4O_2^- \rightarrow 4CO_2 + 3H_2O + 4e^-$$

According this equation, 11 O atoms presences in the reactants, among which 8 O atoms are extracted from the lattice with the $^{18}O/^{16}O$ = 15%/85%. Therefore, the presence possibility of ^{18}O and ^{16}O in the reactant can be calculated as:

$$p_{^{16}O} = \frac{4 \times 2 \times p_{^{16}O} + 3}{4 \times 2 + 3} = 0.890909$$
$$p_{^{18}O} = 1 - p_{^{16}O} = 0.109091$$

Then, the formation possibility of $C^{16/16}O_2$, $C^{18/16}O_2$, $C^{18/16}O_2$ can be calculated as:

$$p_{C^{16/16}O_2} = p_{^{16}O} \times p_{^{16}O} = 0.890909 \times 0.890909 = 0.793719 \approx 0.7937$$
$$p_{C^{18/16}O_2} = A_2^1 \times p_{^{18}O} \times p_{^{16}O} = 2 \times 0.109091 \times 0.890909 = 0.19438 \approx 0.1944$$
$$p_{C^{18/18}O_2} = p_{^{18}O} \times p_{^{18}O} = 0.109091 \times 0.109091 = 0.011901 \approx 0.0119$$

Appx. 4. Operando DEMS using ^{18}O-labelled $LiNi^{II}_{0.5}Mn^{IV}_{1.5}O_4$

The synthesis of $LiNi^{II}_{0.5}Mn^{IV}_{1.5}O_4$ followed the R-F gel methodology as mentioned in 3.3.3, but the dwell temperature was 750°C to form disordered spinel phase. The preparation of ^{18}O-labelled $LiNi^{II}_{0.5}Mn^{IV}_{1.5}O_4$ used the same methodology as mentioned in section Appx. 2 but heated at 750°C. The Operando DEMS experiment used the same calibration and configuration as mentioned in section 5.3.2.

The $LiNi^{II}_{0.5}Mn^{IV}_{1.5}O_4$ spinel material is not expected to have O extracted from lattice, as the charge compensation is achieved by the transition metal redox ($Ni^{2+}\rightarrow Ni^{3+}\rightarrow Ni^{4+}$) when charged to 5 V cut-off. Indeed, on the Operando DEMS, O_2 evolution is not observed for the entire charging process. Besides, only a small amount (less than 10% compared with the case for ^{18}O-labelled $Li_{1.2}Ni_{0.13}^{II}Co_{0.13}^{III}Mn_{0.54}^{IV}O_2$) of CO_2 evolution is observed starting from 4.75 V, in which the presence of $C^{18/16}O_2$ and $C^{18/18}O_2$ is not observed. Such results imply that the CO_2 originated from the direct self-decomposition of PC electrolyte in the region "P" and "T" of the ^{18}O-labelled $Li_{1.2}Ni_{0.13}^{II}Co_{0.13}^{III}Mn_{0.54}^{IV}O_2$ case is negligible. Therefore, the CO_2 evolution observed on the Operando DEMS of ^{18}O-labelled $Li_{1.2}Ni_{0.13}^{II}Co_{0.13}^{III}Mn_{0.54}^{IV}O_2$ is attributed to the decomposition of PC under the attack of oxygen species.

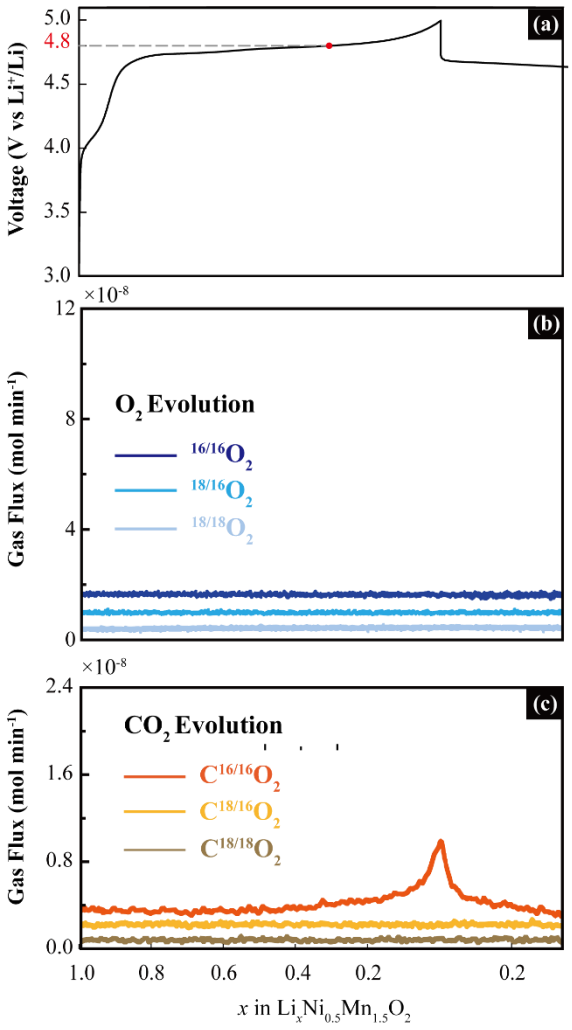

Figure Appx.4-1 Operando DEMS of ^{18}O-labelled $LiNi^{II}_{0.5}Mn^{IV}_{1.5}O_2$ cathode in the 1st cycle. (a) Electrochemical curve of the operando DEMS cell; (b) O_2 and (c) CO_2 evolution are plotted as a function of the state of charge. For clarity purpose, the plots of O_2 and CO_2 evolution are plotted separately along y-axis. Reproduced by permission from Macmillan Publishers Ltd: Nature Chemistry 8: 684-691, copyright 2016.

Appx. 5. Calculations Relevant to Transitions of the O K edge SXAS Spectra

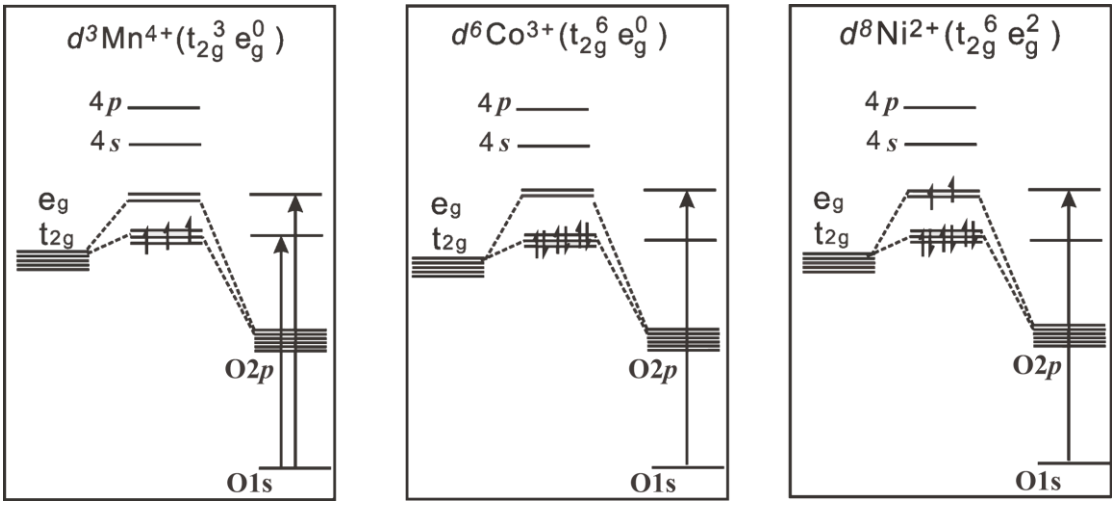

Figure Appx.5-1 Schematic of the electron transition from the O *1s* to the unoccupied hybridized states with each of the transition metal elements in $Li_{1.2}Ni_{0.13}^{II}Co_{0.13}^{III}Mn_{0.54}^{IV}O_2$. The energy difference between the spin-up and spin-down states is not differentiated as the schematic only shows energies for one electron. Reproduced by permission from Macmillan Publishers Ltd: Nature Chemistry 8: 684-691, copyright 2016.

In $Li_{1.2}Ni^{II}_{0.13}Co^{III}_{0.13}Mn^{IV}_{0.54}O_2$, Mn is at +4 oxidation state and there are 7 unoccupied states for it (3 spin-down t_{2g}, 2 spin-up e_g and 2 spin-down e_g). Accounting that there is 0.54 Mn per formula unit, the total unoccupied states is estimated to be 3.78. Similarly, it is 0.52 and 0.26 unoccupied states for Co^{III} and Ni^{II}, respectively (Figure Appx.5-1). Thus, Mn^{IV} accounts for majority (82.9%) of the expected SXAS transitions to the unoccupied states. It, therefore, dominants the SXAS spectra. Furthermore, it is confirmed by the comparison between O K edge SXAS spectra of pristine $Li_{1.2}Ni^{II}_{0.13}Co^{III}_{0.13}Mn^{IV}_{0.54}O_2$ (Figure 5-4(b)-a) and MnO_2 (Figure 5-4(b)-dash line), which is subtracted from the literature[284,319]. The spectra appear to be almost identical, in which the peak sets in the lower energy region ($\lesssim$ 535 eV) of two spectra share the same energies with same intensity ratio. The peak sets are attributed to the spin-down

t_{2g} and spin-up e_g transition, while the higher energy region ($\gtrsim$ 535 eV) is attributed to the spin-down e_g transition[284,320].

In the region "S" on charging of $Li_{1.2}Ni^{II}_{0.13}Co^{III}_{0.13}Mn^{IV}_{0.54}O_2$, the Ni^{2+} and Co^{3+} are oxidized to Ni^{4+} and Co^{4+}, respectively. In such case, two electrons are extracted from Ni^{2+} e_g and one from Co^{3+} t_{2g}. Accounting the chemical content of Ni and Co, it corresponds to in total 0.39 unoccupied states created by the end of the region "S" (Table Appx.5-1). Therefore, the estimated increase of O K edge SXAS transition at the end of the region "S" should be 0.39/4.56≈8.5%, with respect to the transition of the pristine $Li_{1.2}Ni^{II}_{0.13}Co^{III}_{0.13}Mn^{IV}_{0.54}O_2$.

Table Appx.5-1 Unoccupied states in transition metals in the pristine $Li_{1.2}Ni^{II}_{0.13}Co^{III}_{0.13}Mn^{IV}_{0.54}O_2$and in the charged material at the end of region "S"

Transition Metal	Electron Configuration at *d* Orbital	Unoccupied States	Chemical composition per Formula Unit	Total Unoccupied States	Unoccupied States Created[x]
Mn^{IV}	$d^3(t_{2g}^3e_g^0)$	3 spin-down t_{2g} 2 spin-up e_g 2 spin-down e_g	0.54	3.78	0
Co^{III}	$d^6(t_{2g}^6e_g^0)$	2 spin-up e_g 2 spin-down e_g	0.13	0.52	0.13
Ni^{II}	$d^8(t_{2g}^6e_g^2)$	2 spin-down e_g	0.13	0.26	0.26
			Total	4.56	0.39

[x] It refers to the unoccupied states created when charging the material to the end of Region "S", where Ni^{2+} and Co^{3+} have been oxidized to Ni^{4+} and Co^{4+}, respectively.

Appx. 6. PXRD of the Ball-milled $Li_{1.2}Mn_{0.4}Ti_{0.4}O_2$

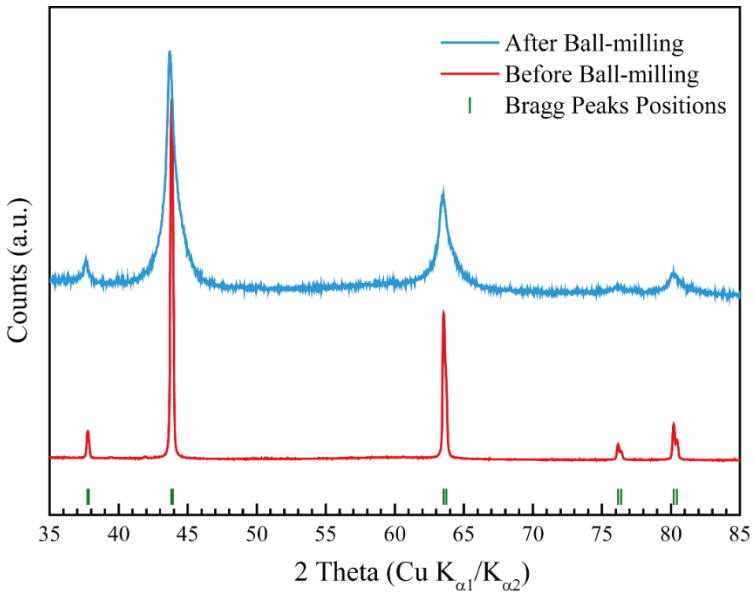

Figure Appx.6-1 PXRD pattern comparison of $Li_{1.2}Mn_{0.4}Ti_{0.4}O_2$ before (in red) and after ball-milling (in blue). The allowed Bragg Peaks Positions are marked in green.

As the particle morphology of the solid-state synthesized $Li_{1.2}Mn_{0.4}Ti_{0.4}O_2$ is not ideal, the as-prepared material is ball-milled to homogenize the particle morphology, so that a stable and reasonable electrochemistry behaviour could be observed, which is essential for the later reaction mechanism study.

As presented in Figure Appx.6-1, the diffraction peaks of the material remain at the same positions before and after ball-milling, as allowed Bragg peaks positions in the *Fm-3m* space group. No presence of new peaks nor absence of existed peaks is observed. This indicates the crystallographic structure of the material maintain unchanged before and after ball-milling. However, a significant peak broadening is observed for the PXRD pattern of the material after ball-milling, which is anticipated by the reduction of particle size. This is also confirmed by the SEM image as presented in Figure 6-1.

Appx. 7. Mn and Ti K edge XANES Spectroscopy of $Li_{1.2}Mn_{0.4}Ti_{0.4}O_2$ at Different State of Charge

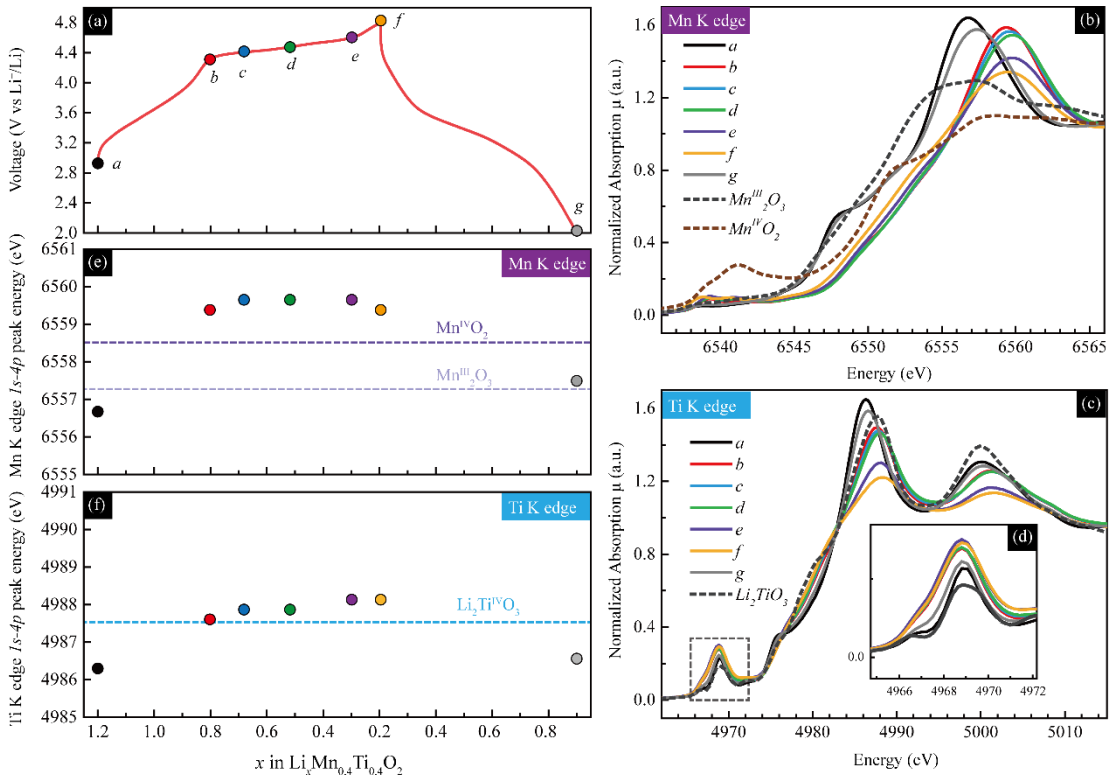

Figure Appx.7-1 (b) Mn and (c) Ti K edge XANES spectra on different state of charge during the 1st cycle; (d) for the purpose of clarity, the pre-edge of Ti K edge XANES is enlarged; (e) Mn and (f) Ti K edge *1s-4p* peak energy is plotted against different state of charge in the 1st cycle. (a) The corresponding state of charge of the measured samples is projected on the electrochemical profile, in which the voltage is plotted versus the lithium content of the cathode material.

The investigation using XANES spectroscopy of Mn and Ti reveals the identical information as the other spectroscopy methodologies.

The main edge shifts towards higher energy on the Mn K edge XANES (Figure Appx.7-1(b)) is in good agreement with the oxidation of Mn to +4 oxidation state. Further charge in the region "P" & "T" brings no change on the main edge, indicating no further oxidation of Mn as is also well-demonstrated by the Mn L edge SXAS (Figure 6-5). When discharged to a 2 V cut-off, the main edge then shifts back to lower

energy and overlap with the spectrum *a* of the pristine material, in accordance with the reduction of Mn to dominantly +3 oxidation state. For the Ti K edge XANES (Figure Appx.7-1(e) & (f)), the pre-edge (Figure Appx.7-1(d)), which corresponds to the Ti *1s-3d* electron transition[213], remains identical peak position throughout the 1st cycle, indicating a stable +4 oxidation state of Ti.

Additionally, by extracting the Mn and Ti K edge *1s-4p* adsorption peak energy and plotting it against the different state of charge (Figure Appx.7-1(c)), both plots show almost no shifts (< 0.3 eV for both) throughout region "P" & "T". This also demonstrates that both the Mn and Ti remain at +4 oxidation state and are not further oxidized.

However, the change on the *1s-4p* adsorption peak intensity is observed for both Mn and Ti K edge spectra and there is even slight change in shape of the Ti K main edge. These changes could be attributed to the geometry distortion of MnO_6 and TiO_6 octahedra[293,297], rather than the change of transition metal oxidation states.

LIST OF PUBLICATIONS

1. Luo K, Roberts MR, **Hao R**. *et al*. *Nano Lett* **16** (12), 7503-7508 (2016)
2. Luo, K.; Roberts, M.; Guerrini, N.; Tapia-Ruiz, N.; **Hao, R.** *et al*. *J Am Chem Soc.* **138** (35), 11211–11218 (2016)
3. Kun Luo, Matthew R.Roberts, **Rong Hao**, *et al. Nature Chemistry* **8**, 684–691 (2016)

ABBREVIATION

Back-Scattered Electrons	……	BSE
Carboxymethyl Cellulose	……	CMC-Na
Diethyl carbonate	……	DEC
Differential Electrochemical Mass Spectrometry	……	DEMS
Dimethyl Carbonate	……	DMC
Electric Vehicle	……	EV
Electron Yield	……	EY
Energy Dispersive X-Ray	……	EDX
Ethylene Carbonate	……	EC
Fluorescence Yield	……	FY
Fourier Transform	……	FT
Inductively Coupled Plasma Optical Emission Spectrometry	……	ICP-OES
Infrared	……	IR
inverse Partial Fluorescence Yield	……	iPFY
$LiFePO_4$	……	LFP
$LiNi_{0.80}Co_{0.15}Al_{0.05}O2$	……	NCA
$LiNi_xCo_yMn_zO_2$	……	NCM
$LiNi_xCo_yMn_zO_2$ (x+y+z=1)	……	NCM
Lithium Ion	……	Li-ion
Lithium Rich	……	Li-rich
Lithium titanium (IV) oxide ($Li_4Ti_5O_{12}$)	……	LTO
Near-Infrared	……	NIR
N-Methyl-2-pyrrolidone	……	NMP
Nuclear Magnetic Resonance	……	NMR
Partial Fluorescence Yield	……	PFY
Polytetrafluoroethylene	……	PTFE
Polyvinylidene Fluoride	……	PVDF
Powder X-Ray Diffraction	……	PXRD
Powder X-Ray Diffraction	……	PXRD
Propylene Carbonate	……	PC
Resonant Inelastic X-Ray Scattering	……	RIXS
Resorcinol – Formaldehyde	……	R-F
Scanning Electron Microscope	……	SEM
Secondary Electrons	……	SE
Soft X-ray Absorption Spectroscopy	……	SXAS
Tetrahydrofuran	……	THF
Time-of-Flight Secondary Ion Mass Spectrometry	……	TOF-SIMS
Total Electron Yield	……	TEY

Total Fluorescence Yield	……	TFY
Ultraviolet	……	UV
X-ray Absorption Near Edge Structure	……	XANES
X-ray Diffraction	……	XRD

LIST OF FIGURES

Figure 1-1 Schematic of a layered $LiCoO_2$ in *R-3m* space group (#166). The Li, Co, and O atoms are represented in blue, orange, and red spheres, respectively. The LiO_6 and CoO_6 octahedra are coloured in light grey and light orange, respectively. 5

Figure 1-2 Schematic of a Li-ion battery with $LiCoO_2$ as the cathode active material and graphite as the anode active material 7

Figure 1-3 Schematic of a spinel $Li_4Ti_5O_{12}$ in Fd-3m space group (#227), in which 1/6 of octahedral sites (16d site) are occupied by Li. The Li, Ti, and O atoms are represented in blue, dark grey, and red spheres, respectively. The TiO_6/LiO_6 octahedra are coloured in light grey.....11

Figure 1-4 structures of different solvents 16

Figure 1-5 Schematic of a layered $LiNi_{0.33}Co_{0.33}Mn_{0.33}O_2$ in *R-3m* space group (#166), in which transition metal (TM) ions are occupying the same crystallographic site (*3b* site). The Li, Ni, Co, Mn and O atoms are coloured in blue, green, orange, purple and red, respectively. The LiO_6 and TMO_6 octahedra are coloured in light blue and light orange, respectively. 22

Figure 1-6 Schematic of a spinel $LiMn_2O_4$ in Fd-3m space group (#227). The Li, Mn, and O atoms are represented in blue, purple, and red spheres, respectively. The MnO_6 octahedra are coloured in light purple 23

Figure 1-7 Schematic of an olivine $LiFePO_4$ in Pnma space group (#62). The Li, Fe, P, and O atoms are represented in blue, green, dark purple and red spheres, respectively. The LiO_6 and FeO_6 octahedra, and PO_4 tetrahedra are coloured in light blue, light green and light brown. 24

Figure 1-8 Schematic of (a) a monoclinic $Li_2M'O_3$ structure in *C2/m* space group (#12), and (b) a rhombohedaral $LiMO_2$ (M= Ni, Co, Fe, Mn, Fe, Cr *etc.*) in *R-3m* space group (#166). Both are viewed from [100] direction. The Li, M', M, and O atoms are represented in blue, purple, orange, and red spheres, respectively. The $M'O_6$ and MO_6 octahedra are coloured in light purple and light orange. 29

Figure 1-9 Issues of layered Li-rich transition metal oxides, taking $Li_{1.2}Ni_{0.13}Co_{0.13}Mn_{0.54}O_2$ as an archetypal example. (a) 1st cycle load curve showing its large irreversible capacity and low couloumbic efficiency, and (b) multiple cycle discharge curves in the 1st, 10th, 20th, 30th, and 40th cycle, showing the voltage and capacity fading. 32

Figure 2-1 Schematic of (a) SEM; (b) the interaction between the Incident electron beam and specimen 38

Figure 2-2 Schematic of the generation of (a) characteristic x-ray and (b) continuum x-ray from specimen atoms after hit by incident electron beam 39

Figure 2-3 Schematic of the deduction of the Bragg Equation, reproduced from Ref.[194] 42

Figure 2-4 (a) The intersection of d^*_{hkl} vectors of the powder sample with the Ewald sphere to illustrate the generation of discrete powder diffraction peaks; (b) Schematic of the Bragg-Brentano geometry. Reproduced from Ref.[196]. 43

Figure 2-5 Schematic of the coin cell parts 48

Figure 2-6 Schematic of (a) an in-house designed electrochemical cell for DEMS; (b) Quadrupole mass spectrometer 50

Figure 2-7 (a) Schematic of an X-ray absorption beamline in the traditional mode (with transmission and fluorescence detectors), reproduced from Ref.[210]; (b) A typical Ti K edge XANES spectroscopy at +4 valence state and 6-coordination environment. 54

Figure 2-8 (a) Examples of the SXAS spectrum: O^{2-} K edge (top) and Ti^{4+} L-edge, both at O_h symmetry; (b) Schematic of the detection of SXAS experimental signals. 55

Figure 2-9 Schematic of (a) direct RIXS process and (b) indirect RIXS process. The momentum and energy differences between the initial (photon-in) and final (photon-out) states are $\hbar k - \hbar k'$ and $\hbar w_k - \hbar w_{k'}$,respectively. 57

Figure 3-1 Schematic of preparing transition metal precursor by the carbonate co-precipitation..... 60

Figure 3-2 Schematic of preparing lithium transition metal precursor by the oxalate co-precipitation . 61

Figure 3-3 Schematic of preparing transition lithium metal precursor by the R-F gel synthesis 62

Figure 3-4 SEM images of the (a) carbonate co-precipitaiton, (b) oxalate co-precipitation, and (c) R-F gel synthesized mateirals. (a) & (c) were taken on a Carl Zeiss Merlin SEM and (b) was taken on a JSM 6700F FEG-SEM at 5 kV, 10 μA. 66

Figure 3-5 PXRD patterns of $Li_{1.2}Ni_{0.13}Co_{0.13}Mn_{0.54}O_2$ synthesized in three different methods, fitted using *R-3m* space group (#166). The "+" marks the observed data. The red and blue line represents the calculated diffraction profile and the difference between the observed and calculated profiles, respectively. The green ticks mark the allowed Bragg peaks. The dashed square indicates the superstructure peaks of *C2/m* space group (#12). To be noticed, the PXRD pattern of the oxalate co-precipitation sample was collected by using a Fe X-ray source. 68

Figure 3-6 a typical load curve of $Li_{1.2}Ni_{0.13}Co_{0.13}Mn_{0.54}O_2$ when charged at 50 mA g^{-1} (C/5), at room temperature. The region corresponding to the conventional transition metal oxidation during charge is marked in dark blue..... 71

Figure 3-7 (a) the load curve, specific (b) charge and (c) discharge capacities versus cycle number plots and (d) discharge rate performance of $Li_{1.2}Ni_{0.13}Co_{0.13}Mn_{0.54}O_2$ synthesized by carbonate co-precipitation (in black), oxalate co-precipitation (in red) and R-F gel (in blue) methodologies. 74

Figure 3-8 (a) Columbic efficiency versus cycle number plots of $Li_{1.2}Ni_{0.13}Co_{0.13}Mn_{0.54}O_2$ synthesized by carbonate co-precipitation (in black square), oxalate co-precipitation (in red dot) and R-F gel (in blue

triangle) methodologies; (b) the initial 10 cycles (light gray region); (c) the subsequent 90 cycles (light blue region) 76

Figure 3-9 Normalized capacity discharge curves of $Li_{1.2}Ni_{0.13}Co_{0.13}Mn_{0.54}O_2$ synthesized by (a) carbonate co-precipitation, (b) oxalate co-precipitation and (c) R-F gel methodologies. Only the data of 1st cycle, 10th cycle, 30th cycle, 50th cycle and 100th cycle are reported. The discharge capacity retention of these materials is shown in the Figure 3-7(c). The specific discharge capacities were normalized to the maximum discharge capacity of their corresponding cycles. This normalization method is as identical as reported[156]. 78

Figure 3-10 Capacity/voltage derivative versus voltage curves (dQ/dV versus V) from 1st (in black) to 100th (in red) cycle of the $Li_{1.2}Ni_{0.13}Co_{0.13}Mn_{0.54}O_2$ synthesized by (a) carbonate co-precipitation, (b) oxalate co-precipitation and (c) R-F gel methodologies. Only the data of 1st cycle, 10th cycle, 30th cycle, 50th cycle and 100th cycle are reported. 80

Figure 4-1 The electrochemical behaviour comparison of the PVDF and PTFE binder electrodes at the cycling rate of 50 mA g^{-1} at 30 °C. (a) 1st cycle load curve; (b) charge (up-triangle) and discharge (down-triangle) capacity over 100 cycles; (c) coulombic efficiency over 100 cycles; (d) specific discharge energy (in square and circle) and average discharge voltage (in up-/down-triangles) over 100 cycles. Additionally, the 1st cycle irreversible capacities of both binder electrodes have been annotated. 88

Figure 4-2 Cross section SEM view of the electrodes with PVDF (a) and PTFE (b) binder, respectively. Both images were generated from the secondary electron signals. 90

Figure 4-3 Cross section SEM images and the EDX element labelled views of the PVDF (the left column) and PTFE (the right column) binder electrodes: (a) & (e) SEM images generated from the secondary electron signals, and the EDX element labelled views on (b) & (f) Manganese, (c) & (g) carbon, and (d) & (h) fluorine. 91

Figure 4-4 SEM fine-view comparison on the PVDF (left column) and PTFE electrodes (right column). (a) & (b) cross-section view on pristine electrodes; (c) & (d) cross-section views and (e) & (f) top-views on electrodes after 100 cycles. These images were generated from the secondary electron signals. 94

Figure 4-5 Structure of PVDF and PTFE 96

Figure 4-6 the electrochemical behaviour comparison of electrodes using the PTFE and CMC-Na binder, respectively. (a) 1st cycle load curve; (b) charge (up-triangle) and discharge (down-triangle) capacity over 100 cycles; (c) coulombic efficiency over 100 cycles; (d) specific discharge energy (in square and circle) and average discharge voltage (in up-/down-triangles) over 100 cycles. 98

Figure 4-7 (a) - (d) Normalized and original specific discharge curves of electrodes with PTFE and CMC-Na binder, respectively; (e) & (f) capacity/voltage derivative versus voltage curves (dQ/dV versus V) from 1st (in black) to 100th (in red) cycle of electrodes with PTFE and CMC-Na binder, respectively. Only the data of 1st cycle, 10th cycle, 30th cycle, 50th cycle and 100th cycle are reported. The specific

discharge capacities were normalized to the maximum discharge capacity of their corresponding cycles, following the reported method[156]. 99

Figure 5-1 A typical 1st cycle load curve of the $Li_{1.2}Ni_{0.13}Co_{0.13}Mn_{0.54}O_2$. For the convenience of discussion in this chapter, the regions are labelled as "S" (Sloppy, in blue), "P" (Plateau-like, in orange) and "T" (Tail-like, in Red), respectively. 107

Figure 5-2 Operando DEMS of ^{18}O-labelled $Li_{1.2}Ni_{0.13}Co_{0.13}Mn_{0.54}O_2$ cathode in the 1st cycle. (a) electrochemical curve of the operando DEMS cell; (b) O_2 and (c) CO_2 evolution plot as a function of the state of charge. For clarity purpose, the plots of O_2 and CO_2 evolution are plotted separately along y-axis. 109

Figure 5-3 Transition metal ((b) Ni, (c) Co, (d) Mn) K edge XANES spectra on different state of charge during the 1st cycle. (a) The corresponding state of charge of the measured samples is projected on the electrochemical profile, in which the voltage is plotted versus the lithium content of the cathode material. 113

Figure 5-4 Oxygen K edge SXAS spectra at different state of charge in the 1st cycle. A spectrum of MnO_2 (reproduced from Ref.[284]) is taken as the reference. The vibration of integrated intensity in the low-energy region (shown in (b)) of the SXAS spectra is plotted versus the state of charge in (c). 114

Figure 5-5 (b) Raman spectra at (a) different state of charge. The spectra of three reference samples (in grey), Li_2O_2, Na_2O_2, ZnO_2 (Alfa Aesar, approximately 50% ZnO_2 in ZnO), refine the region of O-O vibrations. 117

Figure 5-6 (b) Oxygen K edge RIXS spectra with excitation energy of 531.8 eV at (a) different state of charge. 118

Figure 5-7 Transition metal ((b) Ni, (c) Co, (d) Mn) K edge *1s-4p* peak energy plots against different state of charge in the 1st cycle. (a) The corresponding state of charge of the measured samples is projected on the electrochemical profile, in which the voltage is plotted versus the lithium content of the cathode material. 120

Figure 5-8 Schematic of the model for the formation of electron-hole states on oxygen. (a) oxygen coordination environment in $Li_{1.2}Ni_{0.13}Co_{0.13}Mn_{0.54}O_2$; (b) honeycomb-type cation ordering in the transition metal layer, view from ***c*** axis. The oxygen sites at which localized holes can form shown in red spheres; (c) schematic to show the position of the O^-/O^{2-} redox couple 122

Figure 6-1 SEM images of (a) the as-prepared material and (b) the material after ball-milling 130

Figure 6-2 The refined PXRD pattern (in *Fm-3m* space group) of the solid-state synthesized $Li_{1.2}Mn_{0.4}Ti_{0.4}O_2$. The "+" marks the observed data. The red and blue line represent the calculated diffraction profile and the difference between the observed and calculated profiles, respectively. The green ticks mark the allowed Bragg peaks. The schematic of the refined structure is also presented in a polyhedral view. The transition metal sphere consists of three colours (blue-Li, orange-Ti, and purple-

Mn), in which the ratio of coloured area corresponds to the occupancies of transition metal ions at the crystallographic site *4a*. 131

Figure 6-3 (a) A typical 1st cycle load curve of the $Li_{1.2}Mn_{0.4}Ti_{0.4}O_2$ at the room temperature. For the convenience of the discussion in this chapter, the regions are labelled as "S" (Sloppy, in blue), "P" (Plateau-like, in orange) and "T" (Tail-like, in Red), respectively; (b) Specific charge (orange dot, left y axis) and discharge capacities (blue square, left y axis) and coulombic efficiency (red cross, right y axis) in 32 cycles. 133

Figure 6-4 Operando DEMS of $Li_{1.2}Mn^{III}_{0.4}Ti^{IV}_{0.4}O_2$ cathode in the 1st cycle. The electrochemical curve of the operando DEMS cell (in red, refers to the right y-axis), O_2 (in blue) and CO_2 (in orange) evolution (gas in mol per hour, per mol of cathode material, refers to the left y-axis) plot as a function of the state of charge..... 134

Figure 6-5 The ex-situ Mn L edge SXAS spectra at different state of charge: (a) the corresponding state of charge on load curve for ex-situ samples; (b) Mn L edge SXAS spectra at iPFY mode; (c) Mn L edge SXAS spectra at TFY mode. The peak A, B, and C correspond to the characteristic peaks of Mn^{4+} (A^* & B^*) and Mn^{2+} (C^*), in $Mn^{IV}O_2$ and $Mn^{II}O$, respectively. The $Mn^{II}O$, $Mn^{III}_2O_3$, and $Mn^{IV}O_2$ reference spectra are reproduced from Ref.[313], by the permission from Elsevier: Current Applied Physics 13, 544-548, copyright 2013. 138

Figure 6-6 The ex-situ Ti L edge SXAS spectra at PFY mode at different state of charge. The corresponding state of charge is identical as the Figure 6-5(a). The reference spectra of TiO_2 (Rutile) reproduced from the Ref[314]; the weak peak A_1 & A_2 are the pre-edge resonance and the shoulder B is the fingerprint of rutile structure of TiO_2[315,316]; the two weak peaks C & D are due to the Ti 2p, 4s and 4p states coupled with O 2p states[314,317]. 139

Figure 6-7 (b) The ex-situ O K edge SXAS spectra on PFY mode at (a) different state of charge. The O K edge SXAS spectra of Li_2TiO_3, Li_2MnO_3 and Mn_2O_3 are collected as reference..... 141

Figure 6-8 (b) Raman spectra at (a) different state of charge. The spectra of three reference samples (in grey), Li_2O_2, Na_2O_2, ZnO_2 (Alfa Aesar, approximately 50% ZnO_2 in ZnO), refine the region of O-O vibrations. 144

Figure 6-9 (b) Oxygen K edge RIXS spectra with excitation energy of 531.5 eV at (a) different state of charge. 146

Figure 6-10 The ex-situ O K edge SXAS spectra at PFY mode for the pristine material (in black), at the 1st cycle end of charge (in red) and discharge (in green), and the 2nd cycle end of charge (in blue) and discharge (in light brown). 147

Figure 6-11 (b) The OPXRD patterns of $Li_{1.2}Mn_{0.4}Ti_{0.4}O_2$ in its 1st cycle. (c) The 1st and 2nd most intensive peaks in the OPXRD patterns are enlarged for clarity and convenience of discussion. As a comparison, (a) the powder diffraction pattern of the pristine material is presented. The notation *a*, *b*, *c*, *d*, and *e*

correspond to the diffraction patterns of the electrode at beginning of charge (in black), end of region “S” (in blue), end of region “P” (in yellow), end of region “T” (in red), and end of discharge (in green), respectively. 150

Figure Appx.2-1 ToF-SIMS images of the as-prepared ^{18}O-labelled $Li_{1.2}Ni_{0.13}^{2+}Co_{0.13}^{3+}Mn_{0.54}^{4+}O_2$ material. 161

Figure Appx.4-1 Operando DEMS of ^{18}O-labelled $LiNi^{II}_{0.5}Mn^{IV}_{1.5}O_2$ cathode in the 1st cycle. (a) Electrochemical curve of the operando DEMS cell; (b) O_2 and (c) CO_2 evolution are plotted as a function of the state of charge. For clarity purpose, the plots of O_2 and CO_2 evolution are plotted separately along y-axis. Reproduced by permission from Macmillan Publishers Ltd: Nature Chemistry 8: 684-691, copyright 2016. 165

Figure Appx.5-1 Schematic of the electron transition from the O *1s* to the unoccupied hybridized states with each of the transition metal elements in $Li_{1.2}Ni_{0.13}^{II}Co_{0.13}^{III}Mn_{0.54}^{IV}O_2$. The energy difference between the spin-up and spin-down states is not differentiated as the schematic only shows energies for one electron. Reproduced by permission from Macmillan Publishers Ltd: Nature Chemistry 8: 684-691, copyright 2016. 166

Figure Appx.6-1 PXRD pattern comparison of $Li_{1.2}Mn_{0.4}Ti_{0.4}O_2$ before (in red) and after ball-milling (in blue). The allowed Bragg Peaks Positions are marked in green. 168

Figure Appx.7-1 (b) Mn and (c) Ti K edge XANES spectra on different state of charge during the 1st cycle; (d) for the purpose of clarity, the pre-edge of Ti K edge XANES is enlarged; (e) Mn and (f) Ti K edge *1s*-*4p* peak energy is plotted against different state of charge in the 1st cycle. (a) The corresponding state of charge of the measured samples is projected on the electrochemical profile, in which the voltage is plotted versus the lithium content of the cathode material. 169

LIST OF TABLES

Table 3-1 ICP-OES measurement results of $Li_{1.2}Ni_{0.13}Co_{0.13}Mn_{0.54}O_2$ synthesized by different methods 65

Table 3-2 Crystallographic parameters of $Li_{1.2}Ni_{0.13}Co_{0.13}Mn_{0.54}O_2$ materials obtained by three syntheses 70

Table 4-1 Summary of electrodes with different binders and their processing 86

Table 5-1 Theoretical and experimental values of gas evolution in percentage, detailed calculation is given in Appx. 3. 110

Table 5-2 A comparison between the charge transfer (Q_g) corresponding to the gas evolution and the electrochemically recorded equivalents (Q_e) 112

Table 6-1 The energy region of data collection and normalization for O K edge, Ti L edge and Mn L edge SXAS 130

Table 6-2 Result of the ICP-OES 131

Table 6-3 The crystallographic parameters for the $Li_{1.2}Mn_{0.4}Ti_{0.4}O_2$ 132

Table 6-4 A comparison between the charge transfer (Q_g) corresponding to the CO_2 evolution and the electrochemically recorded equivalents (Q_e) 135

Table Appx.1-1 Crystal systems and corresponding parameters and d-spacing 160

Table Appx.5-1 Unoccupied states in transition metals in the pristine $Li_{1.2}Ni^{II}_{0.13}Co^{III}_{0.13}Mn^{IV}_{0.54}O_2$ and in the charged material at the end of region “S” 167

REFERENCES

1 Bruce, P. G., Freunberger, S. A., Hardwick, L. J. & Tarascon, J.-M. Li–O_2 and Li–S batteries with high energy storage. *Nature Materials* **11**, 19 (2011).

2 Bruce, P. G., Scrosati, B. & Tarascon, J.-M. Nanomaterials for Rechargeable Lithium Batteries. *Angewandte Chemie International Edition* **47**, 2930-2946 (2008).

3 Larcher, D. & Tarascon, J. M. Towards greener and more sustainable batteries for electrical energy storage. *Nat Chem* **7**, 19-29 (2015).

4 Goodenough, J. B. & Kim, Y. Challenges for Rechargeable Li Batteries. *Chem. Mat.* **22**, 587-603 (2010).

5 WHITTINGHAM, M. S. Electrical Energy Storage and Intercalation Chemistry. *Science* **192**, 1126-1127 (1976).

6 Rozier, P. & Tarascon, J. M. Review—Li-Rich Layered Oxide Cathodes for Next-Generation Li-Ion Batteries: Chances and Challenges. *Journal of The Electrochemical Society* **162**, A2490-A2499 (2015).

7 Blomgren, G. E. The Development and Future of Lithium Ion Batteries. *Journal of The Electrochemical Society* **164**, A5019-A5025 (2017).

8 Julien, C., Mauger, A., Vijh, A. & Zaghib, K. *Lithium Batteries: Science and Technology*. (Springer International Publishing, 2016).

9 Aurbach, D., Zinigrad, E., Cohen, Y. & Teller, H. A short review of failure mechanisms of lithium metal and lithiated graphite anodes in liquid electrolyte solutions. *Solid State Ion.* **148**, 405-416 (2002).

10 Nagaura, T. & Tozawa, K. in *Progress in Batteries and Solar Cells* Vol. 9 209-217 (1990).

11 *Materials for Advanced Batteries*. (Springer US, 1980).

12 Mizushima, K., Jones, P. C., Wiseman, P. J. & Goodenough, J. B. Li_xCoO_2 (0<x<-1): A new cathode material for batteries of high energy density. *Materials Research Bulletin* **15**, 783-789 (1980).

13 Croguennec, L. & Palacin, M. R. Recent Achievements on Inorganic Electrode Materials for Lithium-Ion Batteries. *Journal of the American Chemical Society* **137**, 3140-3156 (2015).

14 Ohzuku, T., Ueda, A. & Yamamoto, N. Zero-Strain Insertion Material of Li [Li1 / 3Ti5 / 3] O 4 for Rechargeable Lithium Cells. *Journal of The Electrochemical Society* **142**, 1431-1435 (1995).

15 Peled, E., Menachem, C., Bar-Tow, D. & Melman, A. Improved Graphite Anode for Lithium-Ion Batteries Chemically: Bonded Solid Electrolyte Interface and Nanochannel Formation. *Journal of The Electrochemical Society* **143**, L4-L7 (1996).

16 Buiel, E. & Dahn, J. R. Li-insertion in hard carbon anode materials for Li-ion batteries. *Electrochimica Acta* **45**, 121-130 (1999).

17 Obrovac, M. N. & Christensen, L. Structural Changes in Silicon Anodes during Lithium Insertion/Extraction. *Electrochemical and Solid-State Letters* **7**, A93-A96 (2004).

18 Idota, Y., Kubota, T., Matsufuji, A., Maekawa, Y. & Miyasaka, T. Tin-Based Amorphous Oxide: A High-Capacity Lithium-Ion-Storage Material. *Science* **276**, 1395-1397 (1997).

19 Chen, J., Xu, L., Li, W. & Gou, X. α-Fe_2O_3 Nanotubes in Gas Sensor and Lithium-Ion Battery Applications. *Advanced Materials* **17**, 582-586 (2005).

20 Li, Y., Tan, B. & Wu, Y. Mesoporous Co_3O_4 Nanowire Arrays for Lithium Ion Batteries with High Capacity and Rate Capability. *Nano Letters* **8**, 265-270 (2008).

21 Ohzuku, T., Iwakoshi, Y. & Sawai, K. Formation of Lithium-Graphite Intercalation Compounds in Nonaqueous Electrolytes and Their Application as a Negative Electrode for a Lithium Ion (Shuttlecock) Cell. *Journal of The Electrochemical Society* **140**, 2490-2498 (1993).

22 Peled, E. The Electrochemical Behavior of Alkali and Alkaline Earth Metals in Nonaqueous Battery Systems—The Solid Electrolyte Interphase Model. *Journal of The Electrochemical Society* **126**, 2047-2051 (1979).

23 Peled, E. & Menkin, S. Review—SEI: Past, Present and Future. *Journal of The Electrochemical Society* **164**, A1703-A1719 (2017).

24 Park, T.-H. *et al.* Enhancing the rate performance of graphite anodes through addition of natural graphite/carbon nanofibers in lithium-ion batteries. *Electrochimica Acta* **93**, 236-240 (2013).

25 Nazri, G. A. & Pistoia, G. *Lithium Batteries: Science and Technology*. (Springer US, 2008).

26 Goriparti, S. *et al.* Review on recent progress of nanostructured anode materials for Li-ion batteries. *Journal of Power Sources* **257**, 421-443 (2014).

27 Wang, H., Yoshio, M., Abe, T. & Ogumi, Z. Characterization of Carbon-Coated Natural Graphite as a Lithium-Ion Battery Anode Material. *Journal of The Electrochemical Society* **149**, A499-A503 (2002).

28 Yoshio, M. *et al.* Improvement of natural graphite as a lithium-ion battery anode material, from raw flake to carbon-coated sphere. *Journal of Materials Chemistry* **14**, 1754-1758 (2004).

29 Marom, R., Amalraj, S. F., Leifer, N., Jacob, D. & Aurbach, D. A review of advanced and practical lithium battery materials. *Journal of Materials Chemistry* **21**, 9938-9954 (2011).

30 Fujimoto, H., Tokumitsu, K., Mabuchi, A., Chinnasamy, N. & Kasuh, T. The anode performance of the hard carbon for the lithium ion battery derived from the oxygen-containing aromatic precursors. *Journal of Power Sources* **195**, 7452-7456 (2010).

31 Tanaka, S. *et al.* Atomic and electronic structures of $Li_4Ti_5O_{12}/Li_7Ti_5O_{12}$ (001) interfaces by first-principles calculations. *Journal of Materials Science* **49**, 4032-4037 (2014).

32 Chen, Z., Belharouak, I., Sun, Y. K. & Amine, K. Titanium-Based Anode Materials for Safe Lithium-Ion Batteries. *Advanced Functional Materials* **23**, 959-969 (2013).

33 Szczech, J. R. & Jin, S. Nanostructured silicon for high capacity lithium battery anodes. *Energy & Environmental Science* **4**, 56-72 (2011).

34 Chandrasekaran, R., Magasinski, A., Yushin, G. & Fuller, T. F. Analysis of Lithium Insertion/Deinsertion in a Silicon Electrode Particle at Room Temperature. *Journal of The Electrochemical Society* **157**, A1139-A1151 (2010).

35 Obrovac, M. N. & Krause, L. J. Reversible Cycling of Crystalline Silicon Powder. *Journal of The Electrochemical Society* **154**, A103-A108 (2007).

36 Rhodes, K., Dudney, N., Lara-Curzio, E. & Daniel, C. Understanding the Degradation of Silicon Electrodes for Lithium-Ion Batteries Using Acoustic Emission. *Journal of The Electrochemical Society* **157**, A1354-A1360 (2010).

37 Boukamp, B. A., Lesh, G. C. & Huggins, R. A. All-Solid Lithium Electrodes with Mixed-Conductor Matrix. *Journal of The Electrochemical Society* **128**, 725-729 (1981).

38 Wen, Z. *et al.* Silicon nanotube anode for lithium-ion batteries. *Electrochem. Commun.* **29**, 67-70 (2013).

39 Obrovac, M. N. & Chevrier, V. L. Alloy Negative Electrodes for Li-Ion Batteries. *Chem. Rev.*

(2014).

40 Amereller, M. *et al.* Electrolytes for lithium and lithium ion batteries: From synthesis of novel lithium borates and ionic liquids to development of novel measurement methods. *Progress in Solid State Chemistry*.

41 Xu, K. Nonaqueous Liquid Electrolytes for Lithium-Based Rechargeable Batteries. *Chem. Rev.* **104**, 4303-4418 (2004).

42 Daniel, C. & Besenhard, J. O. *Handbook of Battery Materials*. (Wiley, 2012).

43 Huggins, R. *Advanced Batteries: Materials Science Aspects*. Vol. 1 (Springer US, 2009).

44 *Lithium-Ion Batteries: Science and Technologies*. (Springer-Verlag New York, 2009).

45 Zhang, S. S. A review on electrolyte additives for lithium-ion batteries. *Journal of Power Sources* **162**, 1379-1394 (2006).

46 Armand, M., Endres, F., MacFarlane, D. R., Ohno, H. & Scrosati, B. Ionic-liquid materials for the electrochemical challenges of the future. *Nature Materials* **8**, 621 (2009).

47 Manthiram, A., Yu, X. & Wang, S. Lithium battery chemistries enabled by solid-state electrolytes. *Nature Reviews Materials* **2**, 16103 (2017).

48 Aravindan, V., Gnanaraj, J., Madhavi, S. & Liu, H.-K. Lithium-Ion Conducting Electrolyte Salts for Lithium Batteries. *Chemistry – A European Journal* **17**, 14326-14346 (2011).

49 Dudley, J. T. *et al.* Conductivity of electrolytes for rechargeable lithium batteries. *Journal of Power Sources* **35**, 59-82 (1991).

50 Jasinski, R. & Carroll, S. Thermal Stability of a Propylene Carbonate Electrolyte. *Journal of The Electrochemical Society* **117**, 218-219 (1970).

51 Plichta, E. *et al.* An Improved Li/Li_xCoO_2 Rechargeable Cell. *Journal of The Electrochemical Society* **136**, 1865-1869 (1989).

52 Tarascon, J. M. & Guyomard, D. New electrolyte compositions stable over the 0 to 5 V voltage range and compatible with the $Li_{1+x}Mn_2O_4$/carbon Li-ion cells. *Solid State Ion.* **69**, 293-305 (1994).

53 Nanjundiah, C., Goldman, J. L., Dominey, L. A. & Koch, V. R. Electrochemical Stability of $LiMF_6$ (M = P , As , Sb) in Tetrahydrofuran and Sulfolane. *Journal of The Electrochemical Society* **135**, 2914-2917 (1988).

54 Xu, K. Electrolytes and Interphases in Li-Ion Batteries and Beyond. *Chem. Rev.* **114**, 11503-11618 (2014).

55 Wiesboeck, R. A. Tetraacetonitrilolithium Hexafluorophosphate, Tetraacetonitrilolithium Hexafluoroarsenate and Method for the Preparation Thereof. United States patent (1972).

56 Sloop, S. E., Pugh, J. K., Wang, S., Kerr, J. B. & Kinoshita, K. Chemical Reactivity of PF_5 and $LiPF_6$ in Ethylene Carbonate/Dimethyl Carbonate Solutions. *Electrochemical and Solid-State Letters* **4**, A42-A44 (2001).

57 Kawamura, T., Kimura, A., Egashira, M., Okada, S. & Yamaki, J.-I. Thermal stability of alkyl carbonate mixed-solvent electrolytes for lithium ion cells. *Journal of Power Sources* **104**, 260-264 (2002).

58 Foos, J. S. & Stolki, T. J. A New Ether Solvent for Lithium Cells. *Journal of The Electrochemical Society* **135**, 2769-2771 (1988).

59 KOCH, V. R. & YOUNG, J. H. 2-Methyltetrahydrofuran—Lithium Hexafluoroarsenate: A Superior Electrolyte for the Secondary Lithium Electrode. *Science* **204**, 499-501 (1979).

60 Koch, V. R. Reactions of Tetrahydrofuran and Lithium Hexafluoroarsenate with Lithium.

Journal of The Electrochemical Society **126**, 181-187 (1979).

61 Harris, W. S. *Electrochemical studies in cyclic esters*. (Univ. of California, 1958).

62 Jasinski, R. *High-energy batteries*. (Plenum Press, 1967).

63 Selim, R. & Bro, P. Some Observations on Rechargeable Lithium Electrodes in a Propylene Carbonate Electrolyte. *Journal of The Electrochemical Society* **121**, 1457-1459 (1974).

64 Rauh, R. D. & Brummer, S. B. The effect of additives on lithium cycling in propylene carbonate. *Electrochimica Acta* **22**, 75-83 (1977).

65 Aurbach, D., Gofer, Y. & Langzam, J. The Correlation Between Surface Chemistry, Surface Morphology, and Cycling Efficiency of Lithium Electrodes in a Few Polar Aprotic Systems. *Journal of The Electrochemical Society* **136**, 3198-3205 (1989).

66 Dey, A. N. Lithium anode film and organic and inorganic electrolyte batteries. *Thin Solid Films* **43**, 131-171 (1977).

67 Newman, G. H., Francis, R. W., Gaines, L. H. & Rao, B. M. L. Hazard Investigations of LiClO4 / Dioxolane Electrolyte. *Journal of The Electrochemical Society* **127**, 2025-2027 (1980).

68 Aurbach, D., Daroux, M. L., Faguy, P. W. & Yeager, E. Identification of Surface Films Formed on Lithium in Propylene Carbonate Solutions. *Journal of The Electrochemical Society* **134**, 1611-1620 (1987).

69 Guyomard, D. & Tarascon, J. M. Rechargeable $Li_{1+x}Mn_2O_4$ / Carbon Cells with a New Electrolyte Composition: Potentiostatic Studies and Application to Practical Cells. *Journal of The Electrochemical Society* **140**, 3071-3081 (1993).

70 Peled, E., Golodnitsky, D., Menachem, C. & Bar-Tow, D. An Advanced Tool for the Selection of Electrolyte Components for Rechargeable Lithium Batteries. *Journal of The Electrochemical Society* **145**, 3482-3486 (1998).

71 Koetschau, I., Richard, M. N., Dahn, J. R., Soupart, J. B. & Rousche, J. C. Orthorhombic $LiMnO_2$ as a High Capacity Cathode for Li-Ion Cells. *Journal of The Electrochemical Society* **142**, 2906-2910 (1995).

72 Aurbach, D. *et al.* The Study of Electrolyte Solutions Based on Ethylene and Diethyl Carbonates for Rechargeable Li Batteries: II . Graphite Electrodes. *Journal of The Electrochemical Society* **142**, 2882-2890 (1995).

73 Elliott, W. Report No. 1, Contract NAS 3-6015 (N 65-11518). (1964).

74 Pistoia, G. Nonaqueous Batteries with $LiClO_4$-Ethylene Carbonate as Electrolyte. *Journal of The Electrochemical Society* **118**, 153-158 (1971).

75 Pistoia, G., Rossi, M. D. & Scrosati, B. Study of the Behavior of Ethylene Carbonate as a Nonaqueous Battery Solvent. *Journal of The Electrochemical Society* **117**, 500-502 (1970).

76 Luo, K. *et al.* Charge-compensation in 3*d*-transition-metal-oxide intercalation cathodes through the generation of localized electron holes on oxygen. *Nat Chem* **advance online publication** (2016).

77 Xu, K., Ding, S. P. & Jow, T. R. Toward Reliable Values of Electrochemical Stability Limits for Electrolytes. *Journal of The Electrochemical Society* **146**, 4172-4178 (1999).

78 Chou, S.-L., Pan, Y., Wang, J.-Z., Liu, H.-K. & Dou, S.-X. Small things make a big difference: binder effects on the performance of Li and Na batteries. *Phys. Chem. Chem. Phys.* **16**, 20347-20359 (2014).

79 Lestriez, B., Bahri, S., Sandu, I., Roué, L. & Guyomard, D. On the binding mechanism of CMC in Si negative electrodes for Li-ion batteries. *Electrochem. Commun.* **9**, 2801-2806 (2007).

80 Beattie, S. D., Larcher, D., Morcrette, M., Simon, B. & Tarascon, J.-M. Si Electrodes for Li-Ion Batteries - A New Way to Look at an Old Problem. *Journal of The Electrochemical Society* **155**, A158-A163 (2008).

81 Han, Z.-J. *et al.* High-capacity Si-graphite composite electrodes with a self-formed porous structure by a partially neutralized polyacrylate for Li-ion batteries. *Energy & Environmental Science* **5**, 9014-9020 (2012).

82 Liu, G. *et al.* Polymers with Tailored Electronic Structure for High Capacity Lithium Battery Electrodes. *Advanced Materials* **23**, 4679-4683 (2011).

83 Koo, B. *et al.* A Highly Cross-Linked Polymeric Binder for High-Performance Silicon Negative Electrodes in Lithium Ion Batteries. *Angewandte Chemie International Edition* **51**, 8762-8767 (2012).

84 Ryou, M.-H. *et al.* Mussel-Inspired Adhesive Binders for High-Performance Silicon Nanoparticle Anodes in Lithium-Ion Batteries. *Advanced Materials* **25**, 1571-1576 (2013).

85 Choi, J. *et al.* Highly Adhesive and Soluble Copolyimide Binder: Improving the Long-Term Cycle Life of Silicon Anodes in Lithium-Ion Batteries. *ACS Applied Materials & Interfaces* **7**, 14851-14858 (2015).

86 Higgins, T. M. *et al.* A Commercial Conducting Polymer as Both Binder and Conductive Additive for Silicon Nanoparticle-Based Lithium-Ion Battery Negative Electrodes. *ACS Nano* **10**, 3702-3713 (2016).

87 Chou, S.-L., Wang, J.-Z., Liu, H.-K. & Dou, S.-X. Rapid Synthesis of Li4Ti5O12 Microspheres as Anode Materials and Its Binder Effect for Lithium-Ion Battery. *The Journal of Physical Chemistry C* **115**, 16220-16227 (2011).

88 Ryou, M.-H., Hong, S., Winter, M., Lee, H. & Choi, J. W. Improved cycle lives of LiMn2O4 cathodes in lithium ion batteries by an alginate biopolymer from seaweed. *Journal of Materials Chemistry A* **1**, 15224-15229 (2013).

89 Zhang, S. S. A review on the separators of liquid electrolyte Li-ion batteries. *Journal of Power Sources* **164**, 351-364 (2007).

90 Bladwin, R. S. A Review of State-of-the-Art Separator Materials for Advanced Lithium-Based Batteries for Future Aerospace Missions. (NASA Glenn Research Center; Cleveland, OH, United States, NASA Glenn Research Center; Cleveland, OH, United States, 2009).

91 Lee, H., Yanilmaz, M., Toprakci, O., Fu, K. & Zhang, X. A review of recent developments in membrane separators for rechargeable lithium-ion batteries. *Energy & Environmental Science* **7**, 3857-3886 (2014).

92 Deimede, V. & Elmasides, C. Separators for Lithium-Ion Batteries: A Review on the Production Processes and Recent Developments. *Energy Technology* **3**, 453-468 (2015).

93 Arora, P. & Zhang, Z. Battery Separators. *Chem. Rev.* **104**, 4419-4462 (2004).

94 Myung, S.-T., Hitoshi, Y. & Sun, Y.-K. Electrochemical behavior and passivation of current collectors in lithium-ion batteries. *Journal of Materials Chemistry* **21**, 9891-9911 (2011).

95 Ma, T. *et al.* Revisiting the Corrosion of the Aluminum Current Collector in Lithium-Ion Batteries. *The Journal of Physical Chemistry Letters* **8**, 1072-1077 (2017).

96 Braithwaite, J. W. *et al.* Corrosion of Lithium-Ion Battery Current Collectors. *Journal of The Electrochemical Society* **146**, 448-456 (1999).

97 Weaving, J. S. *et al.* Development of high energy density Li-ion batteries based on $LiNi_{1-x-y}Co_xAl_yO_2$. *Journal of Power Sources* **97**, 733-735 (2001).

98 Robert, R., Villevieille, C. & Novak, P. Enhancement of the high potential specific charge in layered electrode materials for lithium-ion batteries. *Journal of Materials Chemistry A* **2**, 8589-8598 (2014).

99 Whittingham, M. S. Lithium Batteries and Cathode Materials. *Chem. Rev.* **104**, 4271-4302 (2004).

100 Amatucci, G. G., Tarascon, J. M. & Klein, L. C. CoO_2, The End Member of the Li_xCoO_2 Solid Solution. *Journal of The Electrochemical Society* **143**, 1114-1123 (1996).

101 Yang, X. Q., Sun, X. & McBreen, J. New phases and phase transitions observed in $Li_{1-x}CoO_2$ during charge: in situ synchrotron X-ray diffraction studies. *Electrochem. Commun.* **2**, 100-103 (2000).

102 Manthiram, A. Materials Challenges and Opportunities of Lithium Ion Batteries. *The Journal of Physical Chemistry Letters* **2**, 176-184 (2011).

103 Dahn, J. R., von Sacken, U. & Michal, C. A. Structure and electrochemistry of $Li_{1\pm y}NiO_2$ and a new Li_2NiO_2 phase with the $Ni(OH)_2$ structure. *Solid State Ion.* **44**, 87-97 (1990).

104 Shannon, R. Revised effective ionic radii and systematic studies of interatomic distances in halides and chalcogenides. *Acta Crystallographica Section A* **32**, 751-767 (1976).

105 Kalyani, P. & Kalaiselvi, N. Various aspects of $LiNiO_2$ chemistry: A review. *Science and Technology of Advanced Materials* **6**, 689-703 (2005).

106 Liu, W. *et al.* Nickel-Rich Layered Lithium Transition-Metal Oxide for High-Energy Lithium-Ion Batteries. *Angew. Chem.-Int. Edit.* **54**, 4440-4457 (2015).

107 Julien, C., Mauger, A., Zaghib, K. & Groult, H. Comparative Issues of Cathode Materials for Li-Ion Batteries. *Inorganics* **2**, 132 (2014).

108 Huang, Y. *et al.* Thermal Stability and Reactivity of Cathode Materials for Li-Ion Batteries. *ACS Applied Materials & Interfaces* **8**, 7013-7021 (2016).

109 Tsutomu, O. & Yoshinari, M. Layered Lithium Insertion Material of $LiCo_{1/3}Ni_{1/3}Mn_{1/3}O_2$ for Lithium-Ion Batteries. *Chemistry Letters* **30**, 642-643 (2001).

110 Reed, J. & Ceder, G. Charge, Potential, and Phase Stability of Layered $Li(Ni_{0.5}Mn_{0.5})O_2$. *Electrochemical and Solid-State Letters* **5**, A145-A148 (2002).

111 Yoon, W.-S., Grey, C. P., Balasubramanian, M., Yang, X.-Q. & McBreen, J. In Situ X-ray Absorption Spectroscopic Study on $LiNi_{0.5}Mn_{0.5}O_2$ Cathode Material during Electrochemical Cycling. *Chem. Mat.* **15**, 3161-3169 (2003).

112 Yin, S. C., Rho, Y. H., Swainson, I. & Nazar, L. F. X-ray/Neutron Diffraction and Electrochemical Studies of Lithium De/Re-Intercalation in $Li_{1-x}Co_{1/3}Ni_{1/3}Mn_{1/3}O_2$ ($x = 0 \rightarrow 1$). *Chem. Mat.* **18**, 1901-1910 (2006).

113 Choi, Y.-M., Pyun, S.-I. & Moon, S.-I. Effects of cation mixing on the electrochemical lithium intercalation reaction into porous $Li_{1-\delta}Ni_{1-y}CoyO_2$ electrodes. *Solid State Ion.* **89**, 43-52 (1996).

114 Zhang, X. *et al.* Minimization of the cation mixing in $Li_{1+x}(NMC)_{1-x}O_2$ as cathode material. *Journal of Power Sources* **195**, 1292-1301 (2010).

115 Li, D., Sasaki, Y., Kobayakawa, K. & Sato, Y. Impact of cobalt substitution for manganese on the structural and electrochemical properties of $LiNi_{0.5}Mn_{0.5}O_2$. *Electrochimica Acta* **51**, 3809-3813 (2006).

116 Xu, J., Lin, F., Doeff, M. M. & Tong, W. A review of Ni-based layered oxides for rechargeable Li-ion batteries. *Journal of Materials Chemistry A* **5**, 874-901 (2017).

117 Thackeray, M. M., David, W. I. F., Bruce, P. G. & Goodenough, J. B. Lithium insertion into

manganese spinels. *Materials Research Bulletin* **18**, 461-472 (1983).

118 Tarascon, J. M., Wang, E., Shokoohi, F. K., McKinnon, W. R. & Colson, S. The Spinel Phase of $LiMn_2O_4$ as a Cathode in Secondary Lithium Cells. *Journal of The Electrochemical Society* **138**, 2859-2864 (1991).

119 Tarascon, J. M. *et al.* Synthesis Conditions and Oxygen Stoichiometry Effects on Li Insertion into the Spinel LiMn2 O 4. *Journal of The Electrochemical Society* **141**, 1421-1431 (1994).

120 David, W. I. F., Thackeray, M. M., De Picciotto, L. A. & Goodenough, J. B. Structure refinement of the spinel-related phases $Li_2Mn_2O_4$ and $Li_{0.2}Mn_2O_4$. *Journal of Solid State Chemistry* **67**, 316-323 (1987).

121 Thackeray, M. M. Manganese oxides for lithium batteries. *Progress in Solid State Chemistry* **25**, 1-71 (1997).

122 Padhi, A. K., Nanjundaswamy, K. S. & Goodenough, J. B. Phospho-olivines as Positive-Electrode Materials for Rechargeable Lithium Batteries. *Journal of The Electrochemical Society* **144**, 1188-1194 (1997).

123 Masquelier, C. & Croguennec, L. Polyanionic (Phosphates, Silicates, Sulfates) Frameworks as Electrode Materials for Rechargeable Li (or Na) Batteries. *Chem. Rev.* **113**, 6552-6591 (2013).

124 Rousse, G., Rodriguez-Carvajal, J., Patoux, S. & Masquelier, C. Magnetic Structures of the Triphylite $LiFePO_4$ and of Its Delithiated Form $FePO_4$. *Chem. Mat.* **15**, 4082-4090 (2003).

125 Gaberscek, M., Dominko, R. & Jamnik, J. Is small particle size more important than carbon coating? An example study on $LiFePO_4$ cathodes. *Electrochem. Commun.* **9**, 2778-2783 (2007).

126 Herle, P. S., Ellis, B., Coombs, N. & Nazar, L. F. Nano-network electronic conduction in iron and nickel olivine phosphates. *Nature Materials* **3**, 147 (2004).

127 Delacourt, C., Wurm, C., Reale, P., Morcrette, M. & Masquelier, C. Low temperature preparation of optimized phosphates for Li-battery applications. *Solid State Ion.* **173**, 113-118 (2004).

128 Rho, Y.-H., Nazar, L. F., Perry, L. & Ryan, D. Surface Chemistry of $LiFePO_4$ Studied by Mössbauer and X-Ray Photoelectron Spectroscopy and Its Effect on Electrochemical Properties. *Journal of The Electrochemical Society* **154**, A283-A289 (2007).

129 Wang, H., Jang, Y. I., Huang, B., Sadoway, D. R. & Chiang, Y. M. TEM Study of Electrochemical Cycling-Induced Damage and Disorder in $LiCoO_2$ Cathodes for Rechargeable Lithium Batteries. *Journal of The Electrochemical Society* **146**, 473-480 (1999).

130 Amatucci, G. G., Tarascon, J. M. & Klein, L. C. Cobalt dissolution in $LiCoO_2$-based non-aqueous rechargeable batteries. *Solid State Ion.* **83**, 167-173 (1996).

131 Venkatraman, S. & Manthiram, A. Synthesis and Characterization of P3-Type CoO2-δ. *Chem. Mat.* **14**, 3907-3912 (2002).

132 Kalyani, P. & Kalaiselvi, N. Various aspects of $LiNiO_2$ chemistry: A review. *Science and Technology of Advanced Materials* **6**, 689 (2005).

133 G. Bruce, P., Robert Armstrong, A. & L. Gitzendanner, R. New intercalation compounds for lithium batteries: layered LiMnO2. *Journal of Materials Chemistry* **9**, 193-198 (1999).

134 Johnson, C. S. *et al.* Structural and electrochemical studies of α-manganese dioxide (α-MnO2). *Journal of Power Sources* **68**, 570-577 (1997).

135 Thackeray, M. M., Johnson, C. S., Vaughey, J. T., Li, N. & Hackney, S. A. Advances in manganese-oxide 'composite' electrodes for lithium-ion batteries. *Journal of Materials Chemistry* **15**, 2257-2267 (2005).

136 Thackeray, M. M. *et al.* Li2MnO3-stabilized LiMO2 (M = Mn, Ni, Co) electrodes for lithium-ion batteries. *Journal of Materials Chemistry* **17**, 3112-3125 (2007).

137 Kalyani, P., Chitra, S., Mohan, T. & Gopukumar, S. Lithium metal rechargeable cells using Li2MnO3 as the positive electrode. *Journal of Power Sources* **80**, 103-106 (1999).

138 Lu, Z. & Dahn, J. R. Understanding the Anomalous Capacity of Li/Li[$Ni_xLi_{(1/3-2x/3)}Mn_{(2/3-x/3)}$]$O_2$ Cells Using In Situ X-Ray Diffraction and Electrochemical Studies. *Journal of The Electrochemical Society* **149**, A815-A822 (2002).

139 Sathiya, M. *et al.* Reversible anionic redox chemistry in high-capacity layered-oxide electrodes. *Nat Mater* **12**, 827-835 (2013).

140 Nayak, P. K. *et al.* Review on Challenges and Recent Advances in the Electrochemical Performance of High Capacity Li- and Mn-Rich Cathode Materials for Li-Ion Batteries. *Advanced Energy Materials*, 1702397-n/a.

141 Lu, Z., Chen, Z. & Dahn, J. R. Lack of Cation Clustering in Li[$Ni_xLi_{1/3-2x/3}Mn_{2/3-x/3}$]$O_2$ ($0<x\leq1/2$) and Li[$Cr_xLi_{(1-x)/3}Mn_{(2-2x)/3}$]$O_2$ ($0<x<1$). *Chem. Mat.* **15**, 3214-3220 (2003).

142 Yu, H. *et al.* High-energy 'composite' layered manganese-rich cathode materials via controlling Li2MnO3 phase activation for lithium-ion batteries. *Phys. Chem. Chem. Phys.* **14**, 6584-6595 (2012).

143 Bareno, J. *et al.* Long-Range and Local Structure in the Layered Oxide Li1.2Co0.4Mn0.4O2. *Chem. Mat.* **23**, 2039-2050 (2011).

144 Wen, J. G. *et al.* Analytical electron microscopy of Li1.2Co0.4Mn0.4O2 for lithium-ion batteries. *Solid State Ion.* **182**, 98-107 (2011).

145 Boulineau, A. *et al.* Evolutions of Li1.2Mn0.61Ni0.18Mg0.01O2 during the Initial Charge/Discharge Cycle Studied by Advanced Electron Microscopy. *Chem. Mat.* **24**, 3558-3566 (2012).

146 Koga, H. *et al.* Li1.20Mn0.54Co0.13Ni0.13O2 with Different Particle Sizes as Attractive Positive Electrode Materials for Lithium-Ion Batteries: Insights into Their Structure. *J. Phys. Chem. C* **116**, 13497-13506 (2012).

147 Ammundsen, B. *et al.* Local Structure and First Cycle Redox Mechanism of Layered Li1.2Cr0.4Mn0.4 O 2 Cathode Material. *Journal of The Electrochemical Society* **149**, A431-A436 (2002).

148 Jarvis, K. A., Deng, Z., Allard, L. F., Manthiram, A. & Ferreira, P. J. Atomic Structure of a Lithium-Rich Layered Oxide Material for Lithium-Ion Batteries: Evidence of a Solid Solution. *Chem. Mat.* **23**, 3614-3621 (2011).

149 Lei, C. H. *et al.* Local structure and composition studies of Li1.2Ni0.2Mn0.6O2 by analytical electron microscopy. *Journal of Power Sources* **178**, 422-433 (2008).

150 McCalla, E., Lowartz, C. M., Brown, C. R. & Dahn, J. R. Formation of Layered-Layered Composites in the Li-Co-Mn Oxide Pseudoternary System during Slow Cooling. *Chem. Mat.* **25**, 912-918 (2013).

151 McCalla, E., Rowe, A. W., Brown, C. R., Hacquebard, L. R. P. & Dahn, J. R. How Phase Transformations during Cooling Affect Li-Mn-Ni-O Positive Electrodes in Lithium Ion Batteries. *Journal of the Electrochemical Society* **160**, A1134-A1138 (2013).

152 McCalla, E., Rowe, A. W., Camardese, J. & Dahn, J. R. The Role of Metal Site Vacancies in Promoting Li-Mn-Ni-O Layered Solid Solutions. *Chem. Mat.* **25**, 2716-2721 (2013).

153 McCalla, E., Rowe, A. W., Shunmugasundaram, R. & Dahn, J. R. Structural Study of the Li-

Mn-Ni Oxide Pseudoternary System of Interest for Positive Electrodes of Li-Ion Batteries. *Chem. Mat.* **25**, 989-999 (2013).

154 Nayak, P. K., Grinblat, J., Levi, M., Markovsky, B. & Aurbach, D. Structural and Electrochemical Evidence of Layered to Spinel Phase Transformation of Li and Mn Rich Layered Cathode Materials of the Formulae xLi[Li1/3Mn2/3]O2.(1-x)LiMn1/3Ni1/3Co1/3O2 (x = 0.2, 0.4, 0.6) upon Cycling. *Journal of The Electrochemical Society* **161**, A1534-A1547 (2014).

155 Shunmugasundaram, R., Senthil Arumugam, R. & Dahn, J. R. High Capacity Li-Rich Positive Electrode Materials with Reduced First-Cycle Irreversible Capacity Loss. *Chem. Mat.* **27**, 757-767 (2015).

156 Sathiya, M. *et al.* Origin of voltage decay in high-capacity layered oxide electrodes. *Nat Mater* **advance online publication** (2014).

157 Croy, J. R., Gallagher, K. G., Balasubramanian, M., Long, B. R. & Thackeray, M. M. Quantifying Hysteresis and Voltage Fade in xLi2MnO3●(1-x)LiMn0.5Ni0.5O2 Electrodes as a Function of Li2MnO3 Content. *Journal of The Electrochemical Society* **161**, A318-A325 (2014).

158 Sun, S. *et al.* AlF3 Surface-Coated Li[Li0.2Ni0.17Co0.07Mn0.56]O2 Nanoparticles with Superior Electrochemical Performance for Lithium-Ion Batteries. *ChemSusChem* **8**, 2544-2550 (2015).

159 Wu, Y. & Manthiram, A. High Capacity, Surface-Modified Layered $Li[Li_{(1-x)/3}Mn_{(2-x)/3}Ni_{x/3}Co_{x/3}]O_2$ Cathodes with Low Irreversible Capacity Loss. *Electrochemical and Solid-State Letters* **9**, A221-A224 (2006).

160 Shi, S. J. *et al.* Enhanced cycling stability of Li[Li0.2Mn0.54Ni0.13Co0.13]O2 by surface modification of MgO with melting impregnation method. *Electrochimica Acta* **88**, 671-679 (2013).

161 Gao, J., Kim, J. & Manthiram, A. High capacity Li[Li0.2Mn0.54Ni0.13Co0.13]O2–V2O5 composite cathodes with low irreversible capacity loss for lithium ion batteries. *Electrochem. Commun.* **11**, 84-86 (2009).

162 Wang, Q. Y., Liu, J., Murugan, A. V. & Manthiram, A. High capacity double-layer surface modified $Li[Li_{0.2}Mn_{0.54}Ni_{0.13}Co_{0.13}]O_2$ cathode with improved rate capability. *Journal of Materials Chemistry* **19**, 4965-4972 (2009).

163 Richard, M. N., Fuller, E. W. & Dahn, J. R. The effect of ammonia reduction on the spinel electrode materials, $LiMn_2O_4$ and $Li(Li_{13}Mn_{53})O_4$. *Solid State Ion.* **73**, 81-91 (1994).

164 Qiu, B. *et al.* Gas-solid interfacial modification of oxygen activity in layered oxide cathodes for lithium-ion batteries. *Nature Communications* **7**, 10 (2016).

165 Zhang, H. Z., Qiao, Q. Q., Li, G. R., Ye, S. H. & Gao, X. P. Surface nitridation of Li-rich layered $Li(Li_{0.17}Ni_{0.25}Mn_{0.58})O_2$ oxide as cathode material for lithium-ion battery. *Journal of Materials Chemistry* **22**, 13104-13109 (2012).

166 Erickson, E. M. *et al.* High-Temperature Treatment of Li-Rich Cathode Materials with Ammonia: Improved Capacity and Mean Voltage Stability during Cycling. *Advanced Energy Materials* **7** (2017).

167 Song, B. H. *et al.* Advances in Sustain Stable Voltage of Cr-Doped Li-Rich Layered Cathodes for Lithium Ion Batteries. *Journal of the Electrochemical Society* **161**, A1723-A1730 (2014).

168 Nayak, P. K. *et al.* Al Doping for Mitigating the Capacity Fading and Voltage Decay of Layered Li and Mn-Rich Cathodes for Li-Ion Batteries. *Advanced Energy Materials* **6**, 13 (2016).

169 Nayak, P. K. *et al.* Understanding the influence of Mg doping for the stabilization of capacity and higher discharge voltage of Li- and Mn-rich cathodes for Li- ion batteries. *Phys. Chem. Chem. Phys.* **19**, 6142-6152 (2017).

170 Chen, H. *et al.* Synthesis and electrochemical study of Zr-doped Li $Li_{0.2}Mn_{0.54}Ni_{0.13}Co_{0.13}O_2$ as cathode material for Li-ion battery. *Ceramics International* **42**, 263-269 (2016).

171 Johnson, C. S. *et al.* The significance of the Li_2MnO_3 component in 'composite' $xLi_2MnO_3{\cdot}(1{-}x)LiMn_{0.5}Ni_{0.5}O_2$ electrodes. *Electrochem. Commun.* **6**, 1085-1091 (2004).

172 Castel, E., Berg, E. J., El Kazzi, M., Novák, P. & Villevieille, C. Differential Electrochemical Mass Spectrometry Study of the Interface of $xLi_2MnO_3{\cdot}(1–x)LiMO_2$ (M = Ni, Co, and Mn) Material as a Positive Electrode in Li-Ion Batteries. *Chem. Mat.* **26**, 5051-5057 (2014).

173 Yabuuchi, N., Yoshii, K., Myung, S.-T., Nakai, I. & Komaba, S. Detailed Studies of a High-Capacity Electrode Material for Rechargeable Batteries, $Li_2MnO_3{-}LiCo_{1/3}Ni_{1/3}Mn_{1/3}O_2$. *Journal of the American Chemical Society* **133**, 4404-4419 (2011).

174 Hy, S., Felix, F., Rick, J., Su, W.-N. & Hwang, B. J. Direct In situ Observation of Li_2O Evolution on Li-Rich High-Capacity Cathode Material, $Li[Ni_xLi_{(1–2x)/3}Mn_{(2–x)/3}]O_2$ ($0{\le}x{\le}0.5$). *Journal of the American Chemical Society* **136**, 999-1007 (2014).

175 Hong, J. *et al.* Critical Role of Oxygen Evolved from Layered Li–Excess Metal Oxides in Lithium Rechargeable Batteries. *Chem. Mat.* **24**, 2692-2697 (2012).

176 Armstrong, A. R. *et al.* Demonstrating Oxygen Loss and Associated Structural Reorganization in the Lithium Battery Cathode $Li[Ni_{0.2}Li_{0.2}Mn_{0.6}]O_2$. *Journal of the American Chemical Society* **128**, 8694-8698 (2006).

177 Jiang, M., Key, B., Meng, Y. S. & Grey, C. P. Electrochemical and Structural Study of the Layered, "Li-Excess" Lithium-Ion Battery Electrode Material $Li[Li_{1/9}Ni_{1/3}Mn_{5/9}]O_2$. *Chem. Mat.* **21**, 2733-2745 (2009).

178 Hy, S., Su, W.-N., Chen, J.-M. & Hwang, B.-J. Soft X-ray Absorption Spectroscopic and Raman Studies on $Li_{1.2}Ni_{0.2}Mn_{0.6}O_2$ for Lithium-Ion Batteries. *The Journal of Physical Chemistry C* **116**, 25242-25247 (2012).

179 Koga, H. *et al.* Different oxygen redox participation for bulk and surface: A possible global explanation for the cycling mechanism of $Li_{1.20}Mn_{0.54}CO_{0.13}Ni_{0.13}O_2$. *Journal of Power Sources* **236**, 250-258 (2013).

180 Koga, H. *et al.* Operando X-ray Absorption Study of the Redox Processes Involved upon Cycling of the Li-Rich Layered Oxide Li1.20Mn0.54Co0.13Ni0.13O2 in Li Ion Batteries. *The Journal of Physical Chemistry C* **118**, 5700-5709 (2014).

181 Pearce, P. E. *et al.* Evidence for anionic redox activity in a tridimensional-ordered Li-rich positive electrode β-Li_2IrO_3. *Nat Mater* **advance online publication** (2017).

182 McCalla, E. *et al.* Visualization of O-O peroxo-like dimers in high-capacity layered oxides for Li-ion batteries. *Science* **350**, 1516-1521 (2015).

183 Sathiya, M. *et al.* High Performance $Li_2Ru_{1–y}Mn_yO_3$ ($0.2{\le}y{\le}0.8$) Cathode Materials for Rechargeable Lithium-Ion Batteries: Their Understanding. *Chem. Mat.* **25**, 1121-1131 (2013).

184 Luo, K. *et al.* Anion Redox Chemistry in the Cobalt Free 3d Transition Metal Oxide Intercalation Electrode Li[Li0.2Ni0.2Mn0.6]O2. *Journal of the American Chemical Society* **138**, 11211-11218 (2016).

185 Erickson, E. M. *et al.* Review - Recent Advances and Remaining Challenges for Lithium Ion Battery Cathodes: II. Lithium-Rich, $xLi_2MnO_3{\cdot}(1\text{-}x)LiNi_aCo_bMn_cO_2$. *Journal of The*

Electrochemical Society **164**, A6341-A6348 (2017).

186 Armstrong, A. R., Dupre, N., Paterson, A. J., Grey, C. P. & Bruce, P. G. Combined Neutron Diffraction, NMR, and Electrochemical Investigation of the Layered-to-Spinel Transformation in LiMnO2. *Chem. Mat.* **16**, 3106-3118 (2004).

187 Croy, J. R., Gallagher, K. G., Balasubramanian, M., Long, B. R. & Thackeray, M. M. Quantifying Hysteresis and Voltage Fade in xLi(2)MnO(3)center dot(1-x)LiMn0.5Ni0.5O2 Electrodes as a Function of Li2MnO3 Content. *Journal of the Electrochemical Society* **161**, A318-A325 (2014).

188 Gallagher, K. G. *et al.* Correlating hysteresis and voltage fade in lithium- and manganese-rich layered transition-metal oxide electrodes. *Electrochem. Commun.* **33**, 96-98 (2013).

189 Dogan, F. *et al.* Re-entrant Lithium Local Environments and Defect Driven Electrochemistry of Li- and Mn-Rich Li-Ion Battery Cathodes. *Journal of the American Chemical Society* **137**, 2328-2335 (2015).

190 West, A. R. *Solid State Chemistry And Its Applications*. (Chichester : Wiley, 1984).

191 Cushing, B. L., Kolesnichenko, V. L. & O'Connor, C. J. Recent Advances in the Liquid-Phase Syntheses of Inorganic Nanoparticles. *Chem. Rev.* **104**, 3893-3946 (2004).

192 Kuo, J. *Electron Microscopy - Methods and Protocols*. Vol. 369 (Humana Press, 2007).

193 Hou, X. & Jones, B. T. *Inductively Coupled Plasma/Optical Emission Spectrometry*. (John Wiley & Sons Ltd, 2000).

194 Birkholz, M. *Thin Film Analysis by X-Ray Scattering*. (Wiley-VCH Verlag GmbH & Co. KGaA, 2006).

195 Kolb, U., Shankland, K., Meshi, L., Avilov, A. & David, W. I. F. *Uniting Electron Crystallography and Powder Diffraction*. (Springer, 2012).

196 Mittemeijer, E. J. & Welzel, U. *Modern Diffraction Methods*. 554 (WILEY-VCH Verlag GmbH & Co. KGaA, 2012).

197 Ashton, S. J. *Design, Construction and Research Application of a Differential Electrochemical Mass Spectrometer (DEMS)*. 224 (Springer-Verlag Berlin Heidelberg, 2012).

198 Rietveld, H. A profile refinement method for nuclear and magnetic structures. *Journal of Applied Crystallography* **2**, 65-71 (1969).

199 Rietveld, H. Line profiles of neutron powder-diffraction peaks for structure refinement. *Acta Crystallographica* **22**, 151-152 (1967).

200 Malmros, G. & Thomas, J. O. Least-squares structure refinement based on profile analysis of powder film intensity data measured on an automatic microdensitometer. *Journal of Applied Crystallography* **10**, 7-11 (1977).

201 Carvajal, J. FULLPROF: A Program for Rietveld Refinement and Pattern Matching Analysis. *Abstracts of the Satellite Meeting on Powder Diffraction of the XV Congress of the IUCr* (1990).

202 Jain, R. K., Gaur, H. C. & Welch, B. J. Chronopotentiometry: A review of theoretical principles. *Journal of Electroanalytical Chemistry and Interfacial Electrochemistry* **79**, 211-236 (1977).

203 Pyun, S.-I., Shin, H.-C., Lee, J.-W. & Go, J.-Y. *Electrochemistry of Insertion Materials for Hydrogen and Lithium*. (Springer-Verlag Berlin Heidelberg, 2012).

204 Wolter, O. & Heitbaum, J. Differential Electrochemical Mass Spectroscopy (DEMS) — a New Method for the Study of Electrode Processes. *Berichte der Bunsengesellschaft für physikalische Chemie* **88**, 2-6 (1984).

205 Ferraro, J. R., Nakamoto, K. & Brown, C. W. *Introductory Raman Spectroscopy*. (Elsevier

Science, 2002).

206 Hester, R. E. & Plane, R. A. Metal-Oxygen Bonds in Complexes: Raman Spectra of Trisacetylacetonato and Trisoxalato Complexes of Aluminum, Gallium, and Indium. *Inorg. Chem.* **3**, 513-517 (1964).

207 Hardcastle, F. D. & Wachs, I. E. Raman spectroscopy of bismuth tungstates. *Journal of Raman Spectroscopy* **26**, 407-412 (1995).

208 Hardcastle, F. D. & Wachs, I. E. Determination of vanadium-oxygen bond distances and bond orders by Raman spectroscopy. *The Journal of Physical Chemistry* **95**, 5031-5041 (1991).

209 Baddour-Hadjean, R. & Pereira-Ramos, J.-P. Raman Microspectrometry Applied to the Study of Electrode Materials for Lithium Batteries. *Chem. Rev.* **110**, 1278-1319 (2010).

210 Che, M. & Védrine, J. C. *Characterization of Solid Materials and Heterogeneous Catalysts: From Structure to Surface Reactivity*. 1181 (Wiley-VCH Verlag GmbH & Co. KGaA, 2012).

211 Alp, E. E., Mini, S. M. & Ramanathan, M. X-ray absorption spectroscopy: EXAFS and XANES - A versatile tool to study the atomic and electronic structure of materials. 25-36 (United States, 1990).

212 van Bokhoven, J. A. & Lamberti, C. *X-Ray Absorption and X-Ray Emission Spectroscopy : Theory and Applications*. (John Wiley & Sons, Incorporated, 2016).

213 Poumellec, B., Cortes, R., Tourillon, G. & Berthon, J. Angular Dependence of the Ti K Edge in Rutile TiO2. *physica status solidi (b)* **164**, 319-326 (1991).

214 Laan, G. v. d. & Kirkman, I. W. The 2p absorption spectra of 3d transition metal compounds in tetrahedral and octahedral symmetry. *J. Phys.: Condens. Matter* **4**, 4189-4204 (1992).

215 de Groot, F. M. F., Fuggle, J. C., Thole, B. T. & Sawatzky, G. A. 2p x-ray absorption of 3d transition-metal compounds: An atomic multiplet description including the crystal field. *Physical Review B* **42**, 5459-5468 (1990).

216 Kang, J. S. *et al.* Soft x-ray absorption spectroscopy and magnetic circular dichroism study of the valence and spin states in spinel $\mathrm{Mn}{\mathrm{Fe}}_{2}{\mathrm{O}}_{4}$. *Physical Review B* **77**, 035121 (2008).

217 Okada, K. & Kotani, A. Complementary Roles of Co *2p* X-Ray Absorption and Photoemission Spectra in CoO. *Journal of the Physical Society of Japan* **61**, 449-453 (1992).

218 Wang, H. *et al.* Integrated X-ray L Absorption Spectra. Counting Holes in Ni Complexes. *The Journal of Physical Chemistry B* **102**, 8343-8346 (1998).

219 Wang, H. *et al.* Nickel L-Edge Soft X-ray Spectroscopy of Nickel−Iron Hydrogenases and Model CompoundsEvidence for High-Spin Nickel(II) in the Active Enzyme. *Journal of the American Chemical Society* **122**, 10544-10552 (2000).

220 Wang, H. *et al.* Soft X-ray absorption spectroscopy and resonant inelastic X-ray scattering spectroscopy below 100 eV: probing first-row transition-metal M-edges in chemical complexes. *Journal of Synchrotron Radiation* **20**, 614-619 (2013).

221 Regier, T. *Limitations and Advancements in Soft x-ray Spectroscopy* Doctor of Philosophy (Ph.D.) thesis, University of Saskatchewan, (2012).

222 Soldatov, M. A. *et al.* On the origin of dips in total fluorescence yield X-ray absorption spectra: Partial and inverse partial fluorescence yield at the L-edge of cobalt aqueous solution. *Chemical Physics Letters* **546**, 164-167 (2012).

223 Achkar, A. J. *et al.* Bulk sensitive x-ray absorption spectroscopy free of self-absorption effects. *Physical Review B* **83**, 081106 (2011).

224 Achkar, A. *Inverse Partial Fluorescence Yield Spectroscopy* Master of Science (M.Sc.) thesis, University of Waterloo, (2011).

225 Ghiringhelli, G. *et al.* SAXES, a high resolution spectrometer for resonant x-ray emission in the 400–1600eV energy range. *Review of Scientific Instruments* **77**, 113108 (2006).

226 Ament, L. J. P., van Veenendaal, M., Devereaux, T. P., Hill, J. P. & van den Brink, J. Resonant inelastic x-ray scattering studies of elementary excitations. *Reviews of Modern Physics* **83**, 705-767 (2011).

227 Schmitt, T., de Groot, F. M. F. & Rubensson, J.-E. Prospects of high-resolution resonant X-ray inelastic scattering studies on solid materials, liquids and gases at diffraction-limited storage rings. *Journal of Synchrotron Radiation* **21**, 1065-1076 (2014).

228 Dell'Angela, M. *et al.* Extreme ultraviolet resonant inelastic X-ray scattering (RIXS) at a seeded free-electron laser. **6**, 38796 (2016).

229 van Veenendaal, M. Polarization Dependence of L- and M-Edge Resonant Inelastic X-Ray Scattering in Transition-Metal Compounds. *Phys Rev Lett* **96**, 117404 (2006).

230 Brink, J. V. D. & Veenendaal, M. V. Correlation functions measured by indirect resonant inelastic X-ray scattering. *Europhys. Letter.* **73**, 121-127 (2006).

231 van den Brink, J. & van Veenendaal, M. Theory of indirect resonant inelastic X-ray scattering. *J Phys Chem Solids* **66**, 2145-2149 (2005).

232 Muhammad, S. *et al.* Evidence of reversible oxygen participation in anomalously high capacity Li- and Mn-rich cathodes for Li-ion batteries. *Nano Energy* **21**, 172-184 (2016).

233 Johnson, C. S., Li, N., Lefief, C., Vaughey, J. T. & Thackeray, M. M. Synthesis, Characterization and Electrochemistry of Lithium Battery Electrodes: $xLi_2MnO_3\cdot(1-x)LiMn_{0.333}Ni_{0.333}Co_{0.333}O_2$ ($0\leq x\leq 0.7$). *Chem. Mat.* **20**, 6095-6106 (2008).

234 Ates, M. N., Mukerjee, S. & Abraham, K. M. A Li-Rich Layered Cathode Material with Enhanced Structural Stability and Rate Capability for Li-on Batteries. *Journal of The Electrochemical Society* **161**, A355-A363 (2014).

235 Wang, D., Belharouak, I., Zhou, G. & Amine, K. Synthesis of Lithium and Manganese-Rich Cathode Materials via an Oxalate Co-Precipitation Method. *Journal of The Electrochemical Society* **160**, A3108-A3112 (2013).

236 Fell, C. R. *et al.* Correlation Between Oxygen Vacancy, Microstrain, and Cation Distribution in Lithium-Excess Layered Oxides During the First Electrochemical Cycle. *Chem. Mat.* **25**, 1621-1629 (2013).

237 Kim, S., Cho, W., Zhang, X., Oshima, Y. & Choi, J. W. A stable lithium-rich surface structure for lithium-rich layered cathode materials. *Nature Communications* **7**, 13598 (2016).

238 Vu, N. H. *et al.* Effect of synthesis temperature on the structural defects of integrated spinel-layered $Li_{1.2}Mn_{0.75}Ni_{0.25}O_{2+\delta}$: a strategy to develop high-capacity cathode materials for Li-ion batteries. *Journal of Materials Chemistry A* **5**, 15730-15742 (2017).

239 Genevois, C. *et al.* Insight into the Atomic Structure of Cycled Lithium-Rich Layered Oxide Li1.20Mn0.54Co0.13Ni0.13O2 Using HAADF STEM and Electron Nanodiffraction. *The Journal of Physical Chemistry C* **119**, 75-83 (2015).

240 Wei, G.-Z. *et al.* Crystal Habit-Tuned Nanoplate Material of Li[Li1/3–2x/3NixMn2/3–x/3]O2 for High-Rate Performance Lithium-Ion Batteries. *Advanced Materials* **22**, 4364-4367 (2010).

241 Drewett, N. E. *Novel routes to high performance lithium-ion batteries* PhD Doctor of Philosophy thesis, University of St Andrews, U.K., (2013).

242 Momma, K. & Izumi, F. VESTA: a three-dimensional visualization system for electronic and structural analysis. *Journal of Applied Crystallography* **41**, 653-658 (2008).

243 Momma, K. & Izumi, F. VESTA 3 for three-dimensional visualization of crystal, volumetric and morphology data. *Journal of Applied Crystallography* **44**, 1272-1276 (2011).

244 McCusker, L. B., Von Dreele, R. B., Cox, D. E., Louer, D. & Scardi, P. Rietveld refinement guidelines. *Journal of Applied Crystallography* **32**, 36-50 (1999).

245 Weill, F., Tran, N., Croguennec, L. & Delmas, C. Cation ordering in the layered $Li_{1+x}(Ni_{0.425}Mn_{0.425}Co_{0.15})_{1-x}O_2$ materials ($0 \leq x \leq 0.12$). *Journal of Power Sources* **172**, 893-900 (2007).

246 Meng, Y. S. *et al.* Cation Ordering in Layered O3 Li[NixLi1/3-2x/3Mn2/3-x/3]O2 ($0 \leq x \leq 1/2$) Compounds. *Chem. Mat.* **17**, 2386-2394 (2005).

247 Kim, J.-S. *et al.* Electrochemical and Structural Properties of xLi2M'O3·(1−x)LiMn0.5Ni0.5O2 Electrodes for Lithium Batteries (M' = Ti, Mn, Zr; $0 \leq x \leqslant 0.3$). *Chem. Mat.* **16**, 1996-2006 (2004).

248 Mohanty, D. *et al.* Correlating cation ordering and voltage fade in a lithium-manganese-rich lithium-ion battery cathode oxide: a joint magnetic susceptibility and TEM study. *Phys. Chem. Chem. Phys.* **15**, 19496-19509 (2013).

249 Courtel, F. M., Niketic, S., Duguay, D., Abu-Lebdeh, Y. & Davidson, I. J. Water-soluble binders for MCMB carbon anodes for lithium-ion batteries. *Journal of Power Sources* **196**, 2128-2134 (2011).

250 Park, H.-K., Kong, B.-S. & Oh, E.-S. Effect of high adhesive polyvinyl alcohol binder on the anodes of lithium ion batteries. *Electrochem. Commun.* **13**, 1051-1053 (2011).

251 Kovalenko, I. *et al.* A Major Constituent of Brown Algae for Use in High-Capacity Li-Ion Batteries. *Science* **334**, 75-79 (2011).

252 Hochgatterer, N. S. *et al.* Silicon/Graphite Composite Electrodes for High-Capacity Anodes: Influence of Binder Chemistry on Cycling Stability. *Electrochemical and Solid-State Letters* **11**, A76-A80 (2008).

253 Magasinski, A. *et al.* Toward Efficient Binders for Li-Ion Battery Si-Based Anodes: Polyacrylic Acid. *ACS Applied Materials & Interfaces* **2**, 3004-3010 (2010).

254 Komaba, S. *et al.* Study on Polymer Binders for High-Capacity SiO Negative Electrode of Li-Ion Batteries. *The Journal of Physical Chemistry C* **115**, 13487-13495 (2011).

255 Feng, X. *et al.* Performance improvement of Li-rich layer-structured Li1.2Mn0.54Ni0.13Co0.13O2 by integration with spinel LiNi0.5Mn1.5O4. *Phys. Chem. Chem. Phys.* **17**, 1257-1264 (2015).

256 Gim, J. *et al.* An in-situ gas chromatography investigation into the suppression of oxygen gas evolution by coated amorphous cobalt-phosphate nanoparticles on oxide electrode. **6**, 23394 (2016).

257 Wu, Y. *et al.* Probing the initiation of voltage decay in Li-rich layered cathode materials at the atomic scale. *Journal of Materials Chemistry A* **3**, 5385-5391 (2015).

258 Li, J.-T. *et al.* Water Soluble Binder, an Electrochemical Performance Booster for Electrode Materials with High Energy Density. *Advanced Energy Materials*, n/a-n/a (2017).

259 Nirmale, T. C., Kale, B. B. & Varma, A. J. A review on cellulose and lignin based binders and electrodes: Small steps towards a sustainable lithium ion battery. *International Journal of Biological Macromolecules* **103**, 1032-1043 (2017).

260 Lee, Y. J., Wang, F., Mukerjee, S., McBreen, J. & Grey, C. P. 6Li and 7Li Magic-Angle Spinning Nuclear Magnetic Resonance and In Situ X-Ray Diffraction Studies of the Charging and Discharging of Li x Mn2 O 4 at 4 V. *Journal of The Electrochemical Society* **147**, 803-812 (2000).

261 Badi, S.-P. *et al.* Direct synthesis of nanocrystalline Li0.90FePO4: observation of phase segregation of anti-site defects on delithiation. *Journal of Materials Chemistry* **21**, 10085-10093 (2011).

262 Chapiro, A., Mankowski, Z. & Schmitt, N. Unusual swelling behavior of films of polyvinyl- and polyvinylidene/fluorides in various solvents. *Journal of Polymer Science: Polymer Chemistry Edition* **20**, 1791-1796 (1982).

263 Nakajima, T. & Groult, H. *Fluorinated Materials for Energy Conversion*. (Elsevier Science, 2005).

264 Black, R. *et al.* Screening for Superoxide Reactivity in Li-O2 Batteries: Effect on Li2O2/LiOH Crystallization. *Journal of the American Chemical Society* **134**, 2902-2905 (2012).

265 Li, J. *et al.* Investigations on cellulose-based high voltage composite cathodes for lithium ion batteries. *Journal of Power Sources* **196**, 7687-7691 (2011).

266 Wang, Z. *et al.* CMC as a binder in LiNi0.4Mn1.6O4 5V cathodes and their electrochemical performance for Li-ion batteries. *Electrochimica Acta* **62**, 77-83 (2012).

267 Xu, J., Chou, S.-L., Gu, Q.-f., Liu, H.-K. & Dou, S.-X. The effect of different binders on electrochemical properties of LiNi1/3Mn1/3Co1/3O2 cathode material in lithium ion batteries. *Journal of Power Sources* **225**, 172-178 (2013).

268 Porcher, W., Lestriez, B., Jouanneau, S. & Guyomard, D. Design of Aqueous Processed Thick LiFePO4 Composite Electrodes for High-Energy Lithium Battery. *Journal of The Electrochemical Society* **156**, A133-A144 (2009).

269 Zhang, S. *et al.* A Novel Strategy to Suppress Capacity and Voltage Fading of Li- and Mn-Rich Layered Oxide Cathode Material for Lithium-Ion Batteries. *Advanced Energy Materials* **7**, n/a-n/a (2017).

270 Porcher, W., Moreau, P., Lestriez, B., Jouanneau, S. & Guyomard, D. Is LiFePO4 Stable in Water?: Toward Greener Li–Ion Batteries. *Electrochemical and Solid-State Letters* **11**, A4-A8 (2008).

271 Tarascon, J. M. & Armand, M. Issues and challenges facing rechargeable lithium batteries. *Nature* **414**, 359-367 (2001).

272 Koga, H. *et al.* Reversible Oxygen Participation to the Redox Processes Revealed for Li1.20Mn0.54Co0.13Ni0.13O2. *Journal of the Electrochemical Society* **160**, A786-A792 (2013).

273 Tarascon, J. M. *et al.* In Situ Structural and Electrochemical Study of Ni1−xCoxO2 Metastable Oxides Prepared by Soft Chemistry. *Journal of Solid State Chemistry* **147**, 410-420 (1999).

274 Peng, Z., Freunberger, S. A., Chen, Y. & Bruce, P. G. A reversible and higher-rate Li-O2 battery. *Science* **337**, 563-566 (2012).

275 Chen, Y., Freunberger, S. A., Peng, Z., Bardé, F. & Bruce, P. G. Li–O2 Battery with a Dimethylformamide Electrolyte. *Journal of the American Chemical Society* **134**, 7952-7957 (2012).

276 Dent, A. J. *et al.* B18: A core XAS spectroscopy beamline for Diamond. *Journal of Physics: Conference Series* **190**, 012039 (2009).

277 Stohr, J. *NEXAFS Spectroscopy*. First edn, Vol. 1 403 (Springer-Verlag Berlin Heidelberg GmbH, 1992).

278 Aurbach, D., Daroux, M., Faguy, P. & Yeager, E. The electrochemistry of noble metal electrodes in aprotic organic solvents containing lithium salts. *Journal of Electroanalytical Chemistry and Interfacial Electrochemistry* **297**, 225-244 (1991).

279 Freunberger, S. A. *et al.* Reactions in the Rechargeable Lithium–O2 Battery with Alkyl Carbonate Electrolytes. *Journal of the American Chemical Society* **133**, 8040-8047 (2011).

280 Simonin, L. *et al.* In situ investigations of a Li-rich Mn-Ni layered oxide for Li-ion batteries. *Journal of Materials Chemistry* **22**, 11316-11322 (2012).

281 Yabuuchi, N. *et al.* High-capacity electrode materials for rechargeable lithium batteries: Li3NbO4-based system with cation-disordered rocksalt structure. *Proceedings of the National Academy of Sciences* **112**, 7650-7655 (2015).

282 Ito, A. *et al.* In situ X-ray absorption spectroscopic study of Li-rich layered cathode material Li[Ni0.17Li0.2Co0.07Mn0.56]O2. *Journal of Power Sources* **196**, 6828-6834 (2011).

283 Kim, J.-M. & Chung, H.-T. The first cycle characteristics of Li[Ni1/3Co1/3Mn1/3]O2 charged up to 4.7 V. *Electrochimica Acta* **49**, 937-944 (2004).

284 de Groot, F. M. F. *et al.* Oxygen 1s x-ray-absorption edges of transition-metal oxides. *Physical Review B* **40**, 5715-5723 (1989).

285 Amalraj, F. *et al.* Study of the Lithium-Rich Integrated Compound xLi2MnO3·(1-x)LiMO2 (x around 0.5; M = Mn, Ni, Co; 2:2:1) and Its Electrochemical Activity as Positive Electrode in Lithium Cells. *Journal of The Electrochemical Society* **160**, A324-A337 (2013).

286 Ruther, R. E., Callender, A. F., Zhou, H., Martha, S. K. & Nanda, J. Raman Microscopy of Lithium-Manganese-Rich Transition Metal Oxide Cathodes. *Journal of The Electrochemical Society* **162**, A98-A102 (2015).

287 Hoang, K. Defect Physics, Delithiation Mechanism, and Electronic and Ionic Conduction in Layered Lithium Manganese Oxide Cathode Materials. *Physical Review Applied* **3**, 024013 (2015).

288 Magnuson, M. *et al.* Self-doping processes between planes and chains in the metal-to-superconductor transition of YBa2Cu3O6.9. **4**, 7017 (2014).

289 Duda, L.-C. *et al.* Bandlike and excitonic states of oxygen in CuGeO3: Observation using polarized resonant soft X-ray emission spectroscopy. *Phys. Rev. B* **61**, 4186-4189 (2000).

290 Carniato, S. *et al.* A new method to derive electronegativity from resonant inelastic x-ray scattering. *The Journal of Chemical Physics* **137**, 144303 (2012).

291 Delmas, C. Battery materials: Operating through oxygen. *Nat Chem* **8**, 641-643 (2016).

292 Luo, K. *et al.* Charge-compensation in 3*d*-transition-metal-oxide intercalation cathodes through the generation of localized electron holes on oxygen. *Nature Chemistry* **8**, 684 (2016).

293 Shigemura, H., Tabuchi, M., Sakaebe, H., Kobayashi, H. & Kageyama, H. Lithium Extraction and Insertion Behavior of Nanocrystalline Li2TiO3 LiFeO2 Solid Solution with Cubic Rock Salt Structure. *Journal of The Electrochemical Society* **150**, A638-A644 (2003).

294 Zhang, L. *et al.* Synthesis and electrochemistry of cubic rocksalt Li–Ni–Ti–O compounds in the phase diagram of LiNiO2–LiTiO2–Li[Li1/3Ti2/3]O2. *Journal of Power Sources* **185**, 534-541 (2008).

295 Obrovac, M. N., Mao, O. & Dahn, J. R. Structure and electrochemistry of LiMO2 (M=Ti, Mn, Fe, Co, Ni) prepared by mechanochemical synthesis. *Solid State Ion.* **112**, 9-19 (1998).

296 Tabuchi, M. *et al.* Fine $Li_{(4-x)/3}Ti_{(2-2x)/3}Fe_xO_2$ ($0.18 \leq x \leq 0.67$) powder with cubic rock-salt structure as a positive electrode material for rechargeable lithium batteries. *Journal of Materials Chemistry* **13**, 1747-1757 (2003).

297 Lee, J. *et al.* A new class of high capacity cation-disordered oxides for rechargeable lithium batteries: Li-Ni-Ti-Mo oxides. *Energy & Environmental Science* **8**, 3255-3265 (2015).

298 Urban, A., Lee, J. & Ceder, G. The Configurational Space of Rocksalt-Type Oxides for High-Capacity Lithium Battery Electrodes. *Advanced Energy Materials* **4**, 1400478-n/a (2014).

299 Lee, J. *et al.* Unlocking the Potential of Cation-Disordered Oxides for Rechargeable Lithium Batteries. *Science* **343**, 519-522 (2014).

300 Islam, M. M. & Bredow, T. Lithium Diffusion Pathways in β-Li2TiO3: A Theoretical Study. *The Journal of Physical Chemistry C* **120**, 7061-7066 (2016).

301 Yabuuchi, N. *et al.* Origin of stabilization and destabilization in solid-state redox reaction of oxide ions for lithium-ion batteries. *Nature Communications* **7**, 13814 (2016).

302 Glazier, S. L., Li, J., Zhou, J., Bond, T. & Dahn, J. R. Characterization of Disordered Li(1+x)Ti2xFe(1–3x)O2 as Positive Electrode Materials in Li-Ion Batteries Using Percolation Theory. *Chem. Mat.* **27**, 7751-7756 (2015).

303 Wang, R. *et al.* A disordered rock-salt Li-excess cathode material with high capacity and substantial oxygen redox activity: Li1.25Nb0.25Mn0.5O2. *Electrochem. Commun.* **60**, 70-73 (2015).

304 Castellanos, M. & West, A. R. Order-disorder phenomena in oxides with rock salt structures: the system Li2TiO3-Mg0. *Journal of Materials Science* **14**, 450-454 (1979).

305 Murphy, S. T. & Hine, N. D. M. Point Defects and Non-stoichiometry in Li2TiO3. *Chem. Mat.* **26**, 1629-1638 (2014).

306 Zhang, L. & Noguchi, H. Novel Layered Li -Cr-Ti-O Cathode Materials Related to the $LiCrO_2$-Li_2TiO_3 Solid Solution. *Journal of The Electrochemical Society* **150**, A601-A607 (2003).

307 Yang, M. *et al.* Cation disordered rock salt phase Li2CoTiO4 as a potential cathode material for Li-ion batteries. *Journal of Materials Chemistry* **22**, 6200-6205 (2012).

308 Pieczonka, N. P. W. *et al.* Understanding Transition-Metal Dissolution Behavior in LiNi0.5Mn1.5O4 High-Voltage Spinel for Lithium Ion Batteries. *The Journal of Physical Chemistry C* **117**, 15947-15957 (2013).

309 Talyosef, Y. *et al.* The study of LiNi0.5Mn1.5O4 5-V cathodes for Li-ion batteries. *Journal of Power Sources* **146**, 664-669 (2005).

310 Xue, Y. *et al.* Investigation on preparation and performance of spinel LiNi0.5Mn1.5O4 with different microstructures for lithium-ion batteries. **5**, 13299 (2015).

311 Knight, J. C., Therese, S. & Manthiram, A. Delithiation Mechanisms in Acid of Spinel LiMn2-xMxO4 (M = Cr, Fe, Co, and Ni) Cathodes. *Journal of The Electrochemical Society* **162**, A426-A431 (2015).

312 Hunter, J. C. Preparation of a new crystal form of manganese dioxide: λ-MnO2. *Journal of Solid State Chemistry* **39**, 142-147 (1981).

313 Gummow, R. J., de Kock, A. & Thackeray, M. M. Improved capacity retention in rechargeable 4 V lithium/lithium-manganese oxide (spinel) cells. *Solid State Ion.* **69**, 59-67 (1994).

314 Qiao, R., Chin, T., Harris, S. J., Yan, S. & Yang, W. Spectroscopic fingerprints of valence and spin states in manganese oxides and fluorides. *Current Applied Physics* **13**, 544-548 (2013).

315 Mo, L.-B. *et al.* Band gap engineering of TiO2 through hydrogenation. *Applied Physics Letters*

105, 202114 (2014).

316 Krüger, P. Multichannel multiple scattering calculation of $L_{2,3}$-edge spectra of TiO_2 and $SrTiO_3$: Importance of multiplet coupling and band structure. *Physical Review B* **81**, 125121 (2010).

317 Thakur, H. *et al.* Irradiation induced ferromagnetism at room temperature in TiO_2 thin films: X-ray magnetic circular dichroism characterizations. *Applied Physics Letters* **98**, 192512 (2011).

318 Finkelstein, L. D. *et al.* Vacant states of TiO_2 with rutile structure and their reflection in different-type x-ray absorption spectra. *X-Ray Spectrometry* **31**, 414-418 (2002).

319 Gilbert, B. *et al.* Multiple Scattering Calculations of Bonding and X-ray Absorption Spectroscopy of Manganese Oxides. *The Journal of Physical Chemistry A* **107**, 2839-2847 (2003).

320 Yoon, W.-S. *et al.* Soft X-Ray Absorption Spectroscopic Study of a $LiNi_{0.5}Mn_{0.5}O_2$ Cathode during Charge. *Journal of The Electrochemical Society* **151**, A246-A251 (2004).